Optical flow estimation with subgrid model for study of turbulent flow

Cyril Cassisa

ÉCOLE CENTRALE LYON

N° d'ordre: 2011-10

Thèse de l'Université de Lyon

délivrée par l'École Centrale de Lyon

Spécialité: Mécanique des fluides

Soutenue publiquement le 7 Avril 2011
A Centrale Pékin dans l'Université de Beihang par

M. Cyril CASSISA

Préparée au Laboratoire de Mécanique des Fluides et d'Acoustique (LMFA)

Titre:

Optical flow estimation with subgrid model for study of turbulent flow

École Doctorale de Mécanique, Énergétique, Génie civil, Acoustique

---

Composition du jury

Jean-Claude	PAUL	DR INRIA & Pr. Tsinghua Univ	- *Rapporteur*
GuiXiang	CUI	Pr. Tsinghua University	- *Rapporteur*
Francis	LEBOEUF	Pr. ECL, LMFA	- *Examinateur*
Thomas	CORPETTI	CR CNRS, LIAMA	- *Examinateur*
Serge	SIMOENS	DR CNRS, LMFA	- *Directeur de thèse*
Liang	SHAO	CR CNRS, LMFA	- *Co-directeur de thèse*

UNIVERSITÉ DE LYON

Acknowledgements

This thesis was a wonderful adventure conducted between France and China. During these last years, I met many people, scientific or not, which helped me, in a way, to successfully accomplish this work. I would like to thank them all for everything.

First, I would like to thank my supervisor, Serge Simoëns, for taking me as his student and allowing me to pursue my research interest, and for his support, his advises and his friendship during the course of this thesis. I would like to thank my co-supervisors, Shao Liang and Véronique Prinet, for their scientific knowledge on turbulence modeling and computer vision respectively. Without them, it would never be possible to realize this thesis. A special thanks to the RSIU team for welcoming me in China during these years. Thanks to these three persons who helped me to write this manuscript.

I want to thank the two referees of my manuscript, Pr. Cui GuiXiang and Pr. Jean-Claude Paul for the time and energy they have put in reading my manuscript and their interesting and valuable comments on my work. I am also grateful to Pr. Francis Leboeuf and Dr. Thomas Corpetti for accepting to be members of the jury.

Also I would like to thank all professors and students from the Laboratory of Fluid Mechanics and Acoustics (LMFA) and the Sino-French Laboratory for Computer Science, Automation and Applied Mathematics (LIAMA). They helped me on both the work and the life when I was in France and China respectively, and they are also concerned with my thesis.

I would like to thank my colleagues at LMFA from the *Club Microfiche*: Philippe Eyraud, Loïc Méès, Wouter Bos, Rémi Zamansky, Delphine Chareyron, Aurélien Hémon, Antoine Godard and others for the nice atmosphere and the coffee break at work and for their discussions which extend my vision and my understanding of fluid mechanics. And I would like to thank my colleagues I met during the last years at LIAMA: Tang FengFeng, He LiangLiang, Charles Baubion, Vincent Etienne, Damien Roussat, Régis Behmo, Yves Piriou, JB Bordes, Tony, Antoine Lefebvre and others for their discussions on computer vision. Also special thank to them for all the good moments in China that we shared together.

Thanks also to my French and Chinese friends who nicely listen me speaking about non-interesting and hardly understandable scientific stuffs, with a special mentioning of Guillaume Coll for changing my mind when it was lost in my research problems and of Noah Schwartz for correcting some of my bad English.

The most special thanks are for all my family, particularly my parents, who support me all my life and encourage me in my choices. Special thanks to Guy Cassisa for having excited me with scientific exercises since my childhood.

Huge thanks to my wife, Wang Ying, to support me and take care of me every days. A last thanks to Cyril Cassisa for having finally completed this thesis before becoming crazy.

Contents

List of Figures

List of Tables

Chapter 1

Introduction

Contents

Atmospheric phenomena are of main importance to understand earth's general behavior such as the rapid climate change, which has received particular attention over the world. Consequently more investigations have being carried out. Over the last few decades, the use of satellites enables us to gather huge amounts of information over large geographic areas. Meanwhile development of new technology now allows more detailed investigations. Resolution, robustness and time acquisition rates of various prediction tools benefit constant improvement. Among the existing predictive techniques, remote sensing is becoming a major contributor not only for analyzing and understanding the phenomena, but also for help making political decisions to prevent human activities that increase the risk of natural disasters. However, physical phenomena themselves are not yet well understood nor fully measured. Different scientific communities around the world are currently working towards a better understanding of the underlying physics. The complexity of correlation pattern between different parameters leaves many rooms for further investigation and improvement.

1.1 Context

Atmospheric flows are known to be highly turbulent. Transportation of particles, aerosols and clouds is thus strongly depending on turbulence, which cannot be simply neglected for predictions. As an example, during the Iceland volcano eruption in spring 2010, dust and hash clouds were transported throughout the atmosphere by turbulent currents. The difference between reality and predictions clearly show that the latest atmospheric model simulations are still far from describing the exact physical phenomenon. Because of these uncertainties (mainly due to turbulence), governments are unable to know with sufficient precision where the particle clouds are going to pass. They have to make preventive decisions by closing airports, even far away from the real path of the clouds.

Turbulent motion fields exist not only in atmosphere. There are also present, in many other domains, as for example in aeronautics, hydraulics, nuclear and chemical engineering, environmental sciences, oceanography, astrophysics or even the human body inner flows. Understanding the physics of turbulence constitutes itself a challenging field of research.

It is well know that turbulent motions present a wide range of different time and space depending scales. Ideally, it is necessary to take the smallest scale interactions into account over extremely large domains and with a very small time frequency sampling. However, when performing calculations over large periods of time in practical situations, it is realistically impossible to compute the numerical solution with current calculation capabilities. Until now, modeling of turbulence is the only suitable solution for global prediction. This modeling needs often to be validated by experimental studies from which the velocity field determination at each time t is of main importance for the natural phenomena understanding and for validation of their simulations.

In practical applications, velocity field can be obtained by numerous techniques (Tachometer, Anemometer, Laser Doppler Anemometry, Hot wire, Particle Image Velocimetry, atmospheric balloon tracking...). Depending on the application, they can be more or less adapted to the situation either because of their size or their price. For details on velocity measurement techniques please refer to [149]. From all these techniques, Cross-Correlation PIV (CC) has a huge advantage to extract instantaneous velocity field for a large spatial 2D area. For In-Situ experiments or data collection as to describe atmospheric and oceanic currents geostationary satellite time sequences can be used. Efficiency and robustness of the estimated velocity field from these time image sequences, is then a key point of validation of turbulent models when applied to solve real situation where turbulence is involved.

Resuming to the context of the present thesis, we are working with natural fluid phenomena that are frequently highly turbulent. Turbulent motion is one of the most important information. It is necessary for understanding their behavior over the time. Regarding the existing prediction tools, image processing seems to be the most suitable and promising technique to estimate the velocity field due to the fast technology improvement. The main objective of this thesis is to further investigate the computer vision technique. The validation of estimations accounting for turbulence relies on further comparisons with reference data that can either be obtained from laboratory experiments or from direct Navier-Stokes equation simulations. It will also be the purpose of this work.

1.2 Motivation and Objectives

Many works have been done on motion estimation since last 30 years. The Optical Flow (OF) describes the apparent velocity field observed from a time image sequence. It exists two principal OF techniques: Cross-correlation (CC) and Differential Optical Flow (DOF) approaches. These methods deal with rigid and de-

formable motions, elastic motions, or fluid motions. Since the 21^{st} century, more efficient approaches have been proposed. However, despite the incredible amount work done over the years, fluid motion in a turbulent environment has still not been considered. Thus, motion estimation of turbulent flow cannot exclusively rely on traditional computer vision techniques. The motion of studied physical quantities is directly linked to the observed quantity, which obeys physical rules defined by known physical properties.

This thesis focuses on motion estimation of scalar transported by a turbulent flow given two-successive in time images. Most of the existing techniques fail to accurately estimate the turbulence. The objective of our work is to propose and validate an original approach that is based on a physical formulation, in the case of scalar transported by turbulent flow.

The evolution of scalar field does not satisfy the brightness constancy hypothesis in time made by classical motion estimation approaches as CC and DOF ones. The scalar concentration evolution is exactly defined by the concentration transport equation with molecular diffusion [160]. However the discretized information imposed by the image recording brings us to consider the fact that the input image sequence has some missing information. This lack of information may not be negligible when the turbulence is high. Referring to the concept of large eddy simulation (LES) of turbulence [139], the resolved information, given by image pixel values, can be seen as related to resolved large-scales eddies. The lack of information could be assimilated as sub-pixel or sub-grid information, i.e., unsolved small-scales of turbulence. Small-scales of the flow cannot be directly extracted from the data while its effects on resolved velocity field are important in highly turbulent flows. They must be modeled in the motion equation. After the filtering - in the LES sense - of the exact concentration equation at a given spatial scale corresponding to the size of pixel, the unsolved small scales appear in the equation as an explicit sub-grid term. This term is usually modeled using a turbulent sub-grid eddy viscosity concept [153] because its main physical property is turbulent diffusion.

Given a time image sequence, the estimation of the velocity field from the filtered concentration transport equation with diffusion is an ill-posed problem. Probabilistic approaches based on a graph, as Markov Random Fields (MRF), are very convenient to define a formulation of a specific problem in image processing. We add a global constraint to mathematically well pose the problem [98]. The constraint is a spatial regularization constraining the spatial distribution of the adjacent turbulent velocity field by a first order derivative function. The choice of this regularization function is familiar in the motion estimation algorithms. Advantage of MRF framework is that it generally allows to use a wider range of functional, while ensuring to find a global (exact or approximated) solution, without being limited to convex functions [168] unlike other popular approaches as variational methods. However, optimization methods for MRF framework are generally defined for finite dicretized random field. In our case, the unknown velocity field is a 2D real velocity field. We propose a complete optimization scheme coupling multiresolution without warping and multigrid technique with an adapted minimization method to find the optimal

solution within a correct computational cost.

To the best of our knowledge, such a way of incorporating turbulence models into the filtered transport equation for motion estimation from time image sequence has never been investigated before. Our work shows that the sub-grid scale model in the filtered concentration equation, improves motion estimation. It opens an interesting new field of research which may lead to a better understanding of passive scalar spread by turbulent flows. This thesis is a multi-disciplinary work from which the aim is to converge knowledge and techniques from fluid mechanic (turbulence) and computer vision (image processing) scientific communities.

1.3 Overview of the thesis

The first part of the thesis proposes an efficient Differential Optical Flow (DOF) approach working on motion equation, large displacement estimation technique and minimization methods [125, 33, 34, 32, 38]. The second part will focus on a physical formulation of the motion equation and on improvements on the DOF approach due to the turbulent viscosity term. This will be studied in the case of scalar transported by turbulent flows [35, 36, 37].

In the second chapter, necessary background requirement on fluid mechanics and turbulence are given. We recall physical equations and present the concept of turbulence and its consequence on the velocity field. We then describe different possibilities in turbulence modeling.

The following chapter describes the motion estimation technique from time image sequence (section 3.1). We only detail the DOF methods to retrieve the flow motion. Description of DOF methods is presented for ordinary motion applications (section 3.2). We will pay special attention to DOF methods defined for fluid motion estimation (section 3.3). For comparison, appendix A describes the Cross-Correlation PIV (CC) technique used to determine velocity field from PIV acquisition in laboratory experiments.

In fourth chapter, we propose an efficient DOF approach. For taking into account more spatial information, motion equation based on the two successive image gradients is defined (section 4.1). To tackle the limitation of DOF equations for large displacements, we propose an unwarping multiresolution by pyramidal decomposition (section 4.2) for which assumption on gradients is made to reduce the number of transformations during the process. We also compare and suggest some improvements of optimization methods (appendixes C and E) for MRF formulation. Results on different type of motions are compared with other existing DOF and CC methods (sections 4.5 and 4.6).

In the fifth chapter, we now treat the problem of scalar transported by turbulent

flow. Based on the proposed algorithm of chapter 4, we suggest a new motion estimation method which takes into account the unresolved scale effect (sub-pixel) on the resolved velocity (pixel resolution) for high turbulent flows for which this effect is, in this case, not negligible and affect the dynamic of the flow. Thus, we use the filtered concentration transport equation with molecular diffusion where the small scale interactions are modeled by a classic turbulent sub-grid eddy viscosity model (section 5.2). Results of application on synthetic and real-time sequences of scalar transport (section 5.3) and solid particles seeding in turbulent flow (section 5.4), are very encouraging and promising. In the last section 5.5, we apply our model to atmospheric events such as dust storms. Remote sensing from geostationary satellite image sequences allows us to estimate the dust cloud motion from our method. A homogeneous invariant brightness method is added to the model to deal with the day light variations.

Conclusions and future directions are presented in chapter 6.

Chapter 2

Fluids and Turbulence

Contents

This chapter gives an introduction of fluids and turbulence. Two descriptions, Lagrangian and Eulerian, can be used to describe the movement of fluid. Fundamental fluid equations such as Continuity, Scalar transport with molecular diffusion and Navier-Stokes equations are presented. For more information on fluid dynamics, we can refer to [15]. An introduction on turbulence is given and different main approaches used to solve numerically the Navier-Stokes equations are aborded in order to demonstrate the difficulty of the turbulence accounting. More details on turbulence and numerical models can be found in [103, 124].

2.1 Movement Representation

2.1.1 Particle and mathematical points

Fluids (gases and liquids) can be viewed at different scales. At molecular scale ($L_{micro} \approx 10^{-20} m$) they are in permanent movement, chocking each others. Description of the motion behavior at this scale is given by Brownian motion. For

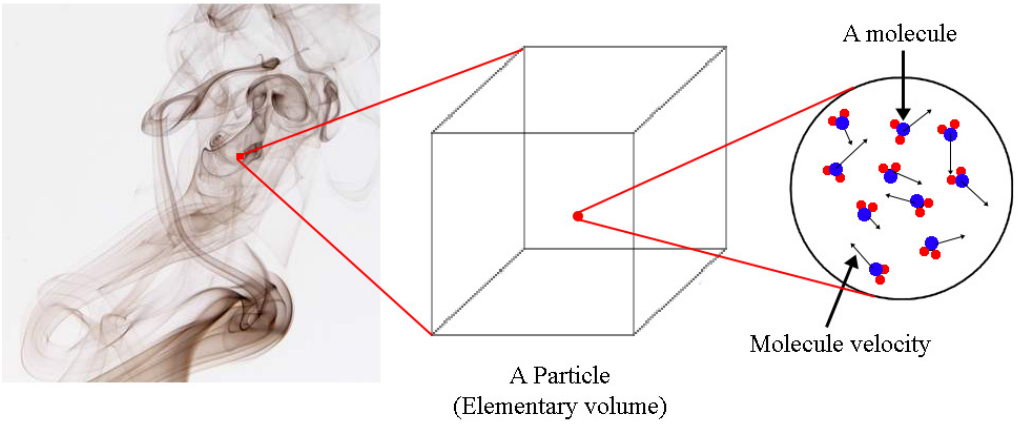

Figure 2.1: *Illustration of different scales and representation of a particle.(photo from* `http://www.astrographics.com/GalleryPrints/Display/GP4293.jpg` *)*

fluid mechanics description, fluid is observed at scale $L_{macro} > 10^{-6}m$, higher than the molecular free path λ determined by the Knudsen number $Kn = L/\lambda > 1$. Physical quantities (density, velocity, pressure...) at scales L_{macro} can be considered continuous in space and time. Elementary volume domain of the smallest scale is called particle or material point P. It has a closed surface of elementary volume dv of density ρ. Figure 2.1 illustrates the different scales representations for an example of smoke evolving in a flow.

A particle has a defined spatial position $\mathbf{X}_p(t_0) = (x_0, y_0, z_0)$ at time t_0 and its position $\mathbf{X}_p(t)$ varies at each time t. In the above example figure 2.1, an interesting goal would be to study the smoke motion. To study this evolution we need to consider the time and space dimensions. Two principal movement descriptions, Lagrangian and Eulerian, could be developed.

2.1.2 Lagrangian / Eulerian descriptions

We can follow the behavior of the particles over the time (Lagrangian) or stay at a fixed position to see different particles going through the position (Eulerian). Figure 2.2 represents the two motion descriptions for two successive times t and $t + dt$.

Lagrangian description: In the Lagrangian description, the observer follows the position and physical properties of the particle P that moves depending on time t. In figure 2.2, the observer look the particle P_1 at position $\mathbf{X}_{P_1}(t)$ at time t and goes to the position $\mathbf{X}_{P_1}(t+dt)$ at time $t+dt$. Positions and deformations of the particle take into account all the history from the initial state at (x_0, y_0, z_0) and time t_0.

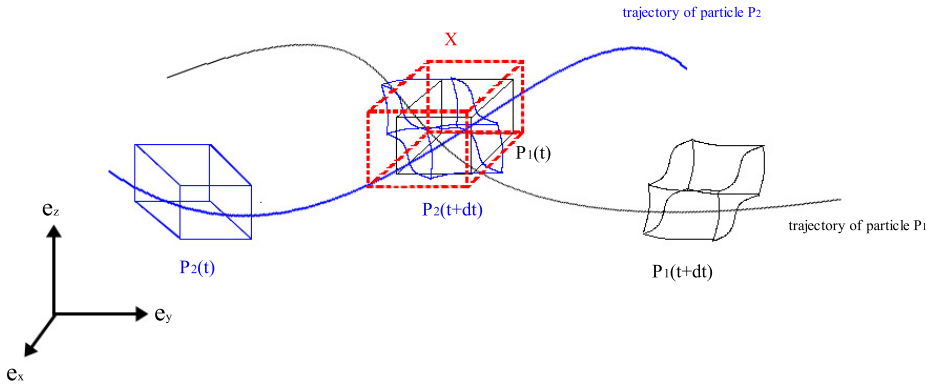

Figure 2.2: *Difference between Lagrangian and Eulerian descriptions.*

The position $\mathbf{X}_p(t)$ at time t is given by:

$$\mathbf{X}_p(t) = \begin{cases} x = f(x_0, y_0, z_0, t) \\ y = g(x_0, y_0, z_0, t) \\ z = h(x_0, y_0, z_0, t) \end{cases} \tag{2.1}$$

where f, g, h are three continuous functions. Lagrangian description may be interesting for studying the behavior evolution of particles over the time as for example the evolution of smoke propagation or dust cloud displacement in the atmosphere during a dust storm event. However, identification of each particle and their tracking can be very difficult.

Eulerian description: In the Eulerian description, the observer stays at a fixed position and describes the evolution of the flow. He does not follow a particle over time axis, but observes the evolution of quantities going through a fixed position $\mathbf{X} = (x, y, z)$ (mathematical point) at each time. In figure 2.2, for point $\mathbf{X}$ at time t, the Eulerian description observes physical quantities of particle $P_1(t)$. At time $t + dt$, he will observe physical quantities of particle $P_2(t + dt)$. For example, one common used physical quantity in Eulerian description is the velocity field $\vec{V}$ defined by its components (U, V, W) as:

$$\vec{V}(\mathbf{X}, t) = \begin{pmatrix} U(x, y, z, t) \\ V(x, y, z, t) \\ W(x, y, z, t) \end{pmatrix} \tag{2.2}$$

$\vec{V}(\mathbf{X}, t)$ is the velocity at fixed point $\mathbf{X}$ for t fixed. This description is often used in fluid mechanics where kinematic properties of the flow are of greater interest than

the shape of a part of the fluid at a reference time t. It is also more convenient in a mathematical point of view, because the spatial domain is fixed. Moreover, in the case of computer vision, Eulerian description fits directly from the image pixel representation. In this thesis, we use this description to describe the motion of the fluid.

Note that we will use $\mathbf{x} = (x, y)$ to represent the point $\mathbf{X} = (x, y, z)$ on the 2D image. At fixed t, $\mathbf{X} = \mathbf{X}_P$ for the particle $\mathbf{X}_P$ located at the point $\mathbf{X}$.

2.1.3 Total Derivative

The Eulerian description defines at each time t the value of a physical quantity φ related to a fixed position of the flow. The variation of this quantity over the time is described by a partial derivative, also called Eulerian derivative. Relation between total derivative and partial derivative of the quantity φ is as follow:

$\varphi(\mathbf{X}_p(t), t)$ depends on time t and its position $\mathbf{X}_p(t) = (x, y, z)$. During an interval of time dt, the particle $\mathbf{X}_p(t) = \mathbf{X}$ at time t has moved to the position $\mathbf{X}_p(t+dt)$ by a displacement $\vec{V}dt$ from its old position ($\mathbf{X}_p(t+dt) = \mathbf{X}_p(t) + \vec{V}dt = \mathbf{X} + \vec{V}dt$).
Variation of the quantity φ is:

$$d\varphi = \varphi(x + Udt, y + Vdt, z + Wdt, t + dt) - \varphi(x, y, z, t) \tag{2.3}$$

First order Taylor expansion gives:

$$d\varphi = \frac{\partial \varphi}{\partial t}dt + Udt\frac{\partial \varphi}{\partial x} + Vdt\frac{\partial \varphi}{\partial y} + Wdt\frac{\partial \varphi}{\partial z} \tag{2.4}$$

Dividing by dt, we have the total derivative usually written as D/Dt:

$$\frac{D\varphi}{Dt} = \frac{\partial \varphi}{\partial t} + U\frac{\partial \varphi}{\partial x} + V\frac{\partial \varphi}{\partial y} + W\frac{\partial \varphi}{\partial z} \tag{2.5}$$

In vector notation:

$$\frac{D\varphi}{Dt} = \frac{\partial \varphi}{\partial t} + \vec{V}.\vec{\nabla}\varphi \tag{2.6}$$

The total derivative is made of two parts:

- $\partial\varphi/\partial t$ is the local rate of change of φ at a given point representing the unsteady behavior of the flow.
- $\vec{V}.\vec{\nabla}\varphi$: is called the convective derivative due to the displacement of the particle, because it is the change, in φ, as a result of convection of the particle from one position to another where the values of φ are different. This convective term is generally non-linear.

The total derivative can be applied to any scalar or vectorial quantities characterizing a fluid particle like density ρ, scalar concentration C, pressure p or velocity $\vec{V}$.

We will see in section 3.2 that the total derivative is the base of the differential optical flow equation proposed by Horn and Schunck in 1981 [77] and improved by others.

2.2 Fundamental Equations

All fluid mechanics is based on conservation laws as for mass, momentum, and energy. These laws can be stated in the differential form, applicable at a point (Eulerian description). Conservation laws in Lagrangian description exist, but in our case of study, they are not adapted to the image recordings used for this work. For that, Eulerian forms are more convenient. We present here the continuity equation, the advection-diffusion equation and Navier-Stokes equations.

2.2.1 Continuity Equation

In fluid dynamics, continuity equation is based on the process that variation of quantity in an infinitesimal volume is equal to the quantity of flow going through the volume surface.
$\mathcal{D}(t)$ is a material volume domain and $\mathcal{S}(t)$ its surface at time t. The density by unity of volume dv is $\rho(\mathbf{X},t)$.
The total mass of $\mathcal{D}(t)$ is: $m = \int_{\mathcal{D}(t)} \rho(\mathbf{X},t)dv$. Hypothesis of mass conservation gives the equality:

$$\frac{dm}{dt} = \frac{d}{dt}\int_{\mathcal{D}(t)} \rho(\mathbf{X},t)dv = 0 \tag{2.7}$$

Using the Reynolds transport theorem (see [132] for demonstration), we can express the time derivative of a volume integration.

$$\frac{d}{dt}\int_{\mathcal{D}(t)} \varphi(\mathbf{X},t)dv = \int_{\mathcal{D}(t)} \frac{\partial\varphi(\mathbf{X},t)}{\partial t}dv + \int_{\mathcal{S}(t)} \varphi(\mathbf{X},t)\vec{V}(\mathbf{X},t).\vec{n}ds \tag{2.8}$$

The first term represents the unsteady behavior of $\varphi(\mathbf{X},t)$ and the second term the movement of the surface $\mathcal{S}(t)$ ($\vec{n}$ is the normal to $\mathcal{S}(t)$). $\varphi(\mathbf{X},t)$ is a physical quantity that is here the density $\rho(\mathbf{X},t)$.

The mass conservation equation is then:

$$\int_{\mathcal{D}(t)} \frac{\partial\rho(\mathbf{X},t)}{\partial t}dv + \int_{\mathcal{S}(t)} \rho(\mathbf{X},t)\vec{V}(\mathbf{X},t).\vec{n}ds = 0 \tag{2.9}$$

Using the divergence theorem: $\int_{\mathcal{S}} \rho(\mathbf{X},t)\vec{V}(\mathbf{X},t).\vec{n}ds = \int_{\mathcal{D}} \vec{\nabla}.(\rho(\mathbf{X},t)\vec{V}(\mathbf{X},t))dv$.
We obtain:

$$\int_{\mathcal{D}(t)} \left[\frac{\partial\rho(\mathbf{X},t)}{\partial t} + \vec{\nabla}.(\rho(\mathbf{X},t)\vec{V}(\mathbf{X},t))\right] dv = 0 \tag{2.10}$$

Because this integral is null for all volume domain $\mathcal{D}(t)$, that implies the expression to be null for each particle (point) of the domain. The continuity equation is finally:

$$\frac{\partial\rho(\mathbf{X},t)}{\partial t} + \vec{\nabla}.(\rho(\mathbf{X},t)\vec{V}(\mathbf{X},t)) = 0 \tag{2.11}$$

This equation can be rewritten as:

$$\frac{D\rho(\mathbf{X},t)}{Dt} + \rho(\mathbf{X},t)\vec{\nabla}.\vec{V}(\mathbf{X},t) = 0 \tag{2.12}$$

In the case of an incompressible fluid, the density of a fluid particle is constant over the time $D\rho/Dt = 0$. Thus, the continuity equation of incompressible fluid is simplified and becomes for each time t:

$$\vec{\nabla}.\vec{V}(\mathbf{X}, t) = 0 \tag{2.13}$$

We will see in section 3.3 that the continuity equation considering a compressible fluid has been linked to optical flow estimation at the beginning of the 21^{st} century in works of [16], [47] or [191]. In our work, we consider the fluid as incompressible, which is a correct hypothesis in the case of aerosols in the atmosphere.

2.2.2 Convection Diffusion Equation

Convection diffusion equation, also called scalar transport equation with molecular diffusion, can be retrieved as for the continuity equation adding the fact that the scalar quantity of the fluid can diffuse (Fick's first law). The rate of change for a scalar quantity C of a fluid particle is given by flow and diffusion into and out of its elementary domain along without any generation or consumption inside:

$$\frac{\partial C(\mathbf{X}, t)}{\partial t} + \vec{\nabla}.\vec{J} = 0 \tag{2.14}$$

Where $\vec{J}$ is the total flux. The total flux is the summation of the convective scalar flux $C\vec{V}$ and the diffusive scalar flux. The diffusive flux is obtained by the Fick's first law which assumes that the flux of the diffusing material in any part of the global system is proportional to the local gradient of C.

$$\vec{J} = C\vec{V} - D\vec{\nabla}C \tag{2.15}$$

where D is the molecular diffusion coefficient (unity m^2/s).
The convection diffusion equation can be written as:

$$\frac{\partial C(\mathbf{X}, t)}{\partial t} + \vec{\nabla}.(C\vec{V}) - D\nabla^2 C = 0 \tag{2.16}$$

For incompressible fluid, the convection diffusion equation becomes:

$$\frac{\partial C(\mathbf{X}, t)}{\partial t} + \vec{V}.\vec{\nabla}C - D\nabla^2 C = 0 \tag{2.17}$$

The scalar transport equation allows to describe the time behavior of scalar quantity considering the molecular diffusion effects. In 1996, Su and Dahm [160, 161] proposed to use this equation for estimating the motion and concentration field of the scalar in a laboratory channel flow. In our work, we want to estimate the motion of scalar carried by a turbulent fluid. This equation will be the basis of our approach.

2.2.3 Navier-Stokes Equations

Navier-Stokes equations arise from applying Newton's second law to fluid motion ($m\frac{D\vec{V}}{Dt} = \sum \vec{f}$) for a fluid particle.

$$\rho\frac{D\vec{V}}{Dt} = \vec{\nabla}.\vec{\vec{\sigma}} + \rho\vec{f} \tag{2.18}$$

where ρ is the density of the fluid, $D\vec{V}/Dt$ the acceleration of the fluid particle, $\vec{f}$ are the volume forces applying to the density of the fluid particles (for example the gravity). $\vec{\vec{\sigma}}$ is the constraint tensor (fluid stress) that represents forces on the fluid particle surface. For incompressible Newtonian fluid, the constraint tensor can be expressed by:

$$\vec{\vec{\sigma}} = -p\vec{\vec{I}} + 2\mu\vec{\vec{D}} \tag{2.19}$$

where p is the pressure that pushes with a force normal to the surface. $\mu\vec{\vec{D}}$ is the viscosity constraint that represents the force on the surface of the particle that tends to stretch it due to viscosity μ ($kg.m^{-1}.s^{-1}$) of fluid particles between each other. Naturally, this force is related to the tensor $\vec{\vec{D}}$, which is the deformation tensor depending on local velocity gradients.

$$D_{ij} = \left(\frac{\partial V_j}{\partial x_i} + \frac{\partial V_i}{\partial x_j}\right) \tag{2.20}$$

with $i, j = (1, 2, 3)$, $(x_1, x_2, x_3) = (x, y, z)$ and $(V_1, V_2, V_3) = (U, V, W)$. Simplifying the Navier-Stokes equations for an incompressible Newtonian fluid, we obtain:

$$\frac{\partial\vec{V}}{\partial t} + \vec{V}.\vec{\nabla}\vec{V} = -\frac{1}{\rho}\vec{\nabla}p + \nu\nabla^2\vec{V} + \vec{f} \tag{2.21}$$

$\nu = \mu/\rho$ the kinematic viscosity ($m^2.s^{-1}$).

The Navier-Stokes equations give an exact description of the evolution of the fluid depending on its initial conditions and fluid properties (ρ, μ). They are the basis of the fluid dynamics. There are only three equations for four unknown (U, V, W and p). It is often added the mass conservation equation in the case of incompressible fluid. Defining the initial conditions, the problem is closed and can be computed. However, due to non linearity of the equation system, principally due to the convection terms, the numerical resolution is very complex. Only scarce flow can be directly computed nowadays because of computer limitations.

The Navier-Stokes equations need a local time sequence of the flow field. In the case of optical flow, it is hardly usable, but recent approaches (2007) proposed to use this as regularization to constrain the flow to have a time fluid coherence [138, 74].

2.2.4 Dimensionless Equations

All the presented fluid equations have dimensional parameters. In fluid dynamics, it is better to transform the equations in a non dimensional form.

To reduce the equations to dimensionless parameters, we define a characteristic scale for each quantity. In the mass, scalar transport with molecular diffusion and Navier-Stokes equations, these scales are T_c, L_c and U_c. Thus:

$$\frac{\mathbf{X}}{\mathrm{L}_c} = \mathbf{X}^* \quad \frac{\vec{V}}{\mathrm{U}_c} = \vec{V}^* \quad \frac{t}{\mathrm{T}_c} = t^* \tag{2.22}$$

are dimensionless. Doing the variable changes in the equations (2.12), (2.17) and (2.21), we obtain respectively, the mass, scalar transport with molecular diffusion and Navier-Stokes non-dimensional equations:

$$\frac{\partial \rho}{\partial t^*} + \vec{V}^*.\vec{\nabla}^*\rho = 0 \tag{2.23a}$$

$$\frac{\partial C}{\partial t^*} + \vec{V}^*.\vec{\nabla}^* C - \frac{1}{ReSc}\nabla^{*2} C = 0 \tag{2.23b}$$

$$\frac{\partial \vec{V}^*}{\partial t^*} + \vec{V}^*.\vec{\nabla}^*\vec{V}^* = -\vec{\nabla}^* p^* + Re^{-1}\nabla^{*2}\vec{V}^* \tag{2.23c}$$

where the dimensionless parameters are $Re = \mathrm{U}_c\mathrm{L}_c/\nu$ and $Sc = \nu/D$. They are respectively the Reynolds number that characterizes the rate of turbulence of the flow and the Schmidt number that represents the diffusivity of the fluid. Note that here; we considered a fluid without volume forces. For an easier readability, we omitted symbol * in the rest of the paper.

In this work, we are focused on turbulent flow. That means high Reynolds number ($Re >> 1$). In turbulent flow, convective terms are dominant.

2.3 Turbulence

Most of the flows encountered in engineering practice and in nature are turbulent. Atmospheric flows, oceanic currents are turbulent. Many other examples of turbulent flows arise in aeronautics, hydraulics, nuclear and chemical engineering, environmental sciences, oceanography, astrophysics... More details on turbulence theory and its applications can be found in [103, 124].

Turbulence remains a huge challenge in the science community nowadays, because its understanding will help us to predict hurricanes, global climate changes, pollution dispersion, energy consumption optimization...

An historical description of turbulence can be found in [114].

2.3.1 Physical Point of View

A good way to survey the turbulence world is through flow motion hand book [56] that shows pictures of different turbulent flows in its variety of application. Another way is to characterize certain number of observable physical properties (more details can be found in [96, 61]). We enumerate here some characteristics of turbulence flows transporting a scalar:

- Dispersion: Turbulent flows can mix transported quantities much faster than if only molecular diffusion is involved. For example, to heat a room, it is better to spread hot air by turbulent jet whereas using hot wires. In this way diffusion of temperature over all the room will be faster due to the high rate of turbulent dispersion. In engineering, efficiency and rapidity of diffusion in an environment may be very important (fuel in engine, heat diffusion ...).

- Random behavior: Physical variables of the flow (velocity and pressure) vary randomly in time and space under turbulence. It is possible to make a statistical description of the turbulent flow solving, for example, average transport equation of velocity and pressure.

- Continuum phenomena in space and time: The smallest scales that appear in a turbulence flow will always be much larger than molecular length scales. In this way, continuum properties can still be applied to turbulent flow quantities.

2.4 Numerical Approaches to Turbulence

From previous sections, we have seen that physical approach does not give nowadays a complete answer of the understanding of turbulence. However, as we already said, most of the flows in the nature and in industrial domains are frequently turbulent. Lot of phenomena as heat or scalar transfers are related to the movement of the fluid. Their study needs some knowledge and computation of flow under consideration. In this way, in engineering and research, numerical simulation of turbulent flows is very important for practical applications (industrial, environmental, medicine...). Numerical simulation emerges as an essential approach in tackling turbulence. Even though, numerical simulation still remains a hard topic and an exciting research domain.

The quality of given information from numerical simulation depends on the level of chosen resolutions to obtain the best possible precision, the simulation have to consider all spatial and time scales that contribute to the dynamic of the flow.

Numerical simulation, direct or using statistic models, took place in the beginning 60's. This evolution is directly related to the improvement of computers. In the 70's, big computers allowed to simulate without statistical models (direct simulation), movement of homogeneous isotropic turbulence for small Reynolds number.

In the next section, we present some methods involved in numerical simulation of turbulent flows: Direct Numerical Simulation (DNS) [182] and two statistical modeling way of turbulence: Reynolds Average Navier-Stokes (RANS) [90] and Large Eddy Simulation (LES) [139].

2.4.1 Direct Numerical Simulation (DNS)

In the Navier-Stokes equations, the fluid is treated as continuum compared to molecular scale. According to this point of view, the most natural idea is to find the turbulent solutions of Navier-Stokes equations by resolving directly the equations.

That means to compute all scales of the flow that compose the turbulent kinetic energy spectrum (from energetic scales to dissipative scales) [87]. The benefit of DNS is to obtain in detail all information of the turbulence. This allows to understand the dynamic of the turbulence and to evaluate lot of quantities that are unreachable experimentally.

To numerically represent the totality of these spatial and time scales, it is necessary for the discretization to be fine enough. That means, the discretization step in space ($\Delta x, \Delta y, \Delta z$) and time ($\Delta t$) of the simulation are respectively smaller than the characteristic length scales and characteristic time scale related to the smallest active ones of the exact solution.

From Kolmogorov cascade theory [87], we can show that the ratio between scales of largest eddies and Kolmogorov scale (scale that characterizes the smallest non laminar scales) is proportional to $Re^{3/4}$. It implies that to get all scales which appear in turbulent flow, we have to use a grid mesh with a number of points in each direction of space proportional to $Re^{3/4}$. That makes an order of $Re^{6/4}$ mesh points for a bidimentional grid or $Re^{9/4}$ mesh points for a tridimentional domain. To give an idea of the Reynolds number amplitude, here are some examples in the air ($\nu \approx 15.10^{-6} m^2.s^{-1}$):

- Cars ($\mathrm{U}_c \approx 3m.s^{-1}$, $\mathrm{L}_c \approx 1m$): $Re \approx 10^6$
- Airplane wings ($\mathrm{U}_c \approx 30m.s^{-1}$, $\mathrm{L}_c \approx 5m$): $Re \approx 10^8$
- Atmospheric flows ($\mathrm{U}_c \approx 10m.s^{-1}$, $\mathrm{L}_c \approx 1km$): $Re \approx 10^{10}$

In so, for cars $Re \approx 10^6$, the number of mesh points would be in 2D: $\mathbf{N} = Re^{6/4} = 10^9$ and in 3D: $\mathbf{N} = 10^{13.5}$. Nowadays, DNS with such number of mesh points is not able due to insufficient computational resources. Looking for the computational cost this type of simulation can be used only for relative simple flows with a limited Reynolds number.

DNS is an exact way to simulate turbulent flows, but it is unable to simulate high Reynolds number turbulent flow because of computer capability. Most of the existing methods in numerical simulation of high Reynolds number flow are based on the insight gained from the phenomenological description of turbulence. These methods model turbulent fluctuations, from Reynolds or Favre decomposition [57] point of view, and can compute the most interesting statistical quantities. However, DNS can be useful to validate these models of turbulence for simple well-known cases.

2.4.2 Reynolds Average Navier-Stokes (RANS)

One of the most important characteristic of turbulent flows is its random character. It seems, then, not able to describe the turbulent motion in all details as a function of time and space coordinates, but it is able to define average values of flow variables (velocity, pressure, scalar concentration) [90].

Reynolds proposed in 1895 [131] a statistical approach. He proposed to separate instantaneous velocity $\vec{V}$ and pressure p variables into a mean (average) component, $\overline{\vec{V}}$ and $\overline{p}$ and a turbulent component (fluctuation), $\vec{V}'$ and p' respectively:

$$\vec{V} = \overline{\vec{V}} + \vec{V}' \qquad\qquad p = \overline{p} + p' \tag{2.24}$$

Time average variables of the flow are defined as:

$$\overline{\vec{V}}(\mathbf{X}, t) = \frac{1}{\mathrm{T}_R} \int_t^{t+\mathrm{T}_R} \vec{V}(\mathbf{X}, t_r) dt_r \tag{2.25a}$$

$$\overline{p}(\mathbf{X}, t) = \frac{1}{\mathrm{T}_R} \int_t^{t+\mathrm{T}_R} p(\mathbf{X}, t_r) dt_r \tag{2.25b}$$

where T_R is a chosen time scale which is high enough compare to turbulent time scale. In case of stationary, for large T_R, average variables do not depend on time t, equation (2.25) gives:

$$\overline{\vec{V}}(\mathbf{X}) = \frac{1}{\mathrm{T}_R} \int_0^{\mathrm{T}_R} \vec{V}(\mathbf{X}, t_r) dt_r \tag{2.26a}$$

$$\overline{p}(\mathbf{X}) = \frac{1}{\mathrm{T}_R} \int_0^{\mathrm{T}_R} p(\mathbf{X}, t_r) dt_r \tag{2.26b}$$

When $\mathrm{T}_R \to \infty$, we have the following properties (identical for all flow variables):

$$\overline{\overline{\vec{V}}} = \overline{\vec{V}} \qquad\qquad \overline{\vec{V}'} = 0 \tag{2.27}$$

Doing time average of the Navier-Stokes equations (2.23c) and continuity equations (2.23a) using decomposition (2.24) and its properties (2.27), we obtained the Reynolds equations for average quantities:

$$\frac{\partial \overline{\vec{V}}}{\partial t} + \overline{\vec{V}}.\vec{\nabla}\overline{\vec{V}} = -\vec{\nabla}\overline{p} + Re^{-1}\nabla^2\overline{\vec{V}} + \overline{\vec{f}} + \vec{\nabla}.\overrightarrow{\overrightarrow{\tau_{Re}}} \tag{2.28a}$$

$$\vec{\nabla}.\overline{\vec{V}} = 0 \tag{2.28b}$$

Where $\overrightarrow{\overrightarrow{\tau_{Re}}} = \overline{\vec{V}\vec{V}} - \overline{\vec{V}}\,\overline{\vec{V}}$ is called Reynolds stress tensor.

The Reynolds stress tensor is unknown variable. The system of Reynolds equation is not anymore a closed system. We could model τ_{Re} to ensure the conservation of fundamental characteristics of the Navier-Stokes equations. This is called one point statistical modeling. Reynolds stress tensor is usually modeled in terms of the average flow variables.

2.4.3 Large Eddy Simulation (LES)

Large Eddy Simulation (LES) [139], in a similar way, use another decomposition of the flow variables of turbulent flow. Large Eddy Simulation (LES) concept relies on the use of a filter which removes numerically unsolvable small scales.

LES is based on the decomposition of instantaneous dynamic variable fields of the flow in two parts corresponding to structures of different sizes. This method separates large scales isolating them by filtering unresolved small scales. The filtering can be done in spatial or spectral space. In the case of spatial space, flow velocity variable is composed as:

$$\vec{V} = \vec{V}^{+} + \vec{V}^{-} \tag{2.29}$$

where $\vec{V}^{+}$ is the resolved velocity (large scales) and $\vec{V}^{-}$ is the unresolved velocity of unresolved small scales. The filtered field representing resolved scales could be defined by a convolution with a filter of bandwidth Δ_s around the point $\mathbf{X}$:

$$\vec{V}^{+}(\mathbf{X}, t) = \int_{\Delta_s} \vec{V}(\mathbf{X}', t)\, \mathcal{W}(\mathbf{X} - \mathbf{X}')\, d\mathbf{X}' \tag{2.30}$$

where $\mathcal{W}$ is the filter. In LES, there are usually three types of spatial filter (see [139]): Top-hat, Gaussian or cutoff. The filters depend on the used numerical approach.

Filtering the Navier-Stokes equations using equation (2.30), we get the following filtered equations:

$$\frac{\partial \vec{V}^{+}}{\partial t} + \vec{V}^{+}.\vec{\nabla}\vec{V}^{+} = -\vec{\nabla}p^{+} + Re^{-1}\nabla^2\vec{V}^{+} + \vec{f}^{+} + \vec{\nabla}.\overrightarrow{\overrightarrow{\tau_s}} \tag{2.31a}$$

$$\vec{\nabla}.\vec{V}^{+} = 0 \tag{2.31b}$$

We obtain an open system due to the unknown term $\overrightarrow{\overrightarrow{\tau_s}} = \left(\vec{V}\vec{V}\right)^{+} - \vec{V}^{+}\vec{V}^{+}$ which is the constraint tensor called sub-grid scale tensor. To model the sub-grid scale tensor, a concept such as turbulent viscosity is generally used. In chapter 5, we will assimilate information given by images with resolved scales of the physical quantity of LES. A simple subgrid scale model will be suggested to improve motion estimation of scalar carried by turbulent flow from time image sequence. For more details on LES sub-grid scale models refer to [139].

LES can be viewed as a hybrid approach between DNS and RANS. It consists to do a complete simulation for resolved turbulent structures and a partial one, modeling unresolved turbulent structure contribution.

2.5 Conclusions

This chapter gives a brief overview of the different points of view that can be adopted to describe fluid motion. In this work, we will use Eulerian motion description because equations governing the flow are well defined in this representation and

because main parts of the laboratory observations are Eulerian. Fluid motion are describes by equations which define evolutions of fluid particle over the time. At low Reynolds number, flow is laminar. Solution can be computed. However when the Reynolds number becomes high, flow regime changes and becomes turbulent. As we saw in section 2.3, solution of fluid motion equations is difficult to reach. Many modeling approaches exist allowing simulation of the flow evolution.

An important point, for understanding turbulent flows, is experiments. From experiments, DNS or turbulence model simulation results could be validated by comparison. Quality of the estimation of the velocity field is thus very important. It is a key point for the validation of turbulent models when applied to solve real situation where turbulence is involved.

Numerical simulations of turbulent flows also need initial conditions. For small variations of initial conditions, solutions of these numerical simulations may diverge. In case of atmospheric flows, a good estimation of cloud, dust or wind motions can be set as initial condition to numerical simulation with the aim to get a better prediction of their transport in the atmosphere.

The next chapter will give descriptions of principal motion estimation approaches and state of the art algorithms in these fields.

Chapter 3

Motion Estimation - State of the Art

Contents

This chapter introduces the foundations and state-of-the-art of some motion estimation techniques.

The first subsection is dedicated to Optical Flow (OF). Optical Flow describes the pattern of apparent motion between two successive images.

The Optical Flow principle was first introduced and popularized by Horn and Schunck [77], and Lucas and Kanade [101], in the early 1980s. Both works rely on a single assumption, but each proposes a different numerical solution of the problem. The technique has considerably evolved since its early age and still improves: mathematical statement (along with the underlying hypothesis) and numerical scheme are made more efficient.

Two main branches of OF techniques are: the so-called Differential Optical Flow (DOF) method — which will be presented in this chapter — and cross-correlation (CC) approach — also coined Cross-correlation Particle Image Velocimetry technique –introduced in the appendix A.1.

Readers can refer to [130] and [14, 111, 11] for more details on CC and DOF respectively.

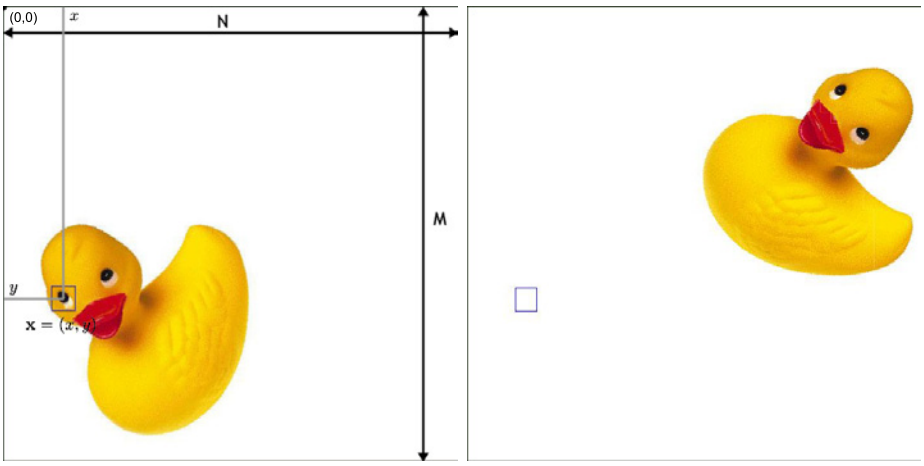

(a) (b)

Figure 3.1: *2 successive images $I_1 = I(\mathbf{x}, t)$ at time t (a) and $I_2 = I(\mathbf{x}, t+\Delta t)$ at time $t + \Delta t$ (b).*

OF relies on an assumption of intensity conservation from one frame to the other. This assumption, valid for rigid motion, becomes unrealistic for the analysis of fluid flow.

The second part of this chapter presents recent approaches dedicated to fluid flow estimation from image sequences. Most of these techniques borrow concepts from fluid mechanics. These physical concepts are incorporated into the image model as new representation of the fluid flow. We will see that traditional DOF technique is often reduced to a particular case of these approaches.

3.1 Motion Field

Let be I, an image recorded at a fixed time t. The image is a set of fixed points (pixels). These pixels can be viewed as a set of point of coordinates $\mathbf{x}$ corresponding to the center of the mesh grid of the image of size $\Delta = (\Delta_x, \Delta_y)$ (for writing simplicity $\Delta_x = \Delta_y$ denoted also Δ). For a time image series, we have a set of successive images recorded at different times (t_1, t_2 ...). Thus shows the same observed scene at successive instants. Over the time, at $\mathbf{x}$, for each image, values of the image intensity $I(\mathbf{x}, t)$ evolved.

Let us consider two successive images $I_1 = I(\mathbf{x}, t)$ and $I_2 = I(\mathbf{x}, t + \Delta t)$, $\mathbf{x} \in \Omega = ([0, N] \times [0, M])$, representing the same observed scene at two different instants t and $t + \Delta t$. The figure 3.1 shows images I_1 and I_2. The square, on bottom left, represents a set of pixels at a fixed position $\mathbf{x}$, $\mathbf{x} \in \Omega_{\text{set}} \subset \Omega$ in both images. We can see that, pixel intensities from t to $t + \Delta t$ are different demonstrating that the object inside is moving from a displacement $\vec{d}$ to determine.

The motion or velocity of the object which is at $\mathbf{x}$ at time t, is the Eulerian

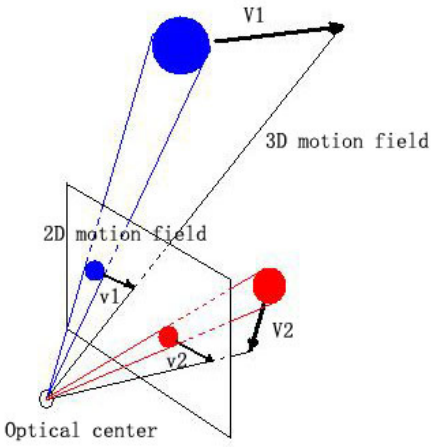

Figure 3.2: *Illustration of apparent motion on the image plan.*

vector velocity in pixel $\mathbf{x}$ corresponding to $\vec{v}(\mathbf{x},t)$ ($\vec{v} = (u,v)$) which gives the displacement $\vec{d}(\mathbf{x},t)$ ($\vec{d} = (d_x, d_y)$) for a time interval Δt and $\vec{v}(\mathbf{x},t) = \vec{d}(\mathbf{x},t)/\Delta t$. In function of the studied object, intensity may vary for every point $\mathbf{x} \in \Omega$. In so the motion or velocity fields correspond to the determination of $\vec{v}$ for every $\mathbf{x} \in \Omega$ as $\vec{v}(\mathbf{x},t) = \vec{d}(\mathbf{x},t)/\Delta t$. The intensity $I(\mathbf{x},t)$ for $\mathbf{x} \in \Omega$ could correspond to solid non-deformable object or temperature, particle or scalar concentration field. Here $\vec{v}$ is the 2D apparent motion field of the 3D projected scene. In case of 3D motion, $\vec{v}$ is the projection on the image plan of the real velocity $\vec{V}$. The figure 3.2 shows the difference between the 2D apparent velocity and real velocity.

Note that all equations, presented in the precedent chapter, are defined in 3D space ($\mathbf{X}$). They are also true in 2D space ($\mathbf{x}$) for any kind of 2D flows for which velocity in the z direction is null. In case of projected 2D representation of the 3D reality space, if the flow is not two dimensional, the described equations in this chapter should be carefully projected from 3D to the 2D plan (for more details see [100]). In our work, we made the assumption of a 2D turbulent flow.

For an optical center location very far from the observed scene, spatial coordinates (x,y) for $\mathbf{X}$ and $\mathbf{x}$ could be considered equivalent. Variation of z is negligible compare to the depth from the scene to optical center. For example, in zoomed remote sensing images or in Particle Image Velocimetry acquisition using laser thin sheet, we have: $(\partial/\partial\mathbf{X})_{x,y} \Leftrightarrow \partial/\partial\mathbf{x}$ for any (x,y) of the image.

We have now to work on the 2D image to express the apparent 2D motion field $\vec{d}(\mathbf{x},t)$. To get this displacement, we consider the 2D material point (particle point) from $\mathbf{x}_p(t) = \mathbf{x}$ at time t to $\mathbf{x}_p(t+\Delta t) = \mathbf{x} + \vec{d}(\mathbf{x},t)$ (section 2.1.1). $\mathbf{x}_p(t)$ denotes the position of particle P in the image. The distance $\vec{d}$ is given by $\mathbf{x}_p(t+\Delta t) - \mathbf{x}_p(t)$. The figure 3.3 represents the displacement $\vec{d}$ for 2 different material points P_1 and

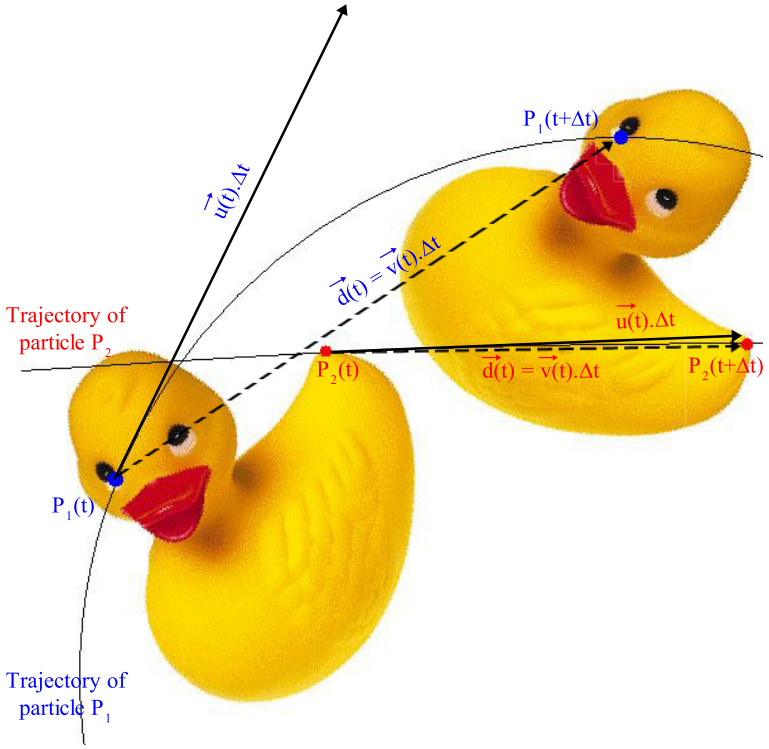

Figure 3.3: *Illustration of displacement $\vec{d}(t)$ from t to $t+\Delta t$ for 2 particles P_1 and P_2 and difference between velocity $\vec{v}(t)$ and instantaneous velocity $\vec{u}(t)$.*

P_2 from time t to time $t+\Delta t$. The velocity $\vec{v}$ is defined as:

$$\vec{v}(\mathbf{x},t) = \frac{\mathbf{x}_p(t+\Delta t) - \mathbf{x}_p(t)}{\Delta t} = \frac{\vec{d}(\mathbf{x},t)}{\Delta t} \tag{3.1}$$

This velocity $\vec{v}$ is measured indirectly, as the displacement $\vec{d}$ of a material point P in a finite time interval Δt.

However the velocity $\vec{v}$ given by the displacement is different from the instantaneous velocity $\vec{u} = \dot{\mathbf{x}} = lim_{dt\to 0} d\mathbf{x}/dt$. In fact, the displacement field only provides the average velocity along the trajectory over a time Δt.

$$\vec{d}(\mathbf{x},t) = \int_t^{t+\Delta t} \vec{u}\left(\mathbf{x}_p(t'),t'\right) dt' \tag{3.2}$$

For a better understanding, on the figure 3.3, we draw the trajectory path of the two material points P_1 and P_2. The distance between material points from time t to time $t+\Delta t$ is represented by dashed line. The instantaneous velocity at time t is given by the tangent vector of the trajectory path. Thus $\vec{u}(\mathbf{x}_p(t),t)$ may be different from $\vec{v}(\mathbf{x},t)$ obtained using $\vec{d}(\mathbf{x},t)$. This depends on the trajectory path of the material point.

$$||\vec{u}(\mathbf{x}_p(t),t) - \vec{v}(\mathbf{x},t)|| < \varepsilon \tag{3.3}$$

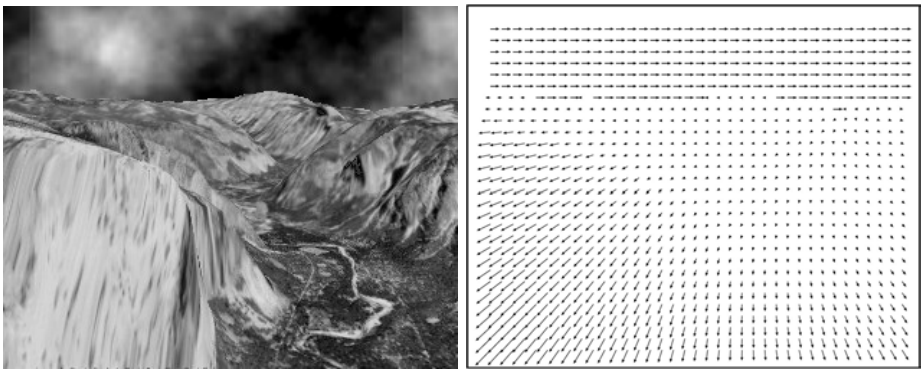

(a) (b)

Figure 3.4: *Yosemite sequence: (a) image* 09*, (b) velocity field* $\vec{v}$ *representation from image* 09 *to* 10

The observed velocity $\vec{v}(\mathbf{x}, t)$ cannot lead to an exact representation of $\vec{u}(\mathbf{x}_p(t), t)$, but approximates it with a finite error ε. This associated error is often negligible, provided that the spatial scale L_c and time scale T_c of the flow are large with respect to the spatial resolution Δ and time resolution Δt. In this work, this hypothesis approximation is good enough most of the time. However, for high turbulent rate, the spatial and time resolutions of our image sequence could be poor due to very small characteristic scales of the flow. In so the observed velocity field is to poor to represent the turbulent flow characteristics. Figure 3.4 shows an image of a time image sequence and its corresponding exact velocity field from one image to the next one. The sequence is the well known Yosemite sequence from computer vision community [14] representing the Yosemite National Park from a flight view over the mountain. In (a), we have the image 09 of the time sequence. In (b) the velocity field is represented by vector arrows every 10 pixels that is a mesh size for visualization clarity. But the velocity field is given for every pixel of the image.

Optical Flow estimations try to determine the velocity field using different techniques. We detail, here, the Differential Optical Flow (DOF) technique. Another technique called Cross-correlation PIV (CC) is widely used in fluid mechanic community. Later on, we will compare our methods with results from CC commercial software. For description of CC technique, we refer to appendix A.1 [130, 149].

3.2 Differential Optical Flow

In early 80s, OF technique has been introduced by Horn and Schunck [77] and Lucas and Kanade [101]. They both proposed a Differential Optical Flow (DOF) equation formulation for their OF approach but each of them used a different numerical solution of the problem (subsection 3.2.2 and 3.2.3).

3.2.1 Brightness Change Constraint Equation (BCCE)

A way to estimate the motion field is based on the brightness conservation hypothesis. We suppose that the brightness values of material points are conserved for a small time interval Δt [77]. We have the following relation, called the Brightness Change Constraint Equation (BCCE):

$$I(\mathbf{x} + \vec{d}(\mathbf{x}, t), t + \Delta t) - I(\mathbf{x}, t) = 0 \tag{3.4}$$

Using a first order Taylor's expansion on $I(\mathbf{x} + \vec{d}, t + \Delta t)$ around $(\mathbf{x}, t)$ gives:

$$I(\mathbf{x} + \vec{d}(\mathbf{x}, t), t + \Delta t) = I(\mathbf{x}, t) + \vec{d}(\mathbf{x}, t).\vec{\nabla} I(\mathbf{x}, t) + \Delta t \frac{\partial I(\mathbf{x}, t)}{\partial t} + \vartheta\left(\vec{d^2}, \Delta t^2\right) \tag{3.5}$$

Here $\vec{\nabla}$ is the 2D spatial derivatives $\left(\frac{\partial}{\partial x}, \frac{\partial}{\partial y}\right)$. Neglecting the second order terms $vartheta\left(\vec{d^2}, \Delta t^2\right)$ for $\vec{d^2}$ and Δt^2 small enough, thus differential form of the BCCE is:

$$\frac{\partial I(\mathbf{x}, t)}{\partial t} + \frac{\vec{d}(\mathbf{x}, t)}{\Delta t}.\vec{\nabla} I(\mathbf{x}, t) = 0 \tag{3.6}$$

From equation 3.1, BCCE can be rewritten with the velocity $\vec{v}(\mathbf{x}, t)$:

$$I_t(\mathbf{x}, t) + \vec{v}(\mathbf{x}, t).\vec{\nabla} I(\mathbf{x}, t) = 0 \tag{3.7}$$

with $I_t(\mathbf{x}, t) = \frac{\partial I(\mathbf{x}, t)}{\partial t}$. The brightness conservation is correct for Δt, thus it is also correct for dt. In fact, BCCE is exactly defined by the total derivative of the intensity quantity (see 2.1.3).

$$\frac{DI(\mathbf{x}, t)}{Dt} = 0 \tag{3.8}$$

This equation is the basis of most of the works done using Differential Optical Flow methods for motion estimations.

This single equation is not sufficient to compute lonely the two unknown components u and v as we have one equation for two unknown values. From BCCE, only the normal component of the velocity vector can be computed. We cannot estimate a unique solution for $\vec{v}$. It is an ill-posed problem. In optical flow, this indetermination is known as the **aperture problem** [14].

Figure 3.5 illustrates it:

- In case 1, we are inside the object. The intensity of the neighborhood pixels are constant therefore the spatial and time gradients are equal to zero. The vector velocity is undetermined (infinite solution from equation 3.7).
- In case 2, we are at a border of the object. We can only estimate the velocity component parallel to the spatial gradient. On the right side of the object, it will be horizontal.
- The case 3 is the angle for which we can compute all the components of the velocity.

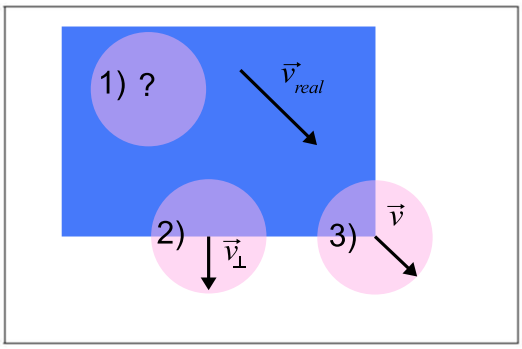

Figure 3.5: *Illustration of the aperture problem*

One way to get solution of the BCCE (equations (3.6),(3.7) or (3.8)) is to use parametric formulations of the velocity field.

$$\vec{v}(\mathbf{x},t) = \begin{cases} f(\mathbf{x},t) \\ g(\mathbf{x},t) \end{cases} \tag{3.9}$$

where functions f and g can be defined as constant, affine, quadratic functions or any others function fitting the observing type of motion [9, 21, 116]. Parameters of the velocity field formulation have to be computed inside the image domain. These formulations get the advantage to define representation of the global velocity. They are quite robust and low computational cost. However, depending on the dynamic complexity of the observed scene, parametric approaches may mainly determine the dominant motion contained in the image sequence. For example the velocity field of many objects having their own motion cannot be obtained in detail by these parametric approaches. As well as for highly turbulent flow, these approaches are not well suited to give full and precise velocities.

Another way to solve BCCE is adding constraints. Two different methods are generally used, local approaches [101] or global approaches [77].

3.2.2 Local Approaches

As we saw in the previous section, a direct solution for equation (3.7) cannot be obtained due to the aperture problem (more variables than equations). Therefore we need additional constraints. One of the simplest methods to overcome this problem is to assume the velocity field to be constant within a fixed neighborhood. These methods are called local approaches. Local approaches are introduced in the early 1980s by Lucas and Kanade [101]. By the way solution of the BCCE on a pixel $\mathbf{x}$, is satisfied around a fixed neighborhood of $\mathbf{x}$: $\mathcal{N}$ (i.e. $\vec{v}(\mathbf{x}) = \vec{v}(\mathbf{x}_0), \forall \mathbf{x} \in \mathcal{N}(\mathbf{x}_0)$).

Lucas and Kanade [101] use a weighted least-squares (LS) fitting of local constraints of BCCE in every small spatial neighborhood $\mathcal{N}$ by minimizing the following energy:

$$E(\vec{v}(\mathbf{x})) = \sum_{\mathbf{x}' \in \mathcal{N}(\mathbf{x})} \mathcal{W}(\mathbf{x}' - \mathbf{x}) \left(I_t(\mathbf{x},t) + \vec{v}(\mathbf{x},t).\vec{\nabla} I(\mathbf{x},t) \right)^2 \tag{3.10}$$

where $\mathcal{W}$ is a window function that gives to the constraints more influence at the center of the neighborhood $\mathcal{N}$ than at the periphery. $\mathcal{W}$ is generally a Gaussian distribution of variance σ^2.

The solution to equation (3.10) is given by:

$$\mathbf{A}^T\mathbf{W}\mathbf{A}\vec{v} = \mathbf{A}^T\mathbf{W}\mathbf{b} \tag{3.11}$$

where, for n points $\mathbf{x}_i \in \mathcal{N}; i = 1, n$ at time t,

$$\begin{aligned}\mathbf{A} &= \left[\vec{\nabla} I(\mathbf{x}_1), ..., \vec{\nabla} I(\mathbf{x}_n)\right]^T \\ \mathbf{W} &= \text{diag}\left[\mathcal{W}(\mathbf{x}_1), ..., \mathcal{W}(\mathbf{x}_n)\right] \\ \mathbf{b} &= -\left(I_t(\mathbf{x}_1), ..., I_t(\mathbf{x}_n)\right)^T\end{aligned}$$

The solution of equation (3.11) is $\vec{v} = \left[\mathbf{A}^T\mathbf{W}\mathbf{A}\right]^{-1}\mathbf{A}^T\mathbf{W}\mathbf{b}$, which is solved in closed form when $\mathbf{A}^T\mathbf{W}\mathbf{A}$ is non singular, as it is a 2×2 matrix:

$$\mathbf{A}^T\mathbf{W}\mathbf{A} = \begin{bmatrix} \sum_{i=1}^n \mathcal{W}(\mathbf{x}_i) I_x^2(\mathbf{x}_i) & \sum_{i=1}^n \mathcal{W}(\mathbf{x}_i) I_x(\mathbf{x}_i) I_y(\mathbf{x}_i) \\ \sum_{i=1}^n \mathcal{W}(\mathbf{x}_i) I_x(\mathbf{x}_i) I_y(\mathbf{x}_i) & \sum_{i=1}^n \mathcal{W}(\mathbf{x}_i) I_y^2(\mathbf{x}_i) \end{bmatrix} \tag{3.12}$$

This approach is robust compare to noise but does not have a global spatial coherency distribution on the velocity field. Note that equation (3.11) is not determined uniquely. In areas where the gray values are, for example, constant or at image edges, there is no single solution. Moreover, assumption of constant velocity inside a neighborhood is often violated in fluid flow, as for CC approaches (appendix A).

Due to these limitations, we did not work with local methods. For more information, readers may refer to the review by Haussecker [71] on different types of local optical flow approaches and extensions.

3.2.3 Global Approaches

For local approaches, velocity field is piecewise constant within an interrogation window. This implies an implicit spatial coherence constraint of the velocity field. Global approach needs to define a regularization function which explicitly uses spatial coherent constraint. Compare to local ones, a new term is added to the BCCE equation that will bring supplementary information on spatial or time velocity distribution. Adding a regularization constraint restricts the class of acceptable solutions which corresponds to transform the ill-posed problem to a well-posed problem of the BCCE (equation (3.7)) where we have only 1 equation for 2 unknown variables (u, v).

The objective function E is now composed by a data conservation energy (data term) E_d combined with an explicit regularization energy E_s. E_s can take the form we want it to be to correctly well-posed the problem. In OF approach, it is generally defined as a smoothness constraint term.

$$E(\vec{v}) = E_d(\vec{v}, I) + E_s(\vec{v}) \tag{3.13}$$

Solution of the problem is given by the minimum of E. The smoothness term is defined as a local constraint over a small spatial neighborhood. A more detailed description of the mathematical background of this energy definition is given in chapter 4.

In the early 80s, Horn and Schunck [77] proposed to constraint spatially the BCCE equation. The data conservation term E_d is formulated as the quadratic function of BCCE. Spatial distribution of the velocity field is constrained by minimizing the norm of the spatial gradients of the velocity field $\vec{v} = (u, v)$.

$$E_d(\vec{v}, I) = \int_\Omega \left(I_t(\mathbf{x}, t) + \vec{v}(\mathbf{x}, t).\vec{\nabla} I(\mathbf{x}, t) \right)^2 d\mathbf{x} \tag{3.14}$$

$$E_s(\vec{v}) = \int_\Omega \alpha \left|\left| \vec{\nabla}\vec{v}(\mathbf{x}, t) \right|\right|^2 d\mathbf{x} \tag{3.15}$$

where $||\vec{\nabla}\vec{v}(\mathbf{x}, t)||^2 = \sum_{i,j} \left(\frac{\partial v_i}{x_j}\right)^2$, with $(i, j) \in [1, 2] \times [1, 2]$, $(x_1, x_2) = (x, y)$ and $(v_1, v_2) = (u, v)$. The parameter α controls the relative importance of the two terms. It is a weighting coefficient. This spatial regularization is obtained via a first order smoothness term of the velocity field because it models the first order spatial continuity properties of the flow. In this way the BCCE formulation is well-posed and solution of the problem can be computed. More the weighting coefficient is large, more the spatial regularization is important compare to the flow equation and more the estimated velocity field will be smoothed. Horn and Schunck [77] used a variational formulation of the problem. They computed Euler-Lagrange differential equations and solve the obtained system equation using Gauss-Seidel iterative method.

Global approaches have a strong advantage compare to local ones as they allow to provide a dense estimated velocity field. For locations for which $||\vec{\nabla} I|| \approx 0$ (i.e. untextured regions), no reliable velocity can be estimated from the data term (equation (3.14)). At these locations, the smoothness term (equation (3.15)) solves this problem by propagation of the velocity due to the neighborhood connexity presents in E_s. This is particularly interesting in the case of particle image where most of the background is untextured and where BCCE contains motion information only on particle gradients. However, this smoothness term spatially constraints the velocity field all over the image domain in an equivalent way. The gain obtained on untextured areas, may be a disadvantage to treat discontinuities of the velocity field (for example, between different moving objects or strong flow mixing). Discontinuities might, in this case, be over smoothed. Many works have been done to improve the regularization functions to fit the application study [65, 20, 177, 29, 122, 136, 74, 12, 162].

3.2.4 Preserving discontinuities

In this section, we give a brief overview of the different methods used to preserve discontinuities of the velocity field. The discussion on these methods is, however, beyond the scope of this manuscript as we focus on the motion equation definition which corresponds to the data term E_d. Insertion of some of these methods

should probably improve the efficiency of our approach for some applications. For a complete review of preserving discontinuity methods, please refer to [65, 20, 177].

Omitting the integration over the image domain Ω for writing clarity, Horn and Schunck [77] regularization function is isotropic $E_s(\vec{v}) = \alpha\Phi\left(||\vec{\nabla}\vec{v}||\right)$. where Φ is a Tikhonov [172] function and is as: $\Phi\left(||\vec{\nabla}\vec{v}||\right) = ||\vec{\nabla}\vec{v}||^2$. This function is isotropic because it affects all direction x, y equivalently. The Tikhonov function is quadratic and tends to penalize stronger the outliers (strong velocity deviations) than other smaller deviations. At discontinuities of the velocity field, robust regularization functions allow stronger variations and then do not constraint them too much.

To preserve discontinuities, we can distinguish two cases: image driven and flow driven functions.

Image driven functions will play on the importance of the smoothness term depending on the image brightness composition. These methods suppose that brightness gradients represent acceptable discontinuity area. An image driven function can be written as:

$$E_s(\vec{v}) = \alpha\ \Phi\left(\left|\left|\vec{\nabla}I\right|\right|\right)\left|\left|\vec{\nabla}\vec{v}\right|\right|^2 \tag{3.16}$$

Function Φ can be supposed as isotropic [5] or anisotropic [145, 177] applying different weight depending on the orientation of the gradient.

Image driven might be useful in the case for which brightness of the image corresponds to different objects with different motions. However in fluid motion, it is mainly wrong. For example in particle images, brightness gradients do not represent disparity areas of the velocity field but only particle contours.

Another method is to focus on the velocity variations to control the regularization function. Variation of the velocity will be higher all around discontinuities. Importance of the constraining weight should be different when there is or not motion discontinuities. A flow driven function can be written as follows:

$$E_s(\vec{v}) = \alpha\ \Phi\left(||\vec{\nabla}\vec{v}||\right) \tag{3.17}$$

where Φ has to be defined to allow strong variations at discontinuities (i.e. $||\vec{\nabla}\vec{v}||$ high) and to constrain local variations (i.e. $||\vec{\nabla}\vec{v}||$). Many strategies have been developed to find these kinds of function based, for example, on diffusion interpretation. The resulting functions Φ are called robust functions as they can deal with outliers. For mathematical demonstration details and necessary conditions that robust functions have to satisfy, we refer to [65, 53].

Robust functions are often non-convex and harder to minimize than convex functions such as quadratic function for example. A variant class called semi-quadratic functions allows to keep the advantage of easy minimization process as quadratic coupling with the advantages of robust functions [65, 20]. An auxiliary variable ζ is needed and the semi-quadratic minimization is the combination of quadratic one and analytical updating of the new variable representing the discontinuity. In image processing [116, 20, 106] and for optical flow estimation [108, 47], many authors used it successfully for inverse problem.

Flow driven regularizations have much more interest for fluid motion because it does not refer to image information but only to the spatial configuration of the velocity field. Today state-of-the-art methods in OF estimation are using robust functions to preserve discontinuity of the velocity field. We can enumerate the following recent works [29, 122, 136, 74, 12, 162].

3.2.5 Multi-Resolution

Differential Optical Flow has a strong limitation concerning the displacement amplitude. When defining the differential BCCE (equation 3.7), there is an implicit assumption of small image displacement leading to ignore the large ones. The second order terms of Taylor expansion are neglected. Two methods can be used to force large displacement determination. For both cases, it consists on reducing spatial resolution to get the larger displacements included in the spatial gradient information.

The first method is the pyramidal decomposition, first proposed by Burt [30]. Today, this technique is used by most DOF algorithms. It is based on subsampling the original image from size $N \times M$ to successive different levels k with resolution of size $N/2^k \times M/2^k$. Original image resolution is for $k = 0$. To generate the pyramidal decomposition different methods have been proposed. The most common is using a Gaussian decomposition [21, 116, 106, 47, 123, 29, 162], but others use wavelet decomposition [99] or steerable pyramid [152]. First of all, number of pyramidal decomposition level has to be arbitrarily defined. The same filter will be used to reduce successively the resolution at each level. The displacement field $\vec{d}_{k+1}$ estimated at level $k+1$ is interpolated and used at level k to transform the image. Therefore, at level k, we are looking for the residual displacement field $\vec{d}_k^r$ following equation (3.18). The total displacement field is then updated at level k by the residual displacement field $\vec{d}_k^r$ considering the interpolated coarser displacement field $\widetilde{\vec{d}_{k+1}}$ where '$\sim$' is the interpolated field from coarser to current pyramidal level. (for more clarity, illustrations are given in chapter 4 figures 4.2 and 4.3).

$$\vec{d}_k = \widetilde{\vec{d}_{k+1}} + \vec{d}_k^r \tag{3.18}$$

Multiresolution by pyramidal decomposition of the differential BCCE is very suitable. Justification can be found in [123]. Nevertheless, careful attention has to be paid to the implementation. A wrong estimation of displacement at a level $k+1$ is increased at level k. Our approach uses pyramidal decomposition technique, a detailed description of it is given in section 4.2.1 and a new pyramidal decomposition technique reducing the number of transformation procedures is proposed in section 4.2.2

In the 90's, another multiresolution technique has been proposed based on scale space theory [156]. This method consists in successive decompositions of the original

image in different space representation. It uses low pass filter of different bandwidths from low to high frequencies. In DOF approaches, multiscale methods have been successfully used [187, 6, 135]. Using convolution derivative property, when filtering the image I by a Gaussian filter $\mathcal{W}$ of variance σ^2, we have:

$$\frac{D\left(\mathcal{W} * I\right)}{Dt} = \frac{D\mathcal{W}}{Dt} * I \tag{3.19}$$

For large bandwidth filter (low frequency), $D\mathcal{W}/Dt$ got large spatial information. Large displacements can be then retrieved from the filtered brightness gradient. Finer information about the displacement is retrieved using smaller bandwidth filters. This iterative technique has the advantage to work on the original image size. However, it still needs warping (see section 4.2) and interpolation of the estimated velocity field obtained using larger bandwidth filter, in the aim to determine the residual displacement using smaller bandwidth filter.

A combined pyramidal decomposition and multiscale approach has been proposed by Ruhnau in [135]. At each pyramidal level additional filters of the multiscale allow to slice the bandwidth into smaller pieces that has the effect to reduce the aliasing along the time frequency axis.

3.2.6 Conclusions

Dense motion estimation using the DOF approaches is now very efficient. Combined local and global constraint has been proposed in [29]. A video set benchmark is available since 2009 [12] enabling to test and compare different methodologies (`http://vision.middlebury.edu/flow/`). Today, the best algorithm tested on these image sequences is proposed by Sun [162]. This approach shows, that the main improvements since Horn and Schunck [77] are on discontinuity preservation, optimization scheme and iterative multiresolution processes. For a larger overview on classical motion estimations and computer vision, readers can refer to the book of Szeliski [166] available online: `http://szeliski.org/Book/`

3.3 Physical Optical Flow Modeling

Differential Optical Flow methods describe in the preceding section may become too restrictive when applied to fluid motions. Only brightness constancy hypothesis or continuity of the solution is made. No specific notion concerning the properties of the observed fluid are used to formulate the problem. However, fluid motion is constituted of regions that move differently and transform differently. This can produce strong brightness variations of intensity information used to determine the velocity field. Brightness constancy (see section 3.2.1) is not anymore a usable hypothesis. In the image, this phenomenon is described by local variation, or gradient, of the brightness that may be strong. The smoothness function defined in equation (3.15) in the global regularization (section 3.2.3) has to account for the spatially

coherence of the velocity field. When there is strong velocity deformation gradient, the smoothness term will under estimate spatial variation of the velocity field.

In the case of fluid motion, classical DOF approaches cannot, most of the time, directly determine correctly the velocity field. It is the reason why the fluid motion estimation, using DOF variation formulations and complex resolution processes, becomes, these last years, a point of interest for many researchers in computer vision and in fluid mechanics [7, 55, 160, 183, 16, 127, 191, 47, 189, 137, 73, 120, 74, 100, 75]. Possible improvements are in equations 3.13: the motion equation definition (data term) attached to the observed brightness intensity values of images and the regularization function (smoothness term) to allow spatial and time fluid velocity field.

3.3.1 Flow Equation

3.3.1.1 Continuity Optical Flow Equation (CE)

The first physical formulation of the flow equation was proposed by Fitzpatrick [59]. He uses the continuity equation for the data term to compute the velocity field. Later on, other works proposed as well to define the data term by the continuity equation [7, 55, 183, 16, 127]. Let be,

$$\frac{\partial \rho}{\partial t} + \vec{\nabla}.(\rho \vec{V}) = 0 \tag{3.20}$$

the continuity equation where ρ is the density function and $\vec{V} = (U, V, W)$ the 3D velocity field.
Let integrate in the vertical direction (z axis) the equation (3.20) between z_0 and z_1:

$$\int_{z_0}^{z_1} \left(\frac{\partial \rho}{\partial t} + \vec{\nabla}.(\rho \vec{V}) \right) dz = a \tag{3.21}$$

Let be a equal to zero due to boundary conditions in z_0 and z_1.

$$\int_{z_0}^{z_1} \frac{\partial \rho}{\partial t} dz + \int_{z_0}^{z_1} \vec{\nabla}.(\rho \vec{V}) dz = 0 \tag{3.22a}$$

$$\int_{z_0}^{z_1} \frac{\partial \rho}{\partial t} dz + \int_{z_0}^{z_1} \left(\frac{\partial (\rho U)}{\partial x} + \frac{\partial (\rho V)}{\partial y} + \frac{\partial (\rho W)}{\partial z} \right) dz = 0 \tag{3.22b}$$

Using the Leibniz integral rule [1]:

$$\frac{\partial}{\partial z} \int_{f(z)}^{g(z)} \varphi(x, z) dx = \int_{f(z)}^{g(z)} \frac{\partial \varphi}{\partial z} dx + \varphi(g(z), z) \frac{\partial g}{\partial z} - \varphi(f(z), z) \frac{\partial f}{\partial z} \tag{3.23}$$

with $f(z)$ and $g(z)$ functions of z. We can commute the integral and the partial derivative because z_0 and z_1 are constant. Thus:

$$\frac{\partial \int_{z_0}^{z_1} \rho dz}{\partial t} + \frac{\partial (\int_{z_0}^{z_1} \rho U dz)}{\partial x} + \frac{\partial (\int_{z_0}^{z_1} \rho V dz)}{\partial y} + \int_{z_0}^{z_1} \frac{\partial (\rho W)}{\partial z} dz = 0 \tag{3.24}$$

Defining an observed apparent motion $\vec{v} = (u, v)$ as a density-weighted average of the horizontal and vertical velocity field as

$$u = \frac{\int \rho U dz}{\int \rho dz} \quad ; \quad v = \frac{\int \rho V dz}{\int \rho dz} \tag{3.25}$$

Equation (3.22b), it becomes:

$$\frac{\partial \int_{z_0}^{z_1} \rho dz}{\partial t} + \frac{\partial \left((\int_{z_0}^{z_1} \rho dz)\, u \right)}{\partial x} + \frac{\partial \left((\int_{z_0}^{z_1} \rho dz)\, v \right)}{\partial y} = -[\rho W]_{z_0}^{z_1} \tag{3.26}$$

The complete continuity equation can be written as:

$$\left(\int_{z_0}^{z_1} \rho dz \right)_t + \vec{\nabla}. \left((\int_{z_0}^{z_1} \rho dz)\, \vec{v} \right) = -[\rho W]_{z_0}^{z_1} \tag{3.27}$$

Thus for any quantity describing the flow, the integration on z can be make as for example, for a recorded image of a flow seeded, we have an integration of information in the direction of the camera or satellite axis $I \propto \int_{z_0}^{z_1} \rho dz$. The projected 3D continuity equation (2D-CE) neglecting the vertical integration of the vertical velocity W is:

$$I_t + \vec{\nabla}. (I\, \vec{v}) = 0 \tag{3.28}$$

The 3D Continuity Equation (3D-CE) which considers the vertical integration of the vertical velocity W term is:

$$I_t + \vec{\nabla}. (I\, \vec{v}) = -[\rho W]_{z_0}^{z_1} \tag{3.29}$$

[55, 183, 16] use directly the L2 norm of the 2D continuity equation (3.28). [7] starts from 2D continuity equation (3.28) and applying it to incompressible fluid, the divergence of the velocity is thus null (equation (2.13)). It brings back the equation to BCCE (equation (3.7)). [127] uses a parametric formulation based on 2D continuity equation (3.28). [191] uses the continuity equation for post processed the cross-correlation allowing to estimate velocity field. [16, 191, 47] make the hypothesis of a 2D motion field and neglect the vertical velocity component. [73] uses the 3D continuity equation (3.29) in a z-layered motion estimation.

3.3.1.2 Integrated Continuity Optical Flow Equation (ICE)

[47, 73] proposed to base the flow equation on an integrated formulation of the continuity equation (3.28) (ICE). They expressed the flow equation function of the displacement field. They assumed that the velocity field is constant between two successive images and integrate the continuity equation along the trajectories from time t to time $t+\Delta t$. Resolving the differential equation (3.28), the ICE formulation becomes:

$$I(\mathbf{x} + \vec{d}(\mathbf{x}), t + \Delta t)\, e^{\vec{\nabla}.(\vec{d}(\mathbf{x}))} - I(\mathbf{x}, t) = 0 \tag{3.30}$$

The integrated formulation of the continuity equation (3.30) contains information of large displacements. However the equation is highly non linear that makes

difficult the process of minimization to get an optimal solution. The authors proposed a multiresolution process by pyramidal decomposition. Displacement is decomposed as in sec.3.2.5: $\vec{d}(\mathbf{x}) = \widetilde{\vec{d}(\mathbf{x})} + \vec{d}^{r}(\mathbf{x})$. The gradient ICE formulation (3.30) is obtained by first order Taylor expansion around the point $\mathbf{x} + \widetilde{\vec{d}(\mathbf{x})}$ as:

$$e^{\vec{\nabla}.\widetilde{\vec{d}(\mathbf{x})}} \left[\mathbf{I} + \vec{d}^{r}(\mathbf{x}) \left(\vec{\nabla}\mathbf{I} + \mathbf{I}\, \vec{\nabla} \left(\vec{\nabla}.\widetilde{\vec{d}(\mathbf{x})} \right) \right) \right] - I(\mathbf{x}, t) = 0 \tag{3.31}$$

with $\mathbf{I} = \mathbf{I}(\mathbf{x} + \widetilde{\vec{d}}, t + \Delta t)$ the warped image by $\widetilde{\vec{d}}$ (see section 4.2 for more details on the multiresolution by pyramidal decomposition). The final gradient formulation ICE (3.31), in the multiresolution process, is attached to warped information of the second image at time $t + \Delta t$. They proposed to use robust functions for data and smoothness terms (see section 3.2.4). Note that the final equation is different of the direct used continuity equation (3.28) in a multiresolution process. For the 3D-ICE, integration of equation (3.29) is not null but it is function of the vertical velocity difference and the divergence of the coarser displacement field. These methods add to this new flow equation formulation a special regularization which is based on divergence and curvature of the velocity field [46] and on an extension using simplified Navier-Stokes equation as spatio-temporal regularization [73].

3.3.1.3 Scalar Transport Equation

At the best of our knowledge, Su and Dahm [160] were the first to propose an optical flow method based on the scalar transport equation with molecular diffusion (convection/diffusion) under its dimensionless formulation (equation (2.23b)), that we call TE:

$$\frac{\partial C}{\partial t} + \vec{V}.\vec{\nabla}C - \frac{1}{ReSc}\nabla^2 C = 0 \tag{3.32}$$

In visualization studies of the concentration field evolution, link exists between C and the brightness I of the recorded images of the studied flow. They directly used the 3D equation (3.32) to determine the three-dimensional velocity fields. For this, they used recorded images by Planar Laser Induced Fluorescence (PLIF) from fluorescent dye evolving in a turbulent flow. To solve the non-unicity of the equation, here 3 unknown variables U, V, W, they used global constraints adding 2 equations: the continuity equation $\vec{\nabla}.\vec{V} = 0$ (equation (2.13)) and a spatial coherency of the velocity field as Horn and Schunck $||\vec{\nabla}\vec{V}|| = 0$ (equation (3.15)). The problem formulation is done through a variational formulation making the summation of the quadratic form of the scalar transport equation with molecular diffusion, continuity equation and the spatial coherency of the velocity field functions. The method does not incorporate multiresolution technique. This necessitates, then, time-resolved measurements of volumetric scalar fields. That was done, in practice, by using a laser-scanning system and a high-speed photosensitive array [50, 60]. Note that such measurements are feasible only when a time interval between two successive scan planes is sufficiently small that a 3D data volume reconstructed from a set of data planes can be considered to be frozen in time. Moreover, the resolution in time

(Δt) and space (3D pixel size) of the time sequence has to be finer than the flow characteristic time and length. Nevertheless the formulated equation misses lower scale information. This is the main point of the present work (chapter 5).

Recently, an interesting work from Liu and Shen [100], extended and generalized the 2D projected flow equation. They gave a direct connection between the DOF and fluid flow methods by projecting the 3D transport or continuity equations onto the image plane to analyze typical flow visualizations, including laser-sheet induced fluorescence, transmittance through transported passive scalar and others (see [100]). They obtained projected motion equation showing that the 2D apparent velocity field is proportional to the path-averaged velocity of fluid or particles.

$$\frac{\partial g}{\partial t} + \vec{\nabla}.(g\vec{v}) = \underbrace{\lambda^2 D \nabla^2 g}_{\text{Diffusion}} + \underbrace{DcB}_{\text{Boundary}} + \underbrace{c\vec{n}.\left(\psi\vec{V}\right)\Big|_{z_0}^{z_1}}_{\text{Accumulation}} \tag{3.33}$$

where $\vec{v}$ is the 2D apparent velocity, $g = g(I)$ is the function of the normalized image intensity that depends on the type of image sequence. z_0, z_1 are the depth between controlled surfaces (layer, laser shit or maximum depth boundary). D is the diffusion coefficient and c a coefficient for fluorescence processes, scalar absorption or particle scattering absorption that are at basis of the recorded information from the flow field enlightened generally by laser.

$$B = -\vec{n}.\vec{\nabla}\psi|_{z_0}^{z_1} - \vec{\nabla}_{12}.\left(\psi|_{z_1}\vec{\nabla}_{12}z_1 + \psi|_{z_0}\vec{\nabla}_{12}z_0\right) \tag{3.34}$$

is a boundary term where $\vec{\nabla}_{12}$ is projected 3D gradient on the plane (x, y), ψ is the scalar concentration in the flow (e.g. fluorescent dye), fluid density in density-varying flows or particle number per unit total volume for loaded flows. Last term $\vec{n}.(\psi\vec{V})|_{z_0}^{z_1}$ represents a rate of accumulation of ψ within the observed area $(x, y, z_1 - z_0)$.

Most of the time, experiments or analyzed image sequences are recorded as the boundary and accumulation terms in equation (3.33) are negligible. In Liu's method, the diffusion term in equation (3.33) is also considered as null. Note that in case of 2D incompressible flows $\vec{\nabla}.\vec{v} = 0$ (equation (2.13)), without diffusion, we retrieve the BCCE equation (3.6) with $g(I) = I$. However, even for 3D incompressible flows $\vec{\nabla}.\vec{v} \neq 0$ because $\vec{\nabla}_{12}.\vec{V}_{12} = -\partial W/\partial z \neq 0$.

It was proved by Liu and Shen that the 2D apparent velocity from the BCCE equation (3.6) and others (equation (3.28),(3.29), (3.32)) respect mathematically the constraint imposed by the flow properties.

Works on the equation of motion have been done linking the continuity equation or transport equations to the optical flow formulation. CE (section 3.3.1.1) differs from BCCE (section 3.2.1) for compressible or 3D incompressible flows where the z component may produce a projected non null divergence as shown just above. TE (section 3.3.1.3) considers the molecular diffusion of the fluid. For fluid with high

Reynolds number ($Re >> 1$) or/and with low diffusion ($Sc >> 1$), the molecular diffusion coefficient D is close to zero. In this condition, for incompressible 2D flows, TE is equivalent to BCCE. In the case of solid particles, we speak of apparent diffusion.

3.3.2 Regularization Functions

In another way, many works have been done concerning the definition of the regularization function. The Horn and Schunck regularization function is too restrictive, especially for disparities or strong velocity gradients. Robust functions as seen in 3.2.4 are a way to deal with such disparities. However improvements can be done on the choice of regularization function definitions that may be more adapted to fluid flow. Here, we give only the main advancements done for optical flow estimation applied to flow motion estimation.

3.3.2.1 Constraints based on Helmholtz decomposition

For a bounded domain Ω containing a 2D velocity field $\vec{v}$, the Helmholtz decomposition states that this velocity field can be interpolated as a superposition of a translation (laminar $\overrightarrow{v_{lam}}$), a divergence free (solenoidal $\overrightarrow{v_{so}}$) and a curl free (irrotational $\overrightarrow{v_{ir}}$) vector fields.

$$\vec{v} = \overrightarrow{v_{lam}} + \overrightarrow{v_{so}} + \overrightarrow{v_{ir}} \tag{3.35}$$

with

$$\vec{\nabla}.\overrightarrow{v_{so}} = \frac{\partial u}{\partial x} + \frac{\partial v}{\partial y} = 0 \tag{3.36}$$

and

$$\vec{\nabla} \times \overrightarrow{v_{ir}} = \frac{\partial v}{\partial x} - \frac{\partial u}{\partial y} = 0 \tag{3.37}$$

In case of non-zero boundary conditions, the laminar term is not null. However, it is easily identifiable and can be removed in a preprocessing step. Assumption about vanishing velocity on boundary can also be made, for example, by extending the domain Ω. Then using the Helmholtz decomposition, the Horn and Schunck regularization formulation (equation (3.15)) can be rewritten in a div-curl one where divergence and curvature are independently constrained.

$$E_s(\vec{v}) = \int_\Omega \left(\alpha \left(\vec{\nabla}.\vec{v}(\mathbf{x}) \right)^2 + \beta \left(\vec{\nabla} \times \vec{v}(\mathbf{x}) \right)^2 \right) d\mathbf{x} \tag{3.38}$$

where $\alpha, \beta > 0$ are weighting coefficients [164]. Horn and Schunck equivalently penalize the divergence and curl of the velocity field. For incompressible flows, as the apparent velocity field is the 2D projection of the real 3D velocity field, the rotational component is usually much higher than the divergence. Therefore, div-curl regularization becomes more advantageous. However, first-order regularization still penalizes spatial variations of the velocity through the divergence and curvature. To overcome this strong smoothing higher order regularizations have been proposed

that constrain variations of divergence and curl instead of directly constrain the velocity variations [8, 165, 68]

$$E_s\left(\vec{v}\right) = \int_\Omega \left(\alpha \left|\left| \vec{\nabla} \left(\vec{\nabla}.\vec{v}(\mathbf{x}) \right) \right|\right|^2 + \beta \left|\left| \vec{\nabla} \left(\vec{\nabla} \times \vec{v}(\mathbf{x}) \right) \right|\right|^2 \right) d\mathbf{x} \tag{3.39}$$

Using a variational formulation, the corresponding Euler-Lagrange equation system consists of two coupled fourth-order Partial Differential Equations (PDEs). [47, 46] proposed a modified second-order div-curl regularization using semi-quadratic minimization by introducing auxiliary variables ζ and ξ

$$\begin{aligned} E_s\left(\vec{v},\zeta,\xi\right) = \int_\Omega \Bigg[& \alpha \left(\left|\left| \vec{\nabla}.\vec{v}(\mathbf{x}) - \zeta(\mathbf{x}) \right|\right|^2 + \left|\left| \vec{\nabla} \times \vec{v}(\mathbf{x}) - \xi(\mathbf{x}) \right|\right|^2 \right) \\ & + \beta \left(\Phi\left(||\vec{\nabla}\zeta(\mathbf{x})|| \right) + \Phi\left(||\vec{\nabla}\xi(\mathbf{x})|| \right) \right) \Bigg] d\mathbf{x} \end{aligned} \tag{3.40}$$

This transforms the fourth-order PDEs into a system of second-order PDEs. Minimization is done by alternatively minimizing the energy for every variables. A robust function is also used as Leclerc function for Φ [47]. Another advantage of the method is that ζ and ξ can be seen as an approximation of the true divergence and curl.

Later on, [86] and [189] proposed to base the regularization on the potential function ς (stream potential) and ω (velocity potential)

$$\overrightarrow{v_{so}} = \vec{\nabla}\omega^\perp = \left(\frac{\partial\omega}{\partial y}, -\frac{\partial\omega}{\partial x} \right) \tag{3.41}$$

$$\overrightarrow{v_{ir}} = \vec{\nabla}\varsigma = \left(\frac{\partial\varsigma}{\partial x}, \frac{\partial\varsigma}{\partial y} \right) \tag{3.42}$$

Depending on the studied flows, it might be interesting to directly look for the potential functions ς and ω to reconstruct the velocity field $\vec{v}$. After subtracting the laminar component of the velocity field, the data term E_d (equation (3.14) becomes:

$$E_d\left(\varsigma,\omega,I\right) = \int_\Omega \left[\left(I_t(\mathbf{x},t) + \left(\vec{\nabla}\varsigma(\mathbf{x},t) + \vec{\nabla}\omega^\perp(\mathbf{x},t) \right) .\vec{\nabla} I(\mathbf{x},t) \right)^2 \right] d\mathbf{x} \tag{3.43}$$

The regularization is then applied to ς and ω in an high-order regularization formulation as in [47]

$$\begin{aligned} & E_s\left(\varsigma,\omega,\zeta,\xi\right) = \\ & \int_\Omega \Bigg[\alpha \left(\left|\left| \vec{\nabla}. \left(\vec{\nabla}\varsigma(\mathbf{x}) \right) - \zeta(\mathbf{x}) \right|\right|^2 + \left|\left| \vec{\nabla} \times \left(\vec{\nabla}\omega^\perp(\mathbf{x}) \right) - \xi(\mathbf{x}) \right|\right|^2 \right) \\ & + \lambda \left(\Phi\left(||\vec{\nabla}\zeta(\mathbf{x})|| \right) + \Phi\left(||\vec{\nabla}\xi(\mathbf{x})|| \right) \right) \Bigg] d\mathbf{x} \end{aligned} \tag{3.44}$$

with Φ quadratic [86]. discretization and minimization convergence are given in [189].

This regularization functions presents the advantage to penalize independently divergence and curl of the velocity field.

3.3.2.2 Physical Based Priors Constraints

As fluids are governed by the well-known Navier-Stokes equations (2.21), it comes naturally in mind to use these equations as regularization function as used in CC methods for the post-processing step [117, 82] (see appendix A). However, the Navier-Stokes equations are dependent on many other variables for which we do not have access from our image sequences. Authors as [136, 137, 73, 120, 74] proposed, then, to simplify the Navier-Stokes equations and to apply them as regularization functions in certain flow cases.

A first method was proposed by Ruhnau [136] for which the velocity field is spatially constrained by the Stokes equations in case of a incompressible stationary 2D flow ($\vec{\nabla}.\vec{v} = 0$ and $\partial\vec{v}/\partial t = 0$). The Stokes equations are correct for small Re number, then the convective terms are much smaller than the viscous terms ($\vec{v}.\vec{\nabla}\vec{v} << \nu\nabla^2\vec{v}$). The system of equations can be written as:

$$-\nu\nabla^2\vec{v} + \vec{\nabla}p = \vec{f} \quad \text{in } \Omega \tag{3.45a}$$

$$\vec{\nabla}.\vec{v} = 0 \qquad \text{in } \Omega \tag{3.45b}$$

$$\vec{v} = \vec{g} \qquad \text{in } \Omega_b \tag{3.45c}$$

Ω_b the boundary of Ω. $\vec{g}$ is a boundary condition on $\vec{v}$. Coupling this system of equation with the classic DOF formulation as BCCE, CE, ICE or TE, they got four unknown variables $u, v, \partial p/\partial x, \partial p/\partial y$. To defined a well-posed problem, [136] proposed to minimize the following energy controlled by variables $\vec{f}, \vec{g}$:

$$\int_\Omega E_s\left(\vec{v}, p, \vec{f}, \vec{g}\right) = \int_\Omega \alpha||\vec{f}||^2 d\mathbf{x} + \beta\int_{\Omega_b} ||\partial_t\vec{g}||^2 d\mathbf{x} \tag{3.46}$$

Details on their numerical resolution can be found in [136]. This method has the advantage to be able to determine the pressure field and the external forces involved in Stokes flows. This regularization method is still coherent for turbulent flows, however variables $\vec{f}, \vec{g}$ do not have anymore physical meaning. Another interesting point is that this regularization function can be applied to only 2 successive images.

Thinking about flow motion, we can imagine a coherency over the time axis of the velocity field evolution. It is there suitable to use spatio-temporal regularization functions and not only spatial ones. This is, of course interesting when the time image sequence contains more than two successive images.

The simple regularization that comes, is to extend the spatial Horn and Schunck smoothness over the time axis. In this way [178] defined the time as the third dimension

$$E_s\left(\vec{v}\right) = \int_\Omega \left(\alpha\left|\left|\vec{\nabla}_3\vec{v}(\mathbf{x}, t)\right|\right|^2\right) d\mathbf{x} \tag{3.47}$$

with $\vec{\nabla}_3 = (\frac{\partial}{\partial x}, \frac{\partial}{\partial y}, \frac{\partial}{\partial t})$ and $||\vec{\nabla}_3\vec{v}(\mathbf{x}, t)||^2 = \sum_{i,j}\left(\frac{\partial v_i}{x_j}\right)^2$, with $i = 1, 2$ and $j = 1, 2, 3$ with $(x_1, x_2, x_3) = (x, y, t)$ and $(v_1, v_2) = (u, v)$. The time smoothness term improves the optical flow estimation but it becomes less sensitive to instantaneous

noise. However, it is not physically motivated.

In recent papers [137, 73, 120, 74], incorporation of physical based equations into regularization functions are used to constrain the velocity field using time information.

[137] proposes to incorporate physical based time smoothing into the div-curl regularization for turbulent 2D incompressible flows. The vorticity transport equation gives the time evolution of the velocity. In case of 2D flows, the vorticity $\varpi = \vec{\nabla} \times \vec{v}$ is a scalar field and:

$$\frac{D\varpi}{Dt} = \frac{\partial \varpi}{\partial t} + \vec{v}.\vec{\nabla}\varpi = \nu \nabla^2 \varpi \tag{3.48}$$

where $\vec{v}$ is the 2D velocity field. Note that in case of 3D flows, projection of vorticity transport equation should be done. In [165] the second-order div-curl regularization penalizes the spatial variations of divergence and vorticity. Considering 2D incompressible flows $\vec{\nabla}.\vec{v} = 0$ (equation (2.13)), only variations of vorticity are interesting. Using the vorticity equation with the last velocity field estimated between times $(t - \Delta t)$ and time t, it is possible to compute a predicted vorticity at time t by solving:

$$\varpi_P(t) = \varpi(t - \Delta t) + \int_{t-\Delta t}^{t} \left(\vec{v}(t').\vec{\nabla}\varpi(t') - \nu \nabla^2 \varpi(t') \right) dt' \tag{3.49}$$

This predicted vorticity field is used to constrain in time the current estimation of vorticity at instant t. This constraint is formulated as a new quadratic term (right term of equation (3.50))in the regularization energy E_s coupled with the second-order div-curl regularization. For the objective energy E, they use the BCCE data term E_d (equation (3.14)).

$$E_s(\vec{v}) = \int_\Omega \left(\underbrace{\alpha\, \Phi\left(\left|\left| \vec{\nabla}\left(\vec{\nabla} \times \vec{v}(\mathbf{x}) \right) \right|\right|^2 \right)}_{2^{nd}\text{order div-curl}} + \underbrace{\beta \left|\left| \varpi_P(t) - \vec{\nabla} \times \vec{v}(\mathbf{x}) \right|\right|^2}_{\text{temporal vorticity constraint}} \right) d\mathbf{x} \tag{3.50}$$

Where Φ is a robust function. For details of the non-trivial discretization and numerical resolution, please refer to [137, 138].

A similar time regularization has been proposed in [73, 74] for determining motion of atmospheric layer. They did not only predict the vorticity field but they used a filtered simplified vorticity-divergence formulation of shallow water models [51] to predict the velocity field.

$$\begin{cases} \frac{\partial \varpi}{\partial t} + \vec{v}.\vec{\nabla}\varpi + \varpi\iota = (\nu_s + \nu)\, \nabla^2 \varpi \\ \frac{\partial \iota}{\partial t} + \vec{v}.\vec{\nabla}\iota + \iota^2 - 2\,|J| = (\nu_s + \nu)\, \nabla^2 \iota \end{cases} \tag{3.51}$$

where $\iota = \vec{\nabla}.\vec{v}$ is the divergence of the velocity field, $|J|$ is the determinant of the Jacobian matrix of variables (u, v), ν_s is the enstrophy-based subgrid scale model

[73] (see section 2.4.3). In the same way as [137] a quadratic time regularization term is added to the energy which constrains the variations of the velocity field compared to the predicted velocity field obtained from equation (3.51). Thus, the smoothness term E_s is:

$$E_s(\vec{v}) = \int_\Omega \left(\alpha \left(\left|\left| \vec{\nabla} \left(\vec{\nabla} \times \vec{v}(\mathbf{x}) \right) \right|\right|^2 + \left|\left| \vec{\nabla} \left(\vec{\nabla} \vec{v}(\mathbf{x}) \right) \right|\right|^2 \right) + \beta \left|\left| \vec{v}(\mathbf{x}) - \overrightarrow{vP}(\mathbf{x}) \right|\right|^2 \right) d\mathbf{x} \tag{3.52}$$

with $\overrightarrow{vP}$ the predicted velocity field using last information at time $(t - \Delta t)$. Here the 2D apparent velocity field $\vec{v}$ is proportional to the path-averaged velocity field of the flow across a volume. Hence it did not satisfy directly the full Navier-Stokes equations but it satisfies, the simplified formulation given by the shallow flow assumptions.

An extension of this method has been proposed in [74]. The authors proposed to use CC estimation as supplement information. In the same way as for the time regularization by the predicted velocity field from shallow water equations, a quadratic term is added to the regularization energy E_s which constrains the velocity field $\vec{v}$ by the cross-correlation estimation $\overrightarrow{v_{cc}}$. This method is very useful when applied to particle images because CC estimation is much more robust and it is thus less sensible to noise than DOF estimation where the error level increase with the multiresolution process. However, this regularization term may bring much more erroneous information in case of scalar images for which CC is poorly efficient.

For turbulent flows, the last proposed method [72] was to include a regularization term that enforces quantities derived from the velocity gradients to be smooth for which second-order spatial regularization function is added to the regularization energy E_s that constrains the velocity field to satisfy the turbulent kinetic energy decay [87].

All these methods use spatio-temporal regularization based on flow conservation equations of different quantities. However these regularizations do not guaranty a continuous respect of the conservation laws over the entire time sequence because they only take into account two successive times at each estimation. An interesting technique, data assimilation, is used by [120, 121, 45, 89] to estimate the motion field over an entire temporal image sequence. The data term E_d (defined by BCCE) is controlled by dynamic equations as the Navier-Stokes. The optimal solution is given by the best configuration of the velocity field satisfying the Navier-Stokes equations with respect to the observing scene represented in the data term E_d. This method is not affected by noisy or incomplete data. Discussion of this technique is beyond the scope of this thesis. However the use of our approach should be very interesting combined with data assimilation based on subgrid scale models for LES formulation of the Navier-Stokes equations.

3.3.3 Conclusions

Global approaches on differential optical flow methods have been improved a lot for the last 20 years. DOF becomes to be applied on flow motion estimation at the beginning of 21^{st} century and becomes explicitly linked to physical properties of fluid in [100]. Many works have been done on the regularization trying to adapt it to flow motion or to use physical flow equation to constrain temporally and spatially the velocity field. Motion equations were derived from continuity or transport equations. Only recently, focus on turbulent flows and differentiation between large and small scales has been done on the regularization functions [74, 72]. Data assimilation [120] is also very promising as it computes the Navier-Stokes equations over the time domain. In this way, they filter all scales satisfying the flow equations. Flow equation (data term) has been left aside of turbulent problem. However, it is the observed information from which we estimate the field of motion. Moreover, observed information is given by images of fixed time and spatial resolutions.

3.4 Discussions

In the appendix A, we will describe the standard algorithm for cross-correlation (CC) particle image velocimetry and have summarized several extensions. CC approaches are the most used techniques in fluid mechanic community. They proved to be robust and fine enough to be able to extract fluid and turbulence statistics.

There is also a very large work on DOF methods. In an attempt to model the physical behavior of fluid flow, alternative formulations have been proposed : volume conservation [7, 16], continuity equation [46], and generalized transport equation applied to particle images [100, 74]. Besides, efforts have been put to improve the regularization term: some authors enforce divergence and vorticity constraints [165, 46] or integrate Navier-Stokes equation [137, 74]. These methods are now adapted to fluid motion. They have the advantage to produce a dense estimated velocity field with high spatial precision. Recent improvements allow to get very small estimation errors with higher spatial resolution than CC. Moreover, they can be applied on particle images but are naturally defined for scalar images because they are derived from continuity and scalar transport equations. Comparisons of the state of the art of DOF approaches with CC on particle images and synopsis of these methods can be found in [75].

For example, in the application of atmospheric motion determination, cross-correlation techniques were the first to be applied to remote sensing images [63, 93]. Improvements of cross-correlation methods are still used, with good results on remote sensing images [190, 27], as they are less sensitive to noise than DOF methods. However, DOF adapted to flow motion determination becomes very efficient when applied on remote sensing images [43, 160, 47, 49, 73, 74]. They have the advantage to estimate coherent dense velocity field of fluid motion. In the next chapter, we propose an efficient DOF approach and compare it to some recent existing DOF and CC approaches.

Chapter 4

Motion Estimation by Differential Optical Flow

Contents

In this chapter, we describe our differential optical flow (DOF) approach. Motion estimation problem is formulated as a Markov Random Field (MRF) framework. The Gibbs energy is defined as the sum of a data term derived from the DOF equation, and a global regularization term acting as a smoothness constraint.

In the first part of this chapter, we explain our problem formulation. We propose a new DOF equation formulation which is defined on the two spatial intensity gradients of two successive in time images (section 4.1). To tackle the limitation of DOF equations for large displacements, we propose an unwarping multiresolution by pyramidal decomposition (section 4.2) for which assumption on gradients is made to reduce the number of transformations during the process. We also compare and suggest some improvements of optimization methods (appendixes C and E).

In the second part, we present a validation applying our algorithm to different time image sequences for rigid and non-rigid motions (sections 4.5 and 4.6). Accuracy of results is compared with other DOF techniques from the literature and CC commercial software for known errors as AAE and RMS velocity (section 4.4 equations (4.44)).

The works done in this chapter have been published or submitted in [125, 33, 34, 32, 38].

4.1 Problem Formulation

In our case, we want to estimate the velocity $\vec{v}(\mathbf{x})$ for each pixel $\mathbf{x}$ from one image $I_1 = I(\mathbf{x}, t)$ at time t to the successive in time image $I_2 = I(\mathbf{x}, t + \Delta t)$. Available information, we have from images are the brightness intensity field of the image pair. We call observation variable field $I = \{I(\mathbf{x}) | \mathbf{x} \in \Omega\}$ the extracted information that we can get from these fields. Ω is the image dimension. The velocity field $\vec{v} = \{\vec{v}(\mathbf{x}) | \mathbf{x} \in \Omega\}$ is, in our problem, the unknown variable for which we are seeking the best configuration which will correspond to the apparent velocity field from I_1 to I_2. The velocity $\vec{v}(\mathbf{x})$ is a continuous 2D variable bounded by $\Gamma = [-\vec{v}_{max}; +\vec{v}_{max}]$

Observed variable field I is known with a certain degree of uncertainty, due in particular to the stochastic process of imaging condition. Consequently, the estimated velocity field, itself, can be estimated only up to a certain accuracy.

The Markov Random Field (MRF) theory is a probabilistic approach which allows to define a mathematical framework of the problem to solve. A review of MRF framework is given in appendix B. MRF-Gibbs equivalence (appendix B.3) gives:

$$P(\vec{v}|I) \propto \exp\left(-E(\vec{v}, I)\right) \tag{4.1}$$

$P(\vec{v}|I)$ is the probability of a configuration of $\vec{v}$ given the pair image information I. A configuration of $\vec{v}$ is any possible velocity field.

The Gibbs energy E is generally defined as:

$$\begin{aligned} E(\vec{v}, I) &= E_d(\vec{v}, I) + E_s(\vec{v}) \\ &= \sum_{\mathbf{x} \in \mathcal{C}_1} V_d\left(\vec{v}(\mathbf{x}), I(\mathbf{x})\right) + \alpha \sum_{\mathbf{x}, \mathbf{x}' \in \mathcal{C}_2} V_s(\vec{v}(\mathbf{x}), \vec{v}(\mathbf{x}')) \end{aligned} \tag{4.2}$$

where E_d is the data energy (data term) and E_s is the regularization energy. And V_d, V_s the associated potential functions [98]. $\mathcal{C}_1$ and $\mathcal{C}_2$ are the single-site and pair-site cliques respectively (see appendix B.2 and figure B.2 for explanation).

MRF is formulated on an undirected graph $G = (s, e)$. Graph is a convenient representation of image for which the observed variable is given in each pixel of the image. Thus, the image domain Ω corresponds to the undirected graph G. The sites s of G are the pixels $\mathbf{x} \in \Omega$ of the pair images and the edges e correspond to the relation between pixels defined by the chosen neighborhood system (4-neighborhood system in our case).

The data energy E_d (equation (4.2)) establishes the link between the observed variable field I, and the unknown variable field $\vec{v}$. This term is defined according to the application. In this chapter, E_d will be defined by the motion equation which is a differential optical flow equation (section 4.1.1). DOF equation (see section 3.2) does not allow to determine a unique solution (2 unknown variables $\vec{v} = (u, v)$ for 1 equation). However, it is reasonable to assume that nearby points are not totally independent, but are animated by similar motions. Hence, contextual constraints ought to be added to the model which transforms the ill-posed problem to a well-posed problem. This modeling of interdependencies between neighbor variables is defined through a regularization energy E_s that we define as a smoothness term applied on the unknown velocity field.

Hence, we seek for the best solution $\widehat{\vec{v}}$ of $\vec{v}$ that maximizes the posterior probability $P(\vec{v} \mid I)$, or equivalently, that minimizes the energy $E(\vec{v}, I)$:

$$\widehat{\vec{v}} = \arg \min_{\vec{v} \in \Gamma^N} E(\vec{v}, I) \tag{4.3}$$

The choice of an MRF framework, associated to efficient optimization technique on graphs, enables to define the functional of the energy E with a certain flexibility (Szeliski and al. [168], Kolmogorov and Zabih [88]). Alternative methods to solve energy minimization problems defined similarly to (4.3), such as variational approaches (Horn and Schunck [77], Heitz and al. [75]), are efficient in practice only if E is a convex function of the unknown $\vec{v}$. Note that DOF approaches presented in last chapter 3.3 were defined using variational framework. Their data E_d and regularization E_s energies were continuous functions ($\int$). However, in our case, the energies are defined on an undirected graph and thus are discretized functions ($\sum$). Results show, in this thesis, that motion estimation using MRF framework is as efficient as and even better than variational ones and allows a 2D real velocity field determination.

In the following, we detail the formulation of E in subsections 4.1.1 and 4.1.2. The optimization procedure is described in sections 4.2.1 and 4.3 and in appendixes C and E.

4.1.1 Data Term and Differential Optical Flow Equation

BCCE (section 3.2.1) has proved to be very powerful in motion estimations since [77]. It is based on the hypothesis of constant brightness of the scene of interest over a small period of time Δt. For a given time image pair $I(\mathbf{x}, t)$ and $I(\mathbf{x}, t + \Delta t)$, BCCE is defined by:

$$I(\mathbf{x} + \vec{d}(\mathbf{x}), t + \Delta t) - I(\mathbf{x}, t) \approx 0 \tag{4.4}$$

$\vec{d}$ is the displacement field.

The 2D velocity $\vec{v}(\mathbf{x}) = (u(\mathbf{x}), v(\mathbf{x}))$ in pixel $\mathbf{x}$ is deduced from an apparent displacement $\vec{d}(\mathbf{x}) = (d_x(\mathbf{x}), d_y(\mathbf{x}))$ that links pixel $\mathbf{x} = (x, y)$ of the first image at time t with its corresponding position $\mathbf{x} + \vec{d}(\mathbf{x})$ in the second image at time $(t + \Delta t)$

(see section 3.1).

$$\vec{v}(\mathbf{x}) = \frac{\vec{d}(\mathbf{x})}{\Delta t} \tag{4.5}$$

From a 1^{st} order Taylor expansion of $I(\mathbf{x} + \vec{d}(\mathbf{x}), t + \Delta t)$ around $\mathbf{x}$, equation (4.4) lead to:

$$I(\mathbf{x}, t + \Delta t) + \vec{d}(\mathbf{x}).\vec{\nabla} I(\mathbf{x}, t + \Delta t) + \vartheta(\vec{d^2}(\mathbf{x})) - I(\mathbf{x}, t) \approx 0 \tag{4.6}$$

where $\vec{\nabla} = (\partial/\partial x, \partial/\partial y)$ is the gradient operator. $\vec{\nabla} I(\mathbf{x}, t + \Delta t)$ are the spatial gradients on the second image (at time $(t + \Delta t)$). If $\vec{d}(\mathbf{x})$ is small enough, higher order terms $\vartheta(\vec{d^2}(\mathbf{x}))$ are negligible. We call the resulting equation BCCE_2:

$$\frac{I(\mathbf{x}, t + \Delta t) - I(\mathbf{x}, t)}{\Delta t} + \vec{v}(\mathbf{x}).\vec{\nabla} I(\mathbf{x}, t + \Delta t) \approx 0 \tag{4.7}$$

This equation was used by [106, 122].

We also perform a Taylor expansion of $I(\mathbf{x} + \vec{d}(\mathbf{x}), t + \Delta t)$ around $\mathbf{x}$ and t. Neglecting higher order terms $\vartheta(\vec{d^2}(\mathbf{x}), \Delta t^2)$, equation (4.4) leads to:

$$I_t(\mathbf{x}, t) + \vec{v}(\mathbf{x}).\vec{\nabla} I(\mathbf{x}, t) \approx 0 \tag{4.8}$$

where $I_t(\mathbf{x}, t) = \partial I(\mathbf{x}, t)/\partial t$ is the time gradient and $\nabla I(\mathbf{x}, t)$ are the spatial gradients on the first image (at time t). Lets call it BCCE_1. This formulation was used by [21].

The finite difference scheme of the time gradient $I_t(\mathbf{x}, t)$ neglecting $\vartheta(\Delta t^2)$, on two successive in time images, is here:

$$I_t(\mathbf{x}, t) = \frac{I(\mathbf{x}, t + \Delta t) - I(\mathbf{x}, t)}{\Delta t} \tag{4.9}$$

Combining equation (4.8), (4.7) and (4.9), we obtain a new non-centered BCCE equation that contains spatial information from $I(\mathbf{x}, t)$ and $I(\mathbf{x}, t + \Delta t)$.

$$I_t(\mathbf{x}, t) + \vec{v}(\mathbf{x}).\frac{1}{2}\left[\vec{\nabla} I(\mathbf{x}, t) + \vec{\nabla} I(\mathbf{x}, t + \Delta t)\right] \approx 0 \tag{4.10}$$

We call this equation TF_BCCE (TI_DOFE in [34, 38]). This equation based on two successive in time images has more information referring to the observed scene than BCCE_1 and BCCE_2. In this way, spatial gradient may better represents displacement orientation. Recently [4] propose to introduce an intermediate image at the half way from the first to the second image $(t - \Delta t/2)$ and $(t + \Delta t/2)$ and uses a symmetrical formulation of BCCE based on two images.

$$I\left(\mathbf{x} + \frac{\vec{d}(\mathbf{x})}{2}, t + \frac{\Delta t}{2}\right) - I\left(\mathbf{x} - \frac{\vec{d}(\mathbf{x})}{2}, t - \frac{\Delta t}{2}\right) \approx 0 \tag{4.11}$$

However, coordinates of the velocity $\vec{v}(\mathbf{x})$ correspond to coordinates of an imaginary intermediate image. Comparing to the formulation of [4], for TF_BCCE, there is no virtual intermediate image to be created via interpolation. We will see in section 4.2 that TF_BCCE will present more advantage than their formulation.

BCCE_1 (equation (4.8)), BCCE_2 (equation (4.7)) and TF_BCCE (equation (4.10)) are three different DOF equations of the BCCE (equation (4.4)). DOF equation is strongly dependent on the displacement amplitude because of the hypothesis made above. For large displacements, DOF equation becomes weaker because of the importance of higher Taylor order expansion terms ($\vartheta(\vec{d}^2(\mathbf{x}), \Delta t^2)$) that can be not anymore neglected. This limitation is resolved using multiresolution techniques introduced in previous chapter 3.2.5 and detailed in the following section 4.2.

The data term E_d in equation (4.2) is defined by a quadratic cost function of the BCCE_1 (equation (4.8)), BCCE_2 (equation (4.7)) or TF_BCCE (equation (4.10)).

The finite difference scheme of the time gradient $I_t(\mathbf{x}, t)$ was given in equation (4.9) neglecting $\vartheta(\Delta t^2)$ terms to formulate the TF_BCCE equation. Finite difference is known to be sensitive to noise. To reduce high frequency artifact and possible noise from the input images, we first smooth them using a Gaussian filter $\mathcal{W}$ of variance σ^2. This will help to determine a better velocity field [100]. The time gradient discretization becomes:

$$I_t(\mathbf{x}, t) = \frac{(\mathcal{W} * I)(\mathbf{x}, t + \Delta t) - (\mathcal{W} * I)(\mathbf{x}, t)}{\Delta t} \tag{4.12}$$

For spatial gradients of the intensity $\vec{\nabla} I(\mathbf{x}, t)$ and $\vec{\nabla} I(\mathbf{x}, t + \Delta t)$, we can also use a finite difference formulation.

As we have a large spatial information in the image, it is better to use the convolution property:

$$\vec{\nabla} (\mathcal{W} * I) = \vec{\nabla} \mathcal{W} \ * \ I \tag{4.13}$$

In this way, the spatial derivative is only computed on the Gaussian filter, then it is convolved with the image. This derivative formulation is less sensible to noise than the finite difference.

In addition to decrease artifact and noise, the Gaussian filter $\mathcal{W}$ removes high spatial frequencies of brightness variations (small scales). This will be the main point discussed in chapter 5 for study of turbulent flows.

The data term E_d of our DOF approaches is defined as follow:
For BCCE_1 equation (4.8):

$$E_d(\vec{v}, I) = \sum_{\mathbf{x} \in \mathcal{C}_1} \left(I_t(\mathbf{x}, t) + \vec{v}(\mathbf{x}, t). \left(\vec{\nabla} I(\mathbf{x}, t) \right) \right)^2 \tag{4.14}$$

For BCCE_2 equation (4.7):

$$E_d(\vec{v}, I) = \sum_{\mathbf{x} \in \mathcal{C}_1} \left(I_t(\mathbf{x}, t) + \vec{v}(\mathbf{x}, t). \left(\vec{\nabla} I(\mathbf{x}, t + \Delta t) \right) \right)^2 \tag{4.15}$$

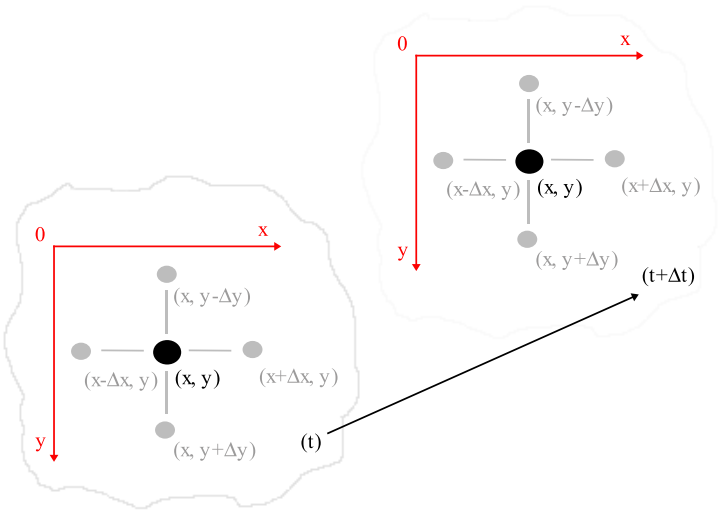

Figure 4.1: *Illustration of the time image sequence discretization scheme.*

For TF_BCCE equation (4.10):

$$E_d\left(\vec{v}, I\right) = \sum_{\mathbf{x}\in\mathcal{C}_1} \left(I_t(\mathbf{x},t) + \vec{v}(\mathbf{x},t).\frac{1}{2}\left(\vec{\nabla} I(\mathbf{x},t) + \vec{\nabla} I(\mathbf{x},t+\Delta t)\right)\right)^2 \tag{4.16}$$

with the above discretization of the gradients. $\mathcal{C}_1$ the single-pair clique corresponding to the image domain Ω.

4.1.2 Regularization term

The regularization energy E_s in Gibbs energy (equation (4.2)) is

$$E_s(\vec{v}) = \alpha \sum_{(\mathbf{x},\mathbf{x}')\in\mathcal{C}_2} V_s(\vec{v}(\mathbf{x}), \vec{v}(\mathbf{x}')) \tag{4.17}$$

We define a 4-neighborhood connexity (Figure 4.1). For pixel $\mathbf{x} = (x, y)$ on x and y axis at time t, the pixel size is $\Delta = (\Delta_x, \Delta_y)$ and pixel $\mathbf{x}$ has an intensity $I(\mathbf{x}, t)$ and a velocity $\vec{v}(\mathbf{x}, t)$. Due to the neighborhood system, we have 4 neighbors of $\mathbf{x}$ defined as:

$$\mathbf{x}'_0 = (x-\Delta x, y)\ ;\ \mathbf{x}'_1 = (x, y-\Delta y)\ ;\ \mathbf{x}'_2 = (x+\Delta x, y)\ ;\ \mathbf{x}'_3 = (x, y+\Delta y) \quad | \quad \mathbf{x}'_i \in \Omega \tag{4.18}$$

There are represented in figure 4.1 by gray color points. Set of pairs $(\mathbf{x}, \mathbf{x}')$, for all $\mathbf{x}$ and $\mathbf{x}'$, defines the clique $\mathcal{C}_2$ (see appendix B and figure B.2).

We also choose a quadratic cost function of the spatial velocity variations on the image. Defining V_s as the following finite difference schemes for each neighbor $\mathbf{x}'$ from equation (4.18), we have:

$$V_s\left(\vec{v}(\mathbf{x}), \vec{v}(\mathbf{x}'_0)\right) = \left|\left| \frac{\vec{v}(x,y) - \vec{v}(x-\Delta x, y)}{\Delta x} \right|\right|^2 \tag{4.19a}$$

$$V_s\left(\vec{v}(\mathbf{x}), \vec{v}(\mathbf{x}'_2)\right) = \left|\left|\frac{\vec{v}(x,y) - \vec{v}(x+\Delta x, y)}{\Delta x}\right|\right|^2 \tag{4.19b}$$

$$V_s\left(\vec{v}(\mathbf{x}), \vec{v}(\mathbf{x}'_1)\right) = \left|\left|\frac{\vec{v}(x,y) - \vec{v}(x, y-\Delta y)}{\Delta y}\right|\right|^2 \tag{4.19c}$$

$$V_s\left(\vec{v}(\mathbf{x}), \vec{v}(\mathbf{x}'_3)\right) = \left|\left|\frac{\vec{v}(x,y) - \vec{v}(x, y+\Delta y)}{\Delta y}\right|\right|^2 \tag{4.19d}$$

neglecting $\vartheta(\Delta x^2)$ and $\vartheta(\Delta y^2)$ terms.

When doing the summation over all the clique $\mathcal{C}_2$ (for all $\mathbf{x}$ and $\mathbf{x}'$), the discrete form of the regularization energy defined in (4.2) is equivalent to the continuous form defined in variational global approaches [14] as in equation (3.15). E_s correspond to a first order spatial continuity of the velocity field. For writing simplification, we pose $\Delta_x = \Delta_y = \Delta$.

$$E_s(\vec{v}) = \alpha \sum_{\mathbf{x},\mathbf{x}' \in \mathcal{C}_2} \left|\left|\frac{\vec{v}(\mathbf{x}) - \vec{v}(\mathbf{x}')}{\Delta}\right|\right|^2 \equiv \alpha \int_\Omega ||\vec{\nabla}\vec{v}(\mathbf{x},t)||^2 d\mathbf{x} \tag{4.20}$$

This discretization scheme is correct if the pixel size $(\Delta x, \Delta y)$ is small enough to neglect second order Taylor terms $\vartheta(\Delta x^2)$ and $\vartheta(\Delta y^2)$. It has the advantage to satisfy the global spatial continuity of the velocity field in a Gibbs energy formulation defined on a graph. The smoothness discretized term is also isotropic. We will use, in the following, this discretization scheme of the smoothness term in our proposed methods presented in this chapter and in the next one.

We use a quadratic penalty formulation of the data energy E_d and regularization energy E_s for an easier convergence of the minimization process used to determine the optimal solution [115]. However, as a drawback, it tends to oversmooth the real discontinuities of the velocity field. As we are studying impact of different data energy formulations for motion estimation, work on robust function presented in section 3.2.4 is not our objective.

4.2 Multiresolution Approach

The DOF formulation (equations (4.8), (4.7) and (4.10)) cannot deal with large displacements as the second and highest orders of Taylor expansion can not be anymore neglected. Multiresolution is a nice way to tackle this problem. This allows to estimate the velocity field from a coarse-to-fine estimation in an incremental way. There are two different multiresolution techniques: The pyramidal decomposition and the scale space decomposition (see section 3.2.5). However, multiresolution necessitates interpolation of velocity field and warping of image data between two pyramidal levels (section 4.2.1). These transformations result in an approximation of the image brightness intensity field from which the residual incremental estimation is computed. We propose, now, a multiresolution technique that reduces the number of these transformations. This unwarped multiresolution is presented in section 4.2.2.

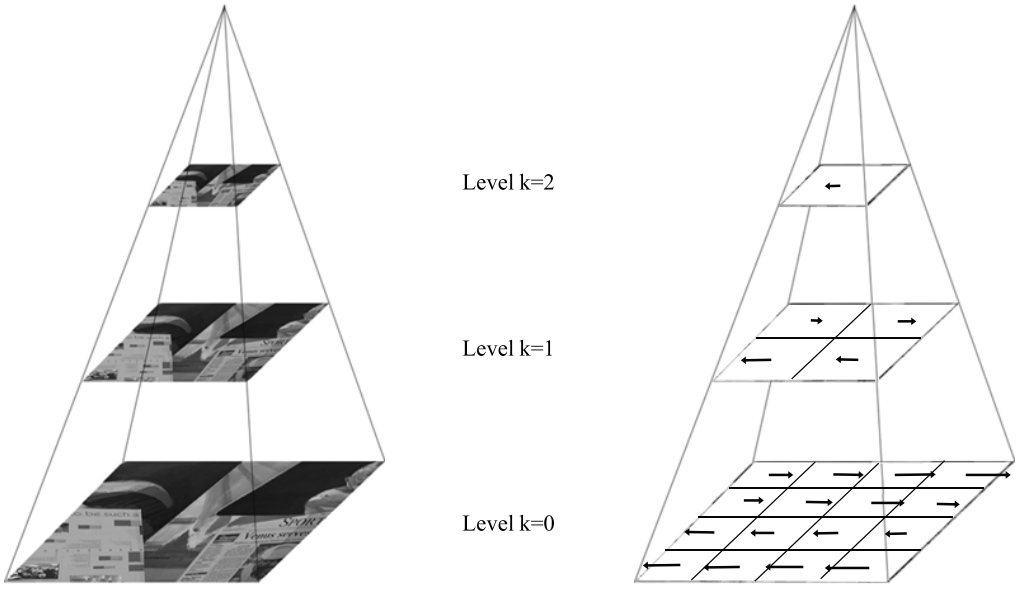

Figure 4.2: *Coarse-to-fine resolution with multiresolution representation of images (a) and corresponding estimated velocity field for each pyramidal level (b)*

4.2.1 Mutliresolution by Pyramidal decomposition technique (W_MR)

Multiresolution by pyramidal decomposition from coarse-to-fine resolution (from level K to level 0) has been proved to be numerically useful for Optical Flow estimation [123]. The image resolution is iteratively reduced in $K+1$ different successive resolution levels making a pyramid of image as illustrated in figure 4.2. This is done using a Gaussian filter between every level k to $k+1$ [30].

Figure 4.2.a. illustrates an example of Gaussian pyramidal decomposition. Because Δt is given by the time image series, large velocities are equivalent to large displacements. From the Gibbs energy E (equation (4.2)), velocity field $\vec{v}$ is expressed in pixel by interval of time. Spatial resolution of image I_k at level k is

$$\Delta_k = (2^k * \Delta \times x, 2^k \times \Delta y) \tag{4.21}$$

for $k = (0, ..., K)$ if $K+1$ levels are necessary and where Δ_0 is the pixel size of original images ($I_0 = I$). This means that the velocity field $\vec{v}$ (in pixel by interval of time) is smaller at coarser level. A representation of the corresponding velocity field at each pyramidal level k is given as example, in figure 4.2.b.

At coarsest level K, $\vec{v}_K$ is small enough to satisfy the BCCE_1 (equation (4.8)), BCCE_2 (equation (4.7)) and TF_BCCE (equation (4.10)).

For level k ($k \neq K$), the velocity $\vec{v}_k(\mathbf{x})$ (and equivalently for the displacement $\vec{d}_k(\mathbf{x})$) is defined as

$$\vec{v}_k(\mathbf{x}) = \widetilde{\vec{v}_{k+1}(\mathbf{x})} + \vec{v}_k^r(\mathbf{x}) \tag{4.22}$$

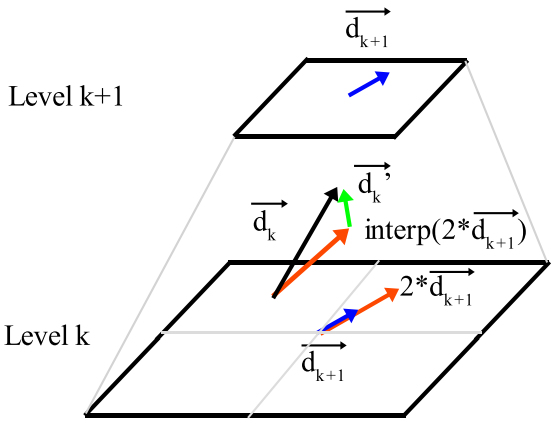

Figure 4.3: *Illustration of the incremental resolution of displacement in the pyramidal decomposition multiresolution from level $k+1$ to level k.*

where $\widetilde{\vec{v}_{k+1}} = \text{interp}\,(2 \times \vec{v}_{k+1})$ is the interpolated velocity field $\vec{v}_{k+1}$ computed at coarser resolution level $k+1$ to the current level k. The figure 4.3 gives an illustration of velocity between level k and $k+1$ (figure shows the displacement, $\vec{v}_k(\mathbf{x}) = \vec{d}_k(\mathbf{x})/\Delta t$). Velocity is multiplied by 2 because pixel resolution is decreased by 2 between level k and $k+1$. The velocity must also be interpolated at the new level pixel grid locations. We use bilinear interpolation. $\widetilde{\vec{v}_{k+1}}$ is considered as known information in the input time image sequence at level k. Then only the residual velocity field at level k, $\vec{v}_k^r$, needs to be estimated ($\widetilde{\vec{v}_{k+1}} >> \vec{v}_k^r$). The condition of small displacement between two successive images for DOF equations is now satisfied (figure 4.3).

Taking $\widetilde{\vec{d}_{k+1}} = \widetilde{\vec{v}_{k+1}}.\Delta t$ into consideration at level k, needs transformation of images by the displacement field $\widetilde{\vec{d}_{k+1}}$. The resulting image is denoted $\mathbf{I}$. This transformation is called warping [122]. There is two possible warping processes:

- Warping image at time t to $t + \Delta t$. It is called forward warping ($\mathbf{I_k}(\mathbf{x} + \widetilde{\vec{d}_{k+1}}(\mathbf{x}), t)$). The brightness constancy equation (4.4) becomes:

$$I_k(\mathbf{x} + \widetilde{\vec{d}_{k+1}}(\mathbf{x}) + \vec{d}_k^r(\mathbf{x}), t + \Delta t) - \mathbf{I_k}(\mathbf{x} + \widetilde{\vec{d}_{k+1}}(\mathbf{x}), t) \approx 0 \tag{4.23}$$

  Redefining the spatial coordinates on warped image at time t making the variable change $\mathbf{x} = \mathbf{x} + \widetilde{\vec{d}_{k+1}}(\mathbf{x})$, equation (4.23) is:

$$I_k(\mathbf{x} + \vec{d}_k^r(\mathbf{x}), t + \Delta t) - \mathbf{I_k}(\mathbf{x}, t) \approx 0 \tag{4.24}$$

  Thus BCCE_1 (equation (4.8)) [21] at level k takes the form:

$$\mathbf{I_k}_t\,(\mathbf{x}, t) + \vec{v}_k^r(\mathbf{x})\ .\ \vec{\nabla}\mathbf{I_k}\,(\mathbf{x}, t) = 0 \tag{4.25}$$

  with

$$\mathbf{I_k}_t\,(\mathbf{x}, t) = \frac{I_k\,(\mathbf{x}, t + \Delta t) - \mathbf{I_k}\,(\mathbf{x}, t)}{\Delta t} \tag{4.26}$$

- Warping image at time $t + \Delta t$ to t which is called backward warping ($\mathbf{I_k}(\mathbf{x} + \widetilde{\vec{d}_{k+1}}(\mathbf{x}) + \vec{d}^r_k(\mathbf{x}) - \widetilde{\vec{d}_{k+1}}(\mathbf{x}), t + \Delta t)$). Here, the brightness constancy equation (4.4) becomes:

$$\mathbf{I_k}(\mathbf{x} + \widetilde{\vec{d}_{k+1}(\mathbf{x})} + \vec{d}^r_k(\mathbf{x}) - \widetilde{\vec{d}_{k+1}(\mathbf{x})}, t + \Delta t) - I_k(\mathbf{x}, t) \approx 0 \tag{4.27}$$

  Thus BCCE_2 (equation (4.8)) [47, 122] at level k takes the form:

$$\mathbf{I_{kt}}(\mathbf{x}, t) + \vec{v}^r_k(\mathbf{x}) \,.\, \vec{\nabla}\mathbf{I_k}(\mathbf{x}, t + \Delta t) = 0 \tag{4.28}$$

  with

$$\mathbf{I_{kt}}(\mathbf{x}, t) = \frac{\mathbf{I_k}(\mathbf{x}, t + \Delta t) - I_k(\mathbf{x}, t)}{\Delta t} \tag{4.29}$$

For TF_BCCE formulation (equation (4.10)), in the same way, images at time t and $t + \Delta t$ has to be forward warping and backward warping by $\widetilde{\vec{d}_{k+1}}/2$. TF_BCCE in a multiresolution by pyramidal decomposition is then similar to [4] because it becomes a centered formulation with the W_MR multiresolution technique. The brightness constancy is:

$$\mathbf{I_k}(\mathbf{x} + \widetilde{\vec{d}_{k+1}(\mathbf{x})} + \vec{d}^r_k(\mathbf{x}) - \frac{\widetilde{\vec{d}_{k+1}(\mathbf{x})}}{2}, t + \Delta t) - \mathbf{I_k}(\mathbf{x} + \frac{\widetilde{\vec{d}_{k+1}(\mathbf{x})}}{2}, t) \approx 0 \tag{4.30}$$

Doing the variable change $\mathbf{x} = \mathbf{x} + \widetilde{\vec{d}_{k+1}(\mathbf{x})}/2$, TF_BCCE at level k becomes:

$$\mathbf{I_{kt}}(\mathbf{x}, t) + \vec{v}^r_k(\mathbf{x}) \,.\, \frac{1}{2}\left(\vec{\nabla}\mathbf{I_k}(\mathbf{x}, t) + \vec{\nabla}\mathbf{I_k}(\mathbf{x}, t + \Delta t)\right) = 0 \tag{4.31}$$

with

$$\mathbf{I_{kt}}(\mathbf{x}, t) = \frac{\mathbf{I_k}(\mathbf{x}, t + \Delta t) - \mathbf{I_k}(\mathbf{x}, t)}{\Delta t} \tag{4.32}$$

For all these formulations (equations (4.25), (4.28) and (4.31)), transformation of images by $\widetilde{\vec{d}_{k+1}}$ is done first, then the time and space gradients are computed. Their precision depends on the accuracy of $\widetilde{\vec{d}_{k+1}}$ which is an estimated displacement field from coarser level and which is not an exact field. It also depends on the efficiency of the used warping technique to generate $\mathbf{I}$. All existing algorithms using pyramidal decomposition, as multiresolution, use a warping process. The efficiency of the approach is then directly related to the used warping method and the quality of estimation of the coarser displacement field $\widetilde{\vec{d}_{k+1}}$. Warping is a non negligible source of errors. To tackle this, we propose in section 4.2.2 an unwarping multiresolution method.

At each pyramidal level k, the velocity field $\vec{v}^r_k$ is estimated by minimization of the Gibbs energy E_k defined in equation (4.2). The data energy E_{k_d}, at level k, is the L2 norm of the equations (4.25), (4.28) and (4.31) for BCCE_1, BCCE_2 and TF_BCCE approaches respectively.

As we are seeking for the velocity field $\vec{v}_k$ from t to $t+\Delta t$ at each level k, the regularization energy E_{k_s}, defined in equation (4.20), should be applied on $\vec{v}_k$. E_{k_s} becomes:

$$\begin{aligned} E_{k_s}(\vec{v}_k) &= \alpha \sum_{\mathbf{x},\mathbf{x}' \in \mathcal{C}_2} \left|\left| \frac{\vec{v}_k(\mathbf{x}) - \vec{v}_k(\mathbf{x}')}{\Delta_k} \right|\right|^2 \\ &= \alpha \sum_{\mathbf{x},\mathbf{x}' \in \mathcal{C}_2} \left|\left| \frac{\left(\widetilde{\vec{v}_{k+1}}(\mathbf{x}) + \vec{v}_k^r(\mathbf{x})\right) - \left(\widetilde{\vec{v}_{k+1}}(\mathbf{x}') + \vec{v}_k^r(\mathbf{x}')\right)}{\Delta_k} \right|\right|^2 \end{aligned} \tag{4.33}$$

where Δ_k takes the value $2^k \times \Delta x$ or $2^k \times \Delta y$ depending on the horizontal or vertical orientation of the pixel pairs $(\mathbf{x}, \mathbf{x}')$. The only change along the pyramid level k is the pixel size Δ_k (equation (4.21)).

After estimation of the residual velocity field $\vec{v}_k^r$, the velocity field $\vec{v}_k$ has to be updated using equation (4.22).

4.2.2 Multiresolution by Unwarped Pyramidal Decomposition technique (noW_MR)

As described in the above section 4.2.1, the multiresolution by pyramidal decomposition needs image warping between each pyramidal level. The time and space gradients, used by DOF equation, are then computed from these transformed images $\mathbf{I}$ in equations (4.25), (4.28) or (4.31). Warping images bring uncertainty related to the quality of the coarser displacement field $\widetilde{\vec{d}_{k+1}}$ and to the method used for the warping. For example, the resulting image brightness field may have some undefined values for which an interpolated value should be given, or some collisions due to the image resolution grid, for which a selection criteria or average method is often used.

We propose here to remove the warping step in W_MR (section 4.2.1) making some assumption on gradient properties. We call this new method noW_MR. At a pyramidal level k, $\vec{d}_k$ is defined by equation (4.22) recalled here:

$$\vec{d}_k(\mathbf{x}) = \widetilde{\vec{d}_{k+1}(\mathbf{x})} + \vec{d}_k^r(\mathbf{x}) \tag{4.34}$$

where $\widetilde{\vec{d}_{k+1}}$ has to be taken into account to determine $\vec{d}_k^r(\mathbf{x})$ using DOF equations (BCCE_1, BCCE_2 or TF_BCCE).

In noW_MR, we consider that the spatial gradients are constant over a small time interval Δt. This means that spatial gradients should not be dependent on $\widetilde{\vec{d}_{k+1}(\mathbf{x})}$ during the pyramidal decomposition technique. In W_MR technique, gradients are affected by the image warping because the resulting image brightness field is transformed by the coarser displacement field $\widetilde{\vec{d}_{k+1}}$ and then interpolated to the pixel grid. In noW_MR, the spatial gradients are computed on the original images at pyramidal level k at time t and at time $t+\Delta t$ depending on the used DOF equations (4.8)) (BCCE_1), (4.7) (BCCE_2) or (4.10) (TF_BCCE).

The figure 4.4 illustrates the difference between the spatial brightness distributions at a pyramidal level k using W_MR or noW_MR methods. For sake of simplicity, the illustration represents a pixel $\mathbf{x}$ with its 4-neighbors $\mathbf{x}'$. Arrows represent the relative coarser displacements $(\widetilde{\vec{d}_{k+1}(\mathbf{x}')} - \widetilde{\vec{d}_{k+1}(\mathbf{x})})$. In $\mathbf{x}$, this relative coarser displacement is thus null. Using the proposed unwarped method (noW_MR) in this section, spatial gradients are computed from the original images. However, using the warping method (W_MR) (previous section), image is warped by the previous relative coarser displacement field. Brightness distribution is transformed, and then interpolated to the image grid resolution to compute the spatial gradients. We can see that, in this example, spatial gradients are affected by the warping process. If the coarser displacement field is correct and if the warping method does not introduce some artifact, W_MR should perform better than our noW_MR. However, this is almost never the case, because estimation of the velocity field is never perfect.

At pyramidal level k, the DOF equations (4.8)) (BCCE_1), (4.7) (BCCE_2) and (4.10) (TF_BCCE) using noW_MR are simplified and take the following forms:

- For BCCE_1 (equation (4.25)), image at time t for pixel $\mathbf{x}$ keeps the intensity value and spatial gradients of the original image after moving to location $\mathbf{x} + \widetilde{\vec{d}_{k+1}(\mathbf{x})}$. Thus BCCE_1 becomes:

$$I_{kt}(\mathbf{x}, t) + \vec{v}_k^r(\mathbf{x}) \,.\, \vec{\nabla} I_k(\mathbf{x}, t) = 0 \tag{4.35}$$

with

$$I_{kt}(\mathbf{x}, t) = \frac{I_k\left(\mathbf{x} + \widetilde{\vec{d}_{k+1}(\mathbf{x})}, t + \Delta t\right) - I_k(\mathbf{x}, t)}{\Delta t} \tag{4.36}$$

- For BCCE_2 (equation (4.28)), image at time $t + \Delta t$ for pixel $\mathbf{x}$ takes the intensity value and spatial gradients on the original image of location $\mathbf{x} + \widetilde{\vec{d}_{k+1}(\mathbf{x})}$. Thus BCCE_2 becomes:

$$I_{kt}(\mathbf{x}, t) + \vec{v}_k^r(\mathbf{x}) \,.\, \vec{\nabla} I_k\left(\mathbf{x} + \widetilde{\vec{d}_{k+1}(\mathbf{x})}, t + \Delta t\right) = 0 \tag{4.37}$$

with

$$I_{kt}(\mathbf{x}, t) = \frac{I_k\left(\mathbf{x} + \widetilde{\vec{d}_{k+1}(\mathbf{x})}, t + \Delta t\right) - I_k(\mathbf{x}, t)}{\Delta t} \tag{4.38}$$

- And by combination of equation (4.35) and (4.37), TF_BCCE (equation (4.31)) becomes:

$$I_{kt}(\mathbf{x}, t) + \vec{v}_k^r(\mathbf{x}) \,.\, \frac{1}{2}\left(\vec{\nabla} I_k\left(\mathbf{x} + \widetilde{\vec{d}_{k+1}(\mathbf{x})}, t + \Delta t\right) + \vec{\nabla} I_k(\mathbf{x}, t)\right) = 0 \tag{4.39}$$

with

$$I_{kt}(\mathbf{x}, t) = \frac{I_k\left(\mathbf{x} + \widetilde{\vec{d}_{k+1}(\mathbf{x})}, t + \Delta t\right) - I_k(\mathbf{x}, t)}{\Delta t} \tag{4.40}$$

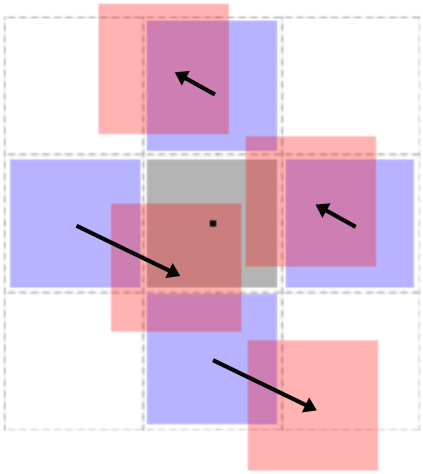

Figure 4.4: *Illustration of the difference with W_MR (red) and noW_MR (original image configuration - blue) methods for spatial gradient computations. Pixel schematization.*

Because of assumption made on gradients in this section, TF_BCCE with noW_MR does not need transformation of both images. The method is then different than the one used in [4] using W_MR.

From these new equations, there are, at maximum, two interpolations depending on the used DOF equations which are the pixel brightness interpolation $I_k\left(\mathbf{x}+\widetilde{\vec{d}_{k+1}(\mathbf{x})}, t+\Delta t\right)$ on image at time $t+\Delta t$ for the computation of $I_{kt}(\mathbf{x},t)$ and the spatial gradients interpolation $\vec{\nabla} I_k\left(\mathbf{x}+\widetilde{\vec{d}_{k+1}(\mathbf{x})}, t+\Delta t\right)$ on image $t+\Delta t$. These interpolations do not correspond to a warping process, it is only an interpolation of the brightness or spatial gradient of image $t+\Delta t$ corresponding to a shift of $\widetilde{\vec{d}_{k+1}(\mathbf{x})}$.

To resume, W_MR needs at each pyramidal level k to warp images which represent an interpolation and a transformation for each image. Time and space gradients depend then on the approximated images. For the noW_MR, we reduce the needed operations to only one or two interpolations depending on the DOF equations (4.8) (BCCE_1), (4.7) (BCCE_2) or (4.10) (TF_BCCE). Time and space gradients are computed on the exact image at time t and $t+\Delta t$.

Another advantage is that the discretization of the time derivative of BCCE_1 (equation (4.36)), BCCE_2 (equation (4.38)) and TF_BCCE (equation (4.40)) is, in the case of noW_MR, the same for all of them. It is not the case using W_MR because of the warping images (equations (4.26), (4.29) and (4.32)) which may result in different transformed images.

In the other hand, the assumption made on gradients imposes a local restriction on spatial deformation as it considers that gradients do not vary over the entire

pyramidal decomposition approach.

The tables 4.1 and 4.2 recall the difference between the DOF equations (BCCE_1, BCCE_2 and TF_BCCE) (section 4.1.1) using W_MR (section 4.2.1) or noW_MR (section 4.2.2) multiresolution techniques for the time and spatial gradients. $\mathbf{I_k}$ is the resulting warped image of I_k by the displacement field $\widetilde{\vec{d}_{k+1}}$.
$I_k\left(\mathbf{x}+\widetilde{\vec{d}_{k+1}(\mathbf{x})}, t+\Delta t\right)$ is the interpolated value of I_k and $\vec{\nabla} I_k$ at location $\mathbf{x}+\widetilde{\vec{d}_{k+1}(\mathbf{x})}$.

W_MR	BCCE_1	BCCE_2	TF_BCCE
I_{k_t}	$\frac{I_k(\mathbf{x},t+\Delta t)-\mathbf{I_k}(\mathbf{x},t)}{\Delta t}$	$\frac{\mathbf{I_k}(\mathbf{x},t+\Delta t)-I_k(\mathbf{x},t)}{\Delta t}$	$\frac{\mathbf{I_k}(\mathbf{x},t+\Delta t)-\mathbf{I_k}(\mathbf{x},t)}{\Delta t}$
$\vec{\nabla} I$	$\vec{\nabla}\mathbf{I_k}(\mathbf{x},t)$	$\vec{\nabla}\mathbf{I_k}(\mathbf{x},t+\Delta t)$	$\frac{1}{2}\left(\vec{\nabla}\mathbf{I_k}(\mathbf{x},t)+\vec{\nabla}\mathbf{I_k}(\mathbf{x},t+\Delta t)\right)$

Table 4.1: *Recall of time and spatial gradients for BCCE_1, BCCE_2 and TF_BCCE using W_MR (section 4.2.1).*

W_MR	BCCE_1	BCCE_2	TF_BCCE
I_{k_t}	$\frac{I_k\left(\mathbf{x}+\widetilde{\vec{d}_{k+1}(\mathbf{x})},t+\Delta t\right)-I_k(\mathbf{x},t)}{\Delta t}$	$\frac{I_k\left(\mathbf{x}+\widetilde{\vec{d}_{k+1}(\mathbf{x})},t+\Delta t\right)-I_k(\mathbf{x},t)}{\Delta t}$	$\frac{I_k\left(\mathbf{x}+\widetilde{\vec{d}_{k+1}(\mathbf{x})},t+\Delta t\right)-I_k(\mathbf{x},t)}{\Delta t}$
$\vec{\nabla} I$	$\vec{\nabla} I_k(\mathbf{x},t)$	$\vec{\nabla} I_k\left(\mathbf{x}+\widetilde{\vec{d}_{k+1}(\mathbf{x})},t+\Delta t\right)$	$\frac{1}{2}\left(\vec{\nabla} I_k(\mathbf{x},t)+\vec{\nabla} I_k(\mathbf{x}+\widetilde{\vec{d}_{k+1}(\mathbf{x})},t+\Delta t)\right)$

Table 4.2: *Recall of time and spatial gradients for BCCE_1, BCCE_2 and TF_BCCE using noW_MR (section 4.2.2).*

4.3 Multigrid Technique

To reduce the computational cost and to help local minimization methods to converge close to the global minimum, multigrid methods [107, 28] are often used.

These methods consist in representing the image domain in different grids $\mathcal{G}$. We choose squared grids of size $N_\mathcal{G} \times N_\mathcal{G}$ pixels. For more information about multigrid, readers can refer to [179, 174]. We describe here briefly such approach as we use it.

At a pyramid level k, we are looking for the velocity $\vec{v}^r_k(\mathbf{x})$ (equation (4.22)). We defined a two stage uniform multigrid process at each pyramidal level. Coupling the multigrid process with the multiresolution by pyramidal decomposition W_MR or noW_MR (section 4.2) for which the velocity $\vec{v}^r_k(\mathbf{x})$ is small at each pyramidal level k (see figure 4.3), a two-stage multigrid is sufficient. The image domain is decomposed in one size grid resolution. We consider the velocity $\vec{v}^r_{k_g}(\mathbf{x})$ uniform inside the grid $\mathcal{G}$ of size $N^2_\mathcal{G}$. Each sub-structure (pixel) of the grid is defined by the uniform grid velocity and by a local velocity component $\vec{v}^r_{k_l}(\mathbf{x})$ as:

$$\vec{v}^r_k(\mathbf{x}) = \vec{v}^r_{k_g}(\mathbf{x}) + \vec{v}^r_{k_l}(\mathbf{x}) \tag{4.41}$$

This method is a variant formulation of the FLTG (From Local To Global) method describes in (appendix C.4) for local minimization in Stereo Matching application.

However, in the multiresolution by pyramidal decomposition, at a pyramidal level k, the smoothness term E_s (equation (4.33)) controls evolution of the total velocity spatial variations. In this case, when generating the grid representation of the image, coarser interpolated velocity field $\widetilde{\vec{v}_{k+1}}$ has to be averaged over pixels inside the grid to get the corresponding coarser grid velocity field $\widetilde{\vec{v}_{(k+1)_g}}$.

In terms of energy, at pyramidal level k for grid level, the Gibbs energy E_k becomes:

$$\begin{aligned} E_k\left(\vec{v}, I\right) \;=\; & \sum_{\mathcal{G}\in\Omega}\sum_{\mathbf{x}\in\mathcal{G}} \left(I_{kt}\left(\mathbf{x},t\right) + \vec{v}^r_{k_g}(\mathbf{x}) \,.\, \vec{\nabla} I_k\left(\mathbf{x},t\right)\right)^2 \\ & + \alpha N_\mathcal{G} \sum_{\mathcal{G},\mathcal{G}'\in\mathcal{C}_{2_\mathcal{G}}} \left|\left| \frac{\left(\widetilde{\vec{v}_{(k+1)_g}} + \vec{v}^r_{k_g}\right) - \left(\vec{v}_{k_{g'}}\right)}{\Delta_k} \right|\right|^2 \end{aligned} \tag{4.42}$$

with $C_{2_\mathcal{G}}$ is the pair-grid cliques ($\mathcal{G}' \in \mathcal{N}_\mathcal{G}$). $\vec{v}_{k_{g'}} = \widetilde{\vec{v}_{(k+1)_{g'}}} + \vec{v}^r_{k_{g'}}$ is the neighbor grid velocity of the grid $\mathcal{G}'$. Here the DOF equation for the data term E_{k_d} is the BCCE_1 using noW_MR (equation (4.35)). We get similar energy using the other DOF equations or the other multiresolution by pyramidal decomposition (section 4.2).

The Gibbs energy E_k for grid level gets $1/(N^2_\mathcal{G})$ less summation terms as smoothness term E_{k_s} only constrains spatial variations of grid velocity field $\vec{v}_{k_g}$. Weight of the smoothness term cost is ponderated by $N_\mathcal{G}$ which represents the number of pixel on the border of the grid for which it is the only case where the velocity difference

between two pixels is non null. Moreover, the grid velocity field is computed through the DOF equation over $N_{\mathcal{G}}^2$ grid pixels. This is equivalent to Local approach (section 3.2.2) combined with Global approach (section 3.2.3). It has to be noted that such obtained grid velocity field $\vec{v}^{\,r}_{k_g}$ is less affected by noise (appendix D.2.3).

Thereafter, at substructure level (pixel), we estimate the local velocity field $\vec{v}^{\,r}_{k_l}$ for every pixel. The Gibbs energy E_k is:

$$\begin{aligned} E_k\left(\vec{v}, I\right) &= \sum_{\mathbf{x}\in\mathcal{C}_1} \left(I_{kt}\left(\mathbf{x}, t\right) + \left(\vec{v}^{\,r}_{k_g}(\mathbf{x}) + \vec{v}^{\,r}_{k_l}(\mathbf{x}) \right) \,.\, \vec{\nabla} I_k\left(\mathbf{x}, t\right) \right)^2 \\ &\quad + \alpha \sum_{\mathbf{x},\mathbf{x}'\in\mathcal{C}_2} \left|\left| \frac{\vec{v}_k(\mathbf{x}) - \vec{v}_k(\mathbf{x}')}{\Delta_k} \right|\right|^2 \end{aligned} \tag{4.43}$$

with $\vec{v}_k = \widetilde{\vec{v}_{(k+1)_g}} + \vec{v}^{\,r}_{k_g} + \vec{v}^{\,r}_{k_l}$ for $\mathbf{x}$ and $\mathbf{x}'$ respectively. At substructure level, it remains only a small quantity to estimate. As the grid velocity field is closed to the optimal solution, the minimization converges faster.

Minimization techniques and other optimization issues for motion estimation are described in appendixes C and E respectively. Results are given in appendix F.

4.4 Evaluation methodology

To validate accuracy of our DOF approaches (section 4.1) with W_MR and noW_MR multiresolution by pyramidal decomposition (section 4.2), we test them on synthetic data from classical sequences of computer vision community. Analysis of multiresolution and optimization issues are described in appendix F. Tests on DOF formulation (BCCE_1, BCCE_2 and TF_BCCE) and unwarped multiresolution (noW_MR), proposed in section 4.1.1 and 4.2.2 respectively, is detailed in the following section 4.5. We also validate our approach on synthetic particle image sequences in section 4.6.

Using the exact velocity field, we calculate the statistical errors to evaluate the quality of algorithm results. In a standard way [14, 11], we computed the Average Angle Error (AAE), Average Endpoint Errors or L1 absolute error (AEPE) and RMS Velocity Error (RMS) as follows:

$$AAE = \frac{1}{\mathbf{N}} \sum_{\mathbf{x}\in\Omega} arccos\left(\frac{\vec{v}_c(\mathbf{x}).\vec{v}_e(\mathbf{x})}{||\vec{v}_c(\mathbf{x})||\ ||\vec{v}_e(\mathbf{x})||}\right) \tag{4.44a}$$

$$AEPE = \frac{1}{\mathbf{N}} \sum_{\mathbf{x}\in\Omega} (||\vec{v}_c(\mathbf{x}) - \vec{v}_e(\mathbf{x})||) \tag{4.44b}$$

$$RMS = \sqrt{\frac{\sum_{\mathbf{x}\in\Omega} (||\vec{v}_c(\mathbf{x}) - \vec{v}_e(\mathbf{x})||^2)}{\mathbf{N}}} \tag{4.44c}$$

with $\vec{v}_c$ and $\vec{v}_e$ are respectively the exact and the estimated velocity fields. $\mathbf{N} = card(\Omega)$ is the total number of pixel $\mathbf{x}$ in the image. The exact velocity field $\vec{v}_c$ from image at time t to time $t + \Delta t$ is called the ground truth.

For visualization of velocity fields $\vec{v}_c$ and $\vec{v}_e$, we used an arrow representation for some image pixels as illustrated in figure 3.4.b. We also used a color mapping visualization proposed by Middlebury (figure 4.5) for which the orientation and amplitude of velocities are representing by a color and a brightness intensity respectively. White color corresponds to a null velocity vector.

Our approaches are compared with state of the art algorithms from both computer vision and fluid mechanic communities.

Figure 4.5: *Flow color coding (Middlebury open source)*

4.5 Experimentation on Middlebury Benchmark

4.5.1 Input Data Sequences

Methods are first tested on different image sequences provided by the Middlebury Flow Team Benchmark [11]. We chose this benchmark because proposed sequences were defined to represent different motion characteristics (discontinuities, light variations, untextured regions...) [12]. The figures 4.6.a illustrate the input images for three sequences: a) Dimetrodon, b) Venus and c) Yosemite. Figures 4.6.b represent the ground truth of these sequences using the velocity color mapping from figure 4.5. Statistical errors AAE, AEPE, RMS (equation (4.44)) are computed for three kinds of image area (*all*, *disc* and *untext*) which allows a better analysis of our approaches accuracy. The figures 4.6.c, 4.6.d and 4.6.e show the different masks used to extract specific image areas which are:

- All the image domain without border (*all*) Figure 4.6.c,
- The motion discontinuities regions (*disc*) Figure 4.6.d,
- The texture less regions (*untext*) Figure 4.6.e.

Before determination of the velocity field, we preprocess the Dimetrodon, Venus and Yosemite time image sequences by convolving them with a Gaussian filter of variance ($\sigma^2 = 1$) (see section 4.1.1 equations (4.12) and (4.13)).

Parameters set for each test is the same for a better comparison. Only, the studied parameter varies.

4.5.2 Analysis of Data Energy Formulation and Unwarping Multiresolution

For all results, we fix the same values of parameters. We use a 4-level pyramidal decomposition for multiresolution ($K = 3$) (section 4.2) and a grid size of 4×4 pixels for the multigrid method (section 4.3). The weighting coefficient α is spatially constant and equal to 100 (equation (4.2)). We use DDE minimization method (appendix C.2). See appendix F for explanation on the chosen parameters and minimization.

Figure 4.7 shows the estimated velocity field computed using the proposed TF_BCCE equation (4.10) with noW_MR unwarping multiresolution scheme (section 4.2.2 equation (4.39)) for Dimetrodon, Venus and Yosemite sequences. The color mapping visualization (figure 4.5) is the same as the ground truth visualization in figure 4.6.b.

The estimated velocity field is very similar to the ground truth. We show in table 4.3 the AAE (equation (4.44a)) errors for the three image sequences for the different DOF formulations BCCE_1 (equation (4.8)), BCCE_2 (equation (4.7)) and TF_BCCE (equation (4.10))) using (W_MR) warping and (noW_MR) unwarping multiresolutions (section 4.2). Performance of our methods is also compared to results shown in [11] given by other Optical Flow algorithms.

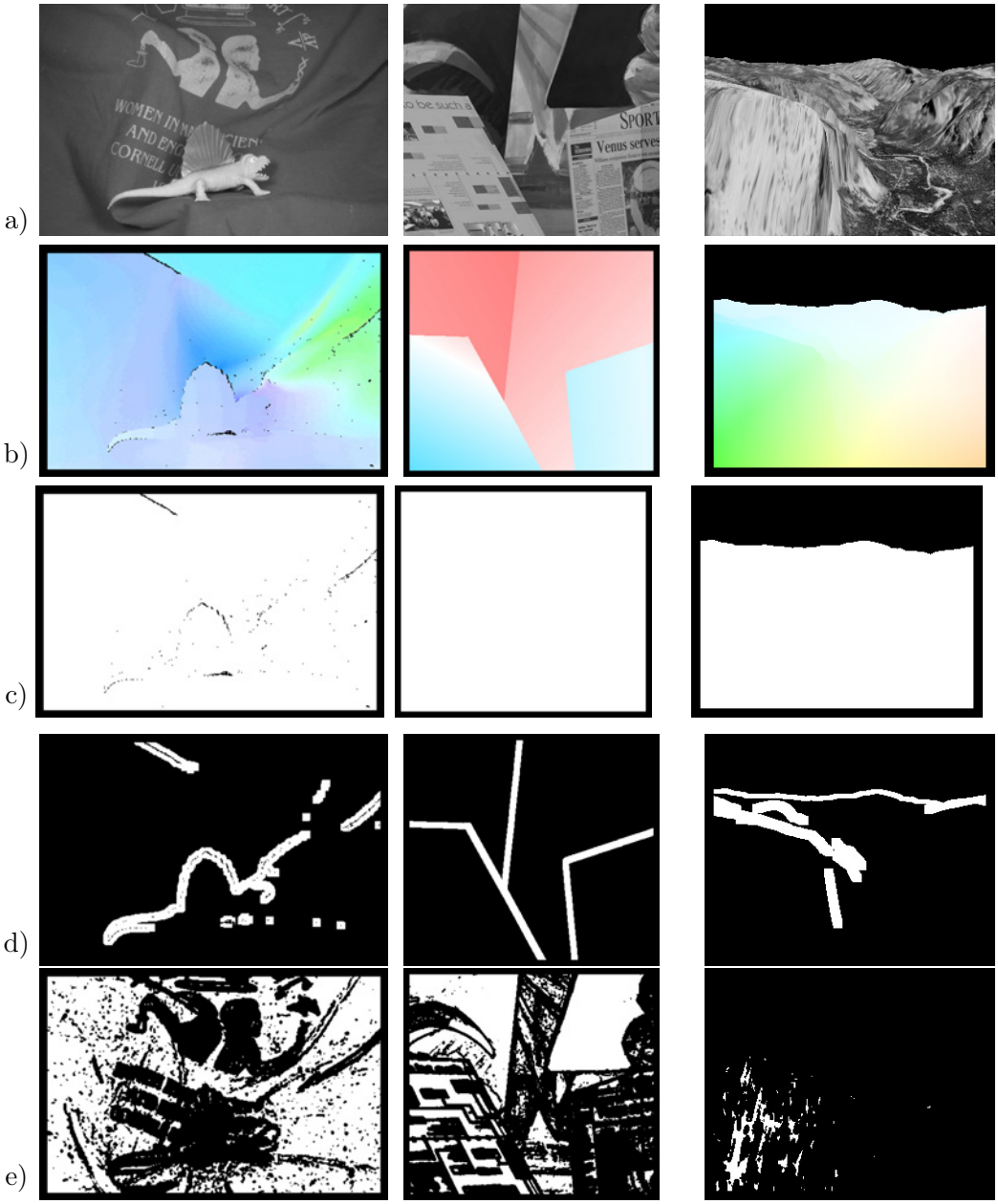

Figure 4.6: *Data: From top to bottom: a) Image sequence, b) ground truth, masks for computation of statistic errors (over white area): c) all domain (all), d) discontinuity (disc), e) untextured zones (untext). From left to right: Dimetrodon, Venus and Yosemite sequences.*

From the table 4.3, we can notice that our approaches outperform algorithms as Pyramid LK [23], MediaPlayer TM [110] and Zitnick [192] and that it gets around the same magnitude of errors (AAE) than Bruhn et al. [29] and Black and Anandan [21]. In bold red, it is the smallest AAE errors over all methods for each sequence.

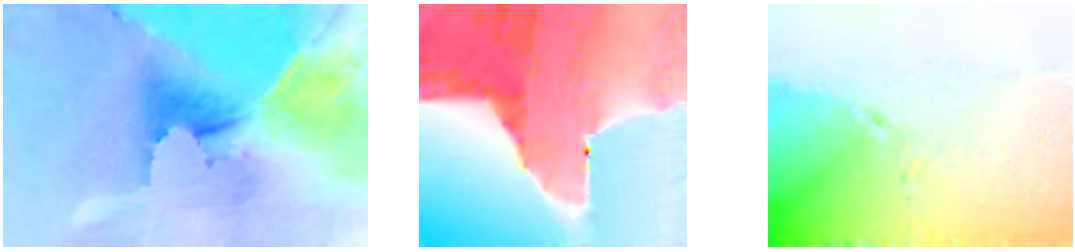

(a) (b) (c)

Figure 4.7: *Estimated velocity field using TF_BCCE with noW_MR for Dimetrodon (a), Venus (b) and Yosemite (c) sequences.*

AAE	dimetrodon			yosemite			venus		
	all	disc	untext	all	disc	untext	all	disc	untext
Bruhn et al. [29]	10.99	**9.41**	14.22	**1.69**	**2.86**	**1.05**	8.73	31.46	8.15
Black and Anandan [21]	**9.26**	10.11	**12.08**	2.65	4.18	1.88	**7.64**	**30.13**	**7.31**
Pyramid LK ([23])	10.27	9.71	13.63	5.22	6.64	4.29	14.61	36.18	24.67
MediaPlayer ([110])	15.82	26.42	16.96	11.09	17.16	10.66	15.48	43.56	15.09
Zitnick [192]	30.10	34.27	31.58	18.50	28.00	9.41	11.42	31.46	11.12
W_MR BCCE_1	5.20	8.62	6.17	3.21	4.88	**1.33**	8.56	34.85	8.21
W_MR BCCE_2	5.43	8.72	6.19	3.49	**4.75**	2.01	9.57	35.17	9.02
W_MR TF_BCCE	**5.00**	**8.43**	**5.89**	**3.17**	4.81	1.35	**8.32**	**34.81**	**7.90**
noW_MR BCCE_1	5.12	8.50	6.02	2.89	**4.13**	1.23	9.03	35.28	8.71
noW_MR BCCE_2	4.99	**8.09**	5.80	2.93	4.15	1.12	8.72	34.37	8.72
TF_BCCE noW_MR	**4.92**	8.21	**5.80**	**2.88**	**4.13**	**1.06**	**8.41**	**33.81**	**8.54**

Table 4.3: *AAE errors comparison of BCCE formulations and warping (W_MR) - unwarping (noW_MR) multiresolution with classic algorithms ([11]) for Dimetrodon, Yosemite and Venus sequences. In bold: smallest AAE errors for classic algorithms, W_MR and noW_MR. In red: smallest AAE errors over all methods.*

Each method produces at least one of the best estimation.

DOF formulation using the two-frame spatial information (TF_BCCE) performs better than BCCE_1 and BCCE_2 which are based on only one image information independently of the used multiresolution scheme. The new unwarping multiresolution method allows most of the time, a better estimation of the displacement field for all kind of DOF formulations.

However, as remarked in appendix F, we can notice that our methods get stronger AAE errors at motion discontinuities (disc). This is mainly due to the energy terms that are defined as quadratic functions (section 4.1).

Note, that for the multigrid, the grid size is set as 4×4 pixels. AAE errors for DDE minimization in table 4.3 becomes most of the time smaller than AAE errors for SA minimization in table F.3 which confirms the figure F.6 of appendix F.

We also participate to the Middlebury Optical Flow comparison survey. TF_BCCE with noW_MR results are available on the website: `http://vision.middlebury.edu/flow/`. The Middlebury evaluation provides the most complete Optical Flow

Average angle error	avg. rank	Army (Hidden texture) GT all	Army (Hidden texture) GT disc	Army (Hidden texture) GT untext	Army (Hidden texture) im0 all	Army (Hidden texture) im0 disc	Army (Hidden texture) im0 untext	Army (Hidden texture) im1 all	Army (Hidden texture) im1 disc	Army (Hidden texture) im1 untext
2D-CLG [1]	24.8	10.1 31	22.6 33	7.59 29	9.84 31	16.9 26	11.1 32	16.9 32	28.2 32	18.8 34
Black & Anandan [4]	24.9	6.81 27	15.4 27	7.43 28	8.77 28	19.5 29	7.35 26	13.0 30	22.9 27	12.5 27
Horn & Schunck [3]	29.2	8.01 30	19.9 31	8.38 31	9.13 30	23.2 32	7.71 28	14.2 31	25.9 31	14.6 31
TI-DOFE [28]	30.5	13.4 35	23.2 34	16.5 35	16.5 34	24.1 34	18.2 34	20.2 35	31.1 35	20.6 35
Pyramid LK [2]	35.2	13.9 36	20.9 32	21.4 36	24.1 36	23.1 31	30.2 36	20.9 36	29.5 33	21.9 36

Grove (Synthetic) GT all	Grove (Synthetic) GT disc	Grove (Synthetic) GT untext	Grove (Synthetic) im0 all	Grove (Synthetic) im0 disc	Grove (Synthetic) im0 untext	Grove (Synthetic) im1 all	Grove (Synthetic) im1 disc	Grove (Synthetic) im1 untext
14.1 32	31.1 32	13.1 32	3.86 22	4.62 18	4.53 28	5.98 18	21.2 26	5.97 23
8.29 28	26.1 29	6.77 28	4.18 26	5.28 27	3.69 18	6.19 20	20.0 23	5.34 18
12.4 31	30.6 31	11.3 31	4.64 28	5.64 28	4.60 29	8.21 29	24.4 33	8.45 29
19.9 34	32.9 34	20.8 34	4.89 31	5.90 30	5.54 31	8.04 28	23.9 32	8.81 30
22.2 35	34.6 36	25.0 35	18.7 36	23.1 36	20.2 36	21.2 36	24.5 34	21.0 36

Urban (Synthetic) GT all	Urban (Synthetic) GT disc	Urban (Synthetic) GT untext	Urban (Synthetic) im0 all	Urban (Synthetic) im0 disc	Urban (Synthetic) im0 untext	Urban (Synthetic) im1 all	Urban (Synthetic) im1 disc	Urban (Synthetic) im1 untext
5.98 18	21.2 26	5.97 23	1.76 2	**3.14** 1	1.46 4	6.29 24	12.9 27	5.81 25
6.19 20	20.0 23	5.34 18	3.63 24	5.05 28	1.79 6	6.45 26	12.2 24	5.17 23
8.21 29	24.4 33	8.45 29	4.01 26	5.41 30	1.95 11	9.16 30	17.5 30	8.86 30
8.04 28	23.9 32	8.81 30	2.97 18	4.34 16	1.88 9	10.9 32	17.7 31	11.9 32
21.2 36	24.5 34	21.0 36	6.41 35	7.02 35	10.8 36	25.6 36	31.5 36	34.5 36

SD angle error	avg. rank	Army (Hidden texture) GT all	Army (Hidden texture) GT disc	Army (Hidden texture) GT untext	Army (Hidden texture) im0 all	Army (Hidden texture) im0 disc	Army (Hidden texture) im0 untext	Army (Hidden texture) im1 all	Army (Hidden texture) im1 disc	Army (Hidden texture) im1 untext
2D-CLG [1]	23.4	15.2 33	24.5 35	11.2 32	15.1 24	25.9 19	13.5 26	27.5 32	33.9 33	24.7 33
Black & Anandan [4]	25.2	10.5 26	18.0 24	8.14 26	21.4 32	32.8 31	16.1 30	26.1 30	32.3 30	21.8 29
Horn & Schunck [3]	27.3	11.8 31	19.3 28	8.85 31	20.1 28	33.5 34	15.3 28	25.5 28	31.2 21	24.0 32
TI-DOFE [28]	27.6	14.6 32	21.1 32	11.7 33	22.4 34	31.6 29	19.6 33	28.6 34	31.2 21	26.3 34
Pyramid LK [2]	33.9	17.0 35	20.4 31	19.4 36	31.7 35	32.1 30	32.5 35	32.9 36	34.8 35	29.9 36

Grove (Synthetic) GT all	Grove (Synthetic) GT disc	Grove (Synthetic) GT untext	Grove (Synthetic) im0 all	Grove (Synthetic) im0 disc	Grove (Synthetic) im0 untext	Grove (Synthetic) im1 all	Grove (Synthetic) im1 disc	Grove (Synthetic) im1 untext
22.2 29	38.3 21	19.0 31	5.67 18	6.44 16	6.29 26	17.5 22	34.3 31	16.4 23
20.8 27	38.9 24	16.1 28	6.29 25	7.41 29	5.62 15	17.1 21	31.2 23	13.7 21
26.1 32	38.6 22	23.5 32	6.12 22	6.99 23	6.34 27	19.9 30	33.9 29	19.6 31
26.3 33	36.0 18	25.1 33	6.43 27	7.34 27	6.67 30	19.1 28	33.8 28	18.9 30
29.4 35	35.3 16	29.9 35	31.7 36	35.5 36	29.8 36	29.9 36	32.3 26	28.0 36

Urban (Synthetic) GT all	Urban (Synthetic) GT disc	Urban (Synthetic) GT untext	Urban (Synthetic) im0 all	Urban (Synthetic) im0 disc	Urban (Synthetic) im0 untext	Urban (Synthetic) im1 all	Urban (Synthetic) im1 disc	Urban (Synthetic) im1 untext
1.47 2	2.68 4	1.54 6	21.7 22	34.6 24	16.9 20			
4.06 29	5.11 30	2.37 12	23.1 23	34.1 23	15.7 16			
3.95 28	4.28 20	2.46 13	25.3 28	37.5 29	22.0 28			
2.88 15	3.15 8	2.82 17	25.7 29	36.6 28	22.3 29			
9.01 33	7.93 33	18.9 33	39.9 33	45.4 36	39.0 36			

Figure 4.8: *Extracted table from Middlebury online statistic error values tables for Average Angle Error (AAE) and Standard Deviations (SD). TF_BCCE is using noW_MR.*

algorithm's comparison. It evaluates performances of approaches on different type of motion on synthetic and real image sequences. It also computes several statistical errors to evaluate the quality of velocity field estimations. Moreover, it contains the most famous Optical Flow approaches and the state-of-art algorithms in the Optical Flow domain.

Figure 4.8 shows part of the evaluation table with Bruhn et al. [29] (2D-CLG), Black & Anandan [21], Horn & Schunck [77], pyramid LK [23] and TF_BCCE with noW_MR methods. In this table, TF_BCCE always gives better AAE errors than pyramid LK and AAE errors close to the multiresolution Horn & Schunck (implemented by [163] in 2008). This is coherent because our DOF equation formulation is similar to Horn & Schunck DOF equation (section 3.2.3). Black & Anandan have smaller AAE errors in other sequences than Yosemite. This is probably due to the fact that we have optimized the parameter set only on Yosemite sequence. An optimization of parameter set over the all training data should improve performance of the present proposed method for the other data sequences.

4.5.3 Model Efficiency on Other Algorithms

To validate TF_BCCE and noW_MR methods, we apply them into other Optical Flow algorithms. We use two Matlab open source codes proposed by [163], in which we incorporated TF_BCCE and noW_MR. One of the open source algorithm is a multiresolution adaptation of the Horn & Schunck [77] (H&S) algorithm and the other of the Black & Anandan [21] (B&A) algorithm.

Results are illustrated in Figure 4.9 on the Rubber Whale sequence that was furnished with the code sources and the running code example. In Figure 4.9, we represent only the first image of the sequence and the corresponding ground truth at the upper line and the estimated velocity fields obtained using TF_BCCE with noW_MR for H&S (Figure 4.9.c) and B&A (Figure 4.9.d).

Statistical AAE errors are shown in table 4.4 comparing the AAE errors with the original code and with the modified code using TF_BCCE and noW_MR. For

(a) first Image

(b) Ground truth

(c) H&S with TF_BCCE

(d) B&A with TF_BCCE

Figure 4.9: *Rubber Whale sequence: First image (a), ground truth (b) and estimated velocity field from Horn & Schunck (H&S) (c) and Black & Anandan (B&A) (d) Matlab codes [163] using TF_BCCE noW_MR*

AAE	H&S	B&A
Deqing Sun	7.277	5.944
TF_BCCE noW_MR	**6.996**	**5.781**

Table 4.4: *AAE error for the improved Horn & Schunck (H&S) and Black & Anandan (B&A) Matlab codes [163] on Rubber Whale sequence with TF_BCCE using noW_MR*

the two algorithms, TF_BCCE noW_MR gives a smaller AAE error. It generalizes and validates that the proposed approach allows a better estimation of the velocity field. This is due to a better motion information extracted from both images and a reduction of image transformation in the multiresolution process (section 4.2).

This work on DOF formulations (section 4.1) and Unwarping multiresolution (section 4.2.2) was published in [34] and submitted in [38].

4.6 Validation on Flow Motion

We applied now our method on synthetic particle image velocimetry (PIV) sequences obtained from experimental studies of turbulent flow field.

Following results are obtained using the TF_BCCE (equation (4.10)) with Unwarping Multiresolution method noW_MR (section 4.2.2). Our approach is compared to other DOF methods [77, 21, 107, 135, 46] and cross-correlation PIV (CC) [119, 128, 91].

Readers can find details on PIV recording technique for laboratory experiments in appendix A.3 and a description of the cross correlation PIV (CC) technique in appendix A.1.

Although, our energy definition $E = E_d + E_s$ (equations (4.16) and (4.17)) is not adapted to flow motion, our method performs as good as other DOF techniques form the literature and CC techniques.

4.6.1 Standard PIV images

Data sequences

The Visualization Society of Japan (VSJ) published in 1999 standard PIV images in order to provide to world researchers available data to test Optical Flow (OF) techniques. These data are available on-line (`www.piv.jp/image-e.html`). In this project, there are eight different synthetic PIV image sequences called standard images. These sequences were generated with the same velocity field (in cm/s) in a wide variety of controlled conditions [118] which allows to evaluate the accuracy of OF approaches with respect to different parameters.

Parameters of the eight sequences are thus detailed in Table 4.5. $\overline{\vec{v}}$ is the average image velocity in pixels by interval of time over the image domain, $||\vec{v}_{max}||$ gives the maximum of image velocity. $\overline{W}$ is the out-of-plane velocity which expresses the three-dimensional effects of the flow field: The intensity of the particles that moves slightly out of the observed plane (if the particle completely leaves the plane the gray value of the particle disappears). P_n is the number of solid particle in the image, $\overline{P_d}$ is the average of solid particle diameter in pixels and $std(P_d)$ is the standard deviation of P_d in pixels. Image sequences n°01, n°02 and n°03 differ only with respect to the magnitude of the velocity field. Image sequences n°04 and n°05 have only different number of particle. Sequences n°06 and n°07 have particles with a different diameter while sequence n°08 has a high out-of-plane velocity.

Figure 4.10.a represents one of the input particle image and figure 4.10.b illustrates the exact velocity field $\vec{v}_c$ for the eight sequences. Only a parse $\vec{v}_c$, every 8×8 pixels, is available.

Approaches and parameters

Some applications of method on these images are available in the literature [119, 128, 135, 46]. The results from these tests are shown here for comparison with ours. To complete the evaluation, we also run the DOF open source Matlab codes of Horn

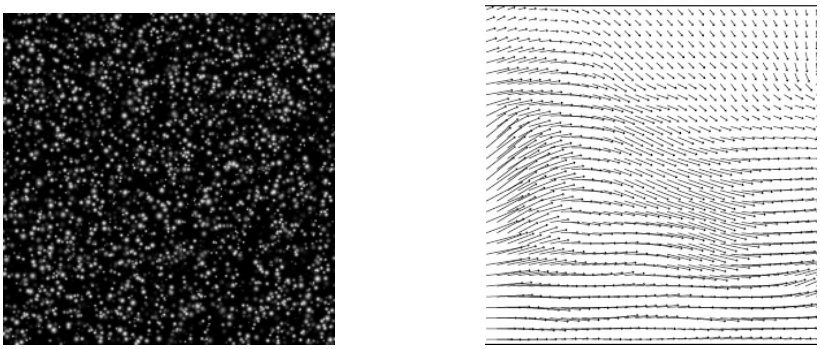

a) b)

Figure 4.10: *a) One of the standard particle image b) and the parse correct velocity field given every* 8×8 *pixels.*

Sequence	$\overline{\vec{v}}$	$\|\|\vec{v}_{max}\|\|$	$\overline{W}$	P_n	$\overline{P_d}$	$std(P_d)$
01	7.4	15.0	0.017	4000	5.0	1.4
02	**22.0**	**45.0**	**0.058**	4000	5.0	1.4
03	**2.5**	**5.1**	**0.006**	4000	5.0	1.4
04	7.4	15.0	0.017	**10000**	5.0	1.4
05	7.4	15.0	0.017	**1000**	5.0	1.4
06	7.4	15.0	0.017	4000	5.0	**0.0**
07	7.4	15.0	0.017	4000	**10.0**	**4.0**
08	7.4	15.0	**0.170**	4000	5.0	1.4

$\overline{\vec{v}}$: average image velocity [pixels/interval]
$||\vec{v}_{max}||$: maximum image velocity [pixels/interval]
$\overline{W}$: average out-of-plane velocity [-/interval]
P_n : number of solid particles [-]
$\overline{P_d}$: average solid particle diameter [pixels]
$std(P_d)$: standard deviation of P_d [pixels]

Table 4.5: *Data List of the Standard Images. Parameter settings of n°01 to n°08 image sequences.*

& Schunck (H&S) and Black & Anandan (B&A) implemented by [163] and the CC commercial software [91].

We briefly present the tests for which errors are compared with our errors.

- TF_BCCE noW_MR (our method): Because of the large velocities in pixel by interval of time of sequence n°02 ($||\vec{v}_{max}|| = 45$), we use for the eight sequences, a 6-level pyramidal decomposition ($K = 5$) (section 4.2.2) with a grid size of 4×4 pixels for the multigrid (section 4.3). Images are previously smoothed with a Gaussian filter of variance $\sigma^2 = 0.75$ and the weighting

coefficient $\alpha = 200$ (equation (4.2)).

- Black & Anandan (B&A-SUN) and Horn & Schunck (H&S-SUN): The open source is available on-line on `http://www.cs.brown.edu/~dqsun/research/software.html`. We used a 5 level pyramidal decomposition ($K = 4$), weighting coefficient was set to $\alpha = 0.5$ for B&A-SUN and $\alpha = 1000$ for H&S-SUN. These approaches use warping multiresolution W_MR (section 4.2.1) and even do 3 successive estimations and warpings at each pyramidal level k. Efficiency comparison of these approaches are available on Middlebury benchmark as shown in section 4.5.2.

- Cross-correlation software (CC Lavision) [91]: Davis Lavision software is the most used CC technique in experimental fluid community. In this test, we use refinement method that is an iterative methods giving first velocity for 128×128 pixels size window to 8×8. Gaussian peak interpolation is used on cross-correlation signal to better retrieve the exact maximum localization. More information on CC technique is given in appendix A.1.

- Robust Multigrid Horn & Schunck (OF-MG) [107]: It is a coupled pyramidal decomposition - multigrid optical flow method. Error values were taken from [46].

- Orthogonal Dynamic Programming (ODP) [128]: It is a dynamic programming [154] based optical flow technique that uses a global regularization of the intensity difference between successive images. Error values were taken from [128].

- Classic CC (CC-Classic) and extended (CC+NS) [119]: It is a CC technique. Interrogation window is taken equal to 9×9 pixels without overlapping, and correlation coefficient is evaluated by direct convolution computation instead of FFT algorithm (usually used). Authors propose a dynamical system correcting the CC by physical equations. Here, the 2D vorticity equation (3.48) and continuity equation ($\vec{\nabla}.\vec{v} = 0$) are employed to govern the CC estimation. Error values were taken from [119].

- Multiscale Horn & Schunck (OF-MS) [135]: Authors propose a pyramidal multiscale decomposition of Horn & Schunck method. A 5 pyramidal decomposition ($K = 4$) with a 9 scale space decomposition levels on every pyramidal level k was chosen. Error values were taken from [135].

- Continuity equation with Div-Curl regularization (ICE-DivCurl) [46]: Authors use the integrated continuity optical flow equation (section 3.3.1.2) with a second-order div-curl robust regularization (section 3.3.2.1). Error values were taken from [46].

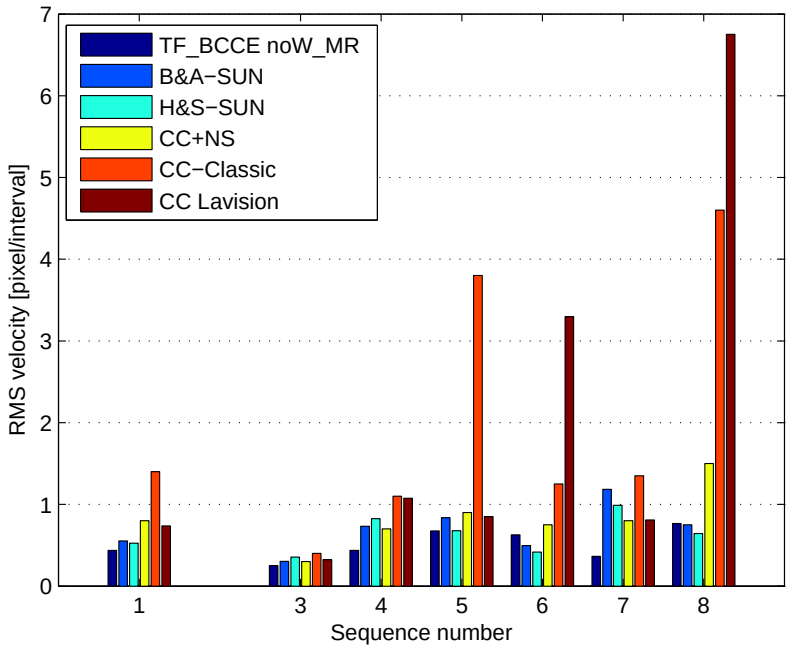

Figure 4.11: *Comparison of the RMS velocity error for our algorithm TF_BCCE noW_MR, B&A-SUN and H&S-SUN [163], CC+NS and CC-Classic [119] and CC Lavision [91] methods.*

Results

Figure 4.11 compares the RMS velocity errors (equation (4.44c)) of CC and DOF approaches mentioned just above with ours from the application of our approach.

We do not have information about sequence n°02 for CC-Classic and CC+NS in [119]. Errors from DOF approaches are compared in figure 4.12 in their application to the eight sequences. In Figure 4.11, RMS velocity errors are always less than 1 pixel by interval for TF_BCCE noW_MR. DOF approaches seem to have constantly the same order of RMS errors. For CC methods, there are some RMS errors strongly different from the others on certain image sequences. While CC techniques are defined for particle images, they give here the strongest RMS errors. It is clear on sequence n°08, where the out-of-plane velocity is the strongest. Out-of-plane velocity will brings particle outside of the light sheet. However, DOF methods and CC+NS incorporate a global regularization of the velocity field. These methods are, then, more robust to out-of-plane velocity variations.

For CC Lavison, RMS error is high for sequence n°06, whereas there is no standard deviation of particle diameters. It is strange as the peak should be easier to detect. However, CC-Classic shown as well a higher RMS error than other methods. It also produces the highest RMS error for sequence n°05 for which there is not lot of particles in the image. This can be explained by the used of meshes of 9×9 pixels

that become too small compared to the number of particles in the image. CC-Classic does not use refinement technique as CC Lavision allowing to get a better velocity field.

CC+NS constraining method always gives lower RMS errors than the same method without physical regularization of the flow (CC-Classic). It strongly reduces the RMS errors where CC method gives higher errors. The global physical regularization form helps the correlation peak detection to find the best matches which satisfies dynamic fluid flow equations. However, we can see here that even with dynamic physical regularization, CC methods return higher RMS errors than DOF approaches (TF_BCCE noW_MR, H&S-SUN and B&A-SUN). These synthetic image sequences are not affected by experimental noise. In case of real PIV acquisition images, CC methods become more robust than DOF methods because cross correlation is more robust in presence of noise.

For DOF methods, TF_BCCE noW_MR has almost constantly smaller RMS errors than B&A-SUN and H&S-SUN. B&A-SUN and H&S-SUN got smaller RMS error only in the case of sequence n°06 where there is no particle diameter variation which means that the brightness constancy is exactly satisfied. In this optimal condition, the pyramidal decomposition with warping procedure may not bring too much erroneous information. However, in Figure 4.12 where the percentage value of the relative L1 amplitude AEPE errors (equation (4.44b)) is plotted, we can see that B&A-SUN and H&S-SUN generally give the highest relative AEPE for which we can confirm that depending on the chosen function to compute errors, different conclusion can be made on approach efficiency.

Figure 4.12 compares relative AEPE errors which are the AEPE errors (equation (4.44b)) divided by the average image velocity $\overline{\vec{v}}$ for the different DOF methods describe above. The average relative AEPE errors of TF_BCCE noW_MR method for image sequences n°01 and n°04 to n°07 are the lowest. We can see that for sequence n°04 corresponding to high particle density, we got the smallest AEPE error. Conversely for sequence n°05, corresponding to low particle density, the error is higher. This means that DOF methods are sensitive to the number of particle on image to treat. In fact, more numerous particles are, more the image brightness is smoothed over the image.

Nevertheless on sequence n°05 and n°06, our algorithm gives the smallest errors compared to other DOF methods. This is due to the TF_BCCE method that contains spatial image information from the two successive images at time t and time $t + \Delta t$.

Even after setting empirically the best parameters for B&A-SUN and H&S-SUN methods to get the smallest errors, these methods still have the highest AEPE errors compare to the other DOF approaches. ODP method also shows higher AEPE errors than our approach.

OF-MG and OF-MS methods are similar approaches based on Horn & Schunck algorithm. AEPE Errors seem also similar. The difference between the two methods is the used multiresolution technique. OF-MG method uses a pyramidal decomposition coupled with a multigrid technique. OF-MS method uses pyramidal

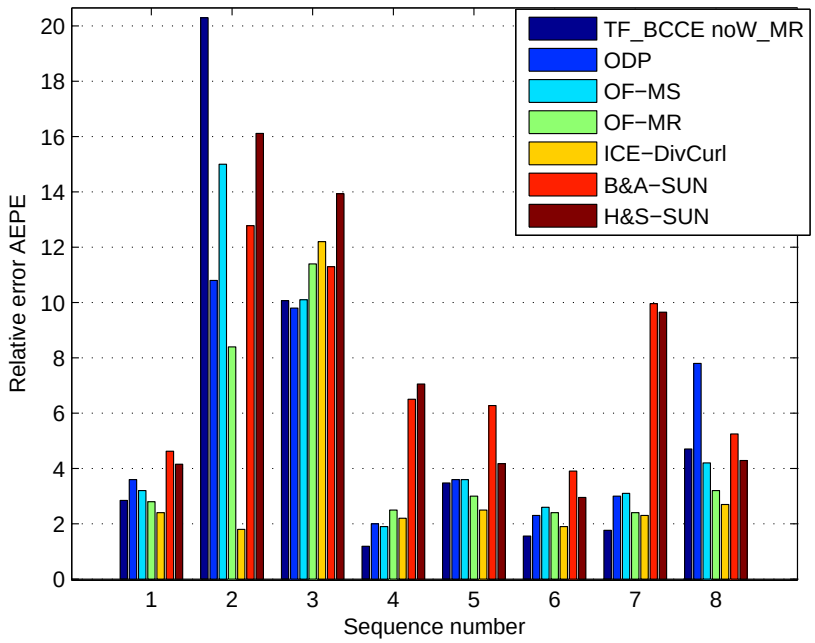

Figure 4.12: *Comparison of the RMS velocity error for TF_BCCE noW_MR, ODP [128], OF-MS [135], OF-MG [107], ICE-DivCurl [46], B&A-SUN and H&S-SUN [163] methods.*

decomposition with multiscale decomposition technique.

ICE-DivCurl method gives the smallest AEPE errors for sequences n°01, n°02 and n°08. For sequence n°01, AEPE error difference with our approach is very small. However on sequence n°02, ICE-DivCurl method clearly outperforms other approaches. This method uses the multiresolution - multigrid technique proposed in OF-MG [107]. We can see that both methods retrieve the lowest error for this sequence. The multigrid method, here, allows to retrieve a better velocity field at the coarsest pyramidal level and then the algorithm is able to correctly estimate the velocity field. For our approach, even if we use an unwarping multiresolution noW_MR, the two-stage uniform multigrid technique is, for this sequence, too restrictive (section 4.3). We should incorporate multi-stage multigrid technique for high velocity sequences (in sequence n°02, $||\vec{v}_{max}|| = 45$ pixels by interval of time in an 256×256 image pixels which represents almost a shift of 20 % of the image). The difference between ICE-DivCurl and OF-MG methods, on this sequence and on sequence n°08, can be explained by the definition of their regularization function E_s. ICE-DivCurl method uses a div-curl regularization (equation (3.40)) which favors more spatial velocity variations than first order velocity derivative (equation (3.15)) used in OF-MG method and in our approach.

For sequence n°03, velocities in pixel by interval of time are small. All methods

give higher relative error, since small estimated error will produces high relative error. In this case, much pyramidal decomposition is not useful and even more may bring some supplementary errors in the estimation. We see that our method gives one of the smallest errors. It is probably due to the noW_MR technique (section 4.2.1) which will not transfer error due to warping and interpolation during the mutliresolution process.

4.6.2 Cemagref Particle Images

We will now apply our approach to treat particle time image sequence of a turbulent flow obtained from a Direct Numerical Simulation (DNS) (section 2.4.1) of known flow case.

Data sequence

This 2D flow is turbulent and the image sequence was generated numerically using DNS by the laboratory of fluid mechanics from Cemagref [31] in the aim to have the exact solution of a flow evolving along the time. The flow has a large range of scale in the energy spectrum sense.

The Reynolds number of the flow is $Re = 3000$. The turbulence is homogeneous and isotropic

They used the 2D vorticity equation with the incompressible condition (equation 3.48) to simulate numerically the flow. The vorticity is computed at each time step in Fourier spectral space. Resulting images have a size of $2\pi \times 2\pi$ with 256×256 pixels (meshes). The DNS input image sequence only contains 1 over 10 images computation results. The average velocity between two successive images from the DNS input image sequence is around 3.5 pixels by interval of time. The sequence is composed by 100 successive image pairs.

Particles are generated as ideal tracers of the fluid which means that they follow the fluid velocity. They are randomly distributed on the image domain at time $t = 0$.

Figure 4.13.a represents the first particle image of the used sequence and figure 4.13.b shows the exact DNS velocity field map which is the ground truth.

Approaches and parameters

On this sequence, we test CC Lavision and three DOF algorithms.

- TF_BCCE noW_MR (our approach): We use a 3 level pyramidal decomposition ($K = 2$) (section 4.2.2) with a grid size of 2×2 pixels for multigrid (section 4.3). Images are previously smoothed with a Gaussian filter of variance $\sigma^2 = 1.0$. Weighting coefficient $\alpha = 50$ (equation (4.2)).

- H&S-SUN: We use a 3 level pyramidal decomposition ($K = 2$), weighting coefficient is set to $\alpha = 250$. See details in [163].

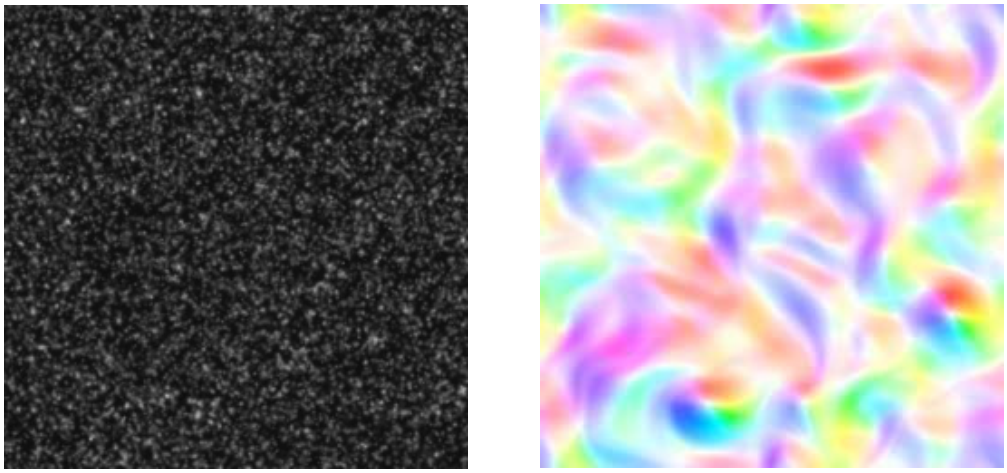

(a) Particle image (b) Exact velocity map

Figure 4.13: *First particle image of the sequence (a) with the corresponding velocity field map (b) using the Middlebury color coding figure 4.5*

- ICE-DivCurl: [46] uses the integrated continuity optical flow equation (equation (3.31)) with a second-order div-curl robust regularization (equation (3.3.2.1)). Estimated velocity fields were provided by the authors and published in [121].
- CC Lavision: CC Lavision is a commercial software [91]. We use iterative refinement method from square meshes of 128×128 pixels to 8×8 pixels with 3 iterations per level (for each mesh size). Gaussian peak interpolation is used to get a sub-pixel localization of the maximum of the cross-correlation peak. The parse velocity field is then bilinear interpolated to all image pixels.

Results

Figure 4.14 shows different velocity maps obtained by the above approaches on the first image pair of the particle DNS image sequence. The color mapping legend, for velocity field, is given in figure 4.5. The color represents the velocity orientation. The brightness represents the velocity amplitude. From the four velocity maps, we use the same color amplitude and orientation. The ground truth has a maximum amplitude of 3.59 pixels by interval of time at the bottom vortex. All approaches got a lower maximum amplitude velocity: H&S (3.39), TF_BCCE noW_MR (3.40) and ICE-DivCurl (3.49). The first order velocity regularization energy (equation (3.15)), used by H&S-SUN and our approach, is too restrictive to be able to recover high velocity fluctuations. This explains the difference of maximum velocity between ICE-DivCurl method which uses a second order velocity regularization based on Div-Curl equation (3.3.2.1). We can observe that the estimated velocity fields for all DOF methods are much noisier than DNS field.

For a better comparison between approaches, we compute AAE (equation (4.44a)) and RMS velocity (equation (4.44c)) errors over the 100 successive images for each image pair. Figure 4.15 and figure 4.16 give the evolution of the AAE and RMS

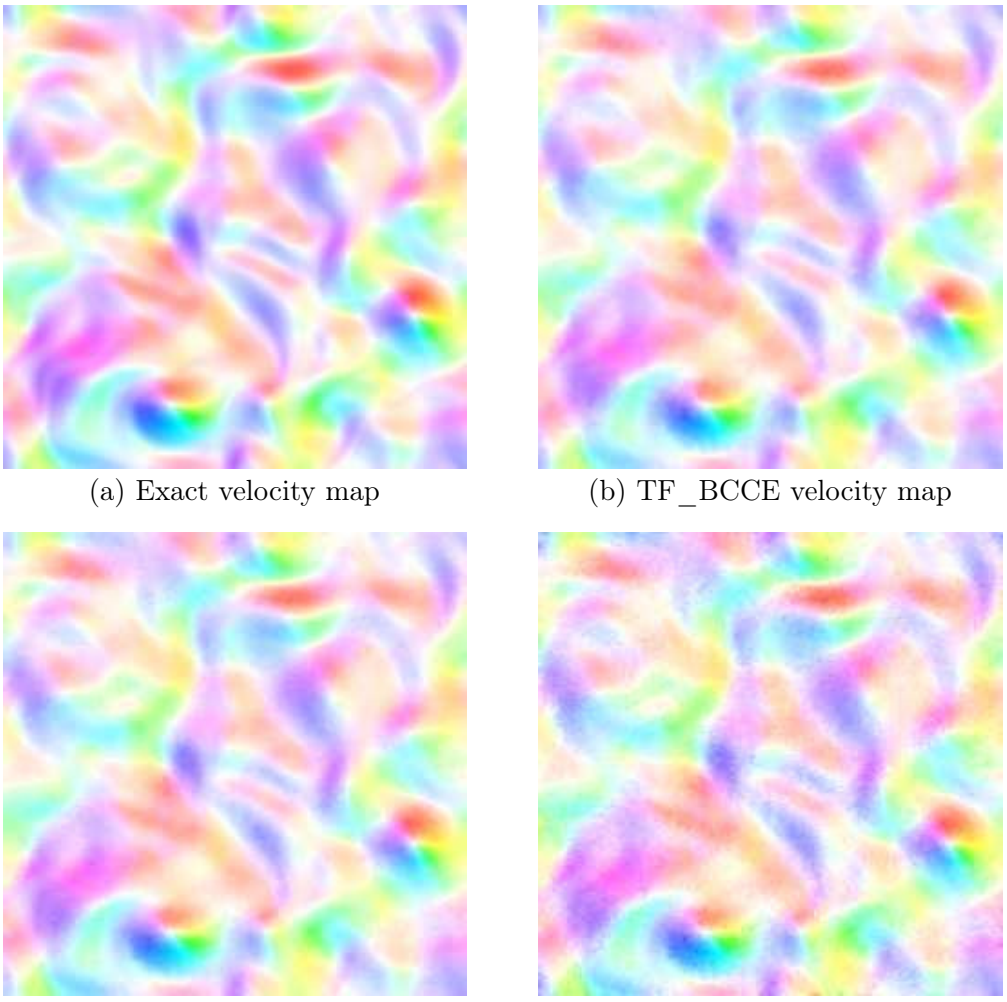

(a) Exact velocity map (b) TF_BCCE velocity map

(c) H&S-SUN velocity map (d) ICE-DivCurl velocity map

Figure 4.14: *Estimated velocity maps on the first image pair of the DNS particle sequence for TF_BCCE (b) (our approach), H&S-SUN (c) [163], ICE-DivCurl (d) [46] compare to the exact velocity map (a). The color mapping is from figure 4.5.*

errors over the 100 image pairs. In these figures, we compare errors from CC Lavision and DOF approaches (H&S-SUN, ICE-DivCurl and TF_BCCE noW_MR). Strangely, ICE-DivCurl produces the strongest errors over the image sequence. The highest maximum velocity is better determined by ICE-DivCurl method. This probably means that weighting coefficient α between data E_d and regularization E_s energies (equation (4.2)) is lower than for other DOF methods which results in a less smoothed estimated velocity field (see figure 4.14.d). ICE-DivCurl with other parameter settings should give smaller errors, at least as small as H&S-SUN and TF_BCCE noW_MR.

Another much more interesting conclusion about these two graphs is that the DOF approaches give similar AAE and RMS velocity errors than the CC approach.

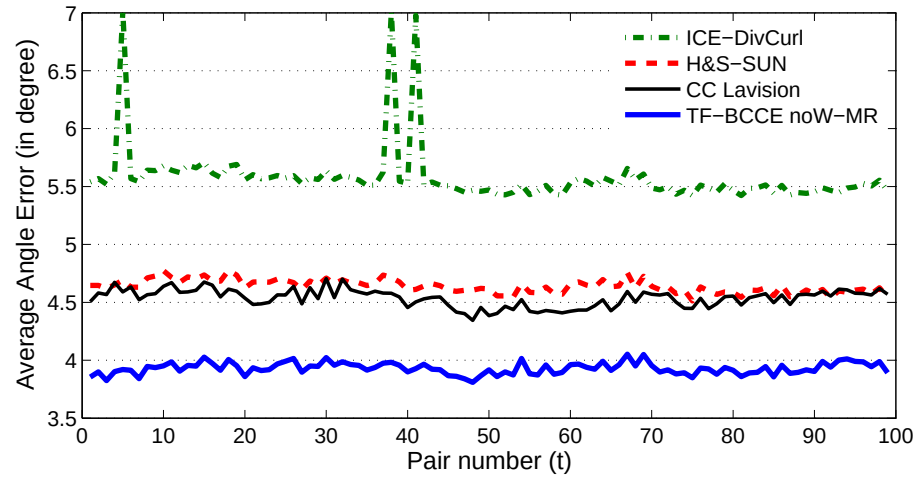

Figure 4.15: *AAE errors for the DNS particle sequence*

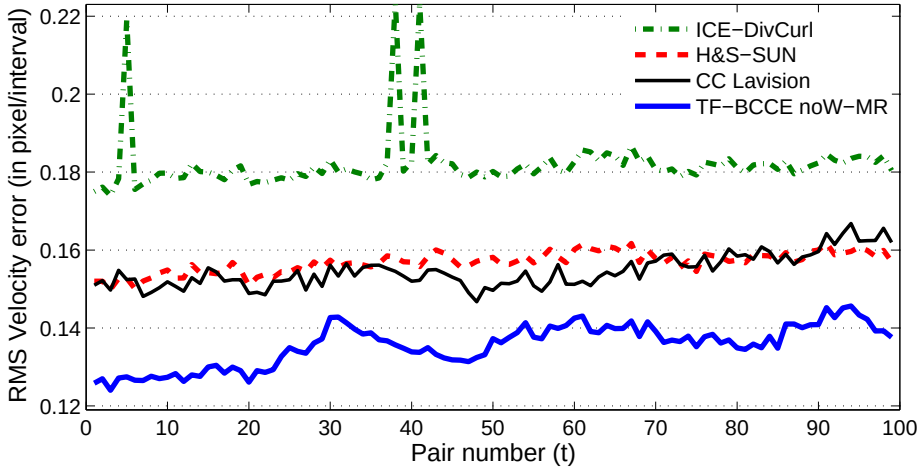

Figure 4.16: *RMS velocity errors for the DNS particle sequence*

CC Lavision is defined for particle image velocimetry estimation which is the case of application here. Images are issued from numerical simulation and do not contain any noise. It is why DOF approaches can get the same error level than CC method. The CC method is limited to 8×8 pixels window size for analysis, giving a parse velocity estimation which is bilinear interpolated to pixel grid locations for every image. In the smallest mesh, the velocity estimation represents the dominant velocity. The DOF approaches do not have this limitation and can estimate velocity field for each pixels. Because of the global regularization and the multiresolution technique, the DOF methods can retrieve a smoothed motion field over the total image domain even over regions where there is no particle. TF_BCCE noW_MR approach gives

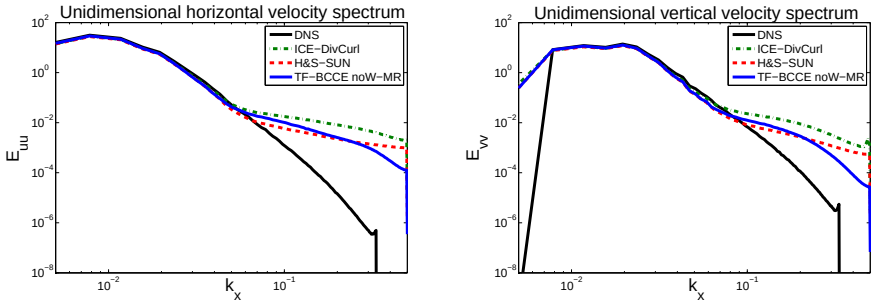

(a) (b)

Figure 4.17: *Power spectral analysis of the turbulent horizontal (a) and vertical (b) velocity components over the lines (log-log scale) on particle DNS sequence. Exact DNS spectrum (thin black line) is compared with spectra obtained with ICE-DivCurl (dashed green line), H&S-SUN (regular-dashed red line) and TF_BCCE (blue line) methods.*

better results than CC and the other DOF approaches even if the defined flow equation TF_BCCE (equation (4.10)) and regularization function (equation (4.20)) is not adapted to fluids.

This DNS is generated for a flow regime of $Re = 3000$. The flow is thus turbulent. The DNS resolves all turbulent scales of the flow. However, the time resolution has been filtered. The input image sequence only represents 1 over 10 computed resulting images. Moreover, DNS input images are filtered by a Gaussian filter of variance $\sigma = 1.0$ before estimation of the velocity field which remove some small scales information. We compute the average horizontal and vertical velocity energy spectra (See Figure 4.17) for H&S-SUN, ICE-DivCurl and TF_BCCE noW_MR. We can thus compare the energy spectra with the exact DNS spectrum. We see that, low frequencies corresponding to large scales can be correctly retrieved by the approaches. At a certain frequency, the highest frequency, corresponding to lower scales, all approaches clearly differs from the DNS spectrum. This is of course, due to the filtered information of the input images. Because they are filtered information, small scales are removed and DOF approaches can only estimate the largest scale velocity components, even if the approach has a second order velocity regularization (ICE-DivCurl). Another supposition for the spectrum difference behavior for highest frequencies could come from the method used to estimate the velocity field. Incremental random value of velocity is generated in the minimization process for each pixel independently from each other (see appendix E). Final solution of velocity field is thus globally smoothed over the image domain but it contains lot of small spatial variations of velocities due to the minimization which may explain the strong energy at highest frequencies.

4.7 Conclusions

In this chapter, we have proposed a new DOF approach coupling a non-centered DOF formulation based on the two spatial image information from instants t and $(t+\Delta t)$ with an unwarping multiresolution (TF_BCCE noW_MR). The optimization is done through the minimization of Gibbs energy (equation (4.2)). For that, different minimization methods have been adapted and tested on different sequences. Local minimization method combined with multigrid approach gives the best compromise between efficiency of the estimated velocity field and time consuming.

We also used a MRF framework to formulate the proposed TF_BCCE noW_MR method. Results are compared with other DOF methods defined within a variational framework [77, 107, 47, 29, 135]. Variational approaches, for solving energy minimization problems, have been very popular and have shown excellent results during the last decades. However, these approaches are efficient only when the total energy functional is convex. The main advantage of MRF methods is that it generally allows to use a wider range of energy functional, while ensuring to find a global (exact or approximated) solution, without being limited to convex functions [168]. Unlike most discrete graph-based optimization framework, our technique enables us to estimate a 2D real velocity field. Results show that our framework is as efficient as continuous ones (variational).

TF_BCCE noW_MR approach was not defined taking account for physical properties of the flow. However, tests on particle sequences of fluid flow shown that it estimates coherent velocity field compared to recent DOF algorithms and compared to CC approaches.

The last test on the DNS particle sequence where the flow is turbulent, shown the limitation of classical DOF approaches. As, in this case, the input image sequence is a filtered information of the reality scene from which smallest scales information is missing, the energy spectra in figure 4.17 clearly show that estimation of small scales becomes at a point strongly different from the exact ones. The tested approaches can not compute or take into account the velocity contribution associated with these small scales.

This point is discussed in the next chapter where we are looking for highly turbulent flow of transported scalar field. This will be discussed in the case for which the input image data is time and space limited. Note that a way to solve the problem of missing information from the input sequence was proposed in [121]. The method uses data assimilation on the BCCE equation (3.14) forcing the velocity field to satisfy simplified Navier-Stokes equations over the entire time sequence. Even if some information is missing in the image sequence, the dynamic regularization by Navier-Stokes equations will allow to retrieve a continuous velocity field at each instant. This method is very promising and gives very interesting results. However, it needs at least 10 successive acquisitions of the scene over the time at regular time step intervals and cannot be applied to an image pair at instants t and $(t+\Delta t)$. This method will also be compared to ours, in the next chapter where we propose a new motion estimation approach for turbulent flows.

Chapter 5

Subgrid Scale Approach of Transport Equation for Motion Estimation

Contents

The study of fluid flow is one of the main challenges in application domains such as aeronautic, acoustic, or environmental sciences. Conclusions drawn from the analysis of experiments are strongly linked to the methodology used for motion estimation.

Cross-Correlation PIV (CC) approaches (appendix A.1) or Differential Optical Flow (DOF) based approaches adapted to fluids (Section 3.3) are competing to provide the best motion estimation from time image sequences.

Most of the fluid flows around us are highly turbulent (Section 2.3): atmospheric motions, ocean currents, vascular flows... Up to now the problem of turbulence is generally ignored in the flow equation of existing DOF methods. Turbulence level of flows are characterized by the Reynolds number $Re = \mathrm{U}_c\mathrm{L}_c/\nu$ where U_c, L_c are the velocity and length scales of the flows and ν the kinetic viscosity of the fluid. For Re high enough, flows are turbulent. The Kolmogorov theory of cascade is a theory that allows to describe certain part of turbulent flow behavior. Its basis is that turbulent flows are constituted of structures or eddies containing energy. The ratio between scales of the largest eddies and the smallest ones in the turbulent flow [87] is proportional to $Re^{3/4}$. This implies, that to account for all scales which appear in the turbulent flow, the time and space resolution of a discrete representation of flow motion have to be proportional to $Re^{3/4}$ (for example, for atmospheric flows $Re \approx 10^{10}$). Generally, time and space image resolution are much coarser than this constraint. Depending on the turbulence regime, missing information in the image sequence has not to be neglected (see discussion in section 4.7). This information is generally associated to the smallest scales. When the influence of these small scales cannot be computed, they should be modeled.

In this chapter, we analyze turbulent fluid flows from image sequences, by analyzing the concentration of particles measured from the observed intensity in these images. We propose here to use a Large Eddy Simulation (LES) decomposition [133] (Section 2.4.3) of the transport equation [160, 161], where the influence of small scales is incorporated via a subgrid scale turbulent viscosity term as a constraint inside a system to solve. We further add a spatial regularization function for unicity of the solution in the system to solve. The proposed formulation is a new approach for optical flow estimation. The velocity field, deduced from the resolution of this system, takes into account effect of small scales through a turbulent viscosity.

The proposed method is tested on synthetic and real image sequences with high Reynolds number. Comparisons with existing approaches are very promising.

The works done in this chapter have been published or submitted in [35, 36, 37].

5.1 Image Scalar Transport Equation

5.1.1 Continuous Transport Equation for Optical Flow Formulation

We want to estimate the velocity field $\vec{v}$ from images containing intensity emitting by molecules of a passive scalar concentration. The field evolution is deduced partly by the scalar transport equation which is written in dimensionless form as follows [160]:

$$\frac{\partial C}{\partial t} + \vec{\nabla}.(C\vec{v}) - \frac{1}{Re\ Sc}\nabla^2 C = 0 \tag{5.1}$$

where C is the scalar concentration field of a specie spread in the studied flow fluid. Remember that the equation and quantities, describing the flow field, in this chapter, are non dimentionalised (section 2.2.4). The 2D apparent velocity is

$\vec{v} = (u, v)$. The space and time partial derivatives are $\vec{\nabla} = \left(\frac{\partial}{\partial x}, \frac{\partial}{\partial y}\right)$ and $\frac{\partial}{\partial t}$, where ∇^2 is the Laplacian operator. Re and Sc are the Reynolds and Schmidt numbers where $Sc = \nu/D$. D is the molecular diffusion.

To account for the integration of 3D information of a flow over the thickness of the plane of view or over transverse direction for global view, this for all images in the sequences, we make the coarse hypothesis that our fluid is a 2D turbulence where the transport equation is considered only on the plane (x, y). The velocity along the z-axis is considered as null ($W = 0$). In the future, we should focus on this 2D integration of real 3D transport equation related to the studied application flow field [100]. The fluid is, here, considered as incompressible (equation (2.13) $\vec{\nabla}.\vec{v} = 0$). The equation (5.1) becomes:

$$\frac{\partial C}{\partial t} + \vec{v} \,.\, \vec{\nabla} C - \frac{1}{Re\ Sc} \nabla^2 C = 0 \tag{5.2}$$

For images we want to treat, information contained in intensity I can be related to the passive scalar concentration C. For cloud motion from satellite images, some authors have proposed $I \propto \int C dz$ [46] or $I \propto \left(\int C dz\right)^{-1}$ [190]. In this thesis, we suppose no absorption and thus we consider that intensity is directly proportional to concentration (observation depth $\delta z << 1$):

$$I \propto \alpha\ C \tag{5.3}$$

where α is a constant independent on time and space. Thus in equation (5.2), we could substitute I/α to C and equation (5.2) takes the following form:

$$\frac{\partial I}{\partial t} + \vec{v} \,.\, \vec{\nabla} I - \frac{1}{Re\ Sc} \nabla^2 I = 0 \tag{5.4}$$

We can notice that for transported quantity with low molecular diffusion or apparent diffusion (solid particle) ($Sc >> 1$), the equation (5.4) becomes similar to the differential form of the BCCE equation proposed by [77] (equation (3.7)) recalled here:

$$\frac{\partial I}{\partial t} + \vec{v} \,.\, \vec{\nabla} I = 0 \tag{5.5}$$

5.1.2 Image Restitution of the Observed Scene

In chapter 4, we focused on brightness time evolution from a studied image sequence. Now, we are interested on the real physical information contains within every image in the sequence. The information contained in the images differs from an exact 2D scene (with very small thickness) in many points:

1. It is a 2D integration of the 3D real scene approximately in the direction orthogonal to the observation.

2. Recorded intensity depends on the scene illumination of the observed quantity and on the properties of light reemission of the observed quantity.

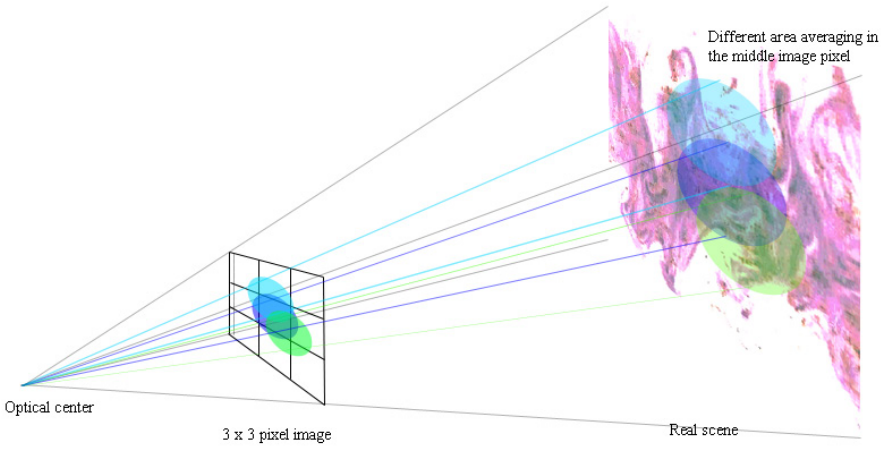

(a)

Figure 5.1: *Illustration of a 3×3 pixel image of an observe scene. Many flow structures are integrated into only one brightness intensity value by pixel.*

3. Brightness intensity is spatially and temporally discretized. Figure 5.1 is a scheme of the light integration and thus discretization over a pixel.

These 3 points involve an error level that is important to evaluate.

For the 1^{st} point (see also chapter 3 and above section), we consider that the observed quantity is integrated over a thickness δz, along the z axis that is much smaller than the size of the observed scene in the horizontal and vertical directions $L_x = [0; N]$, $L_y = [0; M]$ ($\delta z << L_x$ and $\delta z << L_y$). In this way, if the recorded image plane is parallel to plane $(0xy)$, the 3D transport equation with molecular diffusion becomes:

$$\frac{\partial C}{\partial t} + \vec{\nabla}.(C\vec{v}) - \frac{1}{Re\ Sc}\nabla^2 C = 0 \tag{5.6}$$

In so the obtained velocity field $\vec{v}$ is approximated.

For the 2^{nd} point, we have the hypothesis (equation (5.3)) that is mainly justified as soon as there is no absorption. The grey levels are related to the quantity of light reemitted from the scene by the 2D integration over the scene represented by the pixel size Δ. The recorded light is generally noised. In this thesis preprocessing of images is used to remove this (see section 5.4.1 for laboratory images and section 5.5.2 for satellite images). For laboratory experiments the proportionality given in equation (5.3) is perfectly justified via the Beer-Lambert law. We also use this hypothesis for the remote sensing application presented in section 5.5. However, this hypothesis is clearly wrong in that case. Scattering diffusion of light should be used in the future to account for this. Research on this topic is beyond a scope of this thesis.

The 3^{rd} point is the space and time discretization. The recording time integration δt has to be small to freeze the motion and to avoid blurring effects. This is generally respected if:

$$\delta t << \frac{\mathrm{L}_c}{\overline{\mathrm{U}_c}} \tag{5.7}$$

As an example, $\delta t = 10^{-9}s$ compared to $\mathrm{L}_c/\overline{\mathrm{U}_c} = 5.10^{-6}s$ for the treated laboratory experimental images.

Concerning the integration over the pixel $\Delta = (\Delta_x, \Delta_y)$ area, the pixel concentration represents a filtered information of the real concentration.

The scalar concentration C^+ observed in the image is thus:

$$C^+ = \int_{\Delta} C(\mathbf{x} - \mathbf{x}')\ \mathcal{W}(\mathbf{x}')\ d\mathbf{x}' \tag{5.8}$$

where $\mathbf{x} = (x, y)$ is the center of a pixel, $\mathbf{x}' = (x', y')$ is the characteristic length of the filter Δ in the x and y directions. The operator $\mathcal{W}(\mathbf{x}')$ can be, for example, Gaussian or Heaviside functions.

However, in the time scale, the temporal image sequence between two successive in time images at time t and at time $t+\Delta t$ is limited by the technology data transfer from the captors to the hard disk. $\Delta t >> \delta t$ and most of the time $\Delta t > \frac{\mathrm{L}_c}{\overline{\mathrm{U}_c}}$. For example, experimental fluid camera, can goes until few μs time acquisition period, and in the case of geostationary satellites, the fastest time rate is about 15 minutes.

If the 3^{rd} point involves a negligible error level, we could deduce the velocity field by solving the equation (5.2) by knowledge of the passive scalar concentration field at two successive instants in a plane of interest [160]. For image acquisition during laboratory experiments or cloud motions study in atmosphere, the acquisition period Δt and the pixel $\Delta = (\Delta_x, \Delta_y)$ are imposed. Moreover, for noise reduction purpose, images are first smoothed by Gaussian filter before computing the DOF equations (section 4.1.1) or the scalar transport equation (5.6).

In the majority of cases, as soon as turbulence is present, the smallest active scales of the flow are much smaller than the filtered information furnished by the image sequence due to the 1^{st} and 3^{rd} points. This observation brings us to use the subgrid scale modeling as for the Large Eddy Simulation (LES) theory [139]. Only the dynamic of the flow until scale resolution larger than the smallest active scales are computed directly. The other ones are accounted for in a model.

We present now, the concept of LES on the scalar transport equation which will lead to the formulation of our optical flow approach for scalar spread in turbulent flows.

5.2 Large Eddy Decomposition

Large Eddy Simulation (LES) concept relies on the use of a filter which removes numerically unsolvable small scales. LES proposes to compute exactly the flow dynamic for resolved scales. An additional term is modeled in the LES equations governing the evolution of the resolved scales to account for the interaction by the smaller scales on the larger ones.
A brief introduction on LES has been described in section 2.4.3, we now detail it.

5.2.1 Filtered Transport Equation

For simplicity, we use the same notation as in section 5.1.2. The pixel area Δ is larger than the smallest active scales of the turbulent flow. Thus, the effect of small scales on the fluid dynamic is not negligible due to the non-linearity of the transport equation [139, 48].

As defined in the above section, C^+ is the resolved large scale contribution to the scalar concentration field (observed in our image). In our case, filter size is Δ which correspond to our LES filter size Δ_s (section 2.4.3).

The instantaneous passive scalar concentration field verifies: $C = C^+ + C^-$ where C^- represents the small scale contribution. Starting from the scalar transport equation (equation (5.1)) and using filtering as described in (equation (5.8)), we obtain:

$$\frac{\partial C^+}{\partial t} + \vec{\nabla}.(C\vec{v})^+ - \frac{1}{Re\ Sc}\nabla^2 C^+ = 0 \tag{5.9}$$

The non linear term $(C\vec{v})^+$ can be rewritten as:

$$(C\vec{v})^+ = C^+\vec{v}^+ + \overrightarrow{\tau_s} \tag{5.10}$$

where $\overrightarrow{\tau_s}$ is the subgrid tensor also called residual stress tensor:

$$\overrightarrow{\tau_s} = \vec{\mathrm{L}} + \vec{\mathrm{R}} + \vec{\mathrm{C}} \tag{5.11}$$

Namely, $\vec{\mathrm{L}} = (C^+\vec{v}^+)^+ - C^+\vec{v}^+$ is the Leonard stress tensor, $\vec{\mathrm{C}} = (C^+\vec{v}^-)^+ - (C^-\vec{v}^+)^+$ is the Cross-stress tensor and $\vec{\mathrm{R}} = (C^-\vec{v}^-)^+$ is the subgrid Reynolds stress tensor [95, 184]. Hence, the filtered transport equation becomes:

$$\frac{\partial C^+}{\partial t} + \vec{\nabla}.\left(C^+\vec{v}^+\right) + \vec{\nabla}.\overrightarrow{\tau_s} - \frac{1}{Re\ Sc}\nabla^2 C^+ = 0 \tag{5.12}$$

For incompressible fluid, equation (5.12) can be simplified and expresses as:

$$\frac{\partial C^+}{\partial t} + \vec{v}^+.\,\vec{\nabla}C^+ + \vec{\nabla}.\overrightarrow{\tau_s} - \frac{1}{Re\ Sc}\nabla^2 C^+ = 0 \tag{5.13}$$

The term $\vec{\nabla}.\overrightarrow{\tau_s}$ (subgrid scale term) contains all the interaction between resolved and unresolved scales. This information is missing in the observed images. If the space and time resolutions of the time image sequence are larger than the smallest

active space and time scales of the flow, $\vec{\nabla}.\overrightarrow{\tau_s}$ participates on the dynamic of the flow and cannot be neglected. It has to be modeled in our approach. Most of the used technique [124, 139] consists in modeling the effect of the subgrid term $\vec{\nabla}.\overrightarrow{\tau_s}$ on the resolved quantity. We choose this method.

5.2.2 Turbulent diffusivity

Many works have been done on the modeling of the subgrid term [87, 188, 67, 113, 126, 48]. The subgrid scale effect on resolved scales is generally considered under spectral Fourier energy formulation. It is defined by the balance of the energy transfer between the two scale ranges. The dominant transfer is from the resolved to unresolved scales. This energy transfer from resolved to subgrid scales could be formulated similarly as the molecular diffusion. We call it the subgrid scale diffusion concept. For the transport equation, the subgrid scale diffusion takes the following form:

$$\vec{\nabla}.\overrightarrow{\tau_s} = -\vec{\nabla}.\left(D_t\ \vec{\nabla}C^+\right) \tag{5.14}$$

where D_t is the turbulent diffusion or subgrid scale diffusion coefficient. This modeling of subgrid scales in the transport equation is strictly similar as the concept of subgrid scale viscosity (also called eddy viscosity) established for the momentum equations [139].

It is known [146, 147] that even in case of the strong inhomogeneous turbulent flow, for such proposed diffusion modeling at subgrid scale level, if this scale is small compared to the largest turbulent scales (that is the case most of time), the turbulent diffusion coefficient D_t can be approximated by a constant, except near the wall in wall bounded turbulent flow which is not the present case. This means that D_t does not vary neither in time and space. The main part of spectral subgrid scale modeling [40] demonstrates the validity of such hypothesis. Nevertheless to discuss such hypothesis is beyond the scope of this thesis. Using the formula of Deardorff [52], the constant turbulent diffusion coefficient D_t can be computed from the turbulent subgrid scale kinetic energy q_{sgs}:

$$q_{sgs} = C_{sgs} * \left(\frac{D_t}{\Delta_s}\right)^2 \tag{5.15}$$

where Δ_s is the filter size (mesh size). The turbulent subgrid scale kinetic energy q_{sgs} is generally unknown but it can be approximated by the knowledge of the power spectrum E_{uu} that is given or deductible from experimental fact or theory even for real atmosphere. In the present case, E_{uu} is estimated with a simple theoretical model using power law assumption from K_c to ∞ for E_{uu} [44]. This gives:

$$q_{sgs} = \frac{3}{2} * \int_{K_c}^{\infty} E_{uu}(K)dK \tag{5.16}$$

where $K_c = \frac{\pi}{\Delta_s}$.The constant C_{sgs} usually takes values around 0.1 [52]. This is what we have done for the scalar DNS in section 5.3 and the laboratory experiment in section 5.4 using their known power spectrum E_{uu} and the size of the used filter.

From equations (5.15) and (5.16) we obtain:

$$D_t = \Delta_s * \left(\frac{3}{2\, C_{sgs}} \int_{K_c}^{\infty} E_{uu}(K) dK \right)^{\frac{1}{2}} \tag{5.17}$$

Our modeling, to account for subgrid scale turbulence in the estimation of the local velocity field, is thus perfectly determined knowing the power spectrum and the filter size [44].

5.2.3 Conclusions

In this work, we propose, in a first instance, to define the turbulent diffusion coefficient D_t as a statistical constant over the entire spatial domain. We want to measure the influence of the insertion of a turbulent diffusivity in the transport equation (equation (5.13)) on the accuracy of the estimated velocity field.

Turbulent diffusion D_t could be modeled using many other different approaches. Reader can refer to [139, 41]. More precise study of the turbulent diffusion behavior and comparison of the possible adaptation into the problem of scalar motion estimation from temporal image sequences will be the subject to future research project.

Finally, inserting equation (5.14) in equation (5.13) leads to:

$$\frac{\partial C^+}{\partial t} + \vec{v}^+ . \vec{\nabla} C^+ - \left(\frac{1}{Re\, Sc} + D_t \right) \nabla^2 C^+ = 0 \tag{5.18}$$

Such subgrid scale scalar transport equation (TE-SGS) is a new approach for optical flow estimation. At the best of our knowledge nobody took into account for subgrid scale effect of the small turbulent scales on flow motion estimation with OF formulation. Note that for high Reynolds number ($Re >> 1$) or scalar with low molecular diffusion ($Sc >> 1$), the contribution from turbulent diffusion becomes large compared to molecular diffusion ; it is the case, for example, for dust cloud particles in the atmosphere. Some works as [70, 64] add a diffusion term with space and time variability but they accounted for physical effect under molecular as [160] or thermal similarity concept which is physically different than the turbulent diffusivity concept.

The motion estimation problem is formulated in the same way as in chapter 4.

Equation (5.18) defines the evolution of the scalar C^+. It establishes the relationship between the observed quantity C^+ and the unknown velocity vector $\vec{v}^+$, at each point $\mathbf{x}$ of the image domain. However, the resolution of equation (5.18) is not possible directly (it is a mathematically ill-posed equation), unless another function (regularization term) is added to the system.

In LES, all resolved quantities for C^+ and $\vec{v}^+$ are exactly computed. For our concern, it is not the case. The filtered concentration field C^+ is given as an observed quantity. This observed quantity is known with a certain degree of uncertainty due in particular to the 3 points enumerated in section 5.1.2. Consequently, the

unknown velocity field we want to determine can be estimated only up to a certain accuracy. Moreover, equation (5.18) only gives the evolution of the filtered concentration in the fluid. The evolution of the velocity field $\vec{v}$ is also defined by the Navier-Stokes equations. But, it is not convenient to use these equations to well-posed the problem in our case (only two successive in time images). Another function defining the evolution of the velocity field has to be added. This function traduces the interdependencies between neighbors of the velocity field.

For above comments, Markov Random Fields (MRF) theory provides us with the theoretical foundations necessary to deal with the issues of i) modeling the uncertainty , ii) modeling interdependencies between neighbor variables. A recall on MRF is given in appendix B.

The problem is then established under the form of a Gibbs energy E (equation (B.13)), recalled here:

$$E(\vec{v}^+, C^+) = \sum_{\mathbf{x}\in\mathcal{C}_1} E_d(\vec{v}^+(\mathbf{x}), C^+(\mathbf{x})) + \sum_{\mathbf{x},\mathbf{x}'\in\mathcal{C}_2} E_s(\vec{v}^+(\mathbf{x}), \vec{v}^+(\mathbf{x})') \tag{5.19}$$

for which the observed field is C^+ and the random variable field is $\vec{v}^+$. $\mathcal{C}_1$ and $\mathcal{C}_2$ are the single-site clique and the pair-site clique respectively (see appendix B.2).

E_d is the data energy which establishes the link between observed and unknown variables. It is defined according to the application which is, in our case, the TE-SGS equation (5.18).

E_s is the regularization energy constraining the evolution of the velocity field. For the same reason than in chapter 4.1.2, we define E_s as in equation (4.20) which is equivalent to a first order spatial continuity of the velocity field. Note that it is now applied to the filtered velocity field $\vec{v}^+$.
Finally, the approach with subgrid scale model is defined by the following energy E:

$$\begin{aligned} E(\vec{v}, I) \;=\; & \sum_{\mathbf{x}\in\mathcal{C}_1} \left(\frac{\partial C^+(\mathbf{x},t)}{\partial t} + \vec{v}^+(\mathbf{x},t).\,\vec{\nabla} C^+(\mathbf{x},t) - \left(\frac{1}{Re\;Sc} + D_t\right) \nabla^2 C^+(\mathbf{x},t) \right)^2 \\ & + \alpha \sum_{\mathbf{x},\mathbf{x}'\in\mathcal{C}_2} \left|\left| \frac{\vec{v}^+(\mathbf{x}) - \vec{v}^+(\mathbf{x}')}{\Delta_s} \right|\right|^2 \end{aligned} \tag{5.20}$$

Δ_s is the mesh size (pixel).

Note that for $D_t = 0$, there is no subgrid scale modeling in the transport equation, effect of subgrid scales being neglected in equation (5.18). The filtered transport equation without subgrid model (TE) is:

$$\frac{\partial C^+}{\partial t} + \vec{v}^+.\,\vec{\nabla} C^+ - \frac{1}{Re\;Sc} \nabla^2 C^+ = 0 \tag{5.21}$$

This equation is used in the formulation of the data energy E_d. The Gibbs energy

using TE is:

$$E(\vec{v}, I) = \sum_{\mathbf{x}\in\mathcal{C}_1} \left(\frac{\partial C^+(\mathbf{x},t)}{\partial t} + \vec{v}^+(\mathbf{x},t).\, \vec{\nabla} C^+(\mathbf{x},t) - \frac{1}{Re\, Sc} \nabla^2 C^+(\mathbf{x},t) \right)^2 + \alpha \sum_{\mathbf{x},\mathbf{x}'\in\mathcal{C}_2} \left|\left| \frac{\vec{v}^+(\mathbf{x}) - \vec{v}^+(\mathbf{x}')}{\Delta_s} \right|\right|^2 \tag{5.22}$$

We denote TE-SGS the motion estimation method **with** subgrid scale modeling and TE the method **without** subgrid scale modeling. For TE and TE-SGS methods, multiresolution by pyramidal decomposition noW_MR (section 4.2.2) can be used to determine large velocities. Multigrid technique (section 4.3) and DDE minimization (appendix C.2 and E) are used to minimize the energy E.

5.3 Tests on scalar DNS image sequence

A true velocity field could be obtained from a DNS computation. In so, we can evaluate statistical errors, as described in section 4.4, comparing with results from our approach. For synthetic image sequences of motion of scalar in a turbulent flow, we use the Direct Numerical Simulation (DNS) generated by [31].

5.3.1 Data test description

In section 4.6.2, we worked on a particle DNS image sequence where the velocity field is computed by 2D vorticity equations (3.48) [31]. Authors propose also a passive scalar concentration image sequence which is generated by DNS computation for a 2D turbulence of an incompressible fluid. The 2D vorticity equations (3.48) and advection-diffusion equation (5.1) are used to calculate the velocity and passive scalar concentration fields at each instant [31]. The scalar DNS has been done, in the aim to have the same vorticity field for particle sequence presented in section 4.6.2. Sequence properties are identical for particle and scalar sequences: The size of images is $2\pi \times 2\pi$ with 256×256 pixels (meshes), the Reynolds number is $Re = 3000$ and the Schmidt number is $Sc = 0.7$. The maximum velocity is about 3.5 pixels by interval of time Δt. Remember that equations are classically non dimensionalised, the DNS computation time step is $\Delta t_{\text{DNS}} = 0.01$, we will use as input image sequence a regularly sampled sequence from the DNS. The time step in the sequence, that we will treat, is then $\Delta t = 10\Delta t_{\text{DNS}}$. The treated sequence is composed by 100 successive image pairs. The Figure 5.2 shows three scalar field images at time $t = 0$, 40 and 80 (top line) with the corresponding velocity field (bottom line). The scalar concentration image is arbitrarily defined at the beginning of the time sequence (figure 5.2.a). We have a much smoothed distribution of the scalar concentration over the image. Then due to the turbulence, we see strong eddies appearing over the time.

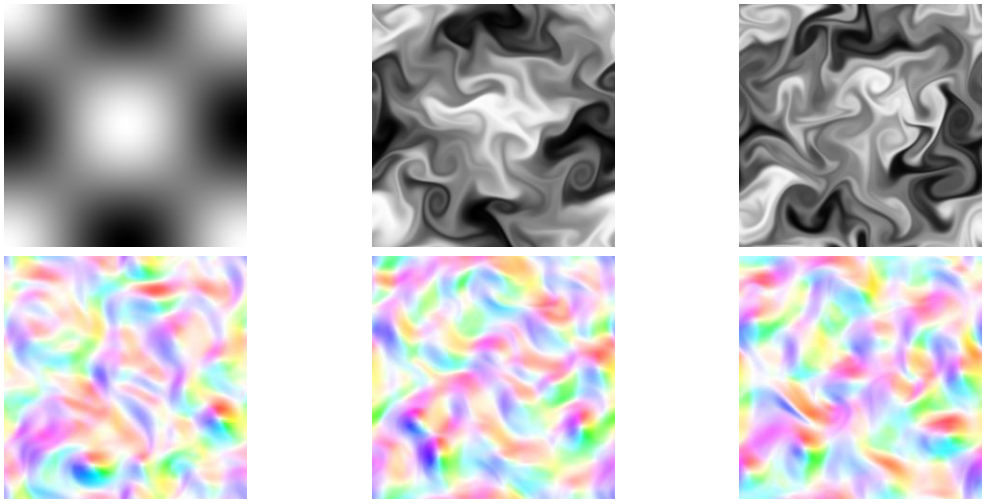

a) $t = 0$ b) $t = 40$ c) $t = 80$

Figure 5.2: *Scalar DNS sequence: Three different concentration fields (top line) and corresponding velocity fields (bottom line with color map from figure 4.5) at time* $t = 0$, 40 *and* 80. *(velocity amplitude brightness bar on the right).*

We will compare now our results with two other DOF algorithms developed for fluid motion:

- The ICE-DivCurl model proposed in [46] uses as constraint a flow equation based on 2D projection of continuity equation (ICE) (equation (3.30)). The authors defines a regularization term E_s based on divergence and vorticity (DivCurl) of the velocity field (equation (3.40)) to constrain the ICE formulation, which is specifically adapted to velocity field of fluids when there is no under-resolution of the original data to treat. For 2D incompressible fluid with low molecular diffusion or high Reynolds number, ICE-DivCurl and TE methods become similar to the differential formulation of the BCCE [77] (equation (3.7)). They only differ by a different regularization function. For low Reynolds number, turbulent diffusion is small compared to convective terms, TE-SGS method (equation (5.20)) is similar to TE method (equation (5.22)). However, when Re becomes high, which is the case in the present scalar DNS sequence, turbulent diffusion cannot be anymore neglected and TE-SGS formulation is necessary.

- The OF-Assim model proposed in [121] uses data assimilation [92, 169] on the BCCE formulation regularizing the velocity field by the 2D vorticity equation (3.48). The estimated field is then constrained to satisfy the 2D vorticity equation over the 100 successive images. This is equivalent to a spatio-temporal physical regularization. In this formulation the observation data term E_d (BCCE equation (3.14)) was not physically motivated and this approach, to be efficient, needs at least 8 successive images taken at regular time interval

that is the case in the present scalar DNS sequence.

For the ICE-DivCurl and OF-Assim approaches proposed by [46] and [121], parameters of their algorithms were not available. Their estimated velocity fields are published in [121] applying on the same scalar DNS sequence as presently. These authors provide us the estimated velocity fields from ICE-DivCurl method. For the OF-Assim method, presented RMS velocity errors in this chapter, are extracted from [121] where OF-Assim were applied on the same scalar DNS from time $t = 0$ to 50.

5.3.2 Test on filtered scalar DNS field

In this section, we will use TE method (without subgrid scale model) (equation (5.21)). It will be applied to spatial filtered and time under sampled scalar concentration field from DNS of known velocity field [31]. For the scalar DNS sequence, we do not use multiresolution by pyramidal decomposition (section 4.2). The reason is described later in this section.

A DNS computation contains all and thus the full kinetic energy of the flow to test our method. We use filtered images in space from the full resolved DNS to test our approaches.

Authors of the DNS sequence provide us a resampled information as explained above. The velocity fields (illustrated in Figure 5.2) are the time integrated velocity field over 10 DNS time computations linking scalar concentration field from one image to the next one. In the same way, we miss information about the scalar concentration field on time as we got only 1 instantaneous field over 10.

We further filter spatially, using equation (5.8), the scalar concentration fields with a Gaussian function of variance $\sigma^2 = 1$. This filtering is used to remove spatial smallest scales. But it is also used to reduce the sensibility of partial derivative computations to image noise (equation (5.18)).

To recover the velocity field from the filtered transport equation without subgrid scale model (equation (5.21)) will loose the effects of the unresolved scales as explained above. We will measure in section 5.3.3, the influence on the estimation if we introduce the proposed subgrid scale model in the filtered transport equation (5.18).

For filtered scalar DNS sequence, the maximum exact velocity amplitude corresponds to about 3.5 pixels by interval of time. In this case of a Gaussian filter of variance $\sigma^2 = 1$, the determination of the maximum velocity amplitude seems to become possible without using multiresolution by pyramidal decomposition noW_MR method (see section 4.2). In the Figure 5.3, we plot the Average Angle Error (AAE) (equation (4.44a)) and Root Mean Square errors (RMS) (equation (4.44c)) of the estimated velocity field from TE method, for different number of pyramidal decompositions from $K = 0$ to 3 for the image pairs at time $t = 40$ and 80. The minimum errors are obtained without pyramidal decomposition. In section 4.6.2, we studied

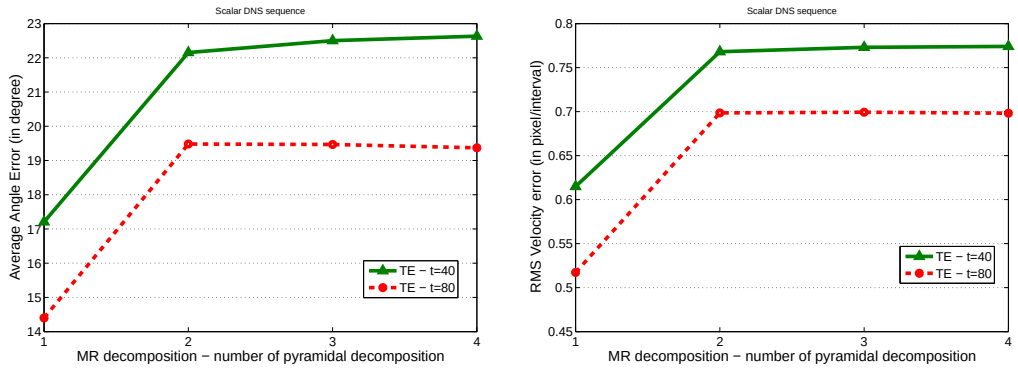

Figure 5.3: *AAE and RMS velocity errors using TE approach for different number of pyramidal decomposition (noW_MR) using Gaussian filter of variance* $\sigma^2 = 1$ *on* **scalar DNS image pair** *at time* $t = 40$ *and* 80.

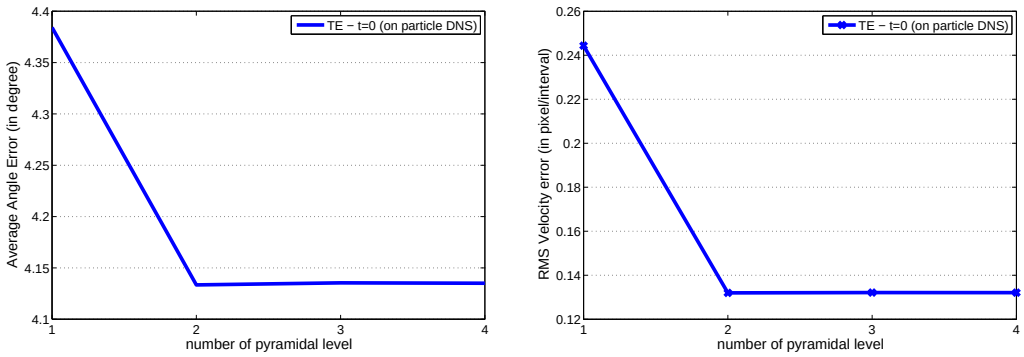

Figure 5.4: *AAE and RMS velocity errors using TE approach for different number of pyramidal decomposition (noW_MR) using Gaussian filter of variance* $\sigma^2 = 1$ *on* **particle DNS image pair** *at time* $t = 0$.

particle images where particle are submitted to the same velocity fields. In this particle DNS case, even using a Gaussian filter of variance $\sigma^2 = 1$, the correct velocity amplitude cannot be determined correctly for the entire image domain. Figure 5.4 shows AAE and RMS errors on image pair at $t = 0$ for different number of pyramidal decomposition ($K = 0$ to 3). This difference on the motion estimation quality between scalar DNS and particle DNS image sequences comes from the fact that the observed quantity is completely different. Scalar DNS images give the evolution of scalar concentration over the all image domain (figure 5.2 first line). However, particle DNS images only give information of the motion of solid particles carried by the fluid where the fluid is invisible in the image. Then most of the image pixel intensities, in that case, correspond to the constant background intensity (figure 4.13.a). In the case of particle DNS images, TE method becomes equivalent to BCCE because for solid particles the molecular diffusion is low ($Sc >> 1$).

Figure 5.5 gives a visual illustration of the spatial filtered scalar concentration

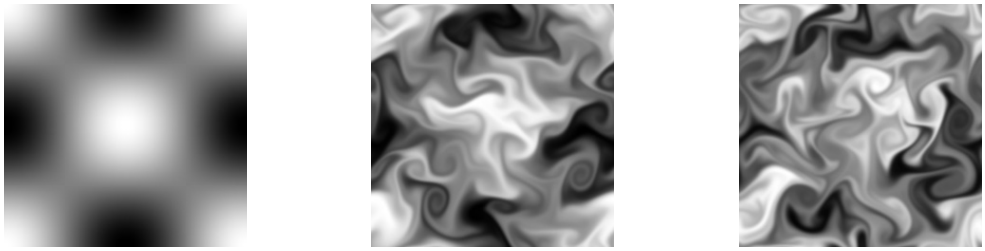

$t = 0$ $t = 40$ $t = 80$

Figure 5.5: *Scalar DNS sequence: Filtered concentration fields for time* $t = 0$, 40 *and* 80.

images at time $t = 0, 40$ and 80. Because of a strongly smoothed concentration at the beginning of the sequence $t = 0$, there is no significant spatial concentration variations. The estimation of the velocity field should be harder than in the middle of the sequence ($t = 40$ or 80).

5.3.3 Analysis of Subgrid Model

Now, we will apply the same formulation constraining the system with equation (5.18) (TE-SGS method) to account for unresolved scales, in place of equation (5.21) (TE method) that was used in above section 5.3.2.

TE and TE-SGS parameter settings:
We recall that the only difference between TE and TE-SGS approaches is the subgrid scale coefficient D_t. Technical parameters (as detailed under) are the same for TE and TE-SGS for a fair comparison. The multiresolution by decomposition pyramidal is not used ($K = 0$). The grid size for multigrid is 2×2 pixels. DNS Images to treat are first filtered by a Gaussian filter of variance $\sigma^2 = 1$ as in section 5.3.2. The weighting coefficient α is set to 0.4 (equation (5.20)). For TE-SGS method (equation (5.18)), the turbulent diffusion coefficient D_t is determined using the equations (5.17). From the filter size used in this test, we get $K_c = 33$. An approximation of the power spectrum decreasing slope in $k^{-5/3}$ is used to determine the turbulent subgrid scale kinetic energy q_{sgs} from equation (5.16). We finally obtain $D_t \approx 0.2$ with $C_{sgs} = 0.1$.

On Figure 5.6, we plot the AAE (equation (4.44a)) and RMS velocity (equation (4.44c)) errors for the spatial filtered scalar DNS images. In order to evaluate the subgrid modeling, we also do run the TE-SGS algorithm for different value of the turbulent diffusion coefficient D_t varying from 0 to 1. We can see that the subgrid scale model in the formulation with the filtered transport equation (TE-SGS) has a significant influence on the velocity field estimation. When $D_t = 0$, this is equivalent to TE method which means that unresolved scales are considered to have a negligible effect on the dynamic of the flow. When D_t increase, the subgrid scale term $D_t \nabla^2 C^+$ takes more importance in the equation (5.18). Increasing D_t should

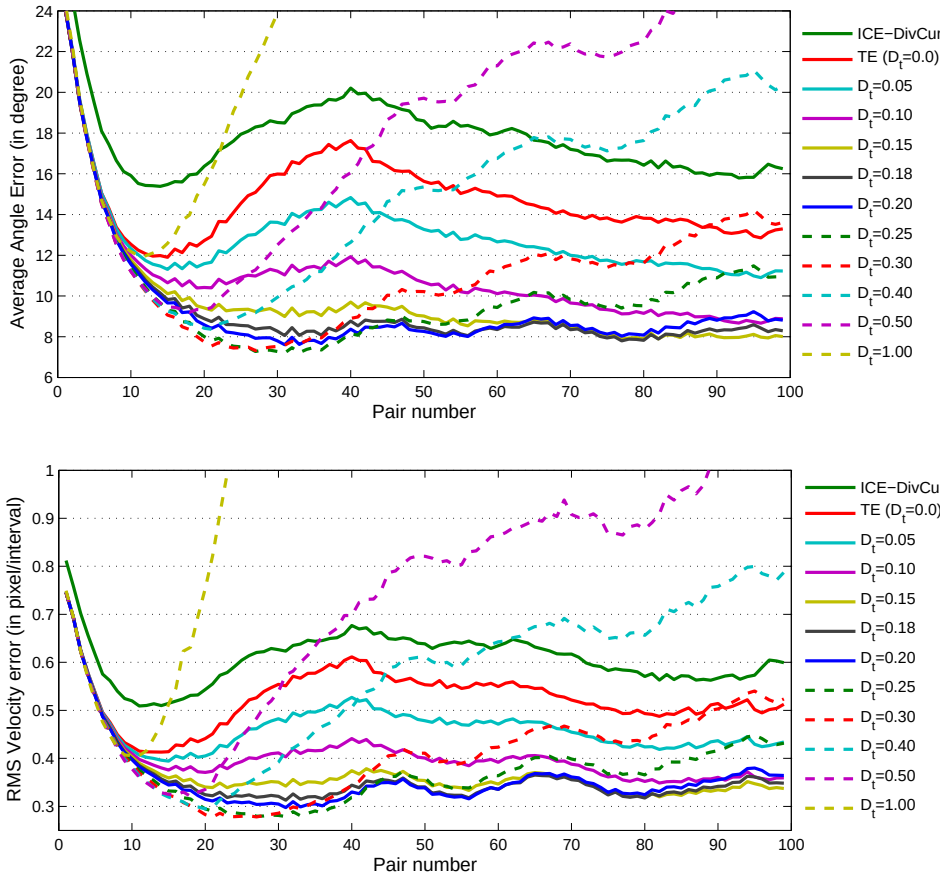

Figure 5.6: *AAE (top) and RMS (bottom) errors for TE and TE-SGS methods with different turbulent diffusion coefficients D_t for the filtered scalar DNS sequence. Best D_t coefficient, given smallest errors over the entire sequence, is obtained around* $0.15 \sim 0.25$.

improve the accuracy of the estimated velocity field. However, when D_t becomes too high, the turbulent diffusion model may not correctly represent the physical action of non-resolved scale effect. Estimation should then be affected by a too high turbulent diffusion coefficient. The Figure 5.6 illustrates clearly this supposition. From $D_t = 0$ to $D_t = 0.18 \sim 0.2$, the errors become smaller. For values D_t greater than 0.2, errors tend to increase. This is clear for time $t > 40$. From time $t = 0$ to 10, the concentration distribution over the images is too smooth. The algorithm is inefficient to retrieve the correct velocity field (for our methods as well as for ICE-DivCurl, see figure 5.9). From time $t = 10$ to 40, when increasing the turbulent diffusion coefficient D_t, AAE and RMS velocity errors decrease significantly. For D_t greater than 1, errors get bigger.

From this figure, we can clearly identify that it exists a value of D_t, of order of $0.15 \sim 0.25$, which allows to estimate a better velocity field over the all time image sequence. For time $t > 20$, where scalar fields are not too smooth, the errors

tend to be of the same order for all image pairs. This confirms the hypothesis of non variability in time and space of the diffusion coefficient D_t made in section 5.2.2. Moreover, the proposed model of D_t in equation 5.17 based on the turbulent subgrid scale kinetic energy q_{sgs} gives, for this filtered scalar DNS sequence, a value of $D_t \approx 0.2$. The tested results are thus coherent with the proposed physical model of the turbulent diffusion coefficient.

Note that in this sequence, amplitude variations of $\nabla^2 C^+$ become bigger along the time. Increasing D_t over 0.2 produces an increase of the level error from the beginning to the end of the sequence conjointly to the evolution of amplitude range of $\nabla^2 C^+$. Thus, one proposition can be suggested as for example that the turbulent diffusion coefficient may also depend spatially on the distribution of the observed resolved concentration C^+.

For the remaining of this section, we set $D_t = 0.2$ (given by equation 5.17) for TE-SGS method. We compare now, our estimations to these of ICE-DivCurl method [46]. Figure 5.7 shows the estimated velocity field and vorticity map obtained from the compared method at three different times (t = 10, 30 and 50). Raws (a) and (b) show the exact scalar field images and the corresponding exact vorticity field obtained by DNS with velocity vector superimposed. Figure 5.7(c) illustrates the estimated velocity fields from ICE-DivCurl; (d) and (e) are respectively estimated velocity fields from our TE and TE-SGS methods. The color legend is identical for all these results. The vector field and vorticity map obtained from ICE-DivCurl and the ones obtained with the TE method (equation (5.21)) are visually similar. Let remind us that the ICE-DivCurl and TE methods differ only by:

1. The regularization term E_s: equation (3.40) for ICE-DivCurl, equation (5.22) for TE.
2. For 2D flow in the data term E_d, the difference is the molecular diffusion factor: equation (3.28) for ICE-DivCurl, equation (5.22) for TE.

However, in the used sequence from DNS simulation the Reynolds number (Re = 3000) is relatively high and thus, molecular diffusion term of equation (5.18) will be negligible; therefore only the regularization E_s distinguishes the two formulations.

The TE-SGS method (equation (5.20)) provides better estimated velocity fields than TE and ICE-DivCurl methods: TE-SGS method allows a more accurate detection of the vortices. Globally, it behaves likely as the original DNS fields.

Figures 5.8 (a) and (b) illustrate an example on a zoom area of the DNS passive scalar concentration field image at time t = 50 where vortices are strong. In Figures 5.8 (d), (e), (f), are represented, respectively, the velocity divergence, the vorticity and the exact velocity vector field. The last raw, Figures 5.8 (g), (h), and (i), shows comparison of the velocity vector fields estimated under ICE-DivCurl, TE and TE-SGS methods. On this figures, we can see that estimated velocity field with TE-SGS method is closer to the DNS results than the other ones with TE and ICE-DivCurl methods for which similar difficulties exist to retrieve vortices around area of strong concentration variations. The subgrid scale model in TE-SGS method overcomes these difficulties.

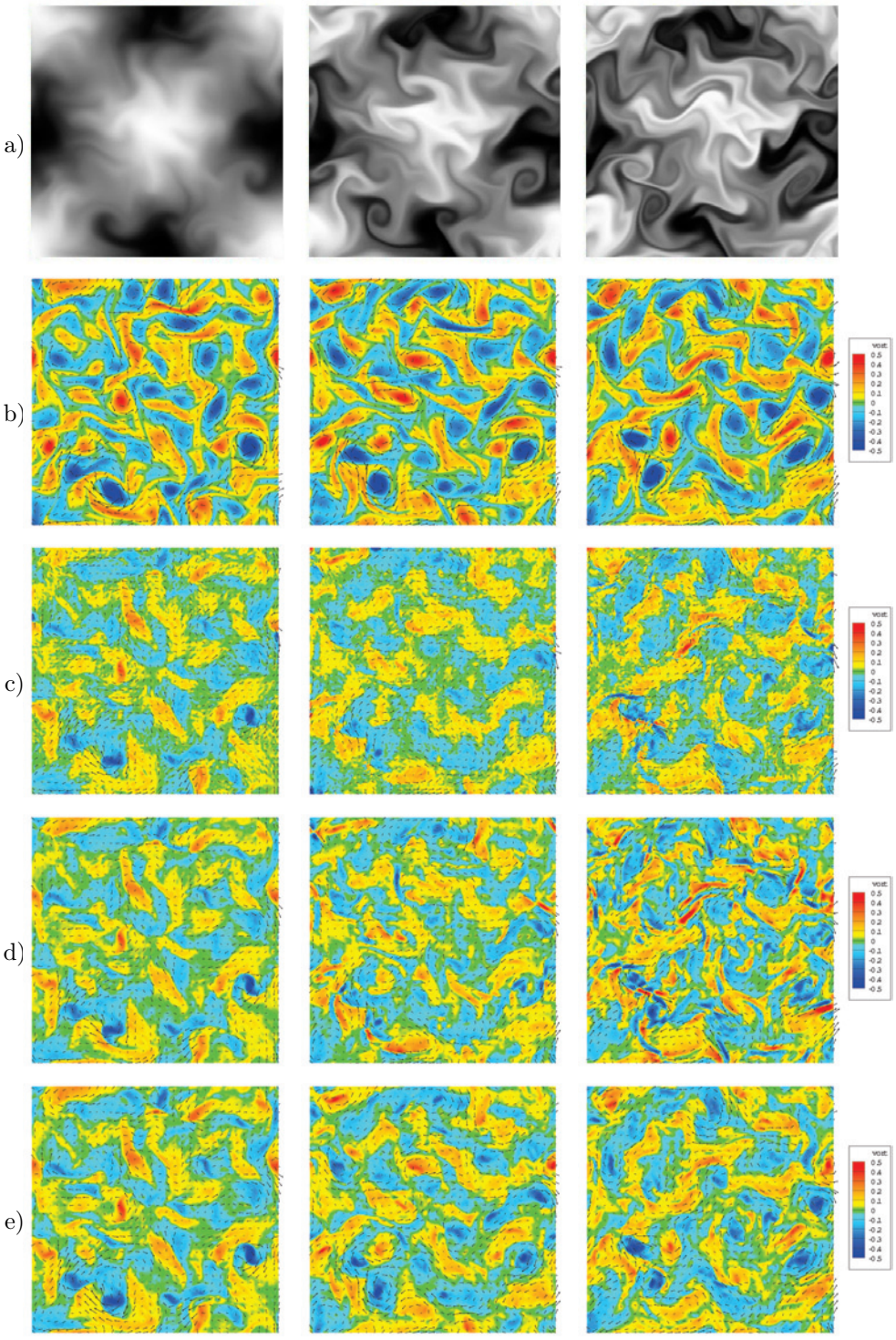

Figure 5.7: *Results on filtered scalar DNS sequence at times ($t = 10$, 30 and 50): Passive scalar concentration field input images (a), exact DNS vorticity fields (b), estimated vorticity maps with superposition of flow vectors obtained by ICE-DivCurl (c), TE (d) and TE-SGS (e) methods.*

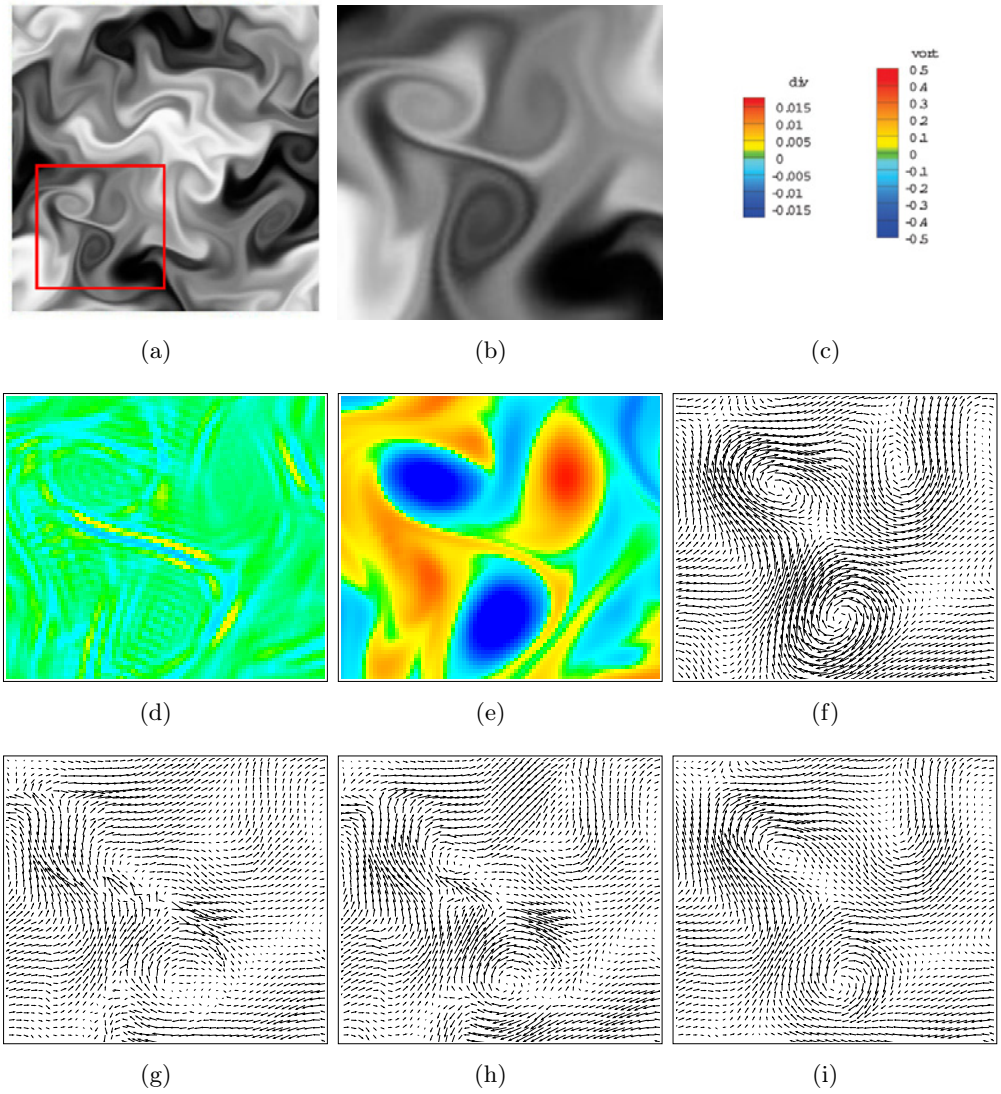

Figure 5.8: *Illustration over a zoomed area at time $t = 50$. Area representation on passive scalar concentration field image (a,b). Exact DNS divergence (d) and vorticity (e) maps (color map legend (c)) and exact DNS flow vector field (f). Estimated velocity vector field for ICE-DivCurl (g), TE (h) and TE-SGS (i) methods applied on the filtered image sequence.*

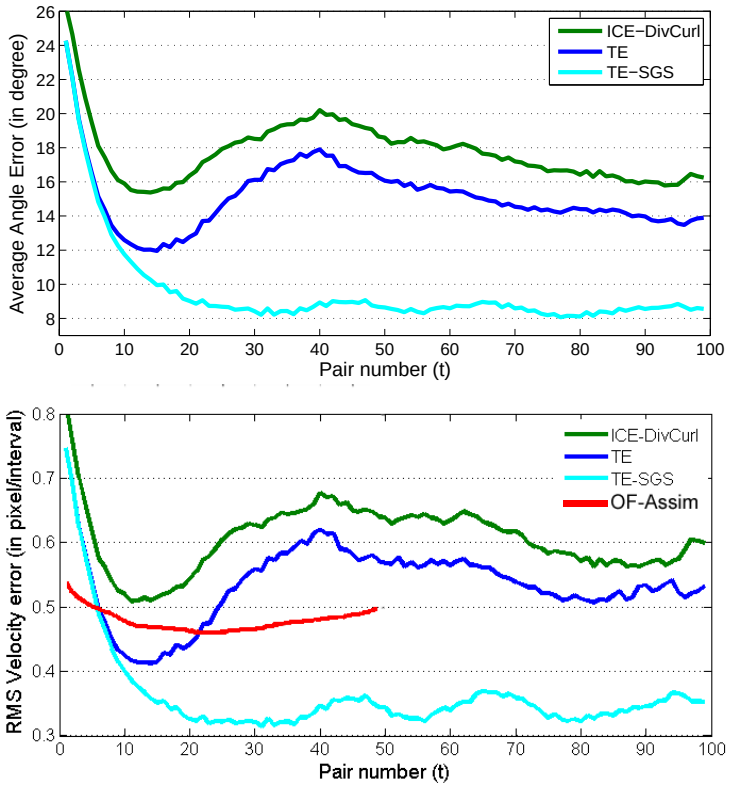

Figure 5.9: *AAE (top) and RMS velocity (bottom) errors of ICE-DivCurl, TE and TE-SGS methods for filtered scalar DNS concentration sequence. On RMS velocity error figure (bottom), the green line from $t = 1$ to $t = 50$ are the errors from the data assimilation proposed by [121] (errors are extracted from the paper).*

Figure 5.9 shows the statistical error AAE (top) and RMS (bottom) (equation (4.44a) and (4.44c)) of the velocity field for the 100 successive image pairs with TE and TE-SGS ($D_t = 0.2$) methods, compared to ICE-DivCurl method [46] and compared to RMS errors in case of estimation by OF-Assim method [121]. The evolution of errors from TE method has the same behavior as the one for ICE-DivCurl method for AAE and RMS formulas. This confirms the remarks made above. The estimation with TE method is slightly more accurate. This is puzzling in some way because TE method contains a first order quadratic regularization energy E_s (equation (4.20)) while ICE-DivCurl method contains a robust semi-quadratic formulation for div-curl regularization energy E_s (equation (3.40)) which is more appropriate to fluid motion (section 3.3.2.1). The reason should come from a non optimal parameter setting of the ICE-DivCurl approach on the scalar DNS sequence (discussions with ICE-DivCurl authors). Anyway, TE-SGS method includes scalar subgrid scale model in the filtered scalar transport equation. This is an improvement from physics of fluid point of view for the estimation of the velocity field compared to TE method.

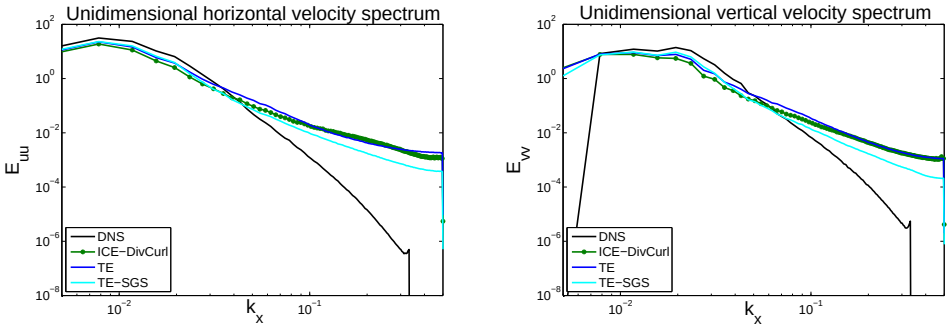

(a) (b)

Figure 5.10: *Power spectral analysis of the turbulent horizontal (a) and vertical (b) velocity components over the lines (log-log scale) on filtered scalar DNS sequence. Exact DNS spectrum (black) is compared with spectra obtained with ICE-DivCurl (green), TE (blue) and TE-SGS (cyan) methods.*

Estimations, for TE-SGS method, are also much better than ICE-DivCurl and OF-Assim estimations. This means that for this scalar turbulent sequence, effects of unresolved small scales on the fluid dynamic are not negligible. The turbulent diffusion term represents these effects.

The time evolution error for TE-SGS method, over the sequence, behaves differently than TE and ICE-DivCurl methods. The TE-SGS method accounts for the lack of information on filtered passive scalar images conversely to the other methods. It allows to retrieves a closer velocity field compared to the exact one. Even if OF-Assim method constrains temporally the velocity field to satisfy the 2D vorticity equation, errors are higher than for TE-SGS method. This is due to the fact that the data function for observed motion does not contain subgrid scale model.

One important conclusion to draw from these experiments is that, improving the data term of the energy functional, in particular via a physical modeling such as our TE-SGS method, is a necessary step to estimate a velocity field closer to the exact ground truth. The role of the regularization term, thought important, is not as crucial as the role of the data term. This can be understood by observing that the main driving force which leads the algorithm towards the optimal solution is precisely the data energy, while the regularization is acting only to smooth out unacceptable solutions (ICE-DivCurl and OF-Assim).

The Figures 5.10(a) and 5.10(b) show plots of the average kinetic energy spectra of horizontal (left) and vertical (right) velocity components. Spectra are defined in [31] and they are of first importance in describing turbulent flows. From both velocity components, energy spectra obtained with TE method (green) and ICE-DivCurl method (red) are almost the same. We can see that the spectrum obtained by TE-SGS method (blue) is closer to the exact DNS spectrum (black). We observe both for large and small wavelengths that the TE-SGS method gives the best rep-

resentation of the velocity spectrum. Again the proposed subgrid scale formulation improves the result, essentially with a better estimation of the finest structures. However, the spectrum obtained with the OF-Assim method (see the paper [121]) is much closer to the exact DNS spectrum. It is not here possible to compare with our results as their spectrum concerns with the vorticity field. This is the result of the time regularization imposed by the 2D vorticity equation in the data assimilation process (see [121]). In their estimation, the velocity field is smoothed accounting for the physics underlying in the 2D vorticity and continuity equations. We can conclude that their assimilation technique can estimate a much less noisy velocity field over the space and time than the other methods. However, AAE and RMS velocity errors for OF-Assim method are higher than TE-SGS method because of the data observation function which does not contain subgrid scale term. Combination of TE-SGS and OF-Assim methods should probably in the future give better results than all existing approaches.

5.3.4 Discussions

Average energy spectra obtained by TE and TE-SGS methods are still too much noisy which is represented in figure 5.10 by too high level energy for small scales. Compared to [121] where the all velocity field is constrained by the 2D vorticity equations which can be seen as a temporal regularization, our regularization energy E_s (equation (4.20)) is not constrained by fluid equations neither in time neither in space. Moreover, the estimation of the velocity field, by TE and TE-SGS methods, is obtained for each pixel independently by incrementation of residual random velocities (appendixes E and F.2 for minimization technique details) which decrease the Gibbs energy (equation (5.20)). This results in very high spatio-temporal velocity variations of the velocity frequencies.

Considering this, as responsible of the high energy for the small scales, observed in the average energy spectra, we propose to smooth the TE and TE-SGS estimated fields by a Gaussian filtering of variance $\sigma^2 = 1$. The figure 5.11 represents the AAE and RMS velocity errors from TE and TE-SGS methods and from their smoothed estimations. We can see that errors are similar. Smoothing the velocity fields can only decrease a little the statistical error levels. It is more evident on TE method estimations than on TE-SGS ones. The subgrid scale model still plays a smoothing role on the estimation of the velocity field. In so, the new filtering has no effect. This can prove the effect of our addition of subgrid scale model in the TE-SGS method compared to TE one.

On the other hand in figure 5.12 which shows plots of the average kinetic energy spectra of horizontal (a) and vertical (b) velocity components, we can see that the spectra obtained by smoothed estimations from TE (red) and TE-SGS (orange) methods are clearly different from spectra obtained using the original estimations from TE (blue) and TE-SGS (cyan) methods. This was expected as the velocity fields were smoothed by a Gaussian filter. What is interesting, is that the energy spectra obtained after using the smoothed TE and TE-SGS methods are now

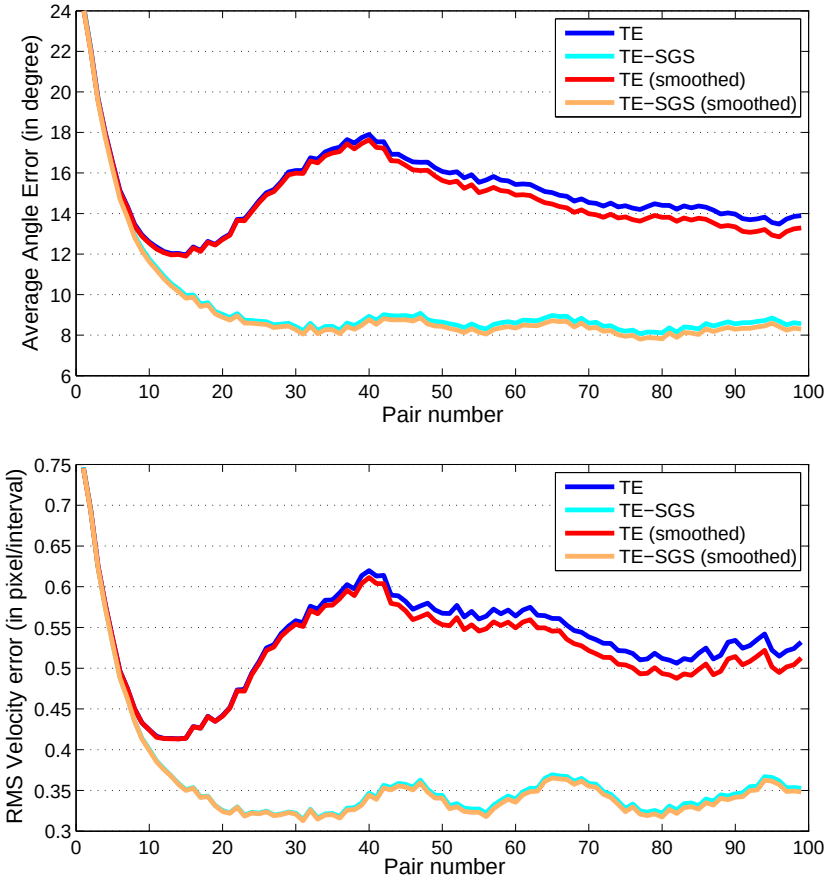

Figure 5.11: *AAE (top) and RMS velocity (bottom) errors of TE and TE-SGS methods for filtered scalar DNS concentration sequence compared with the errors obtained if TE and TE-SGS estimated velocity field is smoothed by a Gaussian filter with* $\sigma^2 = 1$.

much closer to the exact DNS spectrum (black) than the ones obtained applying TE and TE-SGS methods. This is more evident on vertical velocity component energy spectra than on horizontal velocity component energy spectra. The observed differences between smoothed and non-smoothed results for high frequencies (small scales) traduce the fact that the velocity fields are smoother. We cannot conclude that smoothed TE and TE-SGS methods allow to retrieve better small scale information of the flow than from original TE and TE-SGS methods. Moreover, comparing original TE method with TE-SGS method, and also comparing smoothed TE method with smoothed TE-SGS method, as we set the same parameters, the spectra differences cannot only be explained by less noisy fields. Again, for both large and small wavelengths TE-SGS method gives a better representation of the velocity spectrum.

These tests show that a frequency analysis is not sufficient to prove retrieving the

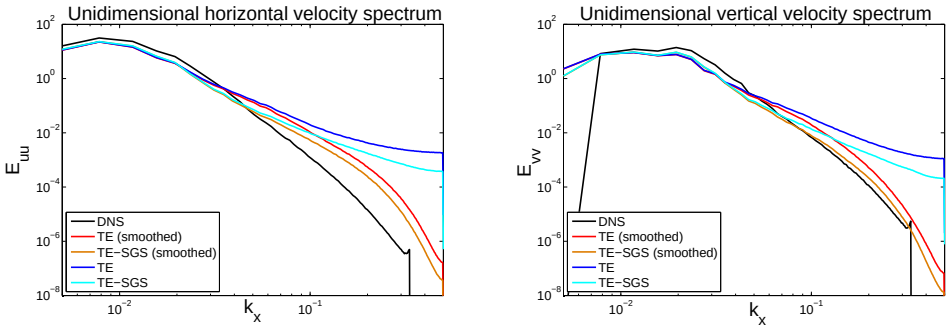

(a) (b)

Figure 5.12: *Power spectral analysis of the turbulent horizontal (a) and vertical (b) velocity components over the lines (log-log scale) on filtered scalar DNS sequence. Exact DNS spectrum (black) is compared with spectra obtained with TE (blue) and TE-SGS (cyan) methods and smoothed TE (red) and TE-SGS (orange) using a Gaussian filter with* $\sigma^2 = 1$.

correct finest structures of the flow. [72] proposed a regularization accounting for the turbulent kinetic energy decay which leads to a good estimated velocity fields satisfying the turbulent kinetic energy decay. This method as well as the other cited methods in the chapter, should probably significantly improved if a subgrid scale model was added into their definition of the motion equation from the resolved observations (C^+).

We are now testing the TE-SGS model on real image sequence from a laboratory experiment.

5.4 Tests on Laboratory Experiment image sequence

Here, the complete TE-SGS method is tested on a real image sequence of particle images, from a fluid flow study, acquired at the Laboratory of Fluid Mechanics and Acoustics (LMFA) [150, 151]. We compare and validate our approach against CC technique Lavision software [91].

5.4.1 Description of the Wind Tunnel Experiment

Experiment and image acquisition were conducted at LMFA ([150, 151]), in order to study the dispersion of a passive scalar spreading within an atmospheric boundary layer in presence of obstacles. The source of scalar is located at mid-distance of the perpendicular to the flow between walls of a canyon represented by two lines of squares whose sections are h^2. Obstacles are transversally disposed in order to be perpendicular to the mean flow; the distance between them is $h = 1cm$. The momentum Reynolds number at source location without obstacle is $Re \approx 10^3$ and

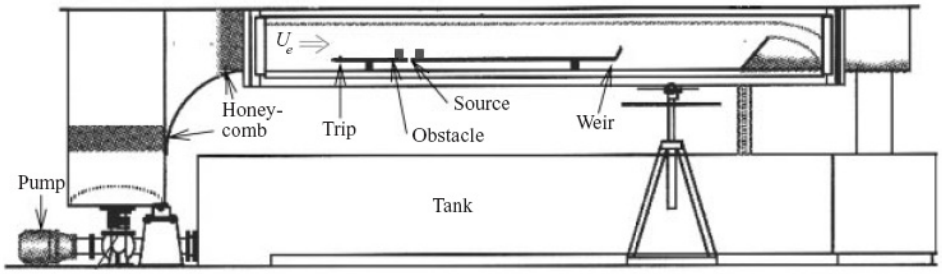

(a)

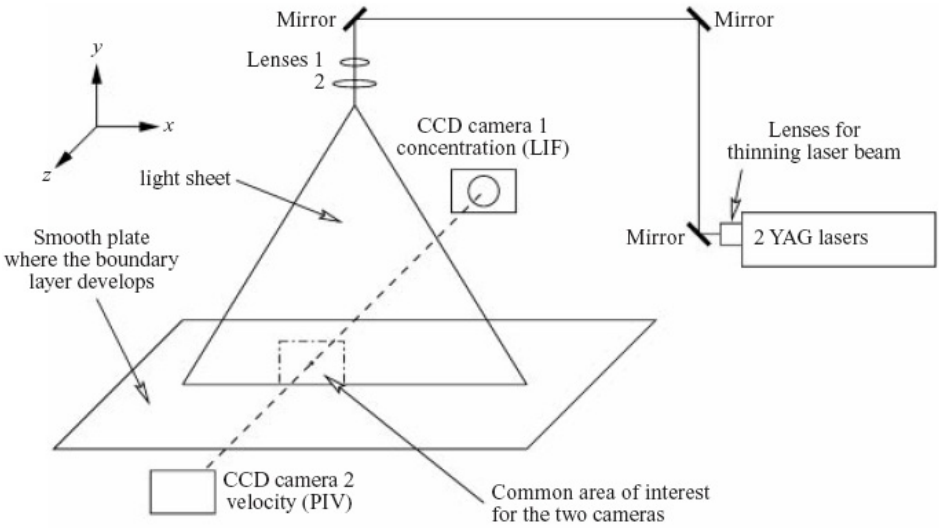

(b)

Figure 5.13: *Sketch of channel (a) and optical set-up arrangements to create laser light sheet (b).*

the scalar Schmidt number is $Sc \approx 10^6$. The sketch of the tunnel is represented in Figure 5.13a. The passive scalar is incense smoke. The source is flushed at the ground. In this experiment, 1^{st} set of images were recorded zooming enough on the area of interest in order to individualize smoke solid sub-microscopic particles. A 2^{nd} set of images were recorded with a zoom less important in order to avoid individualization of particles: Recorded intensities being linked to the number of solid particles leading to their concentration. We used the 1^{st} set of images obtained with the higher zoom that individualizes particle images because the 2^{nd} set does not contains two successive in time images.

The acquisition was made by synchronization of two YAG lasers and a CCD camera. YAG lasers delivered $300mJ$ energy per pulse and had a pulse frequency of $10Hz$ that determined the acquisition frequency of image pairs. Time step between the two laser pulses, δt, for first and second image acquisition of each pair,

was $0.2ms$. Synchronization between camera and laser pulses was achieved by Lavision device. CC Lavision from software [91] allowed to obtain good results using a recursive mesh size method with refinement from 128×128 to 4×4 pixels (see appendix A for technical description). The optical set-up arrangements are shown in Figure 5.13b. More details can be found in [175]. Note that tests were done by [157, 158, 159] that demonstrates that the used CC Lavision is the most efficient CC commercial software in the fluid mechanic community.

We compare now, results we obtain with our TE and TE-SGS methods, with these obtained with CC Lavision technique. For this aim we first calculate the velocity field associate statistics, as on mean velocity field and RMS fluctuating velocity field.

Hereafter statistics are compared.

As for tests on DNS sequence in above section, settings are the same for TE and TE-SGS methods. The maximum amplitude of the velocity field between two instants t and $t+\Delta t$ is about 6 pixels by interval of time. We use our multiresolution noW_MR (section 4.2.2) of 3-level pyramidal decomposition ($K = 2$) and a grid size of 2×2 pixels for multigrid (section 4.3). The experimental images are filtered by a spatial Gaussian filter of variance $\sigma^2 = 1$. The weight α equals to 1 (equation (5.20)). For TE-SGS, the coefficient D_t was determined using the equation 5.17. The power spectrum was the one by Spalart [155] cited in [175] as characterizing the boundary layer of their experiment. The filter size is deduced from the given spatial resolution, $K_c = 211.5$ and $C_{sgm} = 0.1$. This gives us $D_t \approx 2$.

5.4.2 Results

From this experiment, we have a series of 200 pairs of images. We compute instantaneous velocity fields with CC Lavision method and average these fields to obtain the mean velocity field. Figure 5.14 shows an instantaneous image of the scattering diffusion intensity from solid particle seeding the flow (Figure 5.14(a)) and the mean velocity field, over the 200 pairs (Figure 5.14(b)). On background of the CC mean velocity field, we visualize the horizontal velocity component amplitude (color map). Length and velocity scales are normalized by length h and outside boundary layer velocity $U_e \approx 2.3m.s^{-1}$ respectively.

On input images, we define a binary mask that identifies the ground and obstacles. Notice that we have a vertical line in the mask above first obstacle. It is due to a burnt (destroyed) pixel column of the camera. This line influences the estimation of the velocity field around this area as we can see on Figure 5.14(b). However, this line is far from the canyon where the test is significant as this is the single zone where there is a complete repartition of particles. The mask is used to help the algorithms to avoid disturbance due to light reflections on the analyzed area. This is of first importance on the obstacle walls and flat ground of the tunnel. CC Lavision can take into account this mask. In our TE-SGS method algorithm, we added the possibility to use such a mask. Velocity value $\vec{v}(\mathbf{x})$ in the mask area

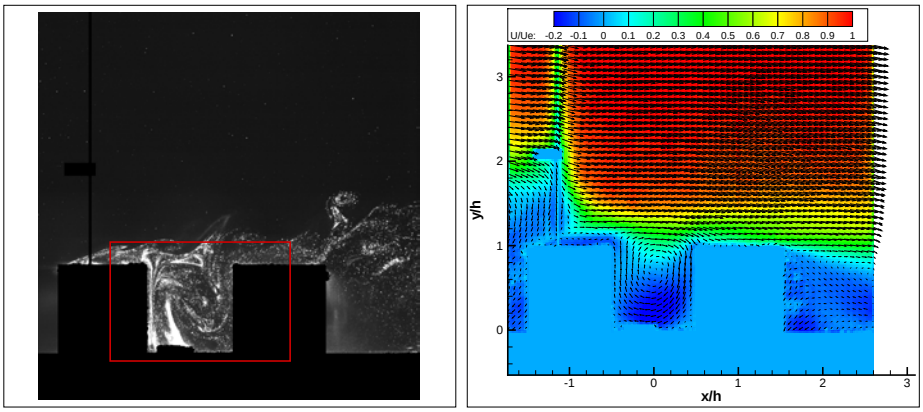

(a) (b)

Figure 5.14: *Instantaneous Mie scattering diffusion image from solid particle seeding the flow with* 2 *obstacles (a) and amplitude map of the average horizontal velocity with the velocity vector representation obtained by CC Lavision (b)*

is set to 0. The clique c of neighbor pixels $\mathbf{x}'$ of pixel $\mathbf{x}$ for the case of one of the pixels is inside and the other outside the mask are removed from the second order clique $\mathcal{C}_2$ (figure B.2). Thus, the smoothness term will not take into account these cases (equation (4.20)). Estimation of the velocity field at the mask border is then not influenced by inside border information.

The results are very sensitive to the quality of experimental acquisitions. Recorded image intensity depends on the light exposure on CCD captors. This light contains information from seeding particle concentration but also information from experimental noise. As mentioned in section 5.1.2, we consider in this work that the image intensity is directly linked to solid particle concentration. In practice, this is not the case as main part of particle images are individualized. We had then to identify and to suppress experimental noise before to be able to apply TE-SGS method correctly.

It is interesting to detail here all our preprocess as this is frequent to have to apply such treatment for real images.
This noise is due to two main causes:

1. The reflections of light on the walls. This can be corrected by knowledge of a background image. It is obtained in the same experimental conditions without seeding the flow.

2. The laser pulse energy that is different for the two instant of a pair. Furthermore as laser beams come from two different lasers with small alignment difference, it provides intensity difference in a same location. This results on an independent brightness variation between images 1 and 2 in a pair. Such noise was classically removed as in [10].

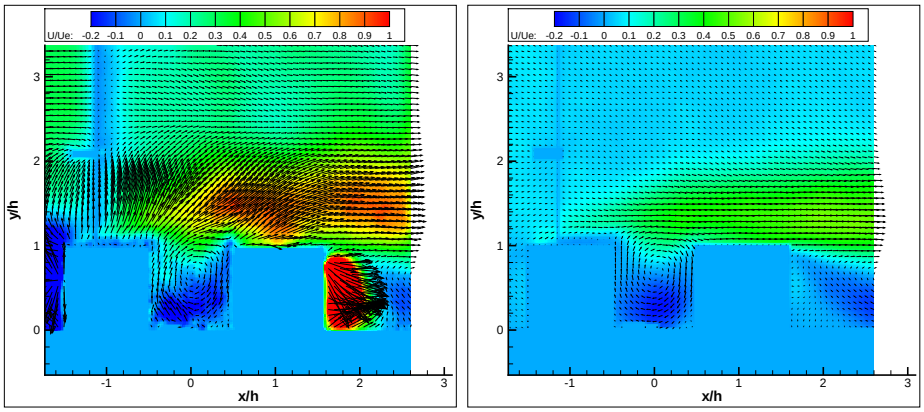

(a) (b)

Figure 5.15: *Amplitude maps of horizontal mean velocity with mean velocity vectors obtained by TE method on original (a) and pretreated (b) image sequence*

Figure 5.16: *Average concentration field with represention of the zone of interest.*

To deal with these experimental noises, we propose a simple but efficient method:

1. Subtract image background on images 1 (1^{st} instant) and 2 (2^{nd} instant) pixel by pixel for all images of the series.

2. Extract a uniform seeding image called image of uniformity. If we don't have this image without particle, we can compute it by taken the minimum intensity value over all the images of the series for each instant at each image pixel.

3. Divide each image of 1^{st} instant, without background (step 1), by the image of uniformity (step 2) (identically for 2^{nd} instant).

We use this process to preprocessed the image pairs to remove the noise and to represent dimensionless information of the particle intensity image [10].

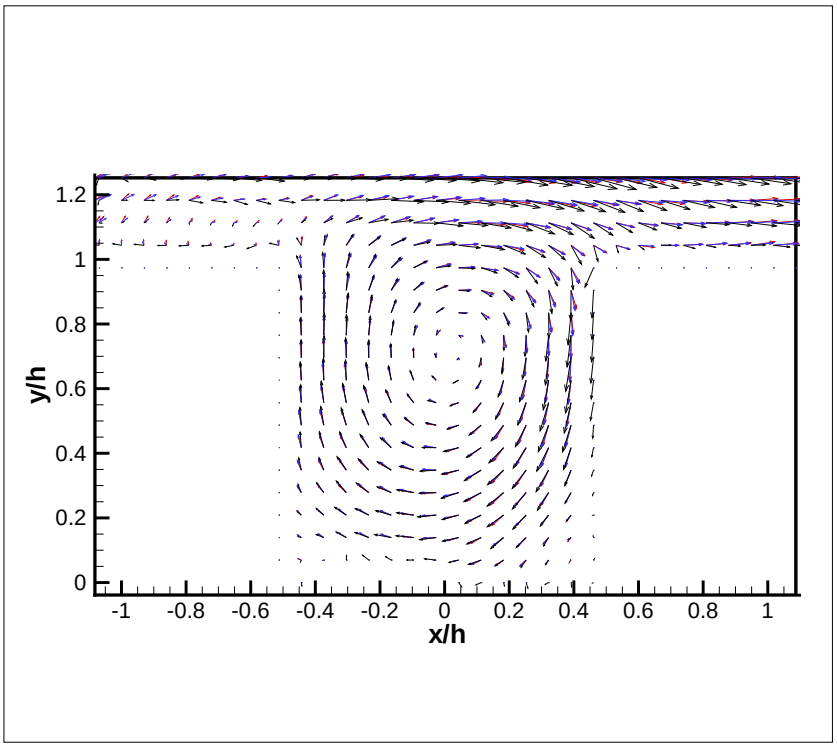

Figure 5.17: *Mean velocity field for the study area with* 200 *pairs of images with CC Lavision (black arrows), our TE method (blue arrows) and TE - SGS (red arrows). For the* 3 *methods, velocity vectors are very similar.*

Figure 5.15 shows the computed mean velocity field obtained by the TE method on the original images (a) and on the preprocessed images (b). Without preprocessing, estimated field is strongly perturbed outside the zone of interest. At border of this zone, there are strong light variations due to stronger impact of experimental noise and reflections; preprocessing proves to remove this light variations. The estimated field on preprocessed images is not influenced by experimental noise. It is more relevant than estimated velocity field on original sequence and it is coherent with the CC Lavision field (Figure 5.14(b)). We can also observe that TE method does not estimate correctly the velocity field over the entire experimental domain. Our approach estimates the velocity field based on scalar transport equation. Thus, this approach will be the most efficient where there is enough particle seeding the field which can be considered as an information about particle concentration. For $y/h \geq 1.3$, there is no more solid particle concentration. Whereas due to a background fluid particle seeding the tunnel, CC Lavision method is still able to retrieve the velocity flow field because of the large size of the CC interrogation window (128×128).

To compare TE and TE-SGS methods, we focus only the analysis on particle concentration velocity inside and close around the canyon. The Figure 5.16 rep-

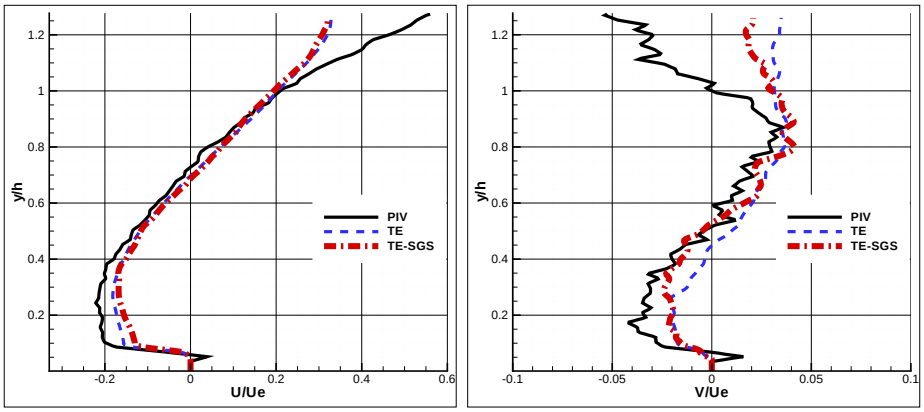

(a) (b)

Figure 5.18: *Vertical profiles of average velocity field of normalized a) horizontal and b) vertical components with CC Lavision, TE and TE-SGS methods. The profile is taken at the center of the canyon ($h = 0$)*

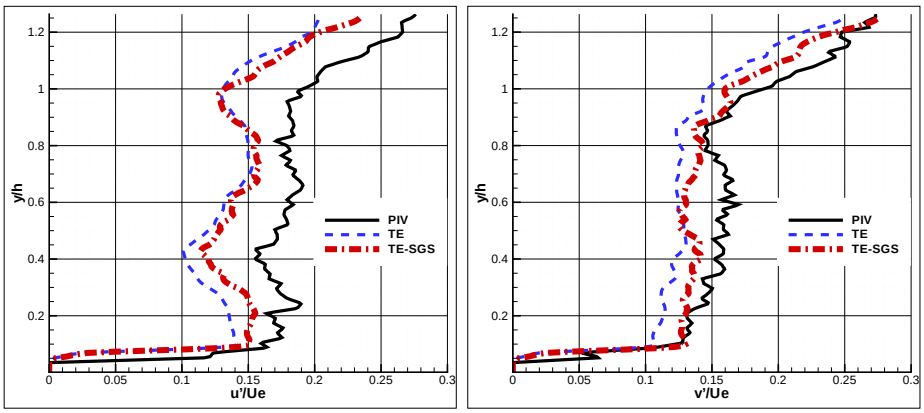

(a) (b)

Figure 5.19: *Vertical profiles of the RMS fluctuating field of normalized a) horizontal and b) vertical components with CC Lavision, TE and TE-SGS methods. The profile is taken at the center of the canyon ($h = 0$)*

resents the zone of interest where there is particle concentration almost for every acquisition. TE and TE-SGS velocity estimates are consistent with the CC Lavision estimates for the area where the average concentration of the scalar is nonzero. To compare the TE and TE-SGS methods, we focus the study of the velocity field on the canyon area (area bounded by the red box on figure 5.16).

Figure 5.17 shows the mean velocity field vectors from CC Lavision, TE and TE-SGS methods. Results for all methods are similar. To exhibit clearly differences

between TE and TE-SGS approaches, we plot the vertical profiles of normalized horizontal (a) and vertical (b) velocity components at the middle of the canyon. Figure 5.18 represents the profiles for the mean velocity fields and figure 5.19 shows the fluctuating RMS profiles for the different methods.

For this experiment, the image acquisition technique has been specially defined to satisfy the best conditions for the use of CC technique. Estimated velocity fields from CC Lavision have been validated compared to the turbulence theory and published in [150, 151]. These velocity fields are, in our case, considered as closest estimation we can made from the reality. On figures 5.18 and 5.19, it seems that TE-SGS method estimates a closest average velocity profile and RMS fluctuating profile to CC Lavision than TE method.

However, our TE and TE-SGS methods can correctly estimates the flow field over particle concentration area. TE-SGS method allows to improve flow field estimation and flow characteristics.

We are now, in the last section, applying TE-SGS method to the motion estimation of an atmospheric event on remote sensing time image series for which assumptions made for the definition of our approach are not anymore satisfied.

5.5 Application to Remote Sensing Atmospheric Event

Satellite observations are currently of major importance in geosciences. Remote sensing is a strong tool to study atmospheric and earth phenomena. In this section, we are concerned with the analysis of dust storm events. These phenomena often appear on four of the five continents. Dust particles can be transported through the atmosphere over thousands of kilometers. Dust Storms have strong impact on health and economy of the touched regions. The estimation of the displacement of dust particle from remote sensing images is important for a better understanding and modeling of this phenomenon. Figure 5.20 gives an illustration of the treated sand storm event in this section.

Monitoring natural phenomena is of major importance for the prevention against possible environmental degradation or to reduce their negative impact. The crucial role of satellite imagery is to make possible the analysis of these dynamic phenomena, in order to better understand them, and eventually to refine, parameterize, or validate physical models whenever they are available. These phenomena, observed from a set of multi-temporal images, are described by their evolution in time (e.g. sand wind motion). Their estimation from multi-temporal images analysis requires taking into account global deterministic characteristics (given by physical laws) and local stochastic characteristics.

Atmospheric motion from geostationary remote sensing image was well studied in meteorological community since the late 1960s [62]. Traditional methods, used to estimate the displacement field, are based on CC techniques [93]. These methods are easy to implement and robust to noise; however they need large interrogation

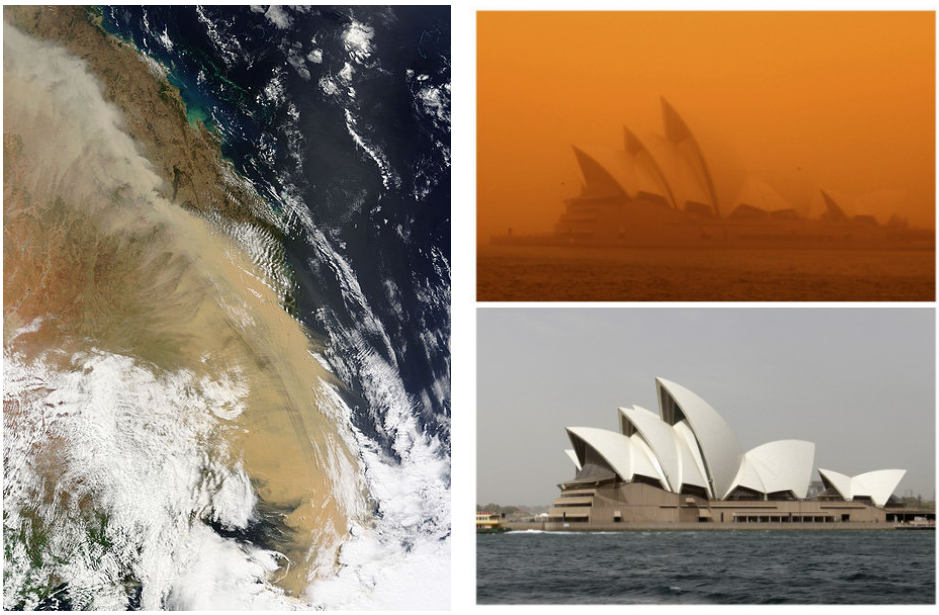

(a) (b)

Figure 5.20: *Colored remote sensing image from MODIS Terra satellite of the dust storm over eastern Australia taken on 23 September 2009 (a) and pictures of the Sydney opera before and during the sand storm (b).*

windows to be able to correctly detect a stable and correct correlation peaks. Moreover they are not suitable for scalar motion estimation where correlation peaks are hardly detectable, as for example in clouds, dust or smoke images.

Here, we test our TE-SGS approach and compare it to CC Lavision [91].

5.5.1 Data description

We use, here, a real pair of optical images from satellite MTSAT-1R taken during the 22 September 2009 dust storm event that happened in Australia. Image sizes are 300 pixels with a resolution of $\Delta = 5km$ by pixel. Δt is 1 hour. The remote sensing time image sequence is from the visible channel. Figure 5.21 shows two successive in time input images with a time separation of 1 hour.

In this image sequence, the pixel $\Delta = 5km$, the image spatial coverage is $1500km \times 1500km$. In the atmosphere, large scales are of the order, or larger than, few hundred kilometers. Because the thickness of dust cloud is only few hundred meters to few kilometers high on z direction [83], the dust cloud motion (even atmospheric motion in general) is considered as quasi-two-dimensional [97]. The hypothesis of 2D motion made in equation (5.6) is then satisfied.

However, small scales in the atmosphere are ranging from $10^{-3}m$ (Kolmogorov scale) to several tenths of kilometers and are strongly three dimensional [97]. In

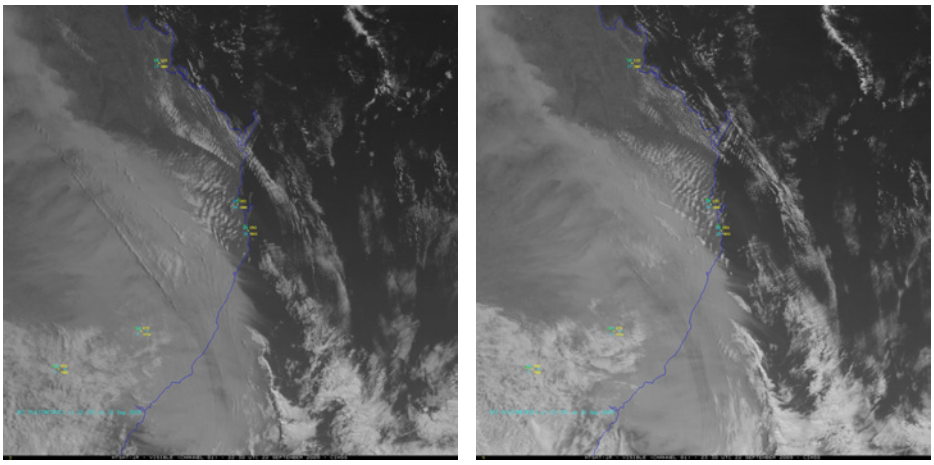

(a) (b)

Figure 5.21: *Two successive MTSAT-1R input satellite images of the dust storm on the 09/22/2009 at time 22:30 (a) and 23:30 (b).*

this sequence, the order of velocity is around 15 pixels by interval of time Δt which corresponds to $U_c \sim 20m.s^{-1}$. As we said above velocity on the z direction is negligible compared to the (Oxy) plane components. In this case, the effect of the component of small scales on the z direction on the dynamic of the flow can also be neglected.

In the atmosphere, the Reynolds number $Re \sim 10^10$. With $U_c \sim 20m.s^{-1}$ and the kinetic viscosity of the air, the characteristic length of the flow in this sequence is of the order of the kilometer $L_c \sim 1km$. Then the characteristic time scale is $T_c \sim 1min$. These length and time scales are much smaller than the one given by the satellite image sequence. Thus small scales will have a non negligible effect on the dynamic of the dust cloud motion. TE-SGS should be used.

We keep, for this test, the direct proportionality between concentration and image brightness intensity made in equation (5.3) even if in this application case, this hypothesis is not totally satisfied. Another point is that the scene lighting is evolving during the day. This will strongly affect the TE-SGS approach since the transport concentration equation is directly related to the image brightness. We propose a simple day light invariant method to tackle this problem.

5.5.2 Brightness Invariant Model

We established, at beginning of this chapter, the relationship between the scalar concentration and the image grey-level value (equation 5.3): $I(\mathbf{x}, t) \propto \alpha\ C^+(\mathbf{x}, t)$. However, this is an over simplification: external factors such as day light variation (or atmosphere humidity and others ...) may lead to global changes of the observation I^+ , thought C^+ may not vary.

To overcome this problem, we assume that the image's grey-level changes linearly from one acquisition to the next : $\partial I^+/\partial t \approx \partial C^+/\partial t \ + \ \beta(t)$. This is equivalent to center the temporal variation of C^+.

At last, the illumination change invariant transport equation defines our data term in equation (5.18); it writes using intensity variable instead of the concentration:

$$E_d(\vec{v}^+, I^+) \ = \ \sum_{\mathbf{x}\in\mathcal{C}_1} \left(\left(\frac{\partial I^+(\mathbf{x})}{\partial t} - \beta(t) \right) + \vec{v}^+(\mathbf{x}).\, \vec{\nabla} I^+(\mathbf{x}) \right. \\ \left. - \left(\frac{1}{Re\ Sc} + D_t \right) \Delta I^+(\mathbf{x}) \right)^2 \tag{5.23}$$

with $\beta(t) = \frac{1}{\mathbf{N}} \sum_{\mathbf{x}\in\Omega} \partial I^+(\mathbf{x})/\partial t$. We name it the $+Bvar$ model.

The invariant light variation model, proposed here, is a sparse approximation of the daylight physical effect on image brightness. However, it shows to improve significantly the motion estimation for geostationary images using the visible channel. Thus, in case of real atmospheric event, further work should be done on brightness invariant model as for example, in [70], the authors proposed to extend OF assumption to light variation problems using diffusion models and in [84], they consider brightness variation as a multiplicative and additive factor to the observed intensity.

5.5.3 Results

We test TE and TE-SGS on the presented satellite sequence in figure 5.21. We compare our results with the ones from CC Lavision software.

For CC Lavision, we use refinement method from 128×128 pixels size window to 16×16. Gaussian peak interpolation is used on cross-correlation signal to better retrieve the exact maximum localization (see appendix A.1 for technical details).

For TE and TE-SGS, we use our noW_MR multiresolution (section 4.2.2) with 4-level pyramidal decomposition ($K = 5$). We set a grid size of 4×4 pixels for the multigrid (section 4.3). Images are previously smoothed with a Gaussian filter of variance $\sigma^2 = 1$ and the weighting coefficient $\alpha = 100$ (equation (4.2)). For this test, D_t was fixed arbitrarily to $D_t = 3$ which shows experimentally to correspond to the best turbulent diffusion coefficient. Further investigation should be made in this kind of sequence in collaboration with atmospheric research institute to determine physically the value of D_t as for the case in section 5.3 and 5.4.

Figure 5.22 (a,b,c) illustrates the corresponding estimated velocity field (left) and streamlines (right) resulting from CC Lavision, TE-SGS and TE-SGS+Bvar approaches. We observe that cross-correlation technique estimates a displacement field which is not smooth; experimentally, it needs large interrogation window size, and the correct correlation peak is difficult to localize due to slowly varying concentration. Results from our TE-SGS+Bvar method give a visually smoother flow field than TE-SGS method which is affected by day light variation. Streamlines generated from results, given by TE-SGS+Bvar method, show the same behavior as CC

LaVision. Dust cloud motion is more identifiable on TE-SGS+Bvar method results and is visually more appealing than from other methods. Advantage of our method compares to cross-correlation approaches is that the motion field is estimated from physical equation (5.18) of the filtered transport equation with the modeling of turbulent diffusivity. Another advantage is that the estimated flow field is dense (one velocity vector by pixel). For CC LaVision, final interrogation windows are 16×16 pixels due to cross-correlation limitation (appendix A.1).

On this real remote sensing image, the proposed simple light invariant model (section 5.5.2) proves to significantly improve motion estimation on visible satellite images. One of the scientific interests is to be able to estimate the more coherent velocity field of dust cloud motion to use it as inlet condition in Large Eddy Simulation atmospheric codes for prediction. In this way, we can bring a correction in real time to the simulation for further dust storm.

Figure 5.23 plots on the image the estimated velocity field from TE+Bvar (blue) and TE-SGS+Bvar (red). The subgrid scale model in TE-SGS, with $D_t = 3$, influence the velocity field. The TE-SGS estimated velocity field seems to detect more spatial variations, as rotations, than TE which seems to oversmooth the velocity field globally over the image domain.

In this section, we applied the proposed sub-grid transport formulation TE-SGS to study atmospheric motion from remote sensing images. In satellite images, in order to compensate for the variation of global illumination from one acquisition to another, we further introduced a brightness variation correction term. Our model takes into account non-observed small scales effects by incorporating a turbulent diffusion term into the scalar transport equation. However, it is hard to evaluate quantitatively the improvement on motion estimation of the subgrid model for this kind of satellite image sequence. Further works in collaboration with atmospheric research institute should be interesting.

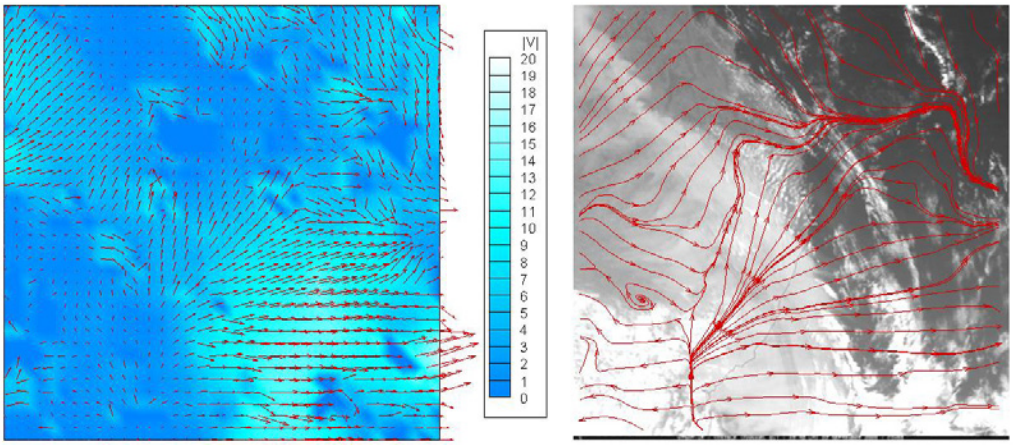

(a) Corresponding estimated motion field and streamlines from CC LaVision cross-correlation algorithm.

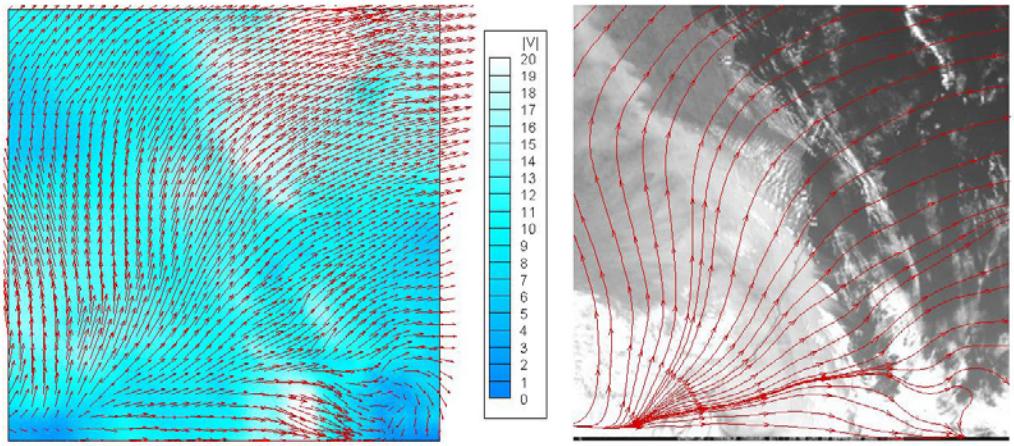

(b) Corresponding estimated motion field and streamlines from TE-SGS algorithm.

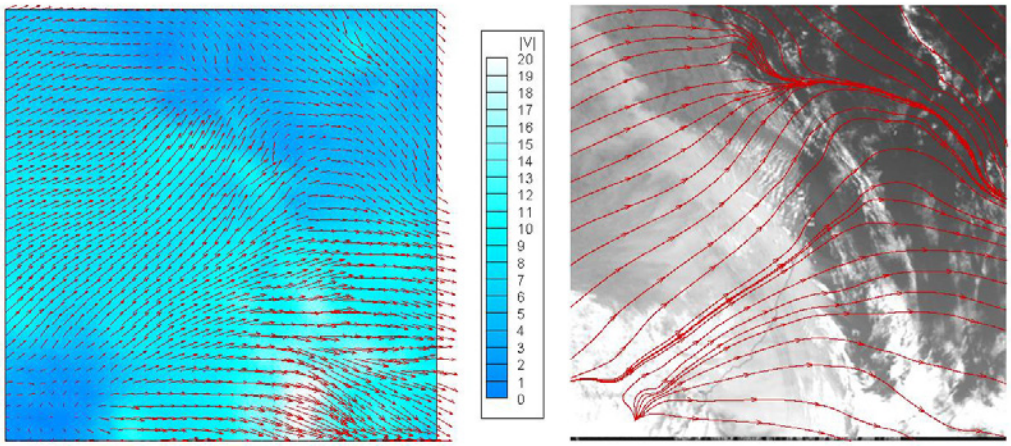

(c) Corresponding estimated motion field and streamlines from TE-SGS+Bvar algorithm.

Figure 5.22: *Real Australian dust storm event in 2009. Comparison of CC Lavision (a) with proposed TE-SGS (b) and TE-SGS+Bvar (c).*

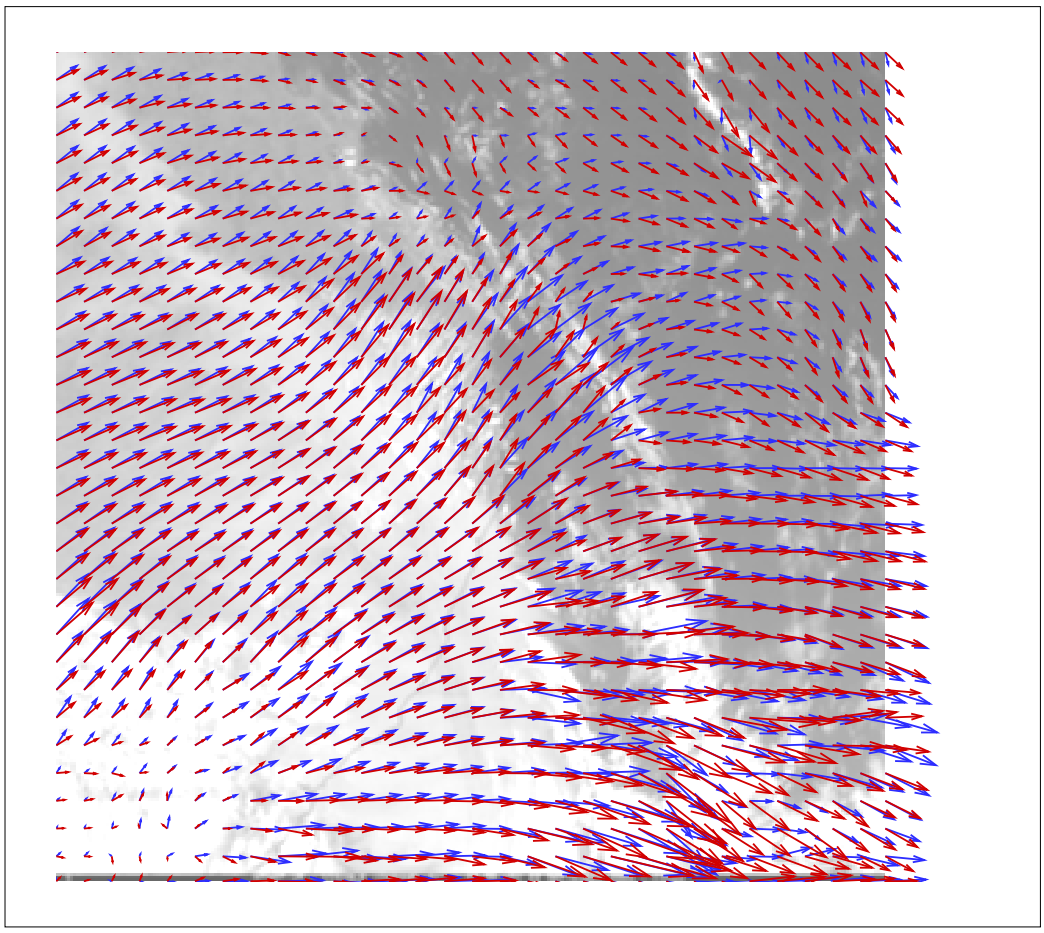

Figure 5.23: *Estimated velocity fields from TE (blue) and TE-SGS (red) using Bvar light invariant method.*

5.6 Conclusions

The filtered transport equation that we have proposed in this chapter takes into account the limitations of the observed information in treated images, incorporating a subgrid scale model based on a turbulent diffusion coefficient D_t in the scalar transport equation (5.18). Tests on synthetic, experimental and atmospheric time image sequences show that the new model improves the estimation of the velocity field for study of passive scalar concentration spread by turbulent flow. It even shows to be robust enough to be applied to non homogeneous solid particle seeding displacements if number of particle in the domain is sufficient to be assimilated to concentration of particle. Subgrid scale model advantages are less important on experimental acquisitions because the illustrated experiment does not fully represent the passive scalar concentration field. In the original laboratory experiment concentration field is obtained only for one instant and not for two successive instants. This was sufficient for obtaining mass fluxes with the pair images for CC Lavision. But this is not sufficient for applying TE-SGS method that necessitates time evolution images of the treated field. However, on the DNS sequence, subgrid scale model outperforms existing optical flow algorithms by considering influence of small scales interactions on the filtered flow field. TE-SGS method allows a better estimation of vortices by modeling the turbulence influence at subgrid scale level. It would be interesting to combine advantages of CC methods with DOF [74] not only by constraining the DOF estimation by the correlation estimations, but also by using a confident weighting coefficient depending on the properties of the studied flow (solid particle or passive scalar transport). A more physical definition of the turbulent diffusion coefficient D_t could also bring an improvement to our model [153, 48]. Incorporation of subgrid scale model in the regularization term and introduction of more physical regularization functions should also be studied. Combination of data assimilation process proposed by [121] with subgrid scale transport equation should strongly improve the motion estimation. Moreover data assimilation can be used to analyze more precisely the turbulent diffusion coefficient D_t, in the aim, to identify the best way in application of subgrid scale modeling in computer vision.

Chapter 6

Conclusions and Further Work

Summary

In this thesis, we were interested on motion estimation problem in the case of turbulent fluid flows. The main issue of this manuscript was to introduce into the motion equation a subgrid scale model using a turbulent diffusion term to tackle the fact that temporal image sequences are discrete information of the reality and that their time and space resolutions may be to large compare to the turbulence scales of the studied flow and therefore to the small active scales on the kinetic of the flow.

The work has been oriented in two principal axes:

- First: Proposition and validation of an efficient motion estimation approach (chapter 4).

  Differential form of BCCE was defined on information from two image spatial gradients (TF_BCCE) (section 4.1.1). Large velocities are retrieved using an unwarping pyramidal decomposition process (noW_MR) (section 4.2.2). Optimization issues have been studied and Direct Descent Energy (DDE) minimization (appendix C) coupling with multigrid techniques proved to be the best compromise between solution accuracy and time consuming (appendix F). The proposed approach is formulated by a Markov Random Field framework. In the past, variational approaches were popular to treat motion estimation problem as the velocity field is 2 dimensional real values. However, we show in this work, that using Markovian framework which formalizes the problem on a discretized graph, estimation of 2D real velocity field is as efficient as variational framework which solves the continuous equations using Euler-Lagrange equations [77]. Moreover, Markovian approaches allow more flexibility on the energy functional definition than variational ones. Results shown to be competitive with existing algorithms in computer vision community, on different temporal image sequences (solids and non-rigid, synthetic and real) and in fluid mechanic community, on synthetic DNS particle sequences. Even if the problem formulation were not physically motivated, results are coherent with other CC and DOF approaches adapted to fluids (sections 4.5 and 4.6).

- Second: Definition of physical based motion equation with turbulence consideration (chapter 5).

  Transport equation with diffusion is filtered to correspond to the observed information given by the image sequence. Small scale interactions are defined

through a subgrid scale model using a turbulent diffusion term (TE-SGS) (section 5.2.1). The turbulent diffusion coefficient D_t is, in this work, defined as a statistical constant invariant in time and space. D_t is determined by the turbulent subgrid scale kinetic energy (section 5.2.2). Results on synthetic scalar filtered sequence are very promising. TE-SGS clearly outperform other approaches and estimates a better velocity field closer to the exact DNS velocity field (section 5.3). Results on real PIV acquisitions are less impressive than the one on scalar sequence but we saw that subgrid scale model may also improve motion estimation for dense particle image sequence (section 5.4). Application on remote sensing has been done for the case of dust storms motion estimation. A brightness invariant model has been proposed to tackle the variation of light over the day time (section 5.5). Qualitative results are interesting for further research.

Improvement on motion estimation by the insertion of subgrid scale model into the motion equation to deal with missing image information in the case of turbulent flows opens a wild field of research where turbulence modeling can be used into computer vision applications for a better analysis of image sequences.

Open problem and Further Work

As said above, this thesis leads to many different research fields.

Subgrid scale model definition

The subgrid scale model, representing the small scale effects on the dynamic of turbulent flows, was defined as a constant in time and space. Study of different subgrid scale models of turbulent diffusion, starting by the simplest Smagorinsky model [87], should be investigated ([188, 67, 113, 126, 48]). From this study, we should evaluate the capacity of subgrid scale model to fit the problem of turbulent motion estimation from temporal image sequence. And, it may also lead to a new subgrid scale model definition adapted to the application which will come to add itself to the many existing models.

Physical regularization function with subgrid scale model

In this work, we focus our research on the motion equation through the definition of filtered transport equation. We use a classical smoothness regularization function [77]. This function can be viewed physically as a constant kinetic energy over time if external forces are neglected. More complex regularization functions, with physical motivation, have been proposed as Div-Curl [47], Stokes [136] or simplified Navier-Stokes [137, 73] equations. These functions can bring improvement to the model as it will force the estimated field to satisfy the regularization. However, functions should be carefully defined depending on the studied flow field and the temporal image sequence.

Moreover, regularization functions were only defined on the filtered velocity field (large scales). As subgrid scale model has been introduced, in this work, in the data term (motion equation) due to no negligible effect of small scales, we should also work on introducing subgrid scale models into the regularization function to correctly constrain the physical observed phenomena.

Another promising solution is presented in next paragraph.

Coupling TE-SGS with data assimilation governing by filtered dynamic equations with subgrid scale model

Methods proposed in [120, 121, 45, 89] are very promising for long temporal image sequences. By experience, it needs at least height regular time interval successive images. In [121], using data assimilation governing by Navier-Stokes equations with an observation function defined by BCCE, the estimated velocity field is temporally forced to satisfy the Navier-Stokes equation over the all sequence according to the observation function. In this way, the regularization function is the exact dynamic equation and it is coherent along the all time axis. The estimated field is less sensitive to noise or even to missing instantaneous observation as it will be filtered by governing Navier-Stokes equations. Moreover data assimilation is a useful tool for analysis of some variables of the observed function.

Introducing TE-SGS as the observed function instead of BCCE is the next step of research. As we can see in [121], when the observation function is an estimated velocity field, the results are different than when it is the BCCE. The observation function has then an important weight on the final estimation. TE-SGS shows much better results than TE on filtered scalar sequence (chapter 5). Then coupling TE-SGS with data assimilation governing by dynamic equations should improve the estimation. Moreover, subgrid scale model should be introduce into the governing equations. Data assimilation will then be useful to analysis and define the best subgrid scale model of turbulent diffusion that fits to turbulent motion estimation from temporal image sequences.

Robust light invariant model

In section 5.5, we propose a simple brightness invariant model which considers the variation of image intensity linearly changes over the time. This assumption is too restrictive and in fact far from the exact light variation phenomenon. More work on brightness variation models should improve robustness. [170, 84] proposed to consider that intensity between two successive images can vary by a proportional coefficient and an additive term. Spatial regularization of the proportional coefficient and additive term is added to the energy definition. [70] proposed different physical possible phenomena which changes brightness intensity over the time as diffusion process for example. Another way, to tackle brightness variation, is to use data assimilation governing by dynamical equations as [121] over a set of successive images (see above paragraph).

3D flow estimation and scattering theory

The hypothesis of 2D turbulent flow is too restrictive. Temporal image sequences give us a 2D projected observation of the real 3D environment. Thus it is important to look to the projected dynamic equations from 3D to 2D plan as [100]. If 3D data temporal sequence is available, the exact dynamic equations can be used in our model.

Another problem of using transport equation as motion equation is that concentration of the observed quantity has to be related to the image intensity. We made the assumption that brightness intensity is directly proportional to concentration. However, brightness intensity comes from light emission, diffusion, refraction of scene components. The link relating the concentration to the brightness intensity may be very complex. Scattering theory should be considered if we want to refine the proposed approach.

Application work

Experimental fluids

In experimental fluids, determination of the velocity field is a requirement for the experience validation. Methods used to retrieve the flow field are most of the time Cross-Correlation (CC) techniques. Fluid needs to be seed by particles, in the aim, to get the correct fields. We show, in chapter 4, that Differential Optical Flow (DOF) based approaches can perform better than CC methods on synthetic particle image sequences and even more on scalar image sequences. DOF based methods have the advantage to give a dense field. Moreover the problem formulation can be defined with physical motivated equations like for example: Motion equation based on filtered transport equation with subgrid scale model (TE-SGS) as we suggested in this thesis, regularization by 2D vorticity equation [137] or data assimilation with simplified Navier-Stokes equations [121]. However, we saw that DOF based approaches are much more sensitive to noise than CC methods. Experimental noise due to the image acquisition is unavoidable. Further work suggested above on robust brightness invariant models is a way to improve the efficiency of DOF based approaches for experimental fluids.

Environmental understanding

Dispersion of pollution, smoke, ashes or even floods and climate change atmospheric models, all these things need velocity field computation or at least a good initial velocity field to be able to correctly do the simulation. The proposed method in this thesis may provide more precise velocity field as initial condition given to the model. On natural phenomena, regular flow estimation from temporal image acquisition of the event can also be used as external forces on the simulation. Insertion

of our approach into atmospheric models [186, 140] is a pretty interesting research topic for real case studies linking estimation, simulation and real-time correction problems.

Meteorology

In meteorology, huge data of temporal image sequences provided by satellite acquisitions are available. Geostationary satellites become more and more precise with a spatial resolution of few km^2 and a temporal acquisition rate of 15 to 30 minutes. However, due to the high turbulence ($Re >> 1$) in the atmosphere, time and space resolutions of satellites are still much larger than turbulence characteristic scales of the events. This thesis work opens a new research field where subgrid scale models should be considered in the motion estimation from remote sensing sequences. Application can be on dust and sand storms as shown in section 5.5 but also on clouds, storms, hurricanes and typhoons (many every years), ashes (eruptions of Eyjafjallajökull in Iceland in 2010) or sea surface temperature or pollution (oil spill in Gulf of Mexico in 2010). Huge problems still remain to study. Satellite images give a vertical integrated information. Flow in this thesis is considered to be 2 dimensional. In reality equations should be the projection of the 3D scene [100]. Vertical velocity field should not be neglected. Hypothesis of stratified flow in the atmosphere can be done [73]. Extraction of the real observed quantity from remote sensing image is not trivial and it is still a challenging problem. Combination of different bandwidth acquisitions as infra-rouge, visible and others can used to extract a better analyzed quantity value as for example, [102, 171] for optical thickness extraction on dust events.

Few words to conclude

This thesis was supervised and supported in a Sino-French cooperation. Moreover, it was held between teams and topics linking two scientific communities: Computer Vision and Fluid Mechanics. Even with large physical distances and differences in scientific knowledge from the both parties, this work has been completed. The results are promising and much remains to be done. Today, collaboration has become stronger through a new project within LIAMA with the participation of French (Rennes, Lyon) and Chinese (Tsinghua, LIAMA) scientists in these area. To conclude, I like to express my deepest gratitude to all the people I met during these last years and with whom I hope to continue to collaborate in the future.

Appendix A

Particle Image Velocimetry (PIV)

A.1 Cross-Correlation Particle Image Velocimetry (CC)

Principe of Particle Image Velocimetry (PIV) is relatively simple and allows to obtain a 2D instantaneous velocity field of the flow. This technique was mainly developed in Fluid Mechanics community [2]. It consists in recording images of the flow of an area lighting by a thin pulse of light probe at different successive instants. This technique is non intrusive because no utensil, that could perturb the flow characteristics, has to be placed inside the fluid. However particles have to be placed in the fluid to be able to visualize something on images and to be able to determined the displacement of the fluid by assimilate it to the displacement of the particles in it. A technical background of the recording technique is presented in appendix A.3. The image analysis to get the displacement of particles is generally based on correlation techniques (CC). For this purpose, we need a seeding of the fluid by particles within a correct concentration of particles. Moreover, it allows to access to all spatial scales of the fluid depending on the spatial resolution of the recorded images. Depending on the turbulence rate and camera specifications, it can contain or not spatial scales of the turbulence. However, for the time rate of image acquisition, the limitation due to camera technology is most of the time insufficient to capture temporal scale of the turbulent flow. PIV can fix turbulent structures in a spatial way.

In our case, we study two successive images representing the same scene at two different times ($I_1 = I(\mathbf{x}, t)$ and $I_1 = I(\mathbf{x}, t + \Delta t)$). Thus we describe here the Cross-Correlation PIV (CC). For a complete overview on PIV recording technique and flow estimation methods, the reader can refer to [130, 94].

CC has become the best-known and most widely used experimental method for flow estimation in fluid mechanics

A.1.1 Cross correlation

The principle of cross correlation is to look for the degree of similarity between two variables. In the case of PIV, variables are considered as square interrogation windows $\mathcal{W}(\mathbf{x})$ centered in pixel $\mathbf{x}$ containing $N^2_{\mathcal{W}}$ pixels. Under hypothesis that particles in image I_1 will also be in image I_2 and considering that particle size and brightness doest not vary so much (BCCE defined in equation 3.4), the cross correlation of interrogation windows between both images will allow us to determine the dominant displacement of particles. The normalized cross correlation function is defined as:

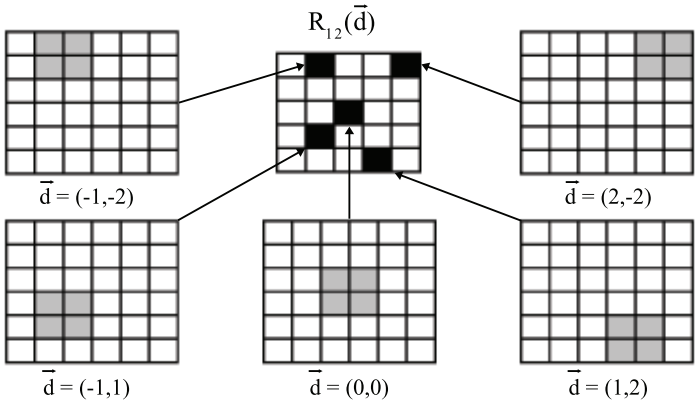

Figure A.1: *Cross-correlation illustration: Cross-correlation plane (middle). A* 2×2 *interrogation window is correlated with a* 6×6 *sample which produces a* 5×5 *correlation plane.*

$$R_{12}(\vec{d^c}) = \frac{\sum_{\mathbf{x}_i \in \mathcal{W}(\mathbf{x})} I_1(\mathbf{x}_i)\ I_2(\mathbf{x}_i + \vec{d^c})}{\sqrt{\sum_{\mathbf{x}_i \in \mathcal{W}(\mathbf{x})} I_1^2(\mathbf{x}_i)\ .\ \sum_{\mathbf{x}_i \in \mathcal{W}(\mathbf{x})} I_2^2(\mathbf{x}_i)}} \tag{A.1a}$$

$$R_{12}(\vec{d^c}) = \frac{\sum_{\mathbf{x}_i \in \mathcal{W}(\mathbf{x})} I(\mathbf{x}_i, t)\ I(\mathbf{x}_i + \vec{d^c}, t + \Delta t)}{\sqrt{\sum_{\mathbf{x}_i \in \mathcal{W}(\mathbf{x})} I^2(\mathbf{x}_i, t)\ .\ \sum_{\mathbf{x}_i \in \mathcal{W}(\mathbf{x})} I^2(\mathbf{x}_i, t + \Delta t)}} \tag{A.1b}$$

$\vec{d^c}$ is the displacement estimated by cross-correlation technique. For each choice of a displacement $\vec{d^c}$, the sum of the products of all gray values in the interrogation windows $\mathcal{W}$ produces one cross-correlation value $R_{12}(\vec{d^c})$. Figure A.1 shows how the cross-correlation is performed in practice for an example of $\mathcal{W}$ of size 2×2 pixels in an image of size 6×6. The original position of $\mathcal{W}$ is in the center of the image (bottom-center representation on figure). $\mathcal{W}$ is linearly shifted over the image. For every integer displacement, the corresponding correlation coefficient is computed using A.1b. We obtained a cross-correlation plane of size 5×5 for this example. Figure A.2 gives a 3D view of the cross-correlation function in the case of two PIV images. The maximum of the cross-correlation function will provide the dominant displacement of particles containing in $\mathcal{W}$ (illustration bottom right on figure A.2).

In the spatial space, the process of finding the highest correlation value for every window is time-consuming. Number of multiplications per correlation value increases in proportion to the interrogation window size. One way to avoid this time-consuming calculations is to use the property of cross-correlation in Fourier space: The cross-correlation of two function is equivalent to a complex conjugate point-wise multiplication of their two-dimensional Fourier-transforms.

$$R_{12} = IFT\left(\Re\left(FT(I_1).FT(I_2)^*\right)\right) \tag{A.2}$$

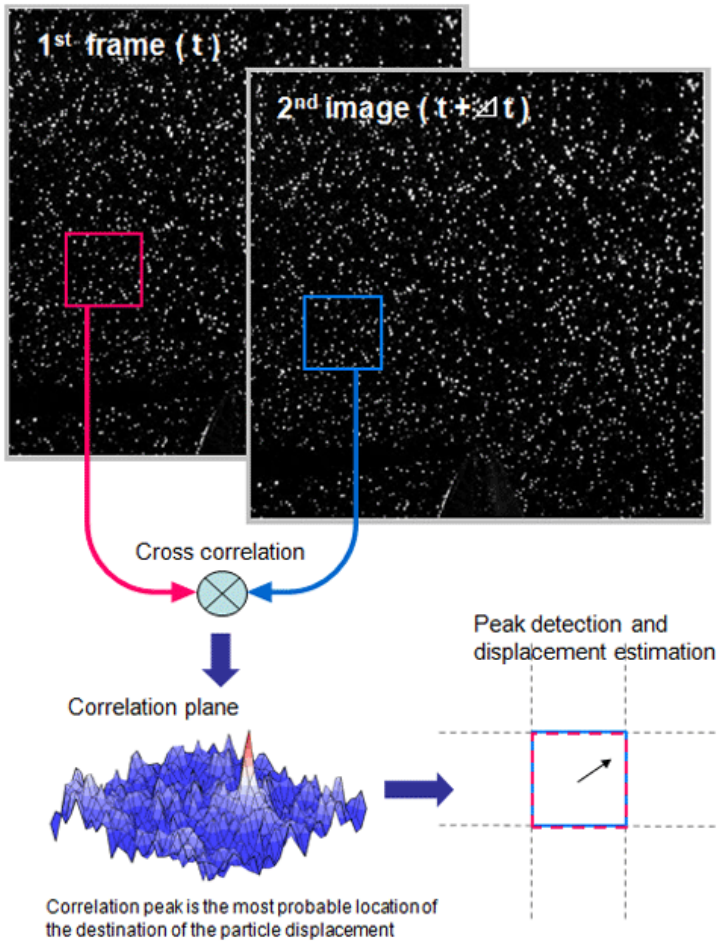

Figure A.2: *Illustration of cross correlation between two PIV images and representation of cross-correlation function. The peak represents the dominant displacement of pixels in the interrogation window. (Figure extracted from* `http://koncerto.biz/` *)*

where $*$ represents the complex conjugate, IFT is the 2D inverse Fourier-transform, FT is the 2D Fourier-transform and $\Re$ is the real part of the complex given by the multiplication of the two Fourier functions.

This standard cross-correlation techniques have some limitation. However, they can be weakened by certain strategies that are presenting in the following subsections.

A.1.2 Peak Locking and Sub-Pixel Interpolation

Cross correlation allows to get only integer value velocity. Fractional displacement can be obtained using correlation peak locking and sub-pixel interpolation.

A CCD camera get the light intensity over the pixel size during a time lap transforming the number of electrons in intensity of gray level. This intensity is an average over all the pixel surface. We only have one information for one pixel. The light signal is not continuous on the image and we don't know values between pixels. It can produce sometimes bias on the measure. The peak locking select the measured displacement at the nearest integer value. It depends on the chosen sub-pixel algorithm, the size of detected object compare to the pixel size of the CCD camera, boundaries of the interrogation window, and density of similar objects. This effect is added to the experimental noise that limit the precision of CC calculation. We can see it when plotting the density of the displacement probability. If the Gaussian is not smoothed, and shows discretization step at integer values, that means there is some bias coming from this phenomenon. It is recommended that particles have an average diameter around two to four pixels. Under this interval, the sub-pixel interpolation is not efficient and can generate this bias. For a detailed discussion of peak locking, we refer to [180]

Many improvements have been proposed to reduce the peak locking bias although it was shown that Gaussian sub-pixel interpolation minimizes this effect.

Cross-correlation can retrieve the closest integer displacement $\vec{d}_I^c$ of the interrogation window. Precision of these methods is $\pm 1/2$ pixel. It is not enough to get the smallest scales of phenomena we want to measure. Sub-pixel techniques are used to improve the precision. Camera has discretized intensity values of gray level, we can make the interpolation between pixels if we know, a priori, the form of objects to correlate. Displacement can be decomposed in an integer component $\vec{d}_I^c$ and a fractional one $\vec{d}_f^c$:

$$\vec{d}^c = \vec{d}_I^c + \vec{d}_f^c \tag{A.3}$$

Sub-pixel interpolation techniques determine the fractional displacement. There is three classical methods to calculate $\vec{d}_f^c$: Peak Centroid, Parabolic Peak Fit and Gaussian Peak Fit.

With good particle images, these interpolation functions can detect peaks with an accuracy up to 0.05 pixels. Gaussian peak fit is the most used peak fit function because particles themselves can be described by Gaussian intensity distributions.

A.1.3 Multi-Pass and Iterative Refinement

Multipass and iterative refinement techniques are used respectively to reduce erroneous estimates and to retrieve high-resolution velocity estimates [181, 142] because CC is sensitive to the interrogation window size. More the interrogation window is large, more the estimation is robust. However, resolution estimation is parser. Small interrogation window gives a higher resolution estimations. However, estimations are more sensitive to noise and provide more erroneous estimates.

Multi-pass technique is based on an iterative process. After the first displacement evaluation of $\mathcal{W}$, a shift corresponding to this displacement is applied to the same interrogation window on the second image. The correlation peak becomes center

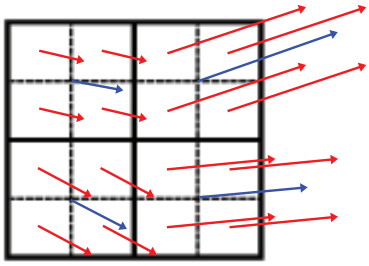

Figure A.3: *Iterative refinement technique illustration (two levels).)*

in zero after the first iteration if the displacement proves to be correct. Else, other displacement evaluation iterations are processed till a fixed convergent criterium. At every iteration, the estimated displacement is added to the previous one. It has been shown [181] that by offsetting the correlation windows, the number of matched particles increases. Usually, three multi-pass steps are performed.

Iterative refinement technique allows to improve the resolution of the velocity estimates [142]. A first displacement estimation is made by multi-pass between two images using a large window size ($N_{\mathcal{W}} \times N_{\mathcal{W}}$). Then the interrogation window is reduce by half ($N_{\mathcal{W}} \times N_{\mathcal{W}} \rightarrow N_{\mathcal{W}}/2 \times N_{\mathcal{W}}/2$). The coarse estimated displacement is projected to the new smaller windows (see figure A.3). A new multi-pass is performed on the smaller windows using the displacement as the first evaluation. This window reduction is done until the desired resolution is reached. Note that outliers have to be detected and replaced by interpolation at each refinement steps. Because, they will strongly affect the final estimated displacement.

Anyway, these techniques do not allow to get a dense resolution estimation. The final interrogation window size should depend on the particle density. It is shown that at least four particle pairs should be located inside both corresponding interrogation windows. Compare to single-pass cross-correlation methods, coupling these techniques improves both estimation efficiency and resolution. However, interrogation windows are not deformed by these methods. There is only one velocity estimate for an interrogation window.

A.1.4 Interrogation Windows Deformation

As we say before, only one displacement estimate is recovered per interrogation window. The highest peak of the cross correlation function is selected has the displacement of the window representing the dominant displacement of windows particles. However, this peak will be less pronounced in regions with a large velocity gradient. Interrogation window deformation techniques [78, 79, 173] can deal with this limitation. Over interrogation windows, the corresponding displacement distributions vary spatially. The spatial displacement distribution can be related to Taylor series. Scarano [141] classifies the different interpolation methods depending on the order

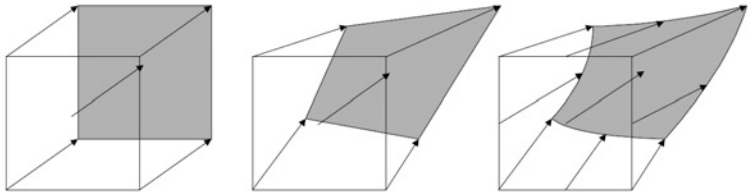

Figure A.4: *Effect of window deformation with a different truncation order of the displacement distribution.)*

of Taylor expansion used to estimate the displacement distribution:

$$\begin{aligned}\vec{d}^c = \vec{d}_0^c &+ \frac{\partial \vec{d}^c}{\partial x}(x - x_0) + \frac{\partial \vec{d}^c}{\partial y}(y - y_0) \\ &+ \frac{1}{2}\left[\frac{\partial^2 \vec{d}^c}{\partial x^2}(x - x_0)^2 + \frac{\partial^2 \vec{d}^c}{\partial x \partial y}(x - x_0)(y - y_0) + \frac{\partial^2 \vec{d}^c}{\partial y^2}(y - y_0)^2\right] \\ &+ \vartheta(\mathbf{x} - \mathbf{x}_0)^3 \end{aligned} \tag{A.4}$$

with $\vec{d}^c$ displacement in $\mathbf{x} = (x, y)$ and $\vec{d}_0^c$ displacement in $\mathbf{x}_0 = (x_0, y_0)$ at the center of the interrogation window $\mathcal{W}$. $x \in \left[x_0 - \frac{1}{2}N_\mathcal{W}, x_0 + \frac{1}{2}N_\mathcal{W}\right]$ and $y \in \left[y_0 - \frac{1}{2}N_\mathcal{W}, y_0 + \frac{1}{2}N_\mathcal{W}\right]$. After a first cross-correlation estimation, the displacement distribution inside the interrogation windows is computed by the used interpolation method. The most used window deformation technique is the 1^{st} order Taylor expansion (linear) interpolation ([78, 79]). Higher order methods are more time consuming due to the increased number of parameters. Figure A.4 represents the different order methods.

A.1.5 Post-Processing

CC does not take into account spatial context when estimating the displacement of an interrogation window. Depending on the quality of the correlation function, it may do wrong displacement estimations. These outliers can be detected based on the magnitude and direction of outliers vectors compare to its neighborhood. Many different techniques for outliers detection and data interpolation have been proposed (see [129, 180, 148]). Most of them combine the following two points:

- Outliers detection: An outlier is detected if the absolute difference of magnitude or direction between the velocity vector and the average of its neighborhood is larger than a defined threshold. Divergence, vorticity or other flow characteristics can be used as well for outliers detection [142].

- Interpolation: Replacement of outliers by interpolation technique using neighborhood velocity vectors.

A.1.6 Physics-Based Priors

An interesting improvement for post-processing methods has been the introduction of physical properties of the flow. For example [117, 82, 3] combined CC and CFD using cost functions. Cross-correlation estimates are constrained to satisfy the continuity equation or the incompressible Navier-Stokes equations. Displacement estimations are spatially corrected in respect to the fluid equations.

[119] proposed a new CC technique based on physics. The obtained velocity field satisfies the governing equation of the fluid. It is possible that not only the velocity but also the pressure is measured, using the Navier-Stokes equations for the dynamic model. This CC method with physical based model is used in section 4.6.1 for comparison with ours on particle image sequence.

A.2 Conclusions on CC

CC technique is attractive for its simplicity. The motion field is retrieved by searching the local displacement that maximizes the cross-correlation between two interrogation windows placed in each of the two images. This approach has proved to be very efficient when satisfying various criteria related to the density of particles or to the local gradient of the studied flow. Nevertheless, there are several limiting factors. At first, the size of the window needs to be chosen carefully: if too small, the cross-correlation peak might not be reliable ; if too big, the particles in the windows might be animated by different movements due to local inhomogeneities of the flow; because CC method estimates a single velocity vector representing the majority displacement of particles in the window, the resulting velocity field will be over-smoothed. In these two cases, the estimated velocity field might be either noisy, either too smooth, or even incorrect. We have seen standard CC limitations can be overcome by iterative schemes and post-processing steps. Note that the error rates of up-to-date image processing methods for CC is under 0.1 pixel size which means that the overall error is mainly caused by the peak-fitting function. A second drawback lies in the fact that CC methods need very specific input data (particle images under certain image conditions). In addition, CC approach cannot be used for scalar field sequences, due to the absence of clear correlation peak in this type of images as correlation relies on high-frequency components of the images.

A.3 Particle Image Velocimetry - Recording Technique

This appendix describes the technical background of the recording process for Particle Image Velocimetry (PIV). For complete description please refer to [130].

PIV is an optical method, used to measure the velocity field in fluids. Because fluids are generally non-textured, to be able to perceive the fluid motion, tracer particles are usually added to the flow. Small solid particles, very thin, are inserted to the fluid. One of PIV hypothesis is that the solid tracer particle are small and light enough to always be in the same fluid particle. In this way the displacement

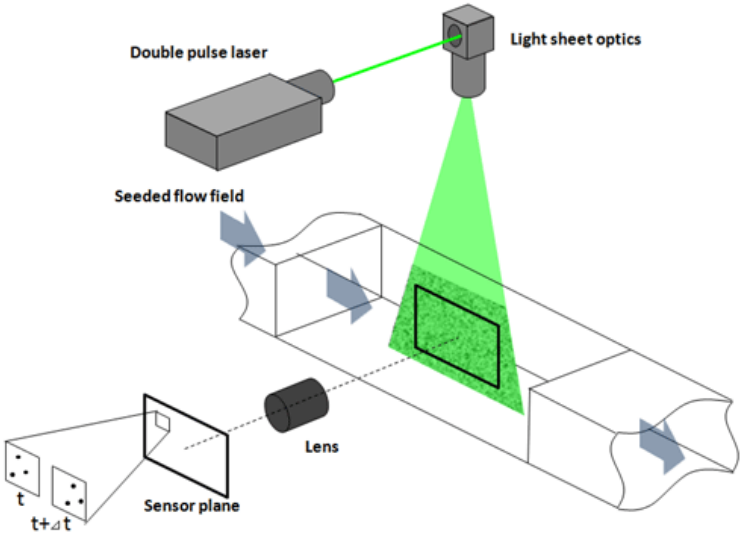

Figure A.5: *Optical sketch of the PIV technique. (http://koncerto.biz/)*

of the particle represents the displacement of the fluid. More information on tracer particles (different materials and sizes) can be found in [104].

A.3.1 Image acquisitions

To get particle images, we have to create a bright plan in the flow. Particles, that will go through this plan, will diffuse the light and we will be able to catch this light on camera CDD. The camera is placed perpendicular to the bright slide. Illustration of technique coupling laser and camera is given in Figure A.5.

Normally, every kinds of light source can be used, but rapidly laser sources became the reference. Because they can generate a high power light and they allow to better control the characteristics of the light plan in particular its divergence. The laser power is chosen in function of the coverage of the light plan, the size of present particles in the flow (diffused intensity by particles is proportional to the square of their diameter), the exposure time (more the flow speed is important, more the exposure time is short). For water flow, the use of classical laser providing few Watts, can be enough. But for other cases, it is often necessary to use some sources much more powerful. These kind of sources is composed by pulsed lasers that can provide until few megawatts (over a time rate of few nanoseconds).

Particle images at different instants can be recorded on the same support (multi-exposition), or on different supports (single-exposition): In the first case, the recording will be analyzed by auto correlation. In the second case, we will use the cross correlation. Typically the time rate Δt between two images of a same particle varies from few microseconds to few milliseconds. To be used, cross correlation has to be associated to a double frame camera allowing to save rapidly two recordings.

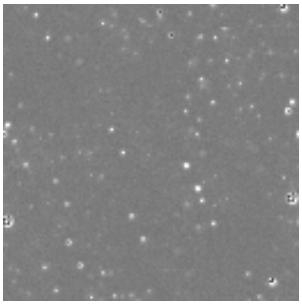

Figure A.6: *Illustration of a multi-exposition image.*

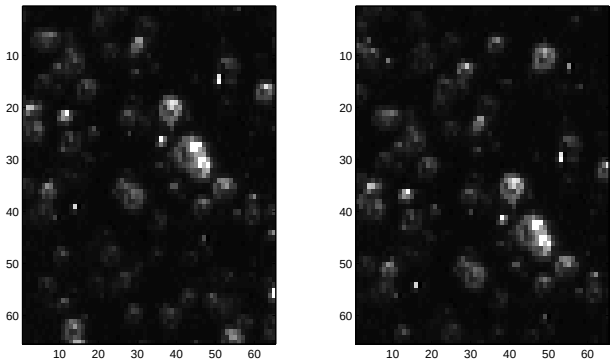

Figure A.7: *Illustration of single-exposition images.*

A.3.2 Synchronization between laser and camera

In multi-exposition many light flashes are superposed on a same support (on the same camera frame for example). Thus, we only need to generate laser pulses when the camera recording is open (illustration of multi-exposition image is shown in figure A.6). In single-exposition, we use double frame cameras, that are able to record two successive images separated by a minimum interval of time in a order length of few microseconds. In our case, we use the single-exposition technique, that gives us two images representing the scene at two successive times. And from these two images, we estimate the displacement of fluid particles. Illustration of single-exposition images is shown in figure A.7 where the fluid is going vertically from the top to the bottom.

For single-exposition, the double frame camera is synchronized with a laser in

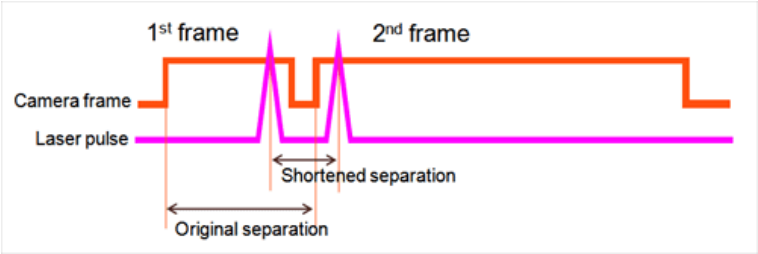

Figure A.8: *Time set of camera and laser synchronization for single-exposure images. (Figure extracted from* `http://koncerto.biz/`*)*

the way to take images of the lighting flow field when there is the laser pulses. Laser pulses have lighting flash inferior to $1\mu s$ of light. This high speed lighting flash allows to get a fixed information of the fluid particles. In the same time, the camera frame is open to record the light diffused by the particles. The first frame acquisition is fully controlled by the user. The opening frame time is larger than the lighting flash time. Thus, first the camera frame is open then the laser pulse is done. The camera frame is closed after the laser pulse. Figure A.8 gives a time chronology of camera and laser synchronization for the two frames. However, the second frame acquisition is constrained, even today, by camera technical limitation. In fact, the camera needs time to transfer the electric charges from the first image to the computer when recording the second image. Because the transfer time is larger than the temporal time rate of acquisition Δt. We can then only take image pairs. Another pair will be taken after that the second image is finished to be transfered. The exposition time of the second frame is not controlled by the user and it is much longer than the first frame. The temporal scheme coupling laser pulses and camera acquisitions is implemented in commercial software as Dantec Dynamics or Lavision. The PIV image sequences used in this work in chapter 5 were generated by Lavision software.

Today, we can find some very fast camera that can take many images with a temporal rate acquisition of order of Δt. However these kind of camera still remains very expensive and few laboratories in the world use it. Due to the limitation of image pairs, temporal information of the flow cannot be taken into consideration. It is for that, in this work, we focus our motion estimation over only two successive in time images. Equation definition using temporal information has temporal constraints or Navier-Stokes equation (section 3.3.2.2) could be used in a later work to improve our estimation.

Another limitation of Particle Image Velocimetry is that for fluid or scalar in the fluid, we have to seed tracers into the fluid. For some real applications, it might be not possible to seed the fluid correctly due to temperature or to a difficult access for seeding particle to the studied location. For scalar experiments, seeding of the fluid may represents some inconvenient, in the way that we need particle to estimate the flow field and the concentration to know its evolution. Fluorescence is often used in

this case.

A last limitation resides that the technique needs an accessible optical path. One for the laser sheet and another one for the camera. In certain cases, a testbed should be specially builded.

Appendix B

Problem formulation using MRF-Gibbs framework

Markov Random Fields (MRF) and Gibbs distributions [69, 17, 66] are at the intersection of statistical physics and probability theory. These methods allow to define a mathematical formulation of many kind of problems in computer vision where solution cannot be analytically computed. They have been extensively used since the early 80's. Many studies based on this approach have been proposed as image restoration [66, 80], segmentation [54, 24], classification [42, 112], optical flow [76, 134] and many others...

We give here a brief presentation of this method. For complete details on the approach, please refer to books [81, 98, 22]. Its application to stereo matching problem is given in appendix D and another application to optical flow problem is given in chapter 4.

B.1 Markov Random Fields

Let have an undirected grid graph $G = (s, e)$ defined by different nodes, called site s, linked each others by undirected edges e.

$$s = \{s_i | i \in \{1, ..., \mathbf{N}\}\} \tag{B.1a}$$

$$e = \{e_{ij} | i, j \in \{1, ..., \mathbf{N}\}\} \tag{B.1b}$$

where $\mathbf{N} = card(G)$ is the size of the graph. The figure B.1 represents two of the most used neighborhood systems $\mathcal{N}$ for a regular grid graph. Figure B.1.a shows a 4-neighborhood system and figure B.1.b a 8-neighborhood system. The neighbors of site s_4 for figures B.1.a and B.1.b are represented with light (cyan) color. Light (red) edges are the linking edges for site s_4 with its neighbors.

A neighborhood system $\mathcal{N}$ for G is:

$$\mathcal{N} = \{\mathcal{N}_{s_i} | \forall s_i \in G\} \tag{B.2}$$

where $\mathcal{N}_{s_i}$ is the set of sites neighboring s_i. $\mathcal{N}_{s_i}$ satisfies the following properties:

1. $s_i \notin \mathcal{N}_{s_i}$
2. $s_i \in \mathcal{N}_{s_j} \Leftrightarrow s_j \in \mathcal{N}_{s_i}$

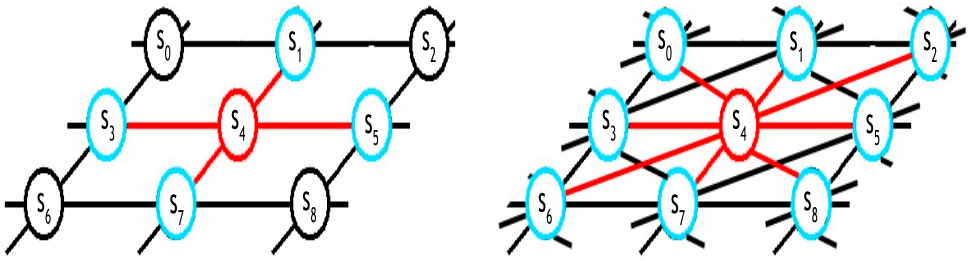

(a) (b)

Figure B.1: *Illustration of undirected graph with different neighborhood systems: 4-neighborhood (a) and 8-neighborhood (b).*

A 4-neighborhood system is generally enough (figure B.1.a). Higher neighborhood systems can be interesting in some cases, but are too much time consuming for a non significant improvement of the estimation in our case.

Let be $Q = \{Q_{s_i} | s_i \in G\}$ a set of random variables indexed by the site s_i in the graph G. In this set Q, each random variable Q_{s_i} takes a value q_{s_i} in Γ (also called state or label). Γ is called the space state of variable Q_{s_i}. The event for which Q_{s_i} takes the value q_{s_i} is noted $Q_{s_i} = q_{s_i}$. Similarly, the joint event is noted $Q = q$ where $q = \{q_{s_i} | s_i \in G\}$ is a configuration of Q corresponding to a realization of the random variable field. The set of all possible configuration q is Λ. The notation $Q_{G-\{s_i\}} = q_{G-\{s_i\}}$ denotes the joint event of the restricted set of Q containing all random variables except the one at site s_i. Probability of a random variable $P(Q_{s_i} = q_{s_i})$ is denoted $P(q_{s_i})$ for writing simplification, and similarly the joint probability $P(Q = q)$ is denoted $P(q)$.

Markov property: Q is called a MRF with respect to a neighborhood system $\mathcal{N}$ if and only if:

$$P(q) > 0 \quad \text{for all} \quad h \in \Lambda \tag{B.3a}$$

$$P\left(q_{s_i} \mid q_{G-\{s_i\}}\right) = P\left(q_{s_i} \mid q_{\mathcal{N}_{s_i}}\right) \tag{B.3b}$$

for all $s_i \in G$. $P(a|b)$ is the conditional probability of a given b. One interesting property of MRF concept is that any joint probability $P(q)$ satisfying equation B.3b is uniquely determined by the local characteristics $P\left(q_{s_i} \mid q_{\mathcal{N}_{s_i}}\right)$ [66] for which the configuration is $q_{\mathcal{N}_{s_i}} = \{q_{s_j} | s_j \in \mathcal{N}_{s_i}\}$.

B.2 MRF - Gibbs equivalence

Hammersley and Clifford theorem [66] states that any probability distribution $P(q)$ having the Markov property, equations (B.3), can be represented with the Gibbs

distribution, given an appropriate energy function E.

The Gibbs distribution gives the probability of the set of random variable Q having the configuration value q as:

$$P(q) = Z^{-1}\exp\left(-\frac{1}{T}E(q)\right) \tag{B.4}$$

where Z, called the partition function, is the normalizing term:

$$Z = \sum_{q\in\Lambda}\exp\left(-\frac{1}{T}E(q)\right) \tag{B.5}$$

where T is a constant called the temperature which controls the sharpness of the distribution. The more probable configurations q are those with the lower Gibbs energies $E(q)$. According to Hammersley and Clifford theorem, if

$$E(q) = \sum_{c\in\mathcal{C}} V_c(q) \tag{B.6}$$

where $V_c(q)$ is a potential function defined over clique c, the $P(q)$ is a MRF and satisfies MRF properties. A clique c is any fully connected subset of s in G. There is different order of cliques depending on the neighborhood system. The figure B.2 gives the different possible cliques for the regular grid graph G presented in figure B.1 for 4-neighborhood system (figure B.2.a) and 8-neighborhood system (figure B.2.b). For 4-neighborhood system we take into account the single-site $\mathcal{C}_1$ and the pair-site $\mathcal{C}_2$ cliques. For 8-neighborhood system, triple-site $\mathcal{C}_3$ and quadruple-site

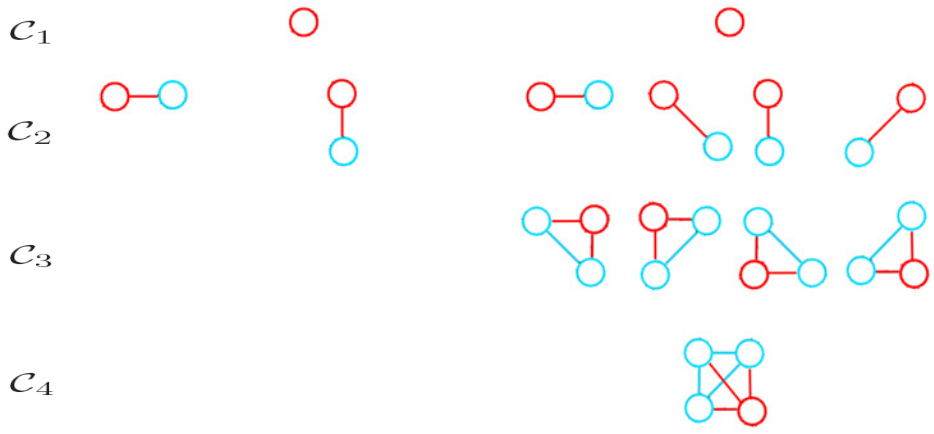

Figure B.2: *Illustration of cliques orders for 4-neighborhood (a) and 8-neighborhood (b). All possible cliques can be obtained by permutation of sites. From top to down: Single-site $\mathcal{C}_1$, pair-site $\mathcal{C}_2$, triple-site $\mathcal{C}_3$ and quadruple-site $\mathcal{C}_4$*

$\mathcal{C}_4$ cliques are possible. Moreover, there is also more possible pair-site cliques than with the 4-neighborhood system. As example, triple-site cliques are not possible with 4-neighborhood system, because all sites inside the cliques are not neighbors each others. The potential function $V_c(q)$ depends on the order of cliques c.

B.3 Gibbs energy functional

Most of the time, we have a known information called observation variable Y from which we want to extract a more meaningful unknown information Q as for example segmented region, classification from one image or optical flow from time image sequence.

We seek for the best configuration of q, denoted $\widehat{q}$, given the observation Y. Using Bayes rule decomposition:

$$P(q|Y) = \frac{P(Y|q)P(q)}{P(Y)} \tag{B.7}$$

where $P(Y)$ and $P(q)$ are prior probabilities and $P(Y|q)$ is the likelihood (conditional probability of Y given q). Y is given by the time image sequence. Thus, $P(Y)$ is a normalizing constant. Then, we have:

$$P(q|Y) \propto P(Y|q)P(q) \tag{B.8}$$

Using MRF-Gibbs property, we have:

$$P(q|Y) \propto \exp\left(-E(q,Y)\right) = \Pi_{c\in\mathcal{C}} P(q_c|Y_c) \tag{B.9}$$

where $Y \supset Y_c$ defined on clique c. Taking the negative log, we finally get:

$$\begin{aligned} E(q,Y) &= \log\left(P(Y|q)\right) + \log\left(P(q)\right) && \text{(B.10)}\\ &= E_d(q,Y) + E_s(q) && \text{(B.11)}\\ &= \sum_{c\in\mathcal{C}_1} E_d(q_c,Y_c) + \sum_{c\in\mathcal{C}_2} E_s(q_c) && \text{(B.12)} \end{aligned}$$

Energy E_d is called the data energy. It represents the cost of generating Y, knowing the configuration q. E_s is the regularization function corresponding to the cost of the configuration q. It is independent of Y but $q = \{q_{s_i} | s_i \in G\}$ where q_{s_i} are dependent each others. The Gibbs energy could be written with potential functions as (figure B.3 gives a representation of the potential functions on a graph for site s_4):

$$E(q,Y) = \sum_{s_i\in\mathcal{C}_1} V_d\left(q_{s_i}, Y_{s_i}\right) + \alpha \sum_{s_i,s_j\in\mathcal{C}_2} V_s\left(q_{s_i}, q_{s_j}\right) \tag{B.13}$$

where $s_j \in \mathcal{N}_{s_i}$. α is a weighting coefficient playing on the contribution of smoothness potential function V_s with respect to data potential function V_d.

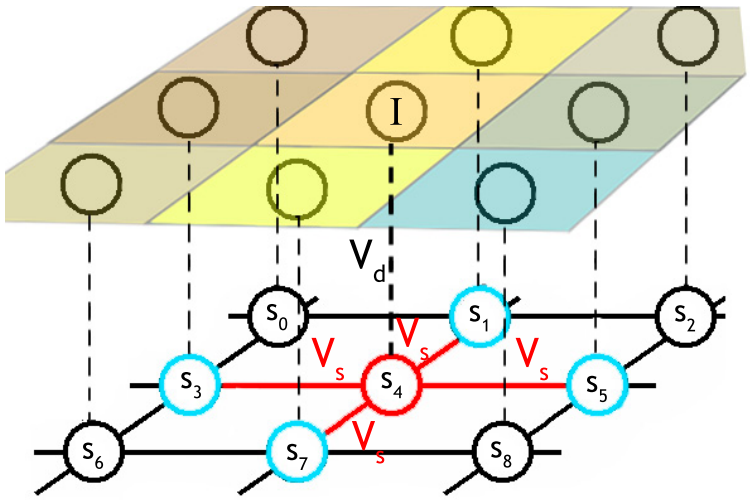

Figure B.3: *Representation of the MRF problem given an image. Dashed line shows the data potential functions V_d and the red line shows the smoothness potential functions V_s in our case of 4-neighborhood system.*

Our goal is to get $\widehat{q}$, the best configuration of q, that recovers the Maximum a Posteriori (MAP). From equation (B.4), it is equivalent to get the minimum of the Gibbs energy $E(q, Y)$. $\widehat{q}$ is defined as:

$$\widehat{q} = \arg\min_{q \in \Lambda} E\left(q, Y\right) \tag{B.14}$$

To obtain $\widehat{q}$, many optimization methods can be used [168]. In this work, we compare few of them and propose some improvement for Stereo Matching and OF approaches (see appendixes C and E).

Appendix C

Optimization Techniques

Problem formulation in computer vision is often modeled via an energy formulation. In this thesis, we use MRF-Gibbs framework to define this energy (appendix B). Solution of the problem correspond to the minimum of the defined energy E.

Energy minimization is often the key point of solving problems in computer vision. For decades, many methods have been proposed (deterministic, stochastic,...). Some can only reach local minimum and others strong local minimum close to the optimal solution (global minimum). Since beginning of 21^{th} century, minimization based on Graph theory have been generalized to find global minimum of multi-labeling problems which means that the random variable can take many different values.

In this work, we study deterministic local minimization methods (Iterated Conditional Modes and Direct Descent Energy), and a stochastic global minimization with an improved Simulated Annealing algorithm.

A new approach formulation to help local minimization to converge to a minimum closed to the global one is proposed. This method combines local and global energy constraints in an multigrid approach.

Results were compared to Graph theory algorithms on simple Stereo Matching application (see appendix D). In optical flow estimation, we also work on Graph Cuts using and adapting alpha-expansion algorithm to the hybrid multiresolution process in aim to get a finer discretized velocity estimate (see section E).

C.1 Iterated Conditional Modes - ICM

ICM [18] is a deterministic method that converges to a local minimum. It iteratively chooses the value (candidate) $q(s) \in \Gamma$ of the random variable $Q(s)$ which decreases the most the Gibbs energy $E(s)$ of each site s until convergence (see appendix B for MRF review). The value $q(s)$ is also called a label. As local methods, it extremely sensitive to initialization especially in high-dimensional spaces with non-convex energies. Experimentally, ICM generally proves to converge to a better minimum of the energy when it is initialized by the random field configuration q given the lowest data energy E_d cost ($min(E_d)$) (equation (B.12)). It has sense because ICM at each iteration selects the candidate minimizing the most the energy for each site according to neighbors states. Fixing all the random field to zero, the minimum of E is the minimum of E_d because the regularization energy E_s only depends on the random field (equation (B.12)). E_d is representing the problem to

solve, so the minimum of E_d is already a good approximation of the problem without spatial regularization.

ICM algo.1 details the minimization process. Y is some known observed quantity. s is a site of the graph G. s' is a neighbor of s ($s' \in \mathcal{N}_s$). $E^i(s)$ is the energy of a site s at loop iteration i. E_d and E_s are the data and regularization energies (equation (B.12)). $E^i_{total} = \sum_{s \in G} E^i(s)$ is the total energy over all pixels.

Our ICM implementation differs from [18] and Middlebury software ICM [168] by a rotation of site order iteration loop at each minimization iteration (algo.1 line.7) which proves to reach faster a better minimum and by an energy logical operator comparison $\leq$ (algo.1 line.12) which allows to go over plateau energy. Convergence of the algorithm is obtained when no configuration can be made, this results in same total energy value (summation of all image pixels) for two successive iterations (algo.1 line.16).

Algorithm 1: Iterated Conditional Modes Minimization

1 ***INITIALIZATION SET TO MIN***(E_d) ;
2 ***MINIMIZATION SCHEME***: **Iteration over** i ;
3 $i \leftarrow 0$;
4 **while** *Stop Condition NON Satisfied* **do**
5 $i \leftarrow i + 1$; $\mathbf{E}^i_{total} \leftarrow 0$;
6 **foreach** *site* $s \in G$ *(minimization)* **do**
7 *(Permutation of site listing way at each loop)* ;
8 $q^i(s) \leftarrow q^{i-1}(s)$;
9 $\mathbf{E}^{i-1}(s) \leftarrow Ed(Y(s), q^{i-1}(s)) + \alpha Er(q^{i-1}(s), q^{i-1}(s'))$;
10 **foreach** *label* $q \in \Gamma$ **do**
11 $\mathbf{E}^i(s) \leftarrow Ed(Y(s), q) + \alpha Er(q, q^{i-1}(s'))$;
12 **if** $(\boldsymbol{E}^i(s) \leq \boldsymbol{E}^{i-1}(s))$ **then**
13 $\mathbf{E}^{i-1}(s) \leftarrow \mathbf{E}^i(s)$;
14 $q^{i-1}(s) \leftarrow q^i(s) \leftarrow q$;
15 $\mathbf{E}^i_{total} \leftarrow \mathbf{E}^i_{total} + \mathbf{E}^{i-1}(s)$;
16 **if** $(\boldsymbol{E}^i_{total} = \boldsymbol{E}^{i-1}_{total})$ **then** Go to 17 **else** Retour in 4 ;
17 ***FINISH*** ;

C.2 Direct Descent Energy - DDE

Classical Direct Descent Energy (DDE) is a variant of the gradient descent algorithm. It is based on a random generation of label candidate q in Γ for each site. The candidate is selected if it decreases the energy. This method is still sensitive to initialization. We propose an improvement of DDE method. Algo 2 details the minimization process. First, to find the best match for a site at an iteration, we generate N times a non repetitive random candidate and choose the one that minimizes the best $E(s)$ for site s (algo.2 line.8-13). This proved to converge faster to a better minimum. Second, we use a logarithmic increasing function for α from 0 to

α_0 depending on iteration i (algo.2 line.16).

$$\alpha(k) = \alpha_0 \left(1 - e^{-b\,i}\right) \tag{C.1}$$

b is a coefficient that defines the increasing speed of α. In this way, we first satisfies the data energy E_d then constraints it more and more by regularization energy E_s. Thus, improved DDE is not very sensitive to initialization.

Iteration is done until convergence. Because of random generation of candidate, it is possible to have an iteration with no diminution of energy that is not representative of the real convergence of the algorithm. Convergence criterium is little changed compare to ICM. Convergence is obtained when 20 successive decreased energy quantities are inferior to a threshold ε. Number of 20 has been chosen empirically to satisfy compromise between enough iterations to allow possible apparition of candidate q decreasing the energy E and not too much iterations in regard to the computational time. Parameter ε allows to play on the rigorousness of the convergence. $\varepsilon = 0$ corresponds to a full convergence, no decreasing of energy over the last 20 iterations. $\varepsilon \neq 0$ allows to stop faster the algorithm in a state very close to the full convergence (algo.2 line.18).

Algorithm 2: Direct Energy Descent Minimization

1 ***MINIMIZATION SCHEME***: **Iteration over** i ;
2 $i \leftarrow 0$; $\alpha(i) \leftarrow 0$; *stop* $\leftarrow 0$;
3 **while** *Stop Condition NON Satisfied* **do**
4 $i \leftarrow i + 1$; $\mathbf{E}^i_{total} \leftarrow 0$;
5 **foreach** *site* $s \in G$ *(minimization)* **do**
6 $q^i(s) \leftarrow q^{i-1}(s)$;
7 $\mathbf{E}^{i-1}(s) \leftarrow Ed\left(Y(s), q^{i-1}(s)\right) + \alpha(i) Er\left(q^{i-1}(s), q^{i-1}(s')\right)$;
8 **foreach** n *from* 0 *to* N **do**
9 Random non-repetitive generation of $q \in \Gamma$;
10 $\mathbf{E}^i(s) \leftarrow Ed\left(Y(s), q\right) + \alpha(i) Er\left(q, q^{i-1}(s')\right)$;
11 **if** $(\boldsymbol{E}^i(s) \leq \boldsymbol{E}^{i-1}(s))$ **then**
12 $\mathbf{E}^{i-1}(s) \leftarrow \mathbf{E}^i(s)$;
13 $q^i(s) \leftarrow q$;
14 $q^{i-1}(s) \leftarrow q^i(s)$ (updating) ;
15 $\mathbf{E}^i_{total} \leftarrow \mathbf{E}^i_{total} + \mathbf{E}^{i-1}(s)$;
16 $\alpha(i) \leftarrow \alpha_0 \left(1 - e^{-bi}\right)$;
17 **if** $(\boldsymbol{E}^{i-1}_{total} - \boldsymbol{E}^i_{total} < \varepsilon)$ **then** *stop* $\leftarrow$ *stop* $+ 1$ **else** *stop* $\leftarrow 0$;
18 **if** $(stop > 20)$ **then** Go to 19 **else** Return in 3;
19 ***FINISH***;

A hierarchical global to local constraints approach is proposed in section C.4 to help local minimization to not be trapped into local minima. In this case, DDE minimization uses logarithm increasing coefficient only at the coarsest level. Then, the weighting coefficient is constant α_0 because the estimation at coarser level $k+1$ is used as initialization at level k.

C.3 Simulated Annealing - SA

Deterministic methods as ICM and DDE stuck into local minima due to the fact that the energy $E(s)$ of a site can only be decreased. These methods find a minimum of energy for each site. In most of cases, the minimum of the total energy is not equal to the summation of the minimum of site energies satisfying a neighborhood configuration of the random field. This is due to the fact that we have an energy cost depending on this neighborhood. To keep converging toward the global minimum, these algorithms should consider the possibility of an increase of the energy allowing a change of the random field configuration which could lead to a better minimum.

Simulated Annealing (SA) (Kirkpatrick [85], Geman [66], Bernard [13]) is an adaptation from Metropolis algorithm [109] to combinatory optimization problem. Algo 3 details the algorithm of the proposed SA in this paper. SA considers possibility of a validation of candidate that increases $E(s)$ at iteration i depending on the following condition (algo 3 line.18-19):

$$\mathcal{U} \leq e^{\left(-\frac{E^i(s)-E^{i-1}(s)}{T(i)}\right)} \tag{C.2}$$

$\mathcal{U}$ is an uniform random value in $[0:1]$. $E^i(s) - E^{i-1}(s)$ is the energy quantity difference between new candidate energy and previous validated candidate energy for the site s. $T(i)$, called "Temperature", represents the selection control parameter of the decreasing energy from the equilibrium point ("freezing point") around this temperature. For $T = 0$, we retrieve DDE algorithm. To converge to strong local minimum close to the optimal, T has to be a decreasing function that slowly decrease around the freezing point. Many functions have been proposed, Geman [66] proposed a logarithmic decreasing function:

$$T(i) = \frac{b}{ln(1 + a\ i)} \tag{C.3}$$

Theoretically, to converge to the optimal solution, T has to slowly decrease to let the algorithm time to find the most stable state for each T. For computational point of view, it will require an infinity of time. In practice, decreasing of T function is set to make compromise between slow decreasing to get the best minimum and fast enough decreasing for a correct computational time. Convergence criteria of SA is reached in this paper when relative decreasing variation of E over the last 20 iterations is inferior to a threshold limit ($\varepsilon = 10^{-8}$) as described in DDE section. The temperature at convergence is then T_{conv}.

Considering a slow decreasing T function, most of the combinatory optimization problem is solved around a certain freezing point (T_c) depending on the random field discretization and the data and regularization energy cost ranges. After what, improvement of random field configuration are fewer with smaller impact on the energy decreasing. Keeping iteration process on Geman T function till $T = 0$ is high time consuming comparing to the minimization improvement. However when convergence criterium is satisfied $T = T_{conv} \neq 0$, SA returns a good minimum close

to the optimal solution but this minimum can easily be improved till $T = 0$. We propose to change T function by adding a second phase to the logarithm decreasing after the algorithm has converged at T_{conv}. Considering the same convergence criteria, T become an decreasing erf function from T_{conv} to 0 converging to the best local minimum from the one reached for T_{conv} (algo 3 line.5). Final convergence is obtained when there is no site changing random value (algo 3 line.27-28). Figure C.1 gives an illustration of the T function over iterations. In this paper, b and a, the decreasing coefficients of the logarithm T function are empirically defined to slowly decrease around T_c, then at T_{conv} decreasing coefficients of the inverse erf function are automatically computed from T_{conv} and number of iteration i at T_{conv}. Further work on optimal T_c parameter computation from the energy definition is interesting.

Algorithm 3: Simulated Annealing Minimization

1 ***MINIMIZATION SCHEME***: **Iteration over** i ;
2 $i \leftarrow 0$; $stop \leftarrow 0$; $n_{sleep}(s) \leftarrow 0$;
3 **while** *(Stop Condition NON Satisfied)* **do**
4 $\quad i \leftarrow i + 1$; $\mathbf{E}^i_{total} \leftarrow 0$;
5 $\quad$ **if** *(1^{st} phase T)* **then** $T(i) = b/ln(1 + a\ i)$ **else** $T(i) = -erf(f(i, T_{conv}))$;
6 $\quad$ **foreach** *(site $s \in G$ (minimization))* **do**
7 $\quad\quad q^i(s) \leftarrow q^{i-1}(s)$;
8 $\quad\quad$ **if** *($n_{sleep}(s) > n_c$ (s asleep))* **then**
9 $\quad\quad\quad$ **if** *($q^{i-1}(s')$ changed)* **then** $n_{sleep}(s) \leftarrow 0$ (wake up s) ;
10 $\quad\quad$ **if** *($n_{sleep}(s) < n_c$ (s awake))* **then**
11 $\quad\quad\quad n_{sleep}(s) \leftarrow n_{sleep}(s) + 1$;
12 $\quad\quad\quad \mathbf{E}^{i-1}(s) \leftarrow Ed\left(Y(s), q^{i-1}(s)\right) + \alpha Er\left(q^{i-1}(s), q^{i-1}(s')\right)$;
13 $\quad\quad\quad n \leftarrow 0$;
14 $\quad\quad\quad$ **while** *($n < N$ & $n_{sleep}(s) \neq 0$)* **do**
15 $\quad\quad\quad\quad n \leftarrow n + 1$;
16 $\quad\quad\quad\quad$ Random non-repetitive generation of $q \in \Gamma$;
17 $\quad\quad\quad\quad \mathbf{E}^i(s) \leftarrow Ed\left(Y(s), q\right) + \alpha Er\left(q, q^{i-1}(s')\right)$;
18 $\quad\quad\quad\quad$ Random generation of uniform value $\mathcal{U} \in [0, 1]$;
19 $\quad\quad\quad\quad$ **if** $\left(\mathcal{U} < exp\left(-\frac{\mathbf{E}^i(s) - \mathbf{E}^{i-1}(s)}{T(i)}\right)\right)$ **then**
20 $\quad\quad\quad\quad\quad \mathbf{E}^{i-1}(s) \leftarrow \mathbf{E}^i(s)$;
21 $\quad\quad\quad\quad\quad q^i(s) \leftarrow q$;
22 $\quad\quad\quad\quad\quad n_{sleep}(s) \leftarrow 0$;
23 $\quad\quad\quad q^{i-1}(s) \leftarrow q^i(s)$ (updating) ;
24 $\quad\quad \mathbf{E}^i_{total} \leftarrow \mathbf{E}^i_{total} + \mathbf{E}^{i-1}(s)$;
25 $\quad$ **if** *($|\boldsymbol{E}^{i-1}_{total} - \boldsymbol{E}^i_{total}| < \varepsilon$)* **then** $stop \leftarrow stop + 1$ **else** $stop \leftarrow 0$;
26 $\quad$ **if** *($stop > 20$)* **then**
27 $\quad\quad$ **if** *(1^{st} phase T)* **then** Pass to 2^{nd} phase T ; $\varepsilon \leftarrow 0$; Go to 3 ;
28 $\quad\quad$ **else** Go to 30 ;
29 $\quad$ **else** Return in 3 ;
30 ***FINISH*** ;

Another improvement is the candidate selection and speed up of the iteration loop. At iteration i for site s, candidate is non repetitively and randomly generated over the range set as for Improved DDE (algo 3 line.13-16). But main difference is

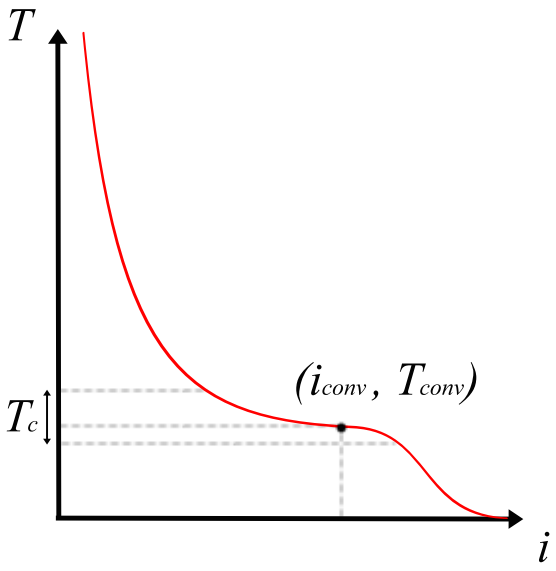

Figure C.1: *Temperature function T over iteration i for improved SA. For visualization, scales don't correspond to reality. 1^{st} decreasing phase in much longer than the 2^{nd} phase.*

that SA does not select the candidate that minimizes the maximum $E(s)$ but select the first candidate that satisfies equation C.2 (algo 3 line.14). $n_{sleep}(s) \neq 0$ means that a candidate has satisfied the validation condition (algo 3 line.22). In this way, at each iteration, we have less rejected candidate. This process allows to reach a better configuration state but increase inside loop computational time around the freezing point. In the other way, a site can be put in a sleeping state if its random value didn't change for n_c successive iterations (algo 3 line.8&11). Thus, it becomes outside minimization process and it can be waking up if a neighbor site changes random value (algo 3 line.9&10). This does not affect the final minimum because of the SA algorithm property of small move minimization but it significantly makes the algorithm faster. We call, the proposed SA method, Improved SA.

C.4 From Global to Local Constraints

Because local minimization strongly depend on the quality of the initialization, the idea was to solve the energy function in an iterative process from local to global constraints.

Local constraints consist to define an interrogation window $\mathcal{W}$ of size $N_{\mathcal{W}} \times N_{\mathcal{W}}$ for which all site s of $\mathcal{W}$ will have the same label $q_{\mathcal{W}}$. The best configuration of $q_{\mathcal{W}}$ represents the dominant disparity over $\mathcal{W}$. More $\mathcal{W}$ is large more the solution is parse but more it is robust.

The global constraints is the smoothness term E_s, it consists to constraint the disparity distribution by a defined function over the all image domain linking neigh-

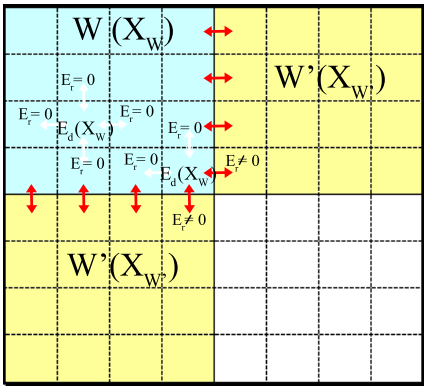

Figure C.2: *Illustration of FLTG energy on an* 8×8 *image with* 4×4 *interrogation window* $\mathcal{W}$.

bor sites.

Coupling local and global constraints, smoothness term is only non-null at borders of 2 interrogation windows $\mathcal{W}$ and $\mathcal{W}'$. The total energy becomes:

$$E(I, q_{\mathcal{W}}) = \sum_{s \in \mathcal{W}} E_d(I(s), q_{\mathcal{W}}) + \alpha \sum_{s \in \mathcal{W}, s' \in \mathcal{W}'} E_s(q_{\mathcal{W}}, q_{\mathcal{W}'}) \tag{C.4}$$

Figure C.2 shows an illustration of the image energy for $\mathcal{W} = 4 \times 4$ on a 8×8 pixel image. $\mathcal{W}$ is on the top left of the image. Its neighbors are $\mathcal{W}'$. Inside $\mathcal{W}$, each pixel has a data energy term of $E_d(I(s), q_{\mathcal{W}})$. Only pixels on the border ($\sum_{s \in \mathcal{W}, s' \in \mathcal{W}'}$) of $\mathcal{W}$ have non-null smoothness terms $Es(q_{\mathcal{W}}, q_{\mathcal{W}'})$ represented by red arrows. Everywhere else, smoothness terms in white arrows are equal to zero.

From local to global constraints (FLTG) method starts the process with $\mathcal{W}$ of image size. Only 1 disparity is obtained for the all image ($E_s = 0$). All the energy is governed by local constraint. Then, $\mathcal{W}$ is reduced by scale of 2 till $\mathcal{W}$ reach the pixel size. When going down in the process $\mathcal{W}$ getting smaller, the local constraint get less important regarding to the global constraint influence. At the last step, $\mathcal{W}$ is of size of a pixel, the energy is finally governed by the global constraint E_s. At each step of the FLTG method, energy is minimized by local minimization ICM (FLTG-ICM) or DDE (FLTG-DDE).

The proposed FLTG method allows to local minimization to reach local minimum close to the global minimum keeping the advantage of slow computational time of ICM and DDE. It is not interesting to apply FLTG method to global minimization because global minimum can be directly obtained at pixel size. FLTG may, however, be used to reduce the computational time of global minimization (illustration in appendix F.2).

Appendix D

Optimization Validation on Stereo Matching

Stereo Matching is a simple case, where each pixel of an image is matched to its correspondent in the other image. The distance separating a pixel with its correspondent is called disparity. Thus, we are looking to the best disparity map allowing to recover every pixel displacement between both images. Most of the time stereo pair images are rectified where horizontal lines are epipolar lines which reduce the displacement dimension from 2D to 1D (horizontal displacement) and in a simplified case displacements are integer value representing the distance in term of pixels. And in the case of fixed scene, the displacement only takes value in one direction from 0 to d_{max}. For all of this, number of possible value of our random variable d (number of label) is limited and strongly discretized. Minimizations based on Graph theory are very efficient. It is for that we proposed, here, to compare our minimization algorithms to these graph minimization on this kind of problem. For optical flow estimation where random variable is 2D real value, number of label is much higher, than our minimization will naturally be less affected by this condition than graph minimizations. Formalization of stereo matching problem is done using MRF framework with the definition of Gibbs energy as explained in appendix B.

D.1 Stereo Matching Equation Formulation

We assume that stereo pair images are rectified where horizontal lines are epipolar lines. Data $Y(s)$ is the observed image intensity $I(s)$ and random variable field $Q(s)$ is the disparity field $d(s)$. Site s is image pixel (x, y) ($\Omega = dim(I)$). $d(s) \in [0 : L[$ is the horizontal integer distance in pixel between a site s on the left image $I^L(s)$ and its corresponding site on the right image $I^R(s + d(s))$. Data term E_d (equation (B.12)) is the simple absolute difference between corresponding sites for each disparity:

$$E_d(I, d) = \sum_{s \in \mathcal{C}_1} \sum_{color} \left| I^L(s) - I^R(s + d(s)) \right| \tag{D.1}$$

$\mathcal{C}_1$ is the single site clique (appendix B.2) corresponding to Ω. Variant formulation of E_d difference computation proposed by Birchfield and Tomasi [19] can be used in our model. Linear interpolation of intensity distributions around a site is calculated to reduce sensitivity of the integration of light intensity over the site area by the camera. Indeed due to camera sampling and material, intensity can be interpreted differently from one image to the other by the camera.

In this paper and like in [168], we consider that different pairings of neighbor disparities can lead to different costs. The smoothness term can be written as:

$$E_s(d) = \sum_{s,s' \in \mathcal{C}_2} \alpha.\beta_{ss'} \; . \; min\left(\Phi\left(\left|d(s) - d(s')\right|\right), V_{max}\right) \tag{D.2}$$

$\mathcal{C}_2$ is the pair-site clique defined by (s, s') for all s and $s' \in \mathcal{N}_s$ (appendix B.2). Φ is L1 or L2 norm. V_{max} allows to truncate the smoothness term.
If $V_{max} = 1$, it becomes Potts function. $\beta_{ss'}$ is a per-pairing weight defined as:

$$\beta_{ss'} = \begin{cases} \gamma & \text{if } |I^L(s) - I^L(s')| < \gamma_{threshold} \\ 1 & \text{else} \end{cases} \tag{D.3}$$

γ is a positive constant coefficient weight transforming the smoothness term in an anisotropy image driven function if left image gradient between s and s' is inferior to a threshold value $\gamma_{threshold}$.

Solution of the stereo matching problem will be given by the best disparity configuration field that minimize the most the defined energy (equation (B.14)).

D.2 Results on Middlebury Stereo Benchmark

Middlebury Stereo Benchmark ([143, 144]) is a dataset of many different stereo image pairs with different characteristics. The benchmark has been done to help comparison of state of the art approaches on identical stereo image pairs. Different statistical errors are computed and an on-line approach performance table is available on `http://vision.middlebury.edu/stereo/eval/`.

D.2.1 Evaluation Methods

We decide to compare our minimizations on four stereo image pairs of this data set. Figure D.1 shows the four stereo image pairs: a) Tsukuba, b) Venus, c) Teddy, d) Cones for which left and right images are represented in the two first columns. The third column give the ground truth which is the exact disparity map. The different gray colors represent different disparities (displacements) in pixel.

Results are also compared with an open source software from [168] available on `http://vision.middlebury.edu/MRF/code/` that contains Graph based minimization algorithms and for which validation has been published. Time consuming and final minimum convergence are compared between algorithms.

As we got the exact disparity map for each sequence, we may compute statistical errors. For that, we use the proposed statistical error definition in [143] which compute the percentage of bad matching pixel, (statistical errors are computed from our disparity map by routine of middlebury stereo team and comparisons are then more objective)

$$Err_{\%} = 100 * \frac{\sum_{s \in \Omega} \left(|d_e(s) - d_c(s)| > \delta_d\right)}{\sum_{s \in \Omega} 1} \tag{D.4}$$

where δ_d is a disparity error tolerance in pixel. For the following results $\delta_d = (0.5; 1; 2)$. In case of $\delta_d = 0.5$, as our disparity discretization is integer value in pixel, it means the percentage of wrong matching pixel without tolerance. Ω is the domain on which we want to compute the statistical errors. As in the middlebury benchmark, we use three different area where to compute $Err_{\%}$, which are defined by different masks shown in Figure D.2. The interest domain is represented by white area. Different masks are focus on different characteristic area of the image as:

- All the image domain (Figure D.2.1 *all*) without borders for Tsukuba and Venus sequence
- Non-occluded regions (Figure D.2.2 *nonocc*)
- Regions near disparity discontinuities (Figure D.2.3 *disc*)

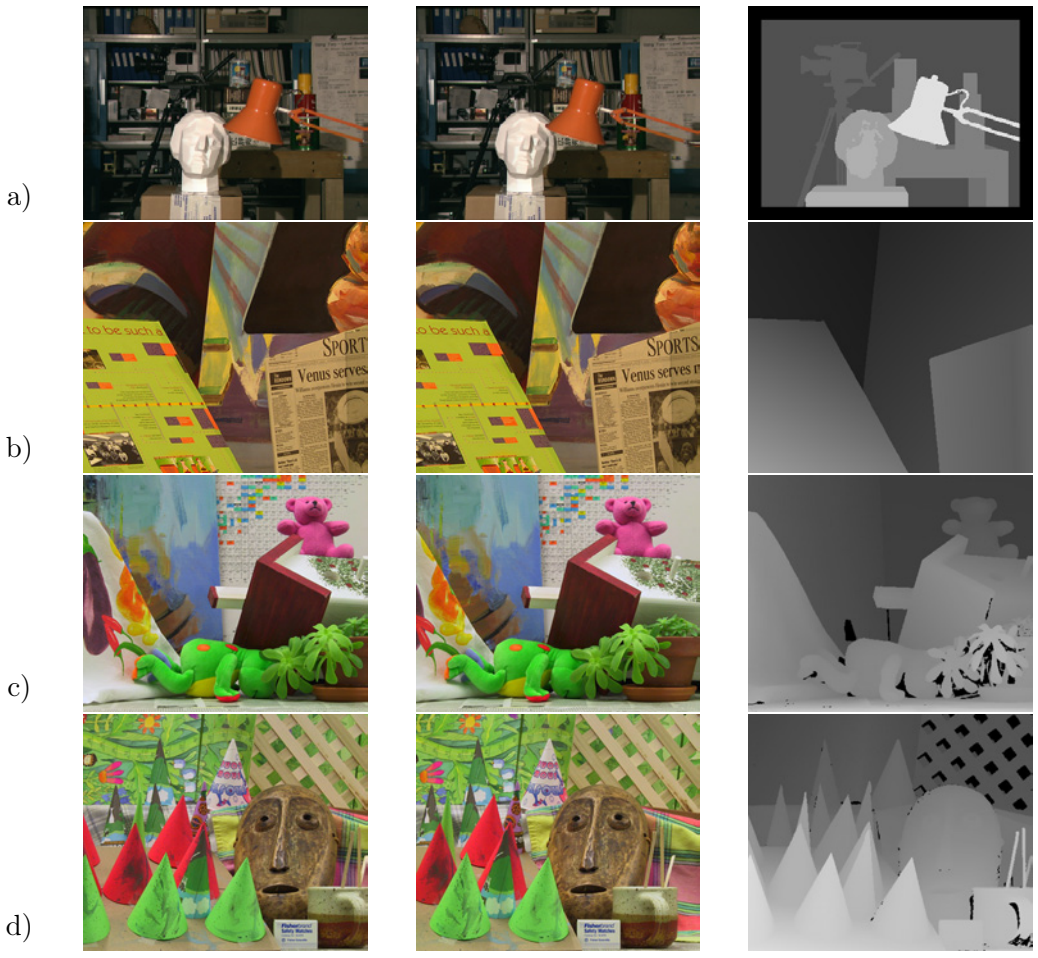

Figure D.1: *Stereo image pairs: a) Tsukuba, b) Venus, c) Teddy, d) Cones. Column from left to right: left input image, right input image, corresponding ground truth (disparity map).*

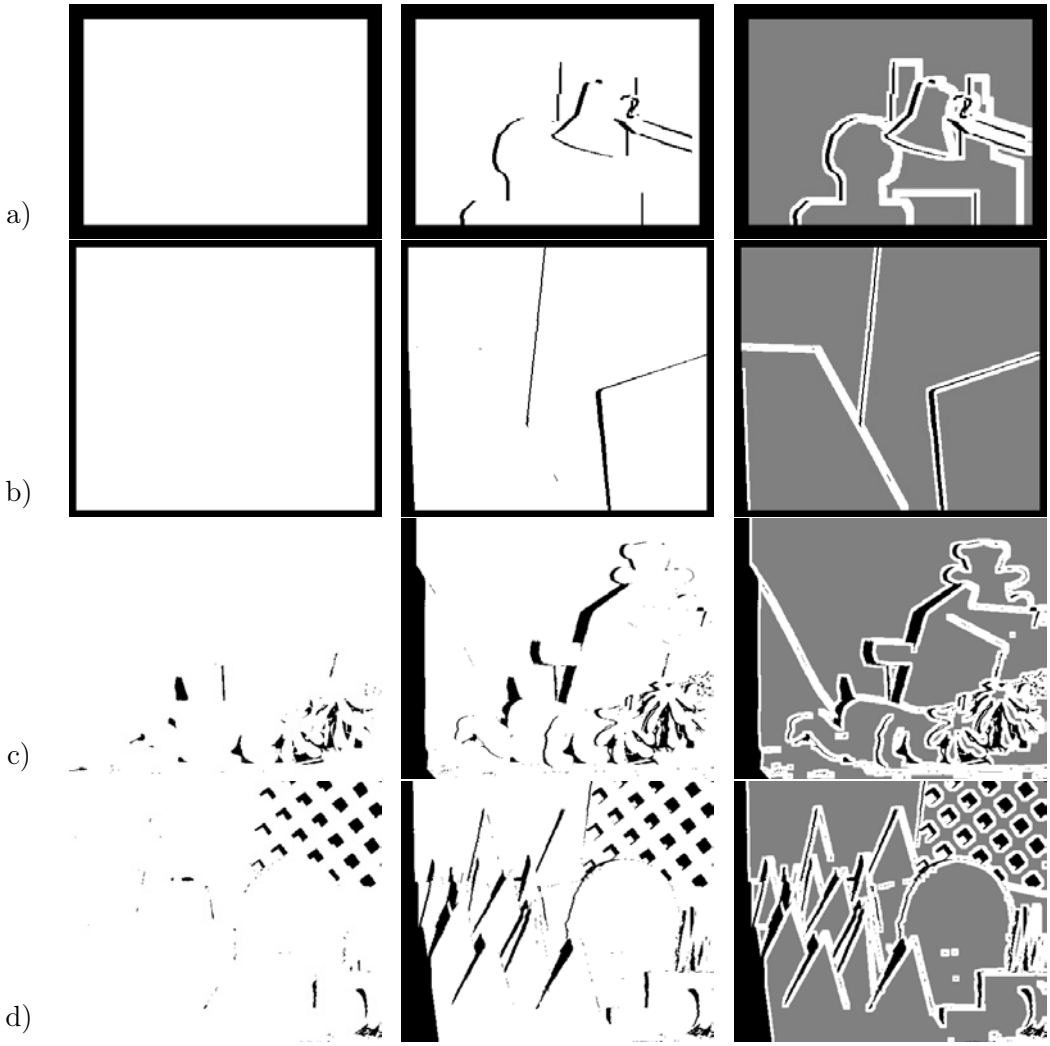

Figure D.2: *Tsukuba (a), Venus (b), Teddy (c) and Cones (d) masks use for computing $Err_{\%}$ for different regions of interest (in white): 1) all: all the image domain, 2) nonocc: non-occluded regions, 3) disc: regions near disparity discontinuities.*

Moreover for accuracy generalization different energy definitions (data and regularization) are set for Tsukuba, Venus and Teddy and compare with Graph based minimization methods as illustrated in [168]. All results and running times presented below were obtained on a 1.73GHz Pentium 4 with 2 Gbyte RAM.

D.2.2 Improved DDE and SA

Here, we test DDE and SA minimization on Tsukuba image. The energy function is E_d using Birchfield and E_s using L1 norm truncated at $V_{max} = 2$. $d_{max} = 16$ ($dim(\Gamma) = nbL = 16$) and $\alpha = 20$.

Improved DDE

In Figure D.3, we illustrate the disparity maps obtained by classical DDE and Improved DDE for different initializations: $d(s) = 0$ (a), configuration of $d(s)$ given the minimum of the data energy E_d (equation (D.1)) (b), random $d(s)$ (c), for all $s \in \Omega$. For Improved DDE, $b = 1$ in α function. Classical DDE is clearly sensitive to initialization compare to Improved DDE. Moreover, Improved DDE disparity maps are spatially smoother and better than classical DDE.

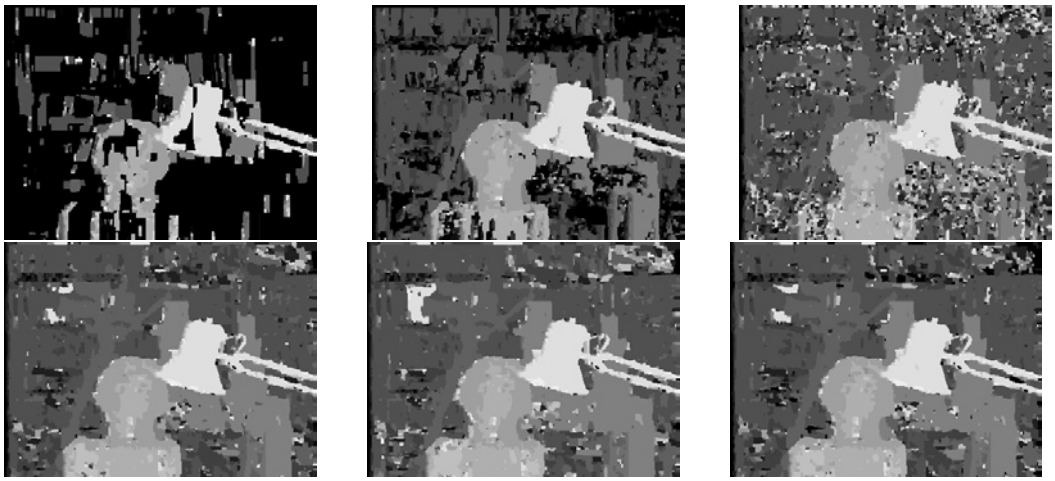

(a) Init null (b) Init $min(E)$ (c) Init random

Figure D.3: *Estimated disparities for Classical DDE (top) and Improved DDE (bottom) for different initializations (columns).*

Figure D.4 shows improvement of energy minimization when using non repetitive generation of candidate. Figure D.4.a plots the total energy function E_{total} along the time t and figure D.4.b plots the number of pixels which changed disparity value. The best minimization of the energy is obtained when at each site, candidate is randomly generated over the all discretization domain (here $nbL = 16$). It reduces convergence time consuming by almost a factor 2 and energy minimum about 20 % compare to one candidate generation at each iteration. If using a constant weighting coefficient, the improved DDE is similar to ICM but the main difference is that candidate generation is random, while in ICM it is incrementally done from 0 to d_{max}. It means that because there is a lot of local minima of the energy, random generation process of potential candidate and site order iteration loop allow to go over some of them.

This proposed improved DDE gives a better minimum than classical DDE and

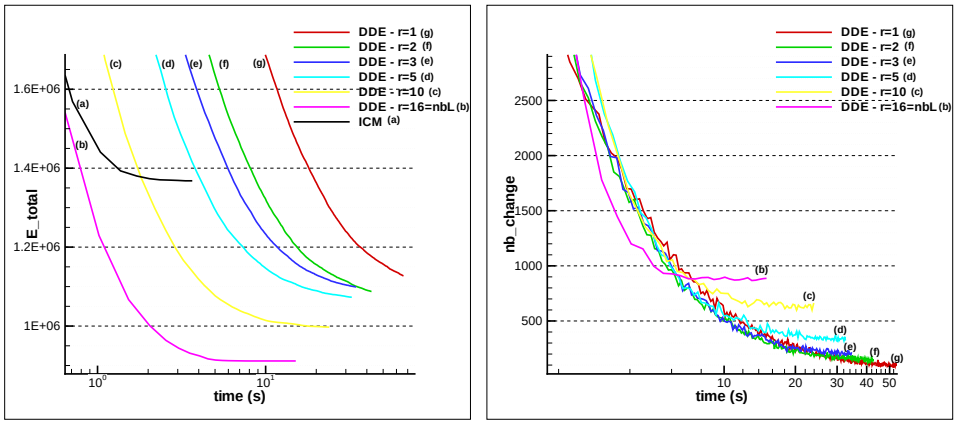

(a) (b)

Figure D.4: *Comparison of the energy minimization for Improved DDE for different repetition numbers (1, 2, 3, 5, 10, nbL) and ICM (a) and evolution of number of changed label at each iteration (b) over the time.*

converge faster. However, final convergence always get stuck in a strong local minima compared to global minimization methods (see section D.2.4).

Improved SA

Figure D.5 shows SA algorithm disparity map estimations: SA-Geman (a) and Improved SA (b). For these algorithms, T logarithmic parameters are $b = 30$ and $a = 0.01$. The erf decreasing function for Improved SA is automatically parametrized by convergence of the first temperature phase. Sleeping condition is $n = 5$ successive times non changing labeling. Improved SA find better minimum than SA-Geman. The estimated disparity map is closer to the ground truth (Figure D.1.a).

We also compare improved SA to the SA algorithm proposed by [167] (paper and open source). For this, we set the same energy definition as indicated in [167]: E_d is the simple quadratic intensity difference without Birchfield formulation and E_r is the Potts model ($V_{max} = 1$). $d_{max} = 16$ and $\alpha = 500$. For Improved SA, $b = 800$, $a = 0.2$ and $n = 5$. Figure D.6a illustrates Improved SA disparity map and the table (figure D.6b) shows number of pixel error where difference between estimated and true disparity is superior or equal to 1 pixel. Our SA error is almost 2 times smaller. Improvement made in algorithmic and in T function definition proved to help the minimization to converge to better minimum closer to the optimal solution.

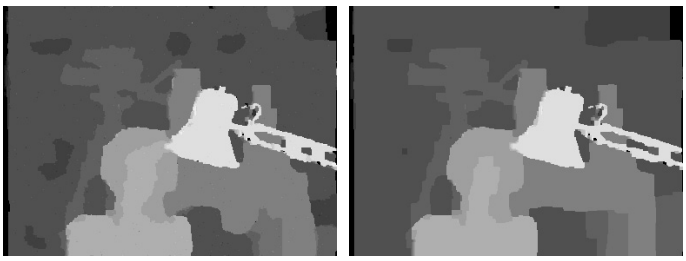

(b) SA-Geman (c) Improved SA

Figure D.5: *Estimated disparities for SA methods: Geman function (a), improved SA (b).*

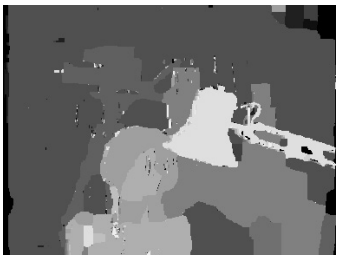

(a) Improved SA

# errors ($\geq \pm 1$)	Total pixels
Image	$84,863$
Annealing [167]	$4,244$
Improved SA	$2,561$

(b) Estimated disparities errors

Figure D.6: *Results of improved SA (a) using same equation and parameters than in [167] (without Birchfield [19] with Potts smoothness term). Number of estimated label error $\geq \pm 1$ (b).*

D.2.3 FLTG and local minimizations

FLTG method proves to improve a lot the performance of local minimization ICM and DDE. To evaluate the energy minimization please refer to next section D.2.4. Here, we illustrate in Figure D.7, the disparity map obtained by FLTG-DDE at different steps for the height of $\mathcal{W} = \text{Image}, 72, 18, 4, 1$ pixels and we compare it to normal DDE. FLTG allows to not be stuck into local minima as happened for DDE. The robustness of local constraints for large $\mathcal{W}$ help the minimization to get good initialization till the pixel resolution. The influence of global constraint when $\mathcal{W}$ gets smaller allows to keep a spatial coherency of disparity distribution. The estimated disparity map obtained by FLTG-DDE is pretty close to the one from SA and global minimization. FLTG method tends to over smooth the disparity field. However, this problem can be reduce with another neighborhood connexity definition or with overlying interrogation windows.

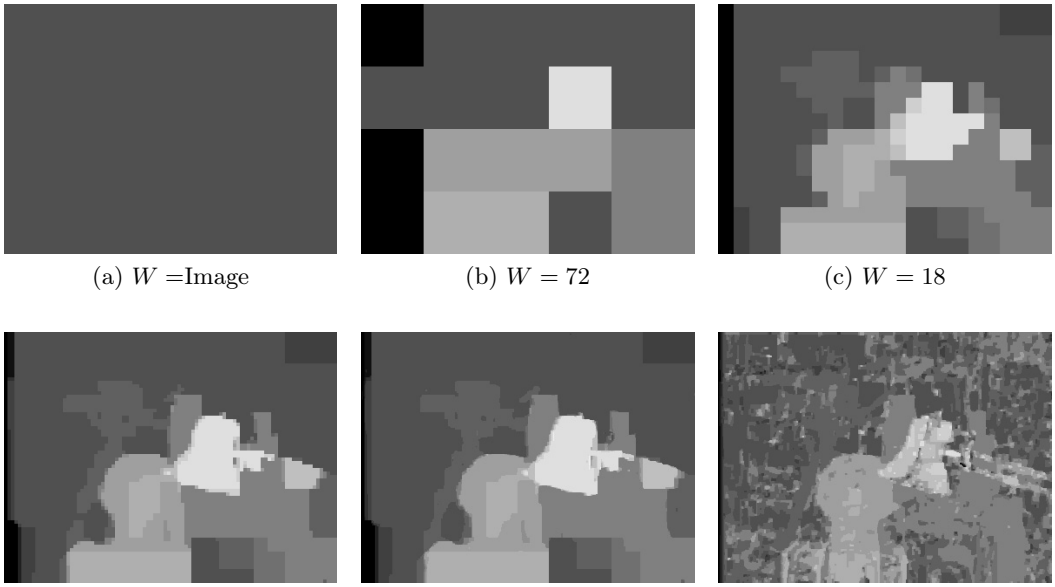

(a) W =Image (b) $W = 72$ (c) $W = 18$

(d) $W = 4$ (e) Final FLTG-DDE (f) DDE

Figure D.7: *Illustration of disparity map for different step* $\mathcal{W} = Image, 72, 18, 4, 1$ *for FLTG-DDE compare with normal DDE.*

D.2.4 Comparison with graph minimizations

Using the soft developed by [168], we test the Graph based methods: Graph Cuts methods (GC-swap and GC-expansion) [25], Max-Product Loopy Belief Propagation (BP-S and BP-M) [58] and Tree-Reweighted Message Passing (TRW-S) [176]. As illustrated in the paper, we complete the comparison study with our proposed approaches on the same stereo images (Figure D.1) with the same parameters. To be sure that we have the same energy formulation, we insert in our implementation GC-swap and GC-expansion algorithms and we retrieve exactly the same results as illustrated in the paper.

- For Tsukuba, $d_{max} = 16$ labels, Φ is L1 norm, $V_{max} = 2$, $\alpha = 20$ and $\beta_{ss'} = 2$ if $|I_s^L - I_{s'}^L| \leq 8$.
- For Venus, $d_{max} = 20$, Φ is L2 norm, $V_{max} = 7$, $\alpha = 50$ and $\beta_{ss'} = 1$.
- For Teddy, $d_{max} = 60$, Φ is L1 norm, $V_{max} = 1$, $\alpha = 10$ and $\beta_{ss'} = 3$ if $|I_s^L - I_{s'}^L| \leq 10$.

Figure D.8 shows the relative energy to the maximum lower bound achieved by TRW-S algorithm of minimization over the time till convergence for each methods. For this three stereo images with different energy configuration, we can tell similar conclusion of the efficiency of minimization methods. For local minimization, DDE always find better minimum than ICM. They are fast but converge to local minimum far from the optimal solution.

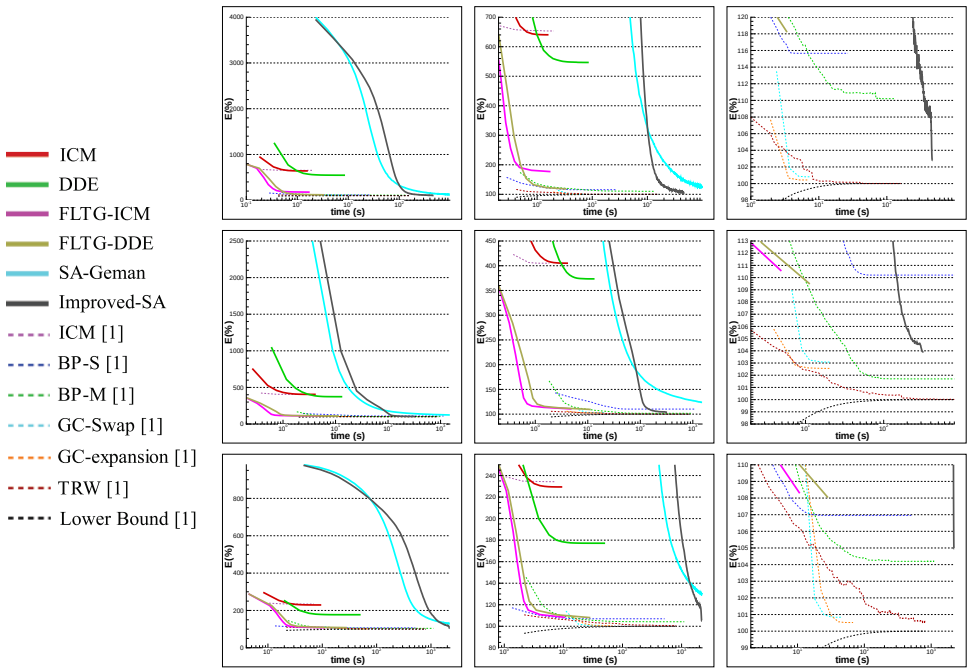

Figure D.8: *Relative energy (to maximum lower bound) over runtime axis (log-scale) for minimization methods on Tsukuba (a), Venus (b) and Teddy (c) images with different energy definitions. From left to right, same plot with different zooms.*

FLTG-ICM and FLTG-DDE minimize much more the energy than ICM and DDE from $E(\%)$ around few hundreds to an $E(\%)$ around 100 %. The FTLG method is very efficient and adapted to local minimization algorithms. FLTG-DDE still get a smaller energy than FLTG-ICM. The final energy for FLTG-DDE is has good ad BP-S. FLTG brings local minimization performance close to the global minimization and Graph based methods.

For global minimization, proposed SA gives always smaller minimum than Geman SA. Moreover it converges to global minimum for the three images around $E(\%) \approx 100$ % as GC, BP and TRW. It even gives better results than BP-S and sometimes BP-M. However, SA is clearly too much time consuming compare to Graph methods even if improved SA is faster than SA-Geman. But SA algorithm has advantage to be easily adaptable to every kind of data and smoothness terms and to high number of labels because it minimizes iteratively the equation by random candidate selection. Same advantage can be notice for local minimization.

On Tab.D.1, we can see final relative energy obtained by the different minimization methods. The proposed SA can reach a minimum as good as BP methods and close to GC-Expansion and GC-Swap. This is much better than conclusions made in [167] and [26] where SA minimum was far from GC minimum. Improved SA is still too much time consuming compare to other minimization methods around 10 to 100 times longer. SA computational time can be reduce for each sequence playing on T function parameters. From the table, we can remark that FLTG methods are

$E\%_{(\text{time})}$	Tsukuba	Venus	Teddy
lower bound	$100_{(113)}$	$100_{(900)}$	$100_{(810)}$
ICM [168]	$653.3_{(2)}$	$405.1_{(2)}$	$234.2_{(7)}$
BP-S [168]	$115.6_{(5)}$	$110.2_{(80)}$	$106.9_{(30)}$
BP-M [168]	$110.2_{(86)}$	$101.6_{(300)}$	$104.1_{(300)}$
Swap [168]	$100.8_{(7)}$	$103.0_{(21)}$	$100.8_{(45)}$
Expansion [168]	$100.4_{(6)}$	$102.5_{(21)}$	$\mathbf{100.5}_{(68)}$
TRW-S [168]	$\mathbf{100.0}_{(44)}$	$\mathbf{100.0}_{(900)}$	$100.6_{(810)}$
ICM	$640.3_{(2)}$	$405.0_{(4)}$	$229.4_{(10)}$
DDE	$389.2_{(8)}$	$342.2_{(13)}$	$205.1_{(50)}$
FLTG-ICM	$176.9_{(2)}$	$110.5_{(4)}$	$108.2_{(10)}$
FLTG-DDE	$118.2_{(4)}$	$109.4_{(11)}$	$108_{(29)}$
SA-Geman	$125.3_{(981)}$	$123.4_{(1624)}$	$129.6_{(2220)}$
Improved SA	$\mathbf{102.7}_{(470)}$	$\mathbf{103.9}_{(323)}$	$\mathbf{104.9}_{(2211)}$

Table D.1: *Final relative energy for minimization algorithms in % with computational time in seconds.*

as good as others. Moreover, they have a very low computational time (few seconds). The computational time can be easily reduce because our implementation is not optimized at all. In case of FLTG-DDE, FLTG method reduces computational time.

D.2.5 Middlebury database

To compare the efficiency of the proposed SA and FLTG methods with state-of-the-art Stereo Matching approaches, we submit our results on the Middlebury Stereo benchmark for the four sequences (Tsukuba, Venus, Teddy and Cones). Approach parameters are constant for the four image pairs. On the online database only results of FLTG-DDE is published.

Figure D.9 gives the rank for all our proposed approaches compared to GC-expansion algorithm for an error threshold of 2. We can see that local minimizations (ICM and DDE) give the poorest estimations. Using FLTG, local minimizations (FLTG-ICM and FLTG-DDE) perform as well as Improved SA and GC-expansion with a respective rank of 66.3, 66.4, 66.6, 63. Here GC has a little better rank than the others. This not really meaningful, the final energy obtained by FLTG, SA or

Algorithm Error Threshold = 2	Avg. Rank	Tsukuba			Venus			Teddy			Cones			Average Percent Bad Pixels
.....	...	...	...	...	...	...	...	...	...	...	...	...	...	.....
BP+MLH [40]	58.6	1.62 47	3.65 62	8.41 53	0.66 54	1.87 62	9.02 63	6.95 59	15.5 74	15.8 65	3.39 48	13.7 72	8.52 44	7.43
GC	63.0	1.53 46	3.23 58	7.79 49	0.58 52	1.97 66	5.46 53	8.05 73	17.1 76	15.7 65	5.95 74	15.9 80	10.9 64	7.86
DOUS-Refine [87]	63.8	2.38 65	3.70 63	10.9 66	1.16 67	1.86 61	12.2 69	5.56 51	9.36 47	13.5 59	5.69 74	11.7 65	15.1 79	7.76
DCBGrid [88]	65.3	4.21 80	5.16 77	17.2 83	0.98 60	1.23 54	7.89 59	7.69 71	10.8 61	15.2 64	3.95 59	9.48 48	11.5 60	7.94
TreeDP [8]	65.7	1.73 52	2.55 47	8.82 56	1.21 70	1.89 63	7.35 57	8.80 76	17.2 77	17.2 71	5.57 73	14.1 75	12.5 71	8.24
CostRelax [11]	65.8	3.91 78	5.20 78	16.9 81	1.05 63	1.95 65	13.6 79	6.05 55	13.2 67	17.9 74	3.44 52	9.04 43	10.5 61	8.56
FLTG-ICM	66.3	2.04 58	3.92 66	10.6 63	1.60 71	3.00 75	16.0 76	7.33 67	15.2 73	18.7 77	3.35 47	12.9 70	9.47 53	8.68
GC [1d]	66.4	1.67 50	3.75 64	8.20 49	0.83 59	2.37 71	8.12 60	9.72 79	18.8 82	17.2 72	4.51 68	15.0 78	11.2 65	8.45
FLTG-DDE	66.4	2.07 58	3.98 66	10.7 64	1.60 71	3.00 75	16.1 76	7.35 67	15.3 73	18.8 77	3.37 47	13.2 70	9.52 53	8.75
Improved-SA	66.6	1.63 49	3.43 60	8.23 50	1.19 70	2.59 74	9.10 64	7.05 64	16.1 75	13.0 52	8.41 83	17.7 86	13.2 72	8.47
CSBP [82]	68.3	1.74 53	3.84 65	9.10 57	1.09 64	2.52 72	12.9 72	8.18 74	17.3 79	20.6 79	4.07 63	14.2 76	11.3 66	8.91
.....	...	...	...	...	...	...	...	...	...	...	...	...	...	.....
Rank+ASW [84]	85.4	5.74 88	7.58 88	16.7 80	8.55 88	9.88 88	27.9 86	12.6 83	21.1 85	25.3 84	9.90 86	19.0 88	16.7 81	15.1
DDE	87.7	15.0 89	16.5 89	15.4 78	30.2 89	31.2 89	28.2 86	31.5 89	37.9 89	31.7 88	29.5 89	36.5 89	28.1 88	27.6
ICM	89.0	42.1 89	42.9 89	29.9 89	40.6 89	41.4 89	30.7 89	51.4 89	56.1 89	50.0 89	53.4 89	58.0 89	44.5 89	45.1

Figure D.9: *Illustration of the middlebury stereo evaluation approach table available online for FLTG-DDE (`http://vision.middlebury.edu/stereo/eval/`)*

GC are very closed with a difference between them about less than 10 % for all image pairs. The rank of our methods in the evaluation table is principally due to the energy definition that is not sufficient to describe the Stereo Matching problem.

D.3 conclusion

We propose, in this work, a complete comparison study of energy minimization methods in the case of stereo matching. Local minimization proved to be able to perform as well as Graph based global minimization when defined with the proposed FLTG process (appendix section C.4). DDE (appendix section C.2) always converge to better minimum than ICM (appendix section C.1), but still too far from global minimum. FLTG-DDE and FLTG-ICM can reach very good minimum with a very low computational time. Proposed global SA (appendix section C.3) performs better than Geman SA and converges to a minimum closed to the global minimum. SA minimum are coherent with Graph based minimization and even as good as BP-S and BP-M. However, SA needs very long computation time to converge to the global minimum. In this paper, we saw that global minimization methods based on Graph theory give a good minimum in a correct computational time. However, for the same energy definition, local minimization when process with FLTG can be as good as Graph based minimization with a smaller time consuming. This work has been publish in [32].

We choose to select FLTG-DDE approach in the case of optical flow estimation in this thesis because this method shows the best compromise between efficiency of energy minimization and computation cost time. Moreover, extension of the approach is proposed in appendix E to obtained a 2D real velocity field estimation.

Appendix E

Optimization Relative Issues

In the case of the optical flow estimation, we want to extract the 2D apparent velocity field $\vec{v}$ (section 3.1) from the motion of objects recorded on two successive images. The 2D velocity field corresponds to random variable field in a MRF formulation of the problem. As explained in appendix B.1, this random variable is bounded as $\vec{v}(\mathbf{x}) \in \Gamma = [-\vec{v}_{max}(\mathbf{x}); \vec{v}_{max}(\mathbf{x})]$. The solution of the problem is given by the best configuration of the velocity field minimizing the Gibbs energy E (section B equation (B.12)).

Optimization techniques, describe in appendix C, are used to minimize the energy E. For optical flow estimation, we seek for real 2D values. The discretization of domain Γ should be fine enough to get an estimation of the velocity field as closed as possible to the real one.

Due to the partial information of DOF equations, the apparent velocity in the image can be retrieved with precision if the velocity amplitude is of the order of magnitude of 1 pixel by interval of time. We use a quantized step of 0.1 pixel by interval of time in the domain $\Gamma = [-1; 1] \times [-1; 1]$. Thus, the total number of possible velocity vectors is $21 \times 21 = 441$. That is much more than for the Stereo Matching application (appendix D). Moreover, the precision of the velocity field is poor, only about 0.1 pixel by interval of time.

Because the number of velocity values is higher, the computational time of minimization methods will also be more important. If we reduce the number of velocity values, we get lower precision on the estimation.

For Direct Descent Energy (DDE - appendix C.2) and Simulated Annealing (SA - appendix C.3) minimization methods use a random candidate selection (random walk) to minimize the energy. We propose to define this random generation as an small incremental vector $\vec{\delta}(\mathbf{x})$ updating the current velocity $\vec{v}(\mathbf{x})$. $\vec{\delta}(\mathbf{x})$ is a real vector following a uniform random distribution in $\Gamma = [-0.1; 0.1] \times [-0.1; 0.1]$. This method shown to improve the precision of the optical flow estimation, but also to reduce the computational time of DDE and SA. Results are given in appendix F.2.

Another improvement of the optimization is the adaptation of other minimization methods (ICM and GC) to the multigrid.

E.1 ICM and GC Adaptation to Multigrid Approach

Other minimization, as Iterated Conditional Modes (ICM - appendix C.2) and Graph Cuts (GC - see [26, 25, 88]), need a finite discretized random variable. Their

computational time strongly depends on the number of velocity vectors and image size.

In the multigrid approach (section 4.3), we can make the hypothesis that the grid velocity $\vec{v}_g(\mathbf{x})$ is a fine representation of the substructure (pixel) velocities $\vec{v}(\mathbf{x}) = \vec{v}_g(\mathbf{x}) + \vec{v}_l(\mathbf{x})$; $(\vec{v}_g(\mathbf{x}) >> \vec{v}_l(\mathbf{x}))$. Considering this hypothesis, the substructure velocities should only differ from the grid velocity about small variations. The figure E.1 gives an illustration for a 1D random variable for simplification. At grid level, the random variables are integer values. Going to substructure level, we consider that the random variables may only differ from the grid level estimation about a cover-range set of $+/-1$ (possible changes are represented by arrows). In the same time, because number of possible configuration of the random variable field is strongly reduced which is equivalent to smaller number of random variable values at substructure level, we also proposed to improve the discretization to get a finer final estimation. In this example, we improve by 2 the precision between grid and substructure levels from 1 to 0.5.

For GC method, we use the GC α-expansion algorithm proposed by [26, 25, 88]. Thus, we modified it and integrate our multigrid adaptation approach. This work was published in [33]. Another similar method was proposed by [185] where the authors limit the possible configuration in a multigrid approach. However, they applied it on the GC $\alpha - \beta$-swap algorithm and the random variable discretization stays the same between multigrid levels.

In figure E.2, we show a weak point of the method because of the hypothesis made above of restricted possible change of the random variable from grid to substructure level. At grid level (2×2 size grid), we only have four different values of $\vec{v}_g$ (see appendix C figure C.2). Then, at substructure level, we represent the ground-truth on the left (figure E.2(a)). In fact, at strong discontinuity regions, the possibility of change of the random value is limited by the defined cover-range (figure E.2(b)). Dark substructure are the propagated errors resulting of the hypothesis of limited cover-range set of possible change from grid to substructure level. In some cases, this cover-range set is not large enough to let the random variable get to the correct value. We propose then to add to the cover-range set the possible configurations of values defined from the grid estimated field corresponding to neighbor's values. Thus, as shown on Figure E.2(c), the new estimation field can now reach the optimal solution. Figure E.3 illustrates the new possible change configuration adapting to the multigrid approach going from grid level to substructure level.

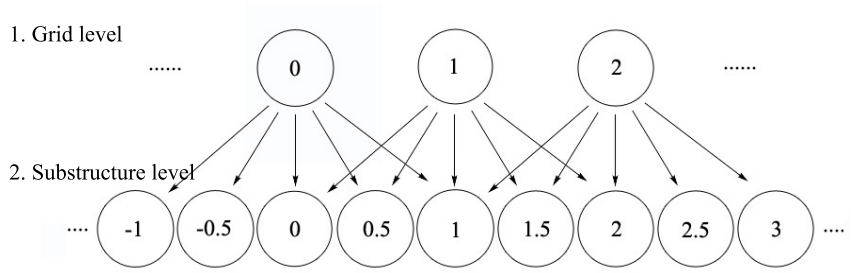

Figure E.1: *illustration of value distribution and possible change from grid to substructure levels.*

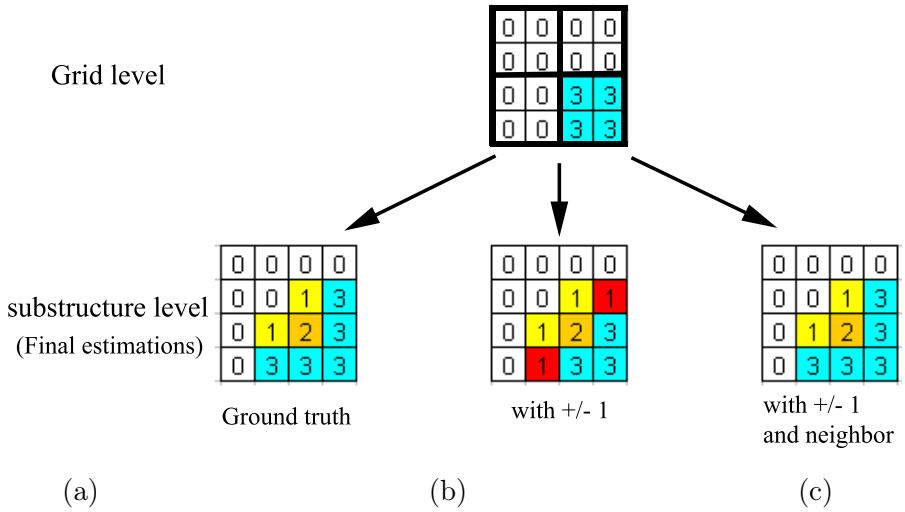

Figure E.2: *Illustration of a possible error configuration.*

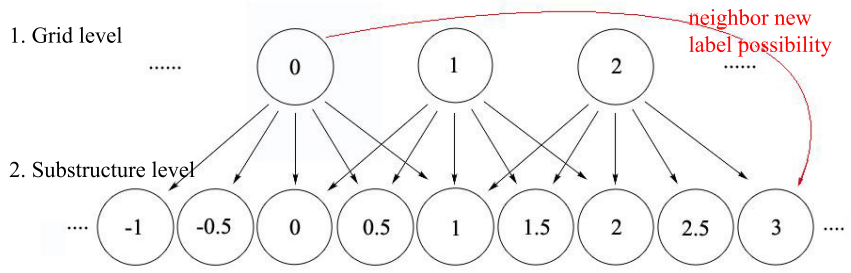

Figure E.3: *illustration of value distribution and possible change from grid to substructure levels, allowing possible jump to neighbor values.*

Appendix F

Tests on Multiresolution and Optimization Issues

F.1 Analyze of classical Multiresolution (W_MR) and Multigrid techniques

Results in this section are shown on the Venus sequence (figure 4.6 middle column). The data energy E_d (equation (4.2)) is the L2 norm of BCCE_1 (equation (4.14)) and the used minimization method is DDE (appendix C.2).

F.1.1 Pyramidal decomposition

Because of partial derivative in DOF equation (4.8), we saw in section 4.2 that this formulation can only retrieve a small velocities between two successive images. Figure F.1 illustrates the estimated velocity map for different level of pyramidal decomposition (section 4.2.1).

We see that under 3 level pyramidal decomposition $K = 2$ ($k = 0, 1, 2$) (section 4.2.1), the algorithm cannot retrieve the real velocity amplitude. We have a lot of small velocity regions that differ from the ground truth. This remark is confirmed by the figure F.2 which plot the AAE error (equation (4.44a)) depending on the number of pyramidal decomposition level K. From 3 to 5 levels, the AAE error is about the same. Strangely, for 5 levels, the AAE error becomes higher than 4 levels. In fact, there is an optimal number of pyramidal decomposition level depending on the maximum velocity amplitude $||\vec{v}_{max}||$. If the number of pyramidal decomposition level is higher than the necessary number, then the pyramidal decomposition technique can introduce to the estimation some errors which are propagated by the coarser estimated velocity field at level $k + 1$ to level k when warping the image (see section 4.2.1). In Venus sequence, the maximum velocity field is about $+/-10$ pixels by interval of time. Thus, 4 level decomposition should be adequate.

In fact, pyramidal decomposition technique is necessary to retrieve the correct velocity amplitude for large velocities over the image domain. But the use of too many levels may bring some errors. [74] proposed to suppress this pyramidal decomposition drawback, which is even more present in noisy image, by adding a global regularization $E_{s_{cc}}$ (section 3.2.3) constraining the velocity field to be closed to cross-correlation PIV (CC) estimation. This method shown to be very powerful in case of particle images where CC is very robust. The CC has the advantage to be able to retrieve large velocity from original images. Description of CC technique

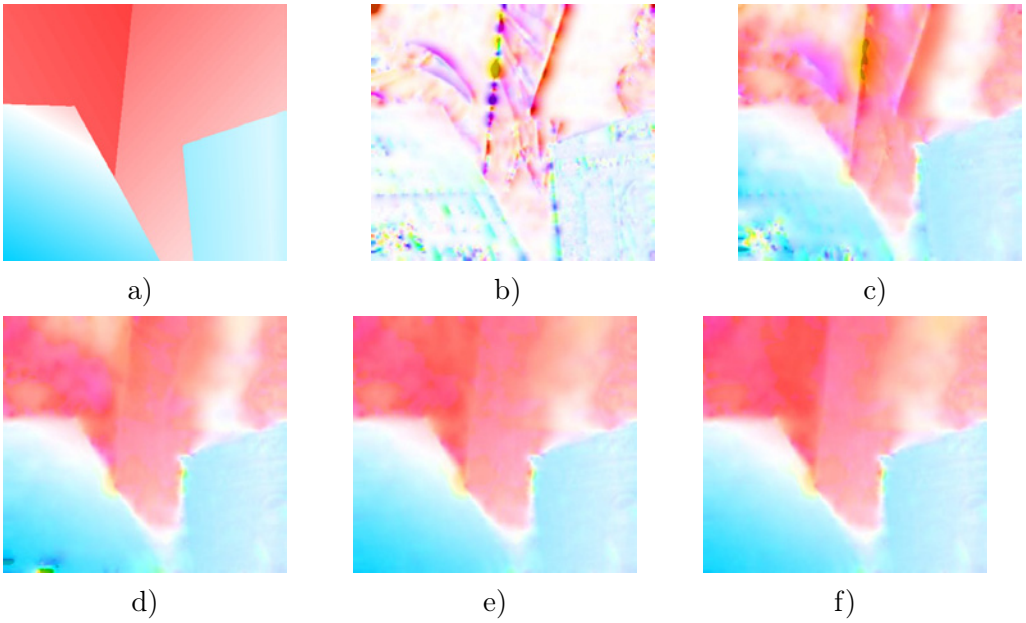

Figure F.1: *Exact velocity field a). Estimated velocity field for different pyramidal decomposition level: b)* 1 *level* $K = 0$*, c)* 2 *level* $K = 1$*, d)* 3 *levels* $K = 2$*, e)* 4 *levels* $K = 3$ *and f)* 5 *levels* $K = 4$*.*

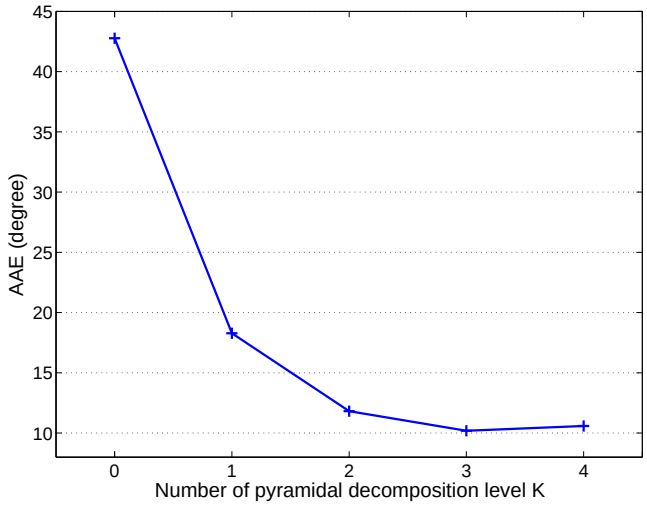

Figure F.2: *AAE error depending on the number of pyramidal decomposition*

can be found in appendix A.1. After using CC, differential optical flow algorithm is used to retrieve the dense velocity field for which solution is obtained from the energy $E = E_d + E_s + E_{s_{cc}}$. Note that the collaborative method will provide poor results on scalar image as the CC will estimate strongly erroneous velocity field.

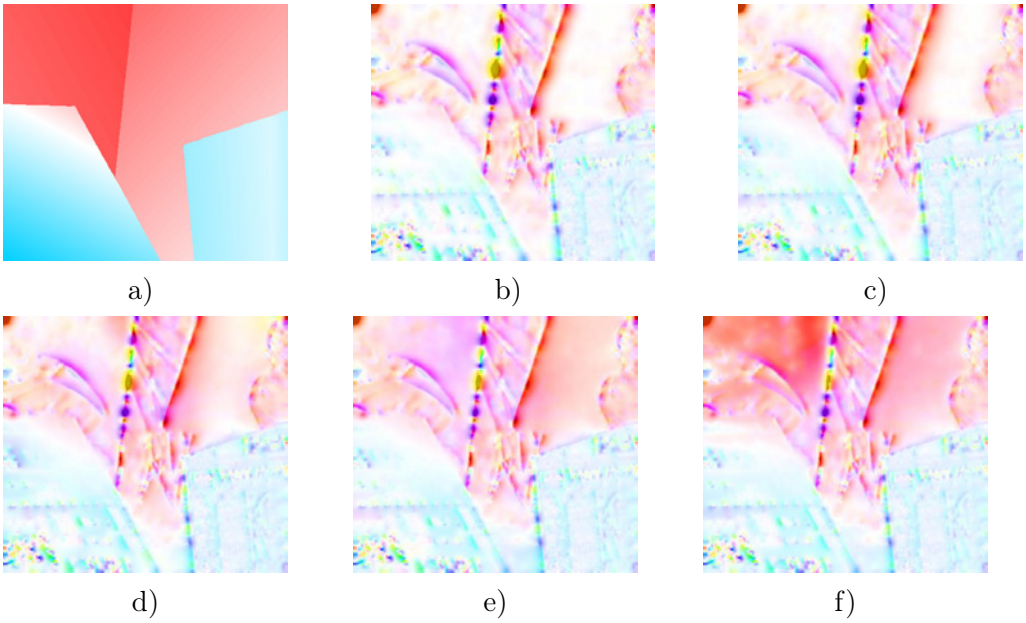

Figure F.3: *Exact velocity field a). Estimated velocity field for different grid size: b)* 1×1*, c)* 2×2*, d)* 4×4*, e)* 8×8 *and f)* 16×16 *pixels.*

F.1.2 Multigrid

In appendix C.4 is shown that multigrid methods allow local minimization algorithms to converge till a local minimum of the energy E which is closed to the global one.

Figure F.3 shows estimated velocity maps for different grid sizes (1×1 (b), 2×2 (c), 4×4 (d), 8×8 (e) and 16×16 (f) pixels) when it is not coupled with W_MR pyramidal decomposition $K = 0$. Estimated velocity fields $\vec{v}_e$ tend to get more and more close to the exact velocity field $\vec{v}_c$. Anyway without pyramidal decomposition, multigrid cannot recover large velocities because second and higher orders of Taylor expansion used to defined BCCE_1 (equation (4.8)) cannot be neglected for large velocities.

Figure F.4 represents the AAE errors for different grid sizes (1×1, 2×2, 4×4, 8×8 and 16×16 pixels) with different number of pyramidal decomposition level ($K = 0$, $K = 1$, $K = 2$, $K = 3$ and $K = 4$). We see that best estimation is obtained for a grid size between 2×2 pixels and 8×8 pixels. Most of the time, we set the grid size to 2×2 or 4×4 pixels in the following experiments (chapters 4 and 5). As we only define a two-stage multigrid approach (grid level and substructure level) for optical flow estimation (section 4.3), the grid size influences the final estimation but it is also limited by the ratio between grid and substructure (pixel) sizes. We see that AAE error gets higher for grid size of 16×16 pixels. Using multi-stage multigrid method as in appendix C.4, tests shown to get similar estimation than when using only two step multigrid method with a grid size of 4×4 pixels.

The principal point of interest is that multigrid always improve accuracy of the estimation even more when it is coupled with multiresolution technique.

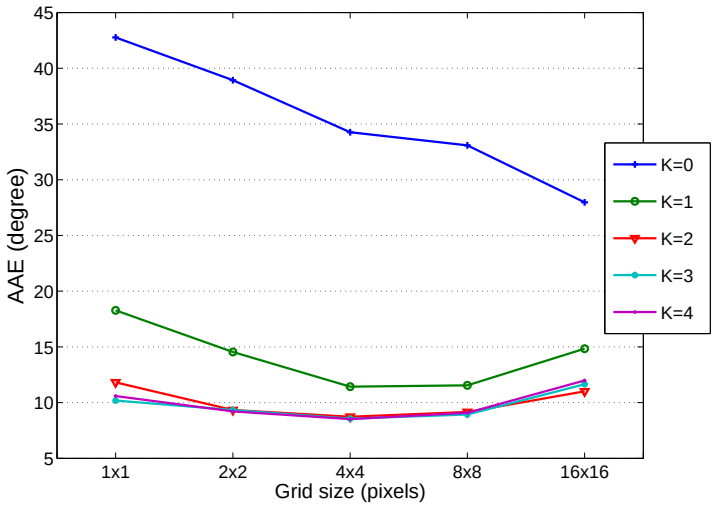

Figure F.4: *AAE error depending on grid size (*1×1, 2×2, 4×4, 8×8 *and* 16×16 *pixels) and level of pyramidal decomposition (*$K=0$, $K=1$, $K=2$, $K=3$ *and* $K=4$*).*

F.2 Analyze of Optimization Issues

As we describe in appendix E, we modify the random walk technique of DDE by introducing an updating residual velocity candidate $\vec{\delta}$ small compare to the current state velocity $\vec{v}$. Figure F.5 and table F.1 illustrate the difference between random velocity candidate generation over the velocity domain $\Gamma=[-1;1]\times[-1;1]$ pixel by interval of time for which discretization is 0.1 pixel by interval of time, with updating residual velocity candidate $\vec{\delta}=(\delta_x,\delta_y)|\delta_x,\delta_y\in\mathcal{N}(0,0.1)$ following uniform random real distribution center in zero and bounded between $+/-0.1$ pixel by interval of time. Estimation by DDE minimization by updating residual value, as proposed in appendix E, is better than the previous one. In fact, the main difference between both minimization algorithms is that one can estimate real velocity vector while the other can only estimate a discretized velocity vector with a precision of 0.1 pixel by interval of time. At each pyramidal level estimation k, the estimate velocity field is more precise using the proposed modified method. Then less errors are propagated from level k to level $k-1$. We can observe it on the estimated velocity field on figure F.5, the final estimated velocity field is much smoother using real residual updating value (denoted $T-I$ in the figure) than using discretized value over Γ (denoted $T-D-D$). Note also that computational time is smaller.

Multigrid technique is useful for local minimization method. Figure F.6 compare

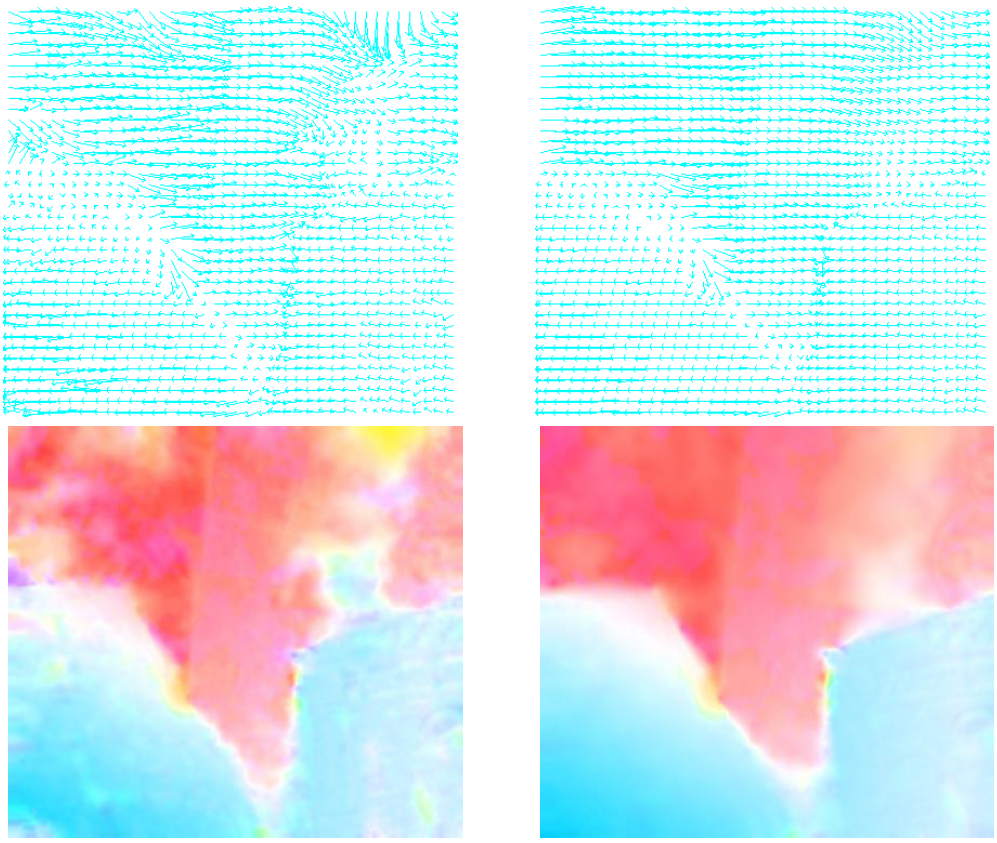

a) b)

Figure F.5: *Velocity field estimation by DDE for a 4 level pyramidal decomposition using a) discretized value over* Γ *(*$T-D-D$*) and b) real residual updating value (*$T-I$*).*

Venus	Computational time (seconds)
$T-D-D$	335
$T-I$	79

Table F.1: *Time consuming for DDE on Venus sequence with randomly candidate generation minimization methods: Over the entire discretization domain* $[-1;1]\times[-1;1]$ *by step of* 0.1 *pixel by interval (*$T-D-D$*) or by incremental real random vector* $(\delta_x,\delta_y)\in\mathcal{N}(0,0.1)$ *(*$T-I$*).*

AAE errors (equation (4.44a)) for DDE, SA (section C.3) and Graph Cut (GC) [88] minimizations for different grid sizes (1×1, 2×2 and 4×4 pixels) using a 4 level pyramidal decomposition ($K=3$). Only local minimization DDE get smaller AAE error when using multigrid. We can remark that SA minimization gives a smaller AAE error than DDE minimization without multigrid, which confirmed the

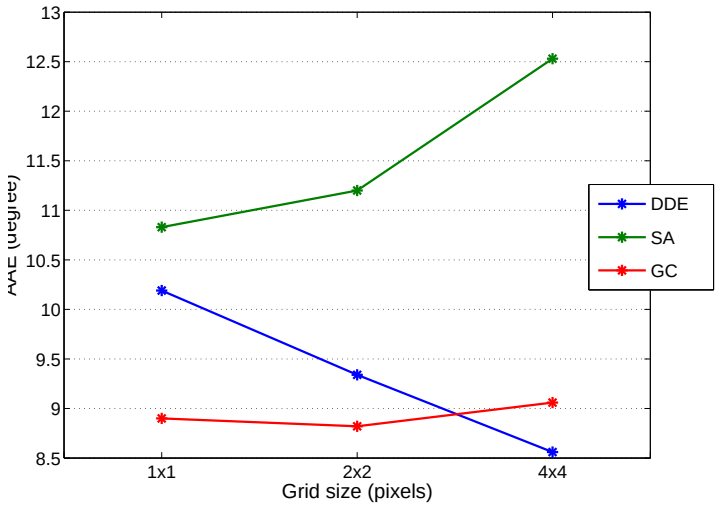

Figure F.6: *AAE error for DDE (blue), SA (purple) and GC (red) on Venus sequence for different grid sizes* (1×1, 2×2 *and* 4×4 *pixels) using* 4 *level pyramidal decomposition* $K = 3$.

difference between global SA method and local DDE method. When using multigrid, SA and DDE methods are equivalent. DDE method even gives a smaller AAE error for grid size of 4×4 pixels. We can conclude that for optical flow estimation using multigrid, local DDE minimization method becomes as good as global SA minimization. Moreover DDE method presents the advantage to be much less time consuming.

For global GC minimization method, AAE error is larger than DDE and SA methods for optical flow estimation. This observation came from two different things:

- The smoothness term E_s, we used, is a quadratic function of the spatial velocity variations (equation (4.33)). This term is not submodular which is a necessary condition for α-expansion GC algorithm to converge to the global minimum of E (equation (4.2)). However, it has been shown in [88] that α-expansion can converge close to the global minimum for non-submodular if non submodular configurations are truncated which becomes an approximative smoothness term submodular function.

- For GC minimization, the random variable field has to be a discretized finite set as defined in appendix E. While DDE and SA use an updating real residual random variable which proves to improve the velocity estimation.

We can also observe on figure F.6 that AAE error for GC method get little higher when using multigrid. This shows the limit of the GC adaptation technique proposed in appendix E.1. Here, we use for the multigrid at grid level, the entire

Computational time (seconds)	without MG	with MG	Time reduction (in %)
DDE	79	61	-25 %
SA	1094	805	-25 %
GC	5212	1347	-75 %

Table F.2: *Computational time for DDE, SA and GC methods on Venus sequence without and using multigrid (MG) of grid size*$= 2 \times 2$ *pixels in a* 4 *level pyramidal decomposition (*$K = 3$*).*

$\Gamma = ([-1;1] \times [-1;1])$ domain with discretization of 0.1 pixel by interval of time for x and y coordinates and at substructure level, we use a cover-range set of $+/-0.1$ pixel by interval of time with precision of 0.05 pixel. More the grid size is large, more substructure velocity $\vec{v}_l$ inside a grid may have larger variations compared to the grid velocity $\vec{v}_g$. In this case, the cover-range set and neighborhood possible change of velocity are not large enough to retrieve all substructure velocity (illustration in figures E.1, E.2 ,E.3), which explain the increasing of AAE error with increasing of grid size of multigrid method. However, the principal objective of the GC adapted method to multigrid, is to reduce the number of possible velocity values at each level, in the aim to reduce the computational time. Table F.2 shows the computational time without and using multigrid MG method (grid size$= 2 \times 2$ pixels). Using MG, the GC time consuming is strongly reduced (-75%) for a low increasing of AAE error (4 %). In the same time, the table shows that multigrid also reduces computational time for DDE and SA methods about 25%. Local DDE method, for optical flow estimation, is much faster than global minimizations.

We test the different minimization methods on three sequences: Dimitrodon, Venus and Yosemite (section 4.5.1). We illustrate, here, in table F.3 the AAE error for ICM, DDE, SA and GC minimization methods when using a 4 level pyramidal decomposition ($K = 3$) and a multigrid with grid size of 2×2 pixels. The weighting coefficient between the data energy E_d and regularization energy E_s is $\alpha = 100$ (equation (4.2)). We compare the efficiency of our BCCE_1 ((equation (4.14)) with W_MR (section 4.2.1)) approach depending on the used minimization methods with other OF algorithms from [11].

AAE values are computed for three different image regions as described in section 4.5.1 which are delimited by masks represented in figure 4.6.c,d,e.

From this results, we can confirm that ICM method does not allow a good estimation of the velocity field (highest AAE errors). GC method gives a closer AAE errors to the ones of DDE and SA methods, but the strongly discretized estimated velocity field influenced the accuracy of velocity estimation as explained above. For DDE and SA methods, AAE error is similar for all the different cases. In fact, these methods fit more to the optical flow problem where the seeking solution is a real 2D vector field than for example as GC method which was first defined for binary minimization problems. DDE and SA methods give the smallest AAE

AAE	Dimetrodon (Hiddentexture)			Yosemite (Synthetic)			Venus (Stereo)		
	all	disc	untext	all	disc	untext	all	disc	untext
Bruhn et al. [29]	10.99	**9.41**	14.22	**1.69**	**2.86**	**1.05**	8.73	31.46	8.15
Black & Anandan [21]	**9.26**	10.11	**12.08**	2.65	4.18	1.88	**7.64**	**30.13**	**7.31**
Pyramid LK [23]	10.27	9.71	13.63	5.22	6.64	4.29	14.61	36.18	24.67
MediaPlayer [110]	15.82	26.42	16.96	11.09	17.16	10.66	15.48	43.56	15.09
Zitnick [192]	30.1	34.27	31.58	18.5	28	9.41	11.42	31.46	11.12
ICM	19.201	20.527	23.646	5.651	6.678	7.300	14.74	36.65	16.92
DDE	6.288	9.751	7.66	3.358	4.920	1.444	9.022	**35.228**	9.355
SA	**5.293**	**8.394**	**6.347**	**3.0669**	**4.916**	**1.340**	**8.864**	35.600	**8.287**
GC	8.032	10.560	9.741	3.760	6.103	2.629	11.2	34.48	10.23

Table F.3: *AAE error comparison of ICM, DDE, SA and GC minimization methods with classic algorithms ([11]) for Dimetrodon, Yosemite and Venus sequences. Our approaches use a* 4 *level pyramidal decomposition and a multigrid with grid size of* 2×2 *pixels. Energy parameters are the same for the* 4 *minimizations.*

error and are faster to converge due to the high number of velocity values. In this table SA almost everywhere gets the smallest AAE, however from figure F.6, we can notice that we use, here, a 2×2 pixels multigrid technique. If using 4×4 grid size, AAE error for DDE method should be smaller. This remark is confirmed in section 4.5.2. Moreover, for DDE method is much less time consuming than SA method for the same order of error.

In table F.3, bold AAE error shown the smallest AAE for all presented approaches. In red, we have the smallest AAE error from our methods. Comparing AAE error from our methods to other approaches, we can see that AAE values are coherent and DDE or SA methods shown AAE error as good as [29] or [21]. Moreover, this table shown that there is no universal optical flow method. Non of these methods gets the best AAE errors over the all sequences (Dimetrodon, Venus and Yosemite) and image regions (all, disc and untext). For Dimetrodon, DDE and SA methods give much lower AAE errors than [29] or [21]. This might be explained perhaps by the use of a smaller number of pyramidal decomposition in these methods that do not allow the complete retrieving of the large velocity (larger in this sequence than in others).

However, at discontinuities, we can see that our methods have often a less accurate AAE error. This is due to the quadratic smoothness term that penalize to much variation of velocity field on continuities (equation (4.14)). [29] or [21] use robust functions.

In this section, we show that DOF method as BCCE_1 (equation(4.8)) needs a multiresolution technique to determine large velocities. We also compare different minimization techniques. DDE minimization (section C.2) proves to obtain the best compromise between accuracy of the velocity estimation and time consuming when using it with a multigrid approach. DDE and multigrid will be used in sections 4.5 and 4.6 and in chapters 5.

Bibliography

[1] M. Abramowitz and I. A. Stegun. *Handbook of Mathematical Functions with Formulas, Graphs, and Mathematical Tables*. 9th printing, New York: Dover, 1972. 33

[2] R.J. Adrian. Statistical properties of particle image velocimetry measurements in turbulent flow. In *Laser Anemometry in Fluid Mechanics - III*, pages 115–129, Lisbon: Instituto Superior Technico, 1988. 121

[3] Y. D. Afanasyev and E. K. Demirov. A variational filtration and interpolation technique for PIV employing fluid dynamical constraints. *Experiments in Fluids*, 39(5):828–835, juillet 2005. 127

[4] L. Alvarez, C.A. Castaño-Moraga, M. García, K. Krissian, L. Mazorra, A. Salgado, and J. Sánchez. Symmetric optical flow. In *International Conference on Computer Aided Systems Theory, LNCS 4739*, pages 676–683, 2007. 46, 47, 52, 55

[5] L. Alvarez, J. Esclarin, M. Lefebure, and J. Sanchez. A pde model for computing the optical flow. In *Proc. XVI Congresso de Ecuaciones Diferenciales y Aplicaciones*, pages 1349–1356, 1999. Las Palmas. 30

[6] L. Alvarez, J. Weickert, and J. Sánchez. Reliable estimation of dense optical flow fields with large displacements. *International Journal of Computer Vision*, 39(1):41–56, 2000. 32

[7] A.A. Amini. A scalar function formulation for optical flow: applications to X-ray imaging. In *Workshop on Biomedical Image Analysis*, pages 117–123, 1994. 33, 34, 42

[8] L. Amodei and M.N. Benbourhim. A vector spline approximation. *Journal of approximation theory*, 67(1):51–79, 1991. 38

[9] S. Ayer and H.S. Sawhney. Compact representations of videos through dominant and multiple motion estimation. *Transactions on Pattern Analysis and Machine Intelligence*, 18(8):514–830, 1996. 27

[10] M. Ayrault and S. Simoens. Turbulent concentration determination in gas flow using multiple ccd cameras. *Journal of Flow Visualization and Image Processing*, 2(2):195–208, 1995. 102, 103

[11] S. Baker, S. Roth, D. Scharstein, M.J. Black, J.P. Lewis, and R. Szeliski. A database and evaluation methodology for optical flow. In *International Conference on Computer Vision*, pages 1–8. IEEE, 2007. vii, 21, 59, 60, 62, 169, 170

[12] S. Baker, D. Scharstein, J.P. Lewis, S. Roth, M.J. Black, and R. Szeliski. A Database and Evaluation Methodology for Optical Flow. Technical report, MSR-TR-2009-179, Microsoft Research, octobre 2009. 29, 31, 32, 60

[13] S.T. Barnard. Stochastic stereo matching over scale. *International Journal of Computer Vision*, 3(1. May 1989):17–32, May 1989. 142

[14] J.L. Barron, D.J. Fleet, and S.S. Beauchemin. Performance of optical flow techniques. *International Journal of Computer Vision*, 12(1):43–77, February 1994. 21, 25, 26, 49, 59

[15] G. K. Batchelor. *An introduction to fluid dynamics*. Cambridge University Press, Cambridge, 1967. 7

[16] D. Bereziat, I. Herlin, and L. Younes. Motion estimation using a volume conservation hypothesis. In *International Conference on Acoustics, Speech, and Signal Processing*, volume 6, pages 3385–3388, Phoenix, US, 1999. 12, 33, 34, 42

[17] J. Besag. Spatial interaction and the statistical analysis of lattice systems. *Journal of the Royal Statistical Society. Series B (Methodological)*, 36(2):192–236, 1974. 133

[18] J. Besag. the statistical analysis of dirty pictures. *Journal of the Royal Society*, 48(3):259–302, 1986. 139, 140

[19] S. Birchfield and C. Tomasi. A pixel dissimilarity measure that is insensitive to image sampling. *Transactions on Pattern Analysis and Machine Intelligence*, 20(4):401–406, April 1998. v, 147, 153

[20] M. Black and A. Rangarajan. On the unification of line processes, outlier rejection, and robust statistics with applications in early vision. *International Journal of Computer Vision*, 19(1):75–104, 1996. 29, 30

[21] M.J. Black and P. Anandan. The robust estimation of multiple motions: Parametric and piecewise-smooth flow-fields. *Computer Vision and Image Understanding*, 63(1):75–104, January 1996. 27, 31, 46, 51, 61, 62, 63, 65, 170, 194

[22] A. Blake, P. Kohli, and C. Rother. *Advances in Markov Random Fields for Vision and Image Processing*. MIT Press, 2011. 133

[23] J. Bouguet. Pyramidal implementation of the lucas-kanade feature tracker: description of the algorithm. Technical report, OpenCV Document, Intel Micropocessor Research Labs, 2000. 61, 62, 63, 170

[24] C. A. Bouman and M. Shapiro. A multiscale random field model for bayesian image segmentation. *Transactions on Image Processing*, 3(2):162–177, 1994. 133

[25] Y. Boykov and V. Kolmogorov. An experimental comparison of min-cut/max-flow algorithms for energy minimization in vision. *Transactions on Pattern Analysis and Machine Intelligence*, 26(9):1124–1137, September 2002. 154, 159, 160

[26] Y. Boykov, O. Veksler, and R. Zabih. Fast approximate energy minimization via graph cuts. *Transactions on Pattern Analysis and Machine Intelligence*, 23(11):1222–1239, November 2001. 155, 159, 160

[27] R. Brad and I.a. Letia. Extracting cloud motion from satellite image sequences. In *7th International Conference on Control, Automation, Robotics and Vision*, pages 1303–1307, 2002. 42

[28] A. Bruhn, J. Weickert, T. Kohlberger, and C. Schnorr. A multigrid platform for real-time motion computation with discontinuity-preserving variational methods. *International Journal of Computer Vision*, 70(3):257–277, December 2006. 57

[29] A. Bruhn, J. Weickert, and C. Schnörr. Lucas/Kanade Meets Horn/Schunck: Combining Local and Global Optic Flow Methods. *International Journal of Computer Vision*, 61(3):211–231, février 2005. 29, 31, 32, 61, 62, 63, 76, 170

[30] P.J. Burt and E.H. Adelson. The laplacian pyramid as a compact image code. *Transactions on Communications*, 31(4):532–540, 1983. 31, 50

[31] J. Carlier and B. Wieneke. Report on production and diffusion of fluid mechanics images and data. Technical report, tech. report, Fluid Project deliverable 1.2, 2005. 71, 86, 88, 96

[32] C. Cassisa. Local vs global energy minimization methods: application to stereo matching. In *Proceedings of the International Progress in Informatics and Computing (PIC'10)*, Shanghai, China, 2010. 4, 44, 157

[33] C. Cassisa, V. Prinet, L. Shao, S. Simoens, and C.L. Liu. Optical flow robust estimation in a hybrid multi-resolution mrf framework. In *International Conference on Accoustics, Speech and Signal Processing, ICASSP'08*, pages 793–796, Las Vegas, USA, 2008. IEEE. 4, 44, 160

[34] C. Cassisa, S. Simoens, and V. Prinet. Two-frame optical flow formulation in an unwarping multiresolution scheme. In *Springer-LNCS 5856. Proceedings of the 14th Iberoamerican Conference on Pattern Recognition (CIARP'09)*, pages 790–797, Guadalajara, Mexico, 2009. 4, 44, 46, 64

[35] C. Cassisa, S. Simoens, V. Prinet, and L. Shao. Formulation physique du flot optique pour l'étude de mouvements turbulents. In *Proceedings of the 13ème Congrés Français de Visualisation et de Traitement d'Images en Mécanique des Fluides (FLUVISU'09)*, Riems, France, 2009. 4, 78

[36] C. Cassisa, S. Simoens, V. Prinet, and L. Shao. Sub-grid physical optical flow for remote sensing of sandstorm. In *Proceedings of the International Geoscience and Remote Sensing Symposium (IGARSS'10)*, pages 2230–2233, Hawai, US, 2010. 4, 78

[37] C. Cassisa, S. Simoens, V. Prinet, and L. Shao. Subgrid scale formulation of optical flow for the study of turbulent flow. *submitted in Experiments in Fluids (major revisions)*, 2011. 4, 78

[38] C. Cassisa, S. Simoens, V. Prinet, L. Shao, and C.L. Liu. Two-frame optical flow formulation in an unwarping multiresolution scheme. *submitted in Pattern Recognition Letters (major revisions)*, 2011. 4, 44, 46, 64

[39] J. Chen and J. Katz. Elimination of peak-locking error in PIV analysis using the correlation mapping method. *Measurement Science and Technology*, 16(8):1605–1618, août 2005.

[40] J.P. Chollet and M. Lesieur. Parameterisation for small scales of three dimensional isotropic turbulence using spectral closure. *Journal of the Atmospheric Sciences*, 38:159–174, 1981. 83

[41] S.G. Chumakov. *Subgrid models for large eddy simulation: Scalar flux, scalar dissipation and energy dissipation.* PhD thesis, University of Wisconsin-Madison, 2005. Thesis. 84

[42] F. S. Cohen, Z. Fan, and M. A. Patel. Classifcation of rotated and scaled textured images using gaussian markov random field models. *Transactions on Pattern Analysis and Machine Intelligence*, 13(2):192–202, February 1991. 133

[43] I. Cohen and I. Herlin. Optical flow and phase portrait methods for environmental satellite image sequences. In *European Conference on Computer Vision*, volume 2, pages 141–150, 1996. 42

[44] G. Comte-Bellot and S. Corrsin. The use of a contraction to improve the isotropy of grid generated turbulence. *Journal of Fluid Mechanics*, 25:657–682, 1966. 83, 84

[45] T. Corpetti, P. Héas, E. Memin, and N. Papadakis. Pressure image assimilation for atmospheric motion estimation. *Tellus A*, 2009. 41, 117

[46] T. Corpetti, D. Heitz, G. Arroyo, E. Menin, and A. Santa-Cruz. Fluid experimental flow estimation based on an optical-flow scheme. *Experiments in Fluid*, 40(1):80–97, 2005. ii, 35, 38, 42, 65, 67, 70, 72, 73, 79, 87, 88, 92, 95, 195

[47] T. Corpetti, E. Memin, and P. Perez. Dense estimation of fluid flows. *Transactions on Pattern Analysis and Machine Intelligence*, 24(3):365–380, mars 2002. 12, 30, 31, 33, 34, 38, 42, 52, 76, 116

[48] G.X. Cui, C.X. Xu, L. Fang, L. Shao, and Z.S. Zhang. A new subgrid eddy-viscosity model for large-eddy simulation of anisotropic turbulence. *Journal of Fluid Mechanics*, 582:377–397, 2007. 82, 83, 113, 116

[49] A. Cuzol and E. Mémin. Vortex and source particles for fluid motion estimation. *Scale Space and PDE Methods in Computer Vision*, pages 254–266, 2005. 42

[50] W.J.A. Dahm, L.K. Su, and K.B. Southerland. A scalar imaging velocimetry technique for fully resolved four-dimensional vector velocity field measurements in turbulent flows. *Physics of Fluids A: Fluid Dynamics*, 4(10):2191, 1992. 35

[51] J. de Saint Venant. Théorie du mouvement non-permanent des eaux, avec application aux crues des rivieres et l'introduction des marees dans leur lit. *Comptes Rendus de l'Académie des Sciences*, 73, 1871. 40

[52] J.W. Deradorff. A numerical study of three-dimensional turbulent channel flow at large Reynolds numbers. *Journal of Fluid Mechanics*, 41:453–480, 1970. 83

[53] R. Deriche and O. Faugeras. Optical flow estimation while preserving its discontinuities: A variational approach. In *2nd Asian Computer Vision*, volume 1, pages 290–295, 1995. 30

[54] H. Derin, H. Elliot, R. Cristi, and D. Geman. Bayes smoothing algorithms for segmentation of binary images modeled by markov random fields. *Transactions on Pattern Analysis and Machine Intelligence*, 6(6):707–719, 1984. 133

[55] V. Devlaminck and J.P. Dubus. Estimation of compressible or incompressible deformable motions for density images. In *International Conference on Image Processing*, C, pages 125–128, 1996. 33, 34

[56] M. Van Dyke. *An Album of Fluid Motion.* The Parabolic Press, 1997. 14

[57] A. Favre. Statistical equations of turbulent gases. In *Problems of Hydrodynamics and Continuum Mechanics*, pages 231–266, 1969. Society for Industrial and Applied Mathematics, Philadelphia, PA. 16

[58] P.F. Felzenszwalb and D.P. Huttenlocher. Efficient belief propagation for early vision. *International Journal of Computer Vision*, 70(1):41–54, October 2006. 154

[59] J.M. Fitzpatrick. A method for calculating velocity in time dependent images based on the continuity equation. In *Conference on Computer Vision and Pattern Recognition*, pages 78–81, 1985. 33

[60] R.D. Frederiksen, W.J.A. Dahm, and D.R. Dowling. Experimental assessment of fractal scale similarity in turbulent flows. Part 2. Higher-dimensional intersections and non-fractal inclusions. *Journal of Fluid Mechanics*, 338:89–126, May 1997. 35

[61] U. Frisch. *Turbulence*. Cambridge University Press, 1995. 14

[62] T. Fujita. A study of mesoscale cloud motions computed from ats-1 and terrestrial photographs from satellite. *Mesometeorological research project*, 71:25, 1968. Dept. of Geophysical Sciences, Univ. of Chicago. 106

[63] T. Fujita, D.L. Bradbury, Ð¡. Murino, and L. Mull. A Study of Mesoscale Cloud Motions Computed from ATS-1 and Terrestrial Photographs from Satellite. *Mesometeorological Research Project Research*, Paper No 71:25, 1968. 42

[64] C.S. Garbe, H. Spies, and B. Jähne. Estimation of surface flow and net heat flux from infrared image sequences. *Journal of Mathematical Imaging and Vision*, 19:159–174, 2003. 84

[65] D. Geman and G. Reynolds. Constrained restoration and the recovery of discontinuities. *Transactions Pattern Analysis and Machine Intelligence*, 14(3):367–383, 1992. 29, 30

[66] S. Geman and D. Geman. Stochastic relaxation, gibbs distribution, and the bayesian restoration of image. *Transactions on Pattern Analysis and Machine Intelligence*, 6(6):721–741, November 1984. 133, 134, 142

[67] M. Germano and U. Piomelli. A dynamic subgrid scale eddy viscosity model. *Physics of Fluids A: Fluid Dynamics*, 3(7):1760–1765, 1991. 83, 116

[68] S.N. Gupta and J.L. Prince. Stochastic models for div-curl optical flow methods. *Signal Processing Letters*, 3(2):32–34, 1996. 38

[69] J.M. Hammersley and P. Clifford. Markov fields on finite graphs and lattices. *Unpublished manuscript*, 1971. 133

[70] H.W. Haussecker and D.J. Fleet. Computing optical flow with physical models of brightness variation. In *Conference on Computer Vision and Pattern Recognition*, volume 2, pages 760–767, 2000. 84, 109, 117

[71] H.W. Haussecker, C.S. Grabe, H. Spies, and B. Jahne. A total least squares framework for low-level analysis of dynamic scenes and processes. *Pattern Recognition. 21th DAGM Symposium*, pages 240–249, 1999. 28

[72] P. Héas, D. Heitz, and E. Mémin. Multiscale regularization based on turbulent kinetic energy decay for PIV estimations with high spatial resolution. In *8TH International Symposium on Particle Image Velocimetry*, 2009. 41, 42, 99

[73] P. Heas, E. Memin, N. Papadakis, and A. Szantai. Layered Estimation of Atmospheric Mesoscale Dynamics From Satellite Imagery. *Transactions on Geoscience and Remote Sensing*, 45(12):4087–4104, décembre 2007. 33, 34, 35, 39, 40, 41, 42, 116, 119, 188

[74] D. Heitz, P. Héas, E. Mémin, and J. Carlier. Dynamic consistent correlation-variational approach for robust optical flow estimation. *Experiments in Fluids*, 45(4):595–608, octobre 2008. 13, 29, 31, 33, 39, 40, 41, 42, 113, 163

[75] D. Heitz, E. Mémin, and C. Schnörr. Variational fluid flow measurements from image sequences: synopsis and perspectives. *Experiments in fluids*, 48(3):369–393, 2010. 33, 42, 45

[76] F. Heitz and P. Bouthemy. Multimodal estimation of discontinuous optical flow using markov random fields. *Transactions on Pattern Analysis and Machine Intelligence*, 15(12):1217–1232, December 1993. 133

[77] B.K.P. Horn and B.G. Schunck. Determining optical flow. *Artificial Intelligence*, 17(1-3):185–203, 1981. 10, 21, 25, 26, 27, 29, 30, 32, 45, 63, 65, 76, 79, 87, 115, 116, 195

[78] H.T. Huang, H.E. Fiedler, and J.J. Wang. Limitation and improvement of PIV. I-Limitation of conventional techniques due to deformation of particle image patterns. *Experiments in Fluids*, 15(3):168–174, 1993. 125, 126

[79] K. Jambunathan, X.Y. Ju, and B.N. Dobbins. An improved cross correlation technique for particle image velocimetry. *Measurement Science and Technology*, 6(5):507–514, 1995. 125, 126

[80] B. D. Jeffs and M. Gunsay. Restoration of blurred star field images by maximally sparse optimization. *Transactions on Pattern Analysis and Machine Intelligence*, 2(2):202–211, April 1993. 133

[81] L.P. Kadanoff. *Statistical Physics: Statistics, Dynamics and Renormalization*. World Scientific Publishing Company, 2000. 133

[82] A. Kaga, K. Yamaguchi, A. Kondo, and Y. Inoue. Combination of PIV data with cfd using cost function method. In *8th International Symposium on Flow Visualization*, page 257, Sorent, Italy, 1998. 39, 127

[83] Y.J. Kaufman, I. Koren, L.A. Remer, D. Tanre, P. Ginoux, and S. Fan. Dust transport and deposition observed from terra-modis spacecraft over the atlantic ocean. *J. Geophys. Res.*, 2005. , 2003JD004436. 107

[84] Y.H. Kim, A.M. Martínez, and A.C. Kak. Robust motion estimation under varying illumination. *Image and Vision Computing*, 23(4):365–375, 2005. 109, 117

[85] S. Kirpatrick, C.D. Gelatt, and M.P. Vecchi. Optimization by simulated annealing. *Science*, 220:671–680, May 1983. 142

[86] T. Kohlberger, E. Mémin, and C. Schnörr. Variational Dense Motion Estimation Using the Helmholtz Decomposition. *Scale-Space 2003, LNCS 2695*, pages 432–448, 2003. 38

[87] A.N. Kolmogorov. The local structure of turbulence in incompressible viscous fluid for very large reynolds numbers. *USSR Academy of Sciences*, 30:299–303, 1941. 16, 41, 78, 83, 116

[88] V. Kolmogorov. What energy functions can be minimized via graph cuts? *Transactions on Pattern Analysis and Machine Intelligence*, 26(2):147–159, February 2004. 45, 159, 160, 167, 168

[89] G. Korotaev, E. Huot, F.X. Le Dimet, I. Herlin, S. Stanichny, D. Solovyev, and L Wu. Retrieving ocean surface current by 4-D variational assimilation of sea surface temperature images. *Remote Sensing of Environment*, 112(4):1464–1475, April 2008. 41, 117

[90] B.E. Launder and D.B. Spalding. *Mathematical models of turbulence.* Academic Press, London, 1972. 15, 16

[91] LaVision. *Software for Intelligent Imaging.* DaVis Software, 2005. ii, 65, 66, 67, 68, 72, 99, 101, 107

[92] F.X. Le Dimet and O. Talagrand. Variational algorithms for analysis and assimilation of meteorological observations: theoretical aspects. *Tellus A*, 38A(2):97–110, 1986. 87

[93] J.A. Leese, C.S. Novak, and B.B. Clark. An automated technique for obtaining cloud motion from geosynchronous satellite data using cross correlation. *Journal of Applied Meteorology*, 10(1):118–132, 1971. 42, 106

[94] J.M. Lenoir. *Temps caracti¿½i¿½ristiques de structures turbulentes porteuses de scalaire passif.* PhD thesis, University of Lyon I, 2011. Thesis. 121

[95] A. Leonard. Energy cascade in large-eddy simulations of turbulent fluid flows. *Advances in Geophysics*, 18(1):237–248, 1974. 82

[96] M. Lesieur. *Turbulence in Fluids.* Kluwer Academic Publishers, 1997. 14

[97] M. Lesieur, O. Metais, and P. Comte. *Large Eddy Simulations of turbulence.* Cambridge University press., 2005. 107

[98] S.Z. Li. *Markov Random Field Modeling in Image Analysis, 3nd ed.* Springer-Verlag, 2009. 3, 44, 133

[99] H. Liu, A. Rosenfeld, and R. Chellapa. Two-frame multi-scale optical flow estimation using wavelet decomposition. In *International Conference on Accoustics, Speech and Signal Processing, ICASSP'02*, volume 4, 2002. 31

[100] T.S. Liu and L.X. Shen. Fluid flow and optical flow. *Journal of Fluid Mechanics*, 614:253–291, 2008. 23, 33, 36, 42, 47, 79, 118, 119

[101] B.D. Lucas and T. Kanade. An iterative image registration technique with an application to stereo vision. In *International Joint Conference on Artificial Intelligence*, volume 3, pages 674–679, 1981. 21, 25, 27

[102] K. Masuda. Retrieval of aerosol optical properties over the ocean using multispectral polarization measurements from space. *Applied Mathematics and Computation*, 116(1-2):103–114, November 2000. 119

[103] J. Mathieu and J. Scott. *Turbulent Flow*. Cambridge University Press, 2000. 7, 14

[104] A. Melling. Tracer particles and seeding for particle image velocimetry. *Measurement Science and Technology*, 12(8):1406–1416, 1997. 128

[105] E. Mémin and P. Pérez. Adaptative multigrid and variable parameterization for optical-flow estimation. Technical report, Technical Teport - IRISA, 1997.

[106] E. Memin and P. Perez. Dense estimation and object-based segmentation of the optical-flow with robust techniques. *Transactions on Image Processing, IP*, 7(5):703–719, May 1998. 30, 31, 46

[107] E. Memin and P. Perez. A multigrid approach to hierarchical motion estimation. In *International Conference on Computer Vision, ICCV'98*, pages 933–938, Bombay, India, January 1998. IEEE. ii, 57, 65, 67, 70, 76, 195

[108] E. Memin and P. Perez. Hierarchical estimation and segmentation of dense motion fields. *International Journal of Computer Vision*, 46(2):129–155, February 2002. 30

[109] N. Metropolis, A. Rosenbluth, M. Rosenbluth, A. Teller, and E. Teller. Equations of state calculations by fast computing machines. *Journal of Chemical Physics*, 21:1087–1091, 1953. 142

[110] Microsoft. Merdia player 9 video quality demos. Technical report, *microsoft.com/windows/windowsmedia/demos/video_quality_demos.aspx*. 61, 62, 170

[111] A. Mitiche and P. Bouthemy. Computation and analysis of image motion: A synopsis of current problems and methods. *International Journal of Computer Vision*, 19(1):29–55, 1996. 21

[112] J. W. Modestino and J. Zhang. A markov random field model-based approach to image interpretation. *R. Chellappa and A. Jain, editors, Markov Random Fields: Theory and Applications*, pages 369–408, 1993. Academic Press, Inc., Boston. 133

[113] P. Moin, K. Squires, W.. Cabot, and S. LLee. A dynamic subgrid scale model for compressible turbulence and scalar transport. *Physics of Fluids A: Fluid Dynamics*, 3(11):2746–2757, 1991. 83, 116

[114] A.S. Monin and A.M. Yaglom. *Statistical Fluid Mechanics: Mechanisms of Turbulence*, volume 1. The MIT Press, 1979. 14

[115] J. Nocedal and S.J. Wright. *Numerical optimization*. Springer, 1999. 49

[116] J.M. Odobez and P. Bouthemy. Robust multiresolution estimation of parametric motion models. *Journal of Visual Communication and Image Representation*, 6(4):348–365, 1995. 27, 30, 31

[117] K. Ogawara, T. Noborizato, and S. Iida. A moving least square PIV algorithm coupled with Navier-Stokes flow solver. In *2nd International Symposium on Particle Image Velocimetry*, pages 125–130, 1997. 39, 127

[118] K. Okamoto, S. Nishio, and T. Saga. Standard images for particle-image velocimetry. *Measurement Science and Technology*, 11(6):685–691, 2000. 65

[119] T. Okuno, Y. Sugii, and S. Nishio. Image measurement of flow field using physics-based dynamic model. *Measurement Science and Technology*, 11:667–676, 2000. ii, 65, 67, 68, 127, 194

[120] N. Papadakis. *Assimilation de données images : application au suivi de courbes et de champs de vecteurs*. PhD thesis, Université de Rennes I, 2007. 33, 39, 40, 41, 42, 117

[121] N. Papadakis and E. Mémin. Variational assimilation of fluid motion from image sequences. *SIAM Journal on Imaging Science*, 4:343–363, 2008. iii, 41, 72, 76, 87, 88, 95, 97, 113, 117, 118, 195

[122] N. Papenberg, A. Bruhn, T. Brox, S. Didas, and J. Weickert. Highly accurate optic flow computation with theoretically justified warping. *International Journal of Computer Vision*, 67(2):141–158, April 2006. 29, 31, 46, 51, 52

[123] N. Papenberg, A. Bruhn, T. Brox, and J. Weickert. Numerical justification for multiresolution optical flow computation. In *International Workshop on Computer Vision and ImageAnalysis, IWCVIA03*, volume 26, pages 7–12, 2003. 31, 50

[124] S.B. Pope. *Turbulent Flows*. Cambridge University Press, 2000. 7, 14, 83

[125] V. Prinet, C. Cassisa, and F.F. Tang. Mrf modeling for optical flow computation for multi-structure objects. In *Proceedings of the International Conference on Image Processing (ICIP'06)*, pages 1093–1096, Atlanta, USA, 2006. 4, 44

[126] D. Pullin. A vortex-based model for the subgrid flux of a passive scalar. *Physics of Fluids*, 12(9):2311–2319, 2000. 83, 116

[127] M Qiu. Computing optical flow based on the mass-conserving assumption. *International Conference on Pattern Recognition*, 3:7041–7045, 2000. 33, 34

[128] G.M. Quénot. Performance evaluation of an optical flow technique applied to particle image velocimetry using the VSJ Standard Images. *Journal of Visualization*, 3(2):125–133, June 2000. ii, 65, 67, 70, 195

[129] M. Raffel, B. Leitl, and J. Kompenhans. Data validation for particle image velocimetry. *Laser Techniques and Applications in Fluids Mechanic*, pages 210–226, 1993. 126

[130] M. Raffel, C. Willert, S.T. Wereley, and J. Kompenhans. *Particle Image Velocimetry*. Springer Berlin Heidelberg, 2007. 21, 25, 121, 127

[131] O. Reynolds. On the dynamical theory of incompressible viscous fluids and the determination of the criterion. *Philosophical Transactions of the Royal Society of London*, 186:123–164, 1895. 17

[132] O. Reynolds. *Papers on mechanical and physical subjects-the sub-mechanics of the Universe*. Collected Work, Volume III, Cambridge University Press, 1903. 11

[133] C.L. Ribault, S. Sakar, and S.A. Stanley. Large eddy simulation of evolution of a passive scalar in plane jet. *American Institute of Aeronautics and Astronautics Journal*, 39:1509–1516, 2001. 78

[134] B. Rouchouze, P. Mathieu, T. Gaidon, and M. Barlaud. Motion estimation based on markov random fields. In *in Proc. IEEE International Conference on Image Procecing*, pages 270–274, 1994. 133

[135] P. Ruhnau, C. Guetter, T. Putze, and C. Schnörr. A variational approach for particle tracking velocimetry. *Measurement Science and Technology*, 16(77):1449–1458, 2005. ii, 32, 65, 67, 70, 76, 195

[136] P. Ruhnau and C. Schnörr. Optical Stokes flow estimation: an imaging-based control approach. *Experiments in Fluids*, 42(1):61–78, novembre 2006. 29, 31, 39, 116

[137] P. Ruhnau, A. Stahl, and C. Schnörr. On-line variational estimation of dynamical fluid flows with physics-based spatio-temporal regularization. *Pattern Recognition*, 4174:444–454, 2006. 33, 39, 40, 41, 42, 116, 118

[138] P. Ruhnau, A. Stahl, and C. Schnörr. Variational estimation of experimental fluid flows with Physics-Based Spatio-Temporal Regularization. *Measurement Science and Technology*, 18:755–763, 2007. 13, 40

[139] P. Sagaut. *Large Eddy Simulation for Incompressible Flows, An Introduction*. 3rd ed., Springer, Berlin, 2006. 3, 15, 18, 81, 82, 83, 84

[140] M. Satoh, T. Matsuno, H. Tomita, H. Miura, T. Nasuno, and S. Iga. Nonhydrostatic icosahedral atmospheric model (NICAM) for global cloud resolving simulations. *Journal of Computational Physics*, 227(7):3486–3514, 2008. 119

[141] F. Scarano. Iterative image deformation methods in PIV. *Measurement Science and Technology*, 13(1):1–19, 2002. 125

[142] F. Scarano and M. L. Riethmuller. Iterative multigrid approach in PIV image processing with discrete window offset. *Experiments in Fluids*, 26(6):513–523, mai 1999. 124, 125, 126

[143] D. Scharstein and R. Szeliski. A taxonomy and evaluation of dense two-frame stereo correspondence algorithms. *International Journal of Computer Vision*, 47(1-3):7–42, April 2002. 148

[144] D. Scharstein and R. Szeliski. High-accuracy stereo depth maps using structured light. *Conference on Computer Vision and Pattern Recognition*, 1(June):195–202, 2003. 148

[145] C. Schnorr. On functionals with greyvalue-controlled smoothness terms for determining optical flow. *Transactions on Pattern Analysis and Machine Intelligence*, 15(10):1074–1079, October 1993. 30

[146] L. Shao, J.P. Bertoglio, and M. Michard. Large Eddy Simulation of the Interaction between Two Distinct Turbulent Velocity Scales. *in Advances in Turbulence 3, Ed. Springer-Verlag*, pages 101–112, 1990. 83

[147] L. Shao, M. Michard, and J.P. Bertoglio. Effect of a Solid Body Rotation on the Turbulent Transport. *Turbulent Shear Flow 8, Selected paper, Ed. Springer-Verlag*, pages 369–381, 1991. 83

[148] A.M. Shinneeb, J.D. Bugg, and R. Balachandar. Variable threshold outlier identification in PIV data. *Measurement Science and Technology*, 15(9):1722–1732, September 2004. 126

[149] S. Simoens and M. Ayrault. Méthodes expérimentales en mécanique des fluides. Technical report, Cours de Master MEGA, Ecole Centrale Lyon, version 2011. 2, 25

[150] S. Simoens, M. Ayrault, and J.M. Wallace. The flow across a street canyon of variable width - part 1: Kinematic description. *Atmospheric Environment*, 41:9002–9017, 2007. 99, 106

[151] S. Simoens and J.M. Wallace. The flow across a street canyon of variable width - part 2: Scalar dispersion from a street level line source. *Atmospheric Environment*, 42:2489–2503, 2008. 99, 106

[152] E.P. Simoncelli. Coarse-to-fine estimation of visual motion. In *8th Workshop on Image and Multidimensional Signal Processing*, pages 128–129, September 1993. 31

[153] J. Smagorinsky. General circulation experiments with the primitive equations i. the basic experiment. *Monthly Weather Review*, 91:99–164, 1963. 3, 113

[154] M. Sniedovich. *Dynamic programming. Foundations and principles.* 2nd ed., Pure and Applied Mathematics (Boca Raton), CRC Press., 2011. 67

[155] P. Spalart. Direct simulation of a turbulent boundary layer up to $Re_\theta = 1410$. *Journal of Fluid Mechanics*, 187:61–98, 1988. 101

[156] J. Sporring. *Gaussian Scale-Space Theory.* Kluwer Academic Publishers, 1997. 31

[157] M. Stanislas, K. Okamoto, and C. J. Kähler. Main results of the First International PIV Challenge. *Measurement Science and Technology*, 14(10):R63–R89, octobre 2003. 101

[158] M. Stanislas, K. Okamoto, C. J. Kähler, and J. Westerweel. Main results of the Second International PIV Challenge. *Experiments in Fluids*, 39(2):170–191, mars 2005. 101

[159] M. Stanislas, K. Okamoto, C. J. Kähler, J. Westerweel, and F. Scarano. Main results of the third international PIV Challenge. *Experiments in Fluids*, 45(1):27–71, avril 2008. 101

[160] L.K. Su and W.J.A. Dahm. Scalar imaging velocimetry measurements of the velocity gradient tensor field in turbulent flows. I. Assessment of errors. *Physics of Fluids*, 8(7):1869–1882, 1996. 3, 12, 33, 35, 42, 78, 81, 84

[161] L.K. Su and W.J.A. Dahm. Scalar imaging velocimetry measurements of the velocity gradient tensor field in turbulent flows. II. Experimental results. *Physics of Fluids*, 8(7):1883–1906, 1996. 12, 78

[162] D. Sun, S. Roth, T.U. Darmstadt, and M.J. Black. Secrets of Optical Flow Estimation and Their Principles. In *Conference on Computer Vision and Pattern Recognition*, 2010. 29, 31, 32

[163] D.Q. Sun. *A modern Matlab implementation of the Horn & Schunck and Black & Anandan algorithms*, 2008. http://www.cs.brown.edu/ dqsun/research/software.html. i, ii, vii, 63, 64, 66, 68, 70, 71, 73, 194, 195

[164] D. Suter. Mixed finite elements and Whitney forms for visual reconstruction. In *Proceedings of SPIE*, volume 2031, pages 51–62. SPIE, 1993. 37

[165] D. Suter. Motion estimation and vector splines. In *Proceedings of IEEE Conference on Computer Vision and Pattern Recognition*, pages 939–942. IEEE Comput. Soc. Press, 1994. 38, 40, 42

[166] R. Szeliski. *Computer Vision : Algorithms and Applications.* Springer, 2010. 32

[167] R. Szeliski and R. Zabih. An experimental comparison of stereo algorithms. In *Vision Algorithms: Theory and Practice, number 1883 in LNCS*, pages 1–19. Springer-Verlag, 1999. v, 152, 153, 155

[168] R. Szeliski, R. Zabih, D. Scharstein, O. Veksler, V. Kolmogorov, A. Agarwala, M. Tappen, and C. Rother. A comparative study of energy minimization methods for markov random fields with smoothness-based priors. *Transactions on Pattern Analysis and Machine Intelligence*, 30(6):1068–1080, June 2008. 3, 45, 76, 137, 140, 148, 150, 154, 156

[169] O. Talagrand and P. Courtier. Variational assimilation of meteorological observations with the adjoint vorticity equation. I: Theory. *Quarterly Journal of the Royal Meteorological Society*, 113(478):1311–1328, 1987. 87

[170] C.H. Teng, S.H. Lai, Y.S. Chen, and W.H. Hsu. Accurate optical flow computation under non-uniform brightness variations. *Computer Vision and Image Understanding*, 97:315–346, 2005. 117

[171] F. Thieuleux, C. Moulin, F.M. Bréon, F. Maignan, J. Poitou, and D. Tanré. Remote sensing of aerosols over the oceans using MSG/SEVIRI imagery. In *Annales Geophysicae*, number 12 in 23, page 3561. Sringer Verlag, 2005. 119

[172] A.N. Tikhonov and V.Y. Arsenin. *Solutions of ill-posed Problems*. John Wiley and Sons, Washington, D.C., 1977. 30

[173] P.T. Tokumaru and P.E. Dimotakis. Image correlation velocimetry. *Experiments in Fluids*, 19(1):1–15, 1995. 125

[174] U. Trottenberg, C.W. Oosterlee, and A. Schüller. *Multigrid*. Academic Press, 2001. 57

[175] J.Y. Vincont, S. Simoens, M. Ayrault, and J.M. Wallace. Passive scalar dispersion in a turbulent boundary layer from a line source at the wall and downstream of an obstacle. *Journal of Fluid Mechanics*, 424:127–167, 2000. 101

[176] M. Wainwright, T. Jaakkola, and A. Willsky. Map estimation via agreement on trees: Message-passing and linear programming. *IEEE Transactions Information Theory*, 51(11):3697–3717, 2005. 154

[177] J. Weickert. *Anisotropic diffusion in image processing*. Teubner, 1998. Stuttgart. 29, 30

[178] J. Weickert and C. Schnorr. Variational optic flow computation with a spatio-temporal smoothness constraint. *Journal of Mathematical Imaging and Vision*, 14(3):245–255, May 2001. 39

[179] P. wesseling. *An introduction to multigrid Methods*. Weiley, Chichester, 1992. 57

[180] J. Westerweel. Efficient detection of spurious vectors in particle image velocimetry data. *Experiments in Fluids*, 16(3-4):236–247, 1994. 124, 126

[181] J. Westerweel, D. Dabiri, and M. Gharib. The effect of a discrete window offset on the accuracy of cross-correlation analysis of digital PIV recordings. *Experiments in Fluids*, 23(1):20–28, May 1997. 124, 125

[182] D.C. Wilcox. *Turbulence Modeling for CFD*. DCW Industries, Berlin, 2006. 15

[183] R.P. Wildes, M.J. Amabile, A.M. Lanzillotto, and T.S. Leu. Physically based fluid flow recovery from image sequences. In *Conference on Computer Vision and Pattern Recognition*, pages 969–975, 1997. 33, 34

[184] GS Winckelmans and TS Lund. A priori testing of subgrid-scale models for the velocity-pressure and vorticity-velocity formulations. In *Proceedings of the Summer Program - Center for Turbulent Research, Standford*, pages 309–388, 1996. 82

[185] J. Worby and W.J. MacLean. Establishing visual correspondence from multi-resolution graph cuts for stereo-motion. *Computer and Robot Vision, Canadian Conference*, 0:313–320, 2007. 160

[186] M. Xue, K. K. Droegemeier, and V. Wong. The Advanced Regional Prediction System (ARPS) - A multi-scale nonhydrostatic atmospheric simulation and prediction model. Part I: Model dynamics and verification. *Meteorology and Atmospheric Physics*, 75:161–193, 2000. 119

[187] Q. Yang and S.D. Ma. Intrinsic multiscale representation using optical flow in the scale-space. *Transactions on Image Processing*, 8(3):444–447, janvier 1999. 32

[188] A. Yoshizawa. Statistical modelling of passive-scalar diffusion in turbulent shear flows. *Journal of Fluid Mechanics*, 195:544–555, 1988. 83, 116

[189] J. Yuan, P. Ruhnau, E. Memin, and C. Schnorr. Discrete orthogonal decomposition and variational fluid flow estimation. *Scale-Space*, pages 267–278, 2005. 33, 38

[190] L. Zhou, C. Kambhamettu, and D.B. Goldgof. Fluid structure and motion analysis from multi-spectrum 2D cloud image sequences. In *Conference on Computer Vision and Pattern Recognition*, pages 744–751. IEEE Comput. Soc, 2000. 42, 79

[191] L. Zhou, C. Kambhamettu, D.B. Goldgof, K. Palaniappan, and A.F. Hasler. Tracking nonrigid motion and structure from 2d satellite cloud images without correspondences. *Transactions on Pattern Analysis and Machine Intelligence*, 23(11):1330–1336, November 2001. 12, 33, 34

[192] C.L. Zitnick, N. Jojic, and S.B. Kang. Consistent segmentation for optical flow estimation. In *International Conference on Computer Vision*, pages 1308–1315, 2005. 61, 62, 170

List of Symbols

(i, j) : Indices, page 13

α, β, γ : Weighting coefficient, page 137

$\beta_{ss'}$: per-pairing weight, page 147

Δt : Time discretization step (s), page 16

Δx : Horizontal discretization step (m), page 16

Δy : Vertical discretization step (m), page 16

Δz : Depth discretization step (m), page 16

δz : Thickness of observed scene, page 80

$\Delta = (\Delta_x, \Delta_y)$: Original image pixel resolution (also denoted Δ_0), page 50

δ_d : Disparity error tolerance in pixel for Stereo Matching, page 148

Δ_k : Image pixel resolution at pyramidal level k; $\Delta_k = (2^k \times \Delta x, 2^k \times \Delta y)$, page 50

Δ_s : Filter size in LES for a mesh, page 18

ε : A finite error quantity ($<< 1$), page 24

$\frac{D}{Dt}$: Total derivative $\frac{D}{Dt} = \frac{\partial}{\partial t} + \vec{V}.\vec{\nabla}$ (Lagrangian), page 10

Γ : State space of the random variable, page 134

ι : Velocity divergence ($\iota = \vec{\nabla}.\vec{v}$), page 41

Λ : Set of all possible configuration of the random variable field values, page 134

λ : The molecular free path (m), page 8

$\mathcal{C}$: Set of cliques $\mathcal{C} = \mathcal{C}_1, \mathcal{C}_2, ..., \mathcal{C}_n$, page 136

$\mathcal{C}_1$: Single-site clique, page 136

$\mathcal{C}_2$: Pair-site clique, page 136

$\mathcal{C}_3$: triple-site clique, page 136

$\mathcal{C}_4$: quadruple-site clique, page 136

$\mathcal{D}(t)$: Volume of a closed domain (material or not) at time t (m^3), page 11

$\mathcal{G}$: A grid of the multigrid method (set of pixel), page 57

$\mathcal{N}$: Neighborhood system; $\mathcal{N}_{\mathbf{x}}$ neighbor set of $\mathbf{x}$, page 133

$\mathcal{S}(t)$: Surface of the volume $D(t)$ at time t (m^2), page 11

$\mathcal{U}$: An uniform random value in $[0:1]$, page 141

$\mathcal{W}$: Filter (Window function): often Gaussian or Heaviside filters, page 27

μ : Dynamic viscosity ($kg.m^{-1}.s^{-1}$), page 13

$\nabla^2(\bullet)$: Laplacian operator, page 12

ν : Kinetic viscosity ($m.s^{-1}$), page 13

ν_s : Enstrophy-based subgrid scale model in [73], page 41

Ω : Image domain $\Omega = [0, N] \times [0, M]$, page 22

ω : Velocity potential function, page 38

Ω_b : boundary of domain Ω, page 39

$\overline{\varphi}$: Reynolds temporal average of physical quantity φ; $\overline{\overline{\varphi}} = \overline{\varphi}$, page 16

$\overline{P_d}$: Average of solid particle diameter, page 65

$\overrightarrow{\overrightarrow{\tau_{Re}}}$: Reynolds stress tensor $\overrightarrow{\overrightarrow{\tau_{Re}}} = \overline{\vec{V}\vec{V}} - \overline{\vec{V}}\,\overline{\vec{V}}$, page 16

$\overrightarrow{\overrightarrow{\tau_s}}$: Subgrid stress tensor in Navier-Stokes equation (2^{th} order tensor), page 18

$\overrightarrow{\tau_s}$: Subgrid stress tensor in Transport equation (1^{th} order tensor), page 82

$\overrightarrow{v_{ir}}$: Velocity of curl free, page 37

$\overrightarrow{v_{lam}}$: Velocity of translation, page 37

$\overrightarrow{v_{so}}$: Velocity of divergence free, page 37

$\Phi(\bullet)$: A function: isotropic or anisotropic, robust or quadratic,..., page 29

$\Re$: Set of the Real number, page 122

ρ : Density of the fluid ($kg.m^{-3}$), page 8

σ^2 : Variance (bandwidth) of a filter, page 32

$\mathbf{A}$: Matrix of image spatial gradients, page 27

$\mathbf{A}^T$: Transposed matrix of $\mathbf{A}$, page 27

$\mathbf{b}$: Matrix of image temporal gradient, page 27

$\mathbf{W}$: Diagonalized matrix, page 27

L_c : Characteristic length scale of the flow (m), page 14

L_{macro} : Order of magnitude macroscopic scale ($\mathrm{L}_{macro} > 10^{-6}m$), page 8

L_{micro} : Order of magnitude microscopic scale ($\approx 10^{-20}m$), page 7

T_c : Characteristic time scale of the flow (s), page 14

T_R : Time scale high enough compare to turbulent time scale T_c, page 16

U_c : Characteristic velocity scale of the flow ($m.s^{-1}$), page 14

φ' : Reynolds fluctuations of physical quantity φ; $\overline{\varphi'} = 0$, page 16

$\varphi(\mathbf{X}_p(t), t)$: A physical quantity function of space and time, page 10

φ^+ : LES large scales of physical quantity φ; $(\varphi^+)^+ \neq \varphi^+$, page 18

φ^- : LES fluctuation of physical quantity φ; $(\varphi^-)^+ \neq 0$, page 18

φ_t : Partial derivative of quantity φ along t, page 10

φ_x : Partial derivative of quantity φ along x, page 10

φ_y : Partial derivative of quantity φ along y, page 10

φ_z : Partial derivative of quantity φ along z, page 10

ϖ : Velocity vorticity ($\varpi = \vec{\nabla} \times \vec{v}$), page 40

ς : Stream potential function, page 38

$\vartheta(a^n)$: n^{th} order and higher term of Taylor expansion, page 26

$\vec{\delta}$: Small incremental updating velocity for DDE and SA minimization methods, page 159

$\vec{\nabla}(\bullet)$: Gradient operator. In 3D: $\left(\frac{\partial}{\partial x}, \frac{\partial}{\partial y}, \frac{\partial}{\partial z}\right)$, in 2D: $\left(\frac{\partial}{\partial x}, \frac{\partial}{\partial y}\right)$ (m^{-1}), page 10

$\vec{\nabla}.(\bullet)$: Divergence operator $\left(\sum_i \frac{\partial \varphi}{\partial x_i}\right)$, page 11

$\vec{\nabla} \times (\bullet)$: Curl operator, page 37

$\vec{\nabla}_3(\bullet)$: Gradient operator 2D + time, page 39

$\vec{\mathrm{C}}$: Cross-stress tensor, page 82

$\vec{\mathrm{L}}$: Leonard stress tensor, page 82

$\vec{\mathrm{R}}$: Subgrid Reynolds stress tensor, page 82

$\vec{\vec{\sigma}}$: Constraint tensor (fluid stress) $(N.m)$, page 13

$\vec{\vec{D}}$: Deformation tensor (s^{-1}), page 13

$\vec{\vec{I}}$: Metric tensor, page 13

$\vec{a}.\vec{b}$: Scalar product of $\vec{a}$, $\vec{b}$, page 7

$\vec{a} \times \vec{b}$: Vectorial product of $\vec{a}$, $\vec{b}$, page 7

$\vec{d}(\mathbf{x}, t)$: 2D apparent displacement vector $\vec{d} = (d_x, d_y)$, page 22

$\vec{d}^c$: 2D displacement field obtained by cross-correlation, page 121

$\vec{d}^c_f$: Fractional displacement component by sub-pixel interpolation from CC, page 124

$\vec{d}^c_I$: Closest integer displacement obtained from CC, page 124

$\vec{d}^r_k$: Residual displacement field at pyramidal level k, page 51

$\vec{d}_k$: 2D displacement field at pyramidal level k; $\vec{d}_k(\mathbf{x}) = \widetilde{\vec{d}_{k+1}(\mathbf{x})} + \vec{d}^r_k(\mathbf{x})$, page 51

$\vec{f}$: Volume forces applied to the fluid $(m.s^{-2})$, page 13

$\vec{g}$: Boundary condition on the velocity $\vec{v}$, page 39

$\vec{J}$: Total flux $(kg.m^{-2}.s^{-1})$, page 12

$\vec{n}$: normal vector, page 11

$\vec{u}(\mathbf{x}_p(t), t)$: Instantaneous velocity at time t for particle $\mathbf{x}_p(t)$, page 24

$\vec{V}(\mathbf{X}, t)$: 3D velocity vector (U, V, W) $(m.s^{-1})$, page 9

$\vec{v}(\mathbf{x}, t)$: 2D apparent velocity vector $\vec{v} = (u, v)$, page 22

$\vec{v}^c$: 2D velocity field obtained by cross-correlation, page 121

$\vec{v}^r_k$: Residual velocity field at pyramidal level k, page 51

$\vec{v}_g$ $(\vec{v}^r_{k_g})$: 2D grid velocity for multigrid method (within multiresolution), page 57

$\vec{v}_k$: 2D velocity field at pyramidal level k; $\vec{v}_k(\mathbf{x}) = \widetilde{\vec{v}_{k+1}(\mathbf{x})} + \vec{v}^r_k(\mathbf{x})$, page 51

$\vec{v}_l$ $(\vec{v}^r_{k_l})$: 2D local velocity for multigrid method (within multiresolution), page 57

$\vec{v}_c$: Exact 2D velocity field (ground truth), page 59

$\vec{v}_e$: Estimated 2D velocity field, page 59

$\widetilde{\varphi}$: Interpolated quantity from coarser level to a finer level ($k+1$ to k), page 31

$\widetilde{\vec{d}_{k+1}}$: Interpolated 2D displacement field from pyramidal level $k+1$ to level k, page 51

$\widetilde{\vec{v}_{k+1}}$: Interpolated 2D velocity field from pyramidal level $k+1$ to level k, page 51

ζ,ξ : Auxiliary variables, page 38

$a,\ b$: Constants, page 140

all : Mask of all image region for error computation, page 60

C : Scalar concentration ($kg.m^{-3}$), page 10

c : A clique (directed subset of sites s), page 136

D : Molecular diffusion coefficient ($m^2.s^-1$), page 12

D_t : Turbulent diffusion or subgrid scale diffusion, page 84

$d_x(\mathbf{x},t)$: Horizontal 2D apparent displacement component, page 22

$d_y(\mathbf{x},t)$: Vertical 2D apparent displacement component, page 22

$disc$: Mask of velocity discontinuity regions for error computation, page 60

ds : Elementary surface (m^2), page 11

dt : Infinitesimal time interval (s), page 8

dv : Elementary volume of a particle (m^3), page 8

E : Gibbs energy (or objective energy), page 136

e : An undirected edge of graph G, page 133

E_d : Data energy - data term (function of motion equation), page 136

E_k : Gibbs energy at pyramidal level k, page 53

E_s : Regularization energy - smoothness term, page 136

E_{k_d} : Data energy at pyramidal level k, page 53

E_{k_s} : Regularization energy at pyramidal level k, page 53

E_{uu} : The power spectrum , page 84

$Err_{\%}$: Percentage of bad matching pixel for Stereo Matching, page 148

$f(x_0, y_0, z_0, t)$: Function given horizontal coordinate of particle P at time t in Lagrangian description, page 9

$f(\mathbf{x}, t)$: Parametric function of u, page 27

$g(x_0, y_0, z_0, t)$: Function given vertical coordinate of particle P at time t in Lagrangian description, page 9

$g(\mathbf{x}, t)$: Parametric function of v, page 27

$G = (s, e)$: An undirected graph, page 133

h : Distance between 2 obstacles in LMFA experience) (m), page 99

$h(x_0, y_0, z_0, t)$: Function given depth coordinate of particle P at time t in Lagrangian description, page 9

I : An image, page 22

$I(\mathbf{x}, t)$: Image intensity brightness at pixel location $\mathbf{x}$ at time t, page 22

I^L : Left image in Stereo Application, page 147

I^R : Right image in Stereo Application, page 147

I_k : Image at pyramidal level k, page 51

K : Coarser image resolution of the multiresolution by pyramidal decomposition, page 50

k : Indice of image level of the pyramidal multiresolution, page 50

Kn : The Knudsen number, page 8

L_x : Width of observed scene (image), page 80

L_y : Height of observed scene (image), page 80

M : Number of vertical pixel in the image I, page 22

m : Total mass of a volume $\mathcal{D}(t)$, page 11

N : Number of horizontal pixel in the image I, page 22

$N_{\mathcal{G}}$: Horizontal and vertical sizes of a grid in pixel for multigrid method, page 57

$N_{\mathcal{W}}$: Size of square interrogation window, page 121

P : A particle, a material point, page 8

p : Pressure ($kg.m^{-1}.s^{-2}$), page 10

$P(A)$: Probability of A (prior probability), page 134

P_n : Number of solid particle, page 65

Q : A set random variables (a field), page 134

q : A configuration of Q (a realization of the random variable field), page 134

Q_{s_i} : A random variable, page 134

q_{s_i} : A value of Q_{s_i}, also called state or label, page 134

q_{sgs} : The turbulent subgrid scale kinetic energy, page 84

R_{12} : Cross-correlation function, page 121

Re : Reynolds number $Re = \mathrm{U}_c\mathrm{L}_c/\nu$, page 14

s : A site (node) of graph G (often pixel), page 133

Sc : Schmidt number $Sc = \nu/D$, page 14

T : Temperature (constant), page 135

t : Time (s), page 8

$U(\mathbf{X}, t)$: Horizontal 3D velocity component ($m.s^{-1}$), page 9

$u(\mathbf{x}, t)$: Horizontal 2D apparent velocity component, page 22

U_e : Outside boundary velocity amplitude in LMFA experiment, page 101

$untext$: Mask of image textureless regions for error computation, page 60

$V(\mathbf{X}, t)$: Vertical 3D velocity component ($m.s^{-1}$), page 9

$v(\mathbf{x}, t)$: Vertical 2D apparent velocity component, page 22

V_d : Data potential functions, page 137

V_s : Smoothness potential functions, page 137

V_{max} : Threshold value for E_s in Stereo Matching, page 147

$W(\mathbf{X}, t)$: Depth 3D velocity component ($m.s^{-1}$), page 9

Z : Normalized constant (partition function), page 135

$\mathbf{I_k}$: Warped image at pyramidal level k (transformed by $\widetilde{\vec{d}_{k+1}}$), page 51

$\mathbf{N}$: Total number of sites, meshes or pixels, page 16

$\mathbf{x} = (x, y)$: 2D spatial coordinates (x, y), page 10

$\mathbf{x}'$: A neighbor of $\mathbf{x}$, page 48

$\mathbf{X} = (x, y, z)$: A fixed position at each time (mathematical point), page 9

$\mathbf{X}_p(t)$: 3D spatial position of a particle P at time t, page 8

$\mathbf{x}_p(t)$: 2D spatial position of particle P at time t (in the image), page 23

2D : Two Dimensional (x, y), page 23

3D : Three Dimensional (x, y, z), page 23

AAE : Average Angle Error (in degree), page 59

AEPE : Average Endpoint Errors or L1 absolute error (in pixel by interval of time), page 59

B&A-SUN : Black and Anadan approach [21] (implementation by [163]), page 63

BCCE : Brightness Change Constraint Equation, page 26

BCCE_1 : DOF method defined on 1^{st} image $I(\mathbf{x}, t)$, page 45

BCCE_1 : DOF method defined on 2^{nd} image $I(\mathbf{x}, t + \Delta t)$, page 45

BP : Max-Product Loopy Belief Propagation minimization method, page 154

CC : Cross-Correlation method, page 25

CC+NS : Dynamical system correcting the CC-Classic approach by physical equations [119], page 67

CC-Classic : Classical cross-correlation approach [119], page 67

CCD : Charge Coupled Device, page 124

CE : Continuity Optical Flow Equation, page 33

DDE : Direct Descent Energy minimization method, page 140

DivCurl : 2^{nd} order Divergence and Curvature regularization, page 38

DNS : Direct Numerical Simulation, page 15

DOF : Differential Optical Flow method, page 21

FLTG : From Global to Local Constraints, page 144

FT : Fourier transform, page 122

GC : Graph Cuts minimization method, page 154

H&S-SUN : Horn and Schunck approach [77] (implementation by [163]), page 63

ICE : Integrated Continuity Optical Flow Equation, page 34

ICE-DivCurl : ICE motion equation and DivCurl regularization approach [46], page 67

ICM : Iterated Conditional Modes minimization method, page 139

IFT : Inverse Fourier Transform, page 122

LES : Large Eddy Simulation, page 15

LMFA : Laboratory of Fluid Mechanics and Acoustics, page 99

MAP : Maximum A Posteriori, page 137

MRF : Markov Random Fields, page 133

noW_MR : Proposed multiresolution by pyramidal decomposition without warping, page 53

ODP : Orthogonal Dynamic Programming OF approach [128], page 67

OF : Optical Flow: method which estimates 2D apparent motion, page 21

OF-Assim : DOF method using data assimilation with 2D vorticity equation [121], page 86

OF-MG : Robust Multiresolution & Multigrid H&S approach [107], page 67

OF-MS : Multiresolutio & multiscale H&S [135], page 67

RANS : Reynolds Average Navier-Stokes, page 15

RMS : Root Mean Square Velocity Error (in pixel by interval of time), page 59

SA : Simulated Annealing minimization method, page 141

TE : Our DOF method using filetered Transport Equation, page 86

TE-SGS : Our DOF method using filetered Transport Equation with SubGrid Scale model, page 86

TF_BCCE : DOF method defined on both images $I(\mathbf{x}, t)$ and $I(\mathbf{x}, t+\Delta t)$, page 45

TRW : Tree-Reweighted Message Passing minimization method, page 154

W_MR : Multiresolution by pyramidal decomposition with Warping, page 50

Résumé:
L'objectif de cette thèse est l'étude de l'évolution de champ scalaire transporté par un écoulement à partir d'une séquence d'images temporelles. L'estimation du champ de vitesse d'un écoulement turbulent est d'une importance majeure pour mieux comprendre le phénomène physique. Jusqu'à présent, le problème de la turbulence est généralement ignoré dans l'équation de mouvement des méthodes existantes. Les images contiennent une information discrète correspondant à la taille du pixel. Selon le niveau de turbulence de l'écoulement, les résolutions des pixels et du temps peuvent devenir trop grandes pour négliger l'effet des petites échelles (sous-pixel) sur le champ de vitesse. Nous proposons pour cela, une équation de mouvement définie par l'équation de transport de concentration filtrée pour laquelle un modèle classique de viscosité turbulente sous-maille est introduit afin de tenir compte de cet effet. Nous utilisons pour formuler le problème, une approche Markovienne. Une méthode de multirésolution par décomposition pyramidale, sans transformation d'image intermédiaire au cours du processus, est proposée. Cela permet de diminuer le nombre d'opérations sur les images. La méthode d'optimisation utilisée, couplée avec une approche multigrille, permet d'obtenir le champ de vitesse réel optimal. Notre approche est testée sur des séquences d'images synthétiques et réelles (expérience PIV et tempête de sable à partir d'image de télédétection) avec des nombres de Reynolds élevés. Les comparaisons avec des approches existantes sont très prometteuses.

Mots clés: Estimation du mouvement, LES, modèle sous-maille, flot optique, MRF, optimisation

---

摘要:
本论文利用时间序列图像，研究流场中夹带标量场的演化问题。在此问题中，湍流速度场的准确估计对物理现象的描述具有重大意义，但截至目前的做法一般都忽略了流场中的湍流问题。图片提供的信息一般基于像素点，是离散化的，随着像素空间和时间间隔的扩大，像素内的小尺度运动造成的影响将变得难以忽略（与湍流度有关）。为此，我们用过滤后的标量输运方程来引入经典的湍流亚格子涡粘模型，用马尔可夫方法以建立问题的数学模型，用金字塔分解的多分辨率法以减少图像的操作次数，并使用与多重网格方法耦合的优化方法来估计二维真实速度场。最后，用高雷诺数的合成和真实图像序列对本方法进行对比测试，结果令人满意。

关键词: 运动估计，大涡模拟, 亚格子模型, 光流, 马尔可夫网络, 优化

Abstract:
The objective of this thesis is to study the evolution of scalar field carried by a flow from a temporal image sequence. The estimation of the velocity field of turbulent flow is of major importance for understanding the physical phenomenon. Up to now the problem of turbulence is generally ignored in the flow equation of existing methods. Information given by images is discrete at pixel size. Depending on the turbulent rate of the flow, pixel and time resolutions may become too large to neglect the effect of sub-pixel small-scales on the pixel velocity field. For this, we propose a flow equation defined by a filtered concentration transport equation where a classic turbulent sub-grid eddy viscosity model is introduced in order to account for this effect. To formulate the problem, we use a Markovian approach. An unwarping multiresolution by pyramidal decomposition is proposed which reduces the number of operations on images. The optimization coupled with a multigrid approach allows to estimate the optimal 2D real velocity field. Our approach is tested on synthetic and real image sequences (PIV laboratory experiment and remote sensing data of dust storm event) with high Reynolds number. Comparisons with existing approaches are very promising.

Keywords: Motion estimation, LES, subgrid scale model, optical flow, MRF, optimization

---